

INFORMATION TO USERS

This manuscript has been reproduced from the microfilm master. UMI films the text directly from the original or copy submitted. Thus, some thesis and dissertation copies are in typewriter face, while others may be from any type of computer printer.

The quality of this reproduction is dependent upon the quality of the copy submitted. Broken or indistinct print, colored or poor quality illustrations and photographs, print bleedthrough, substandard margins, and improper alignment can adversely affect reproduction.

In the unlikely event that the author did not send UMI a complete manuscript and there are missing pages, these will be noted. Also, if unauthorized copyright material had to be removed, a note will indicate the deletion.

Oversize materials (e.g., maps, drawings, charts) are reproduced by sectioning the original, beginning at the upper left-hand corner and continuing from left to right in equal sections with small overlaps. Each original is also photographed in one exposure and is included in reduced form at the back of the book.

Photographs included in the original manuscript have been reproduced xerographically in this copy. Higher quality 6" x 9" black and white photographic prints are available for any photographs or illustrations appearing in this copy for an additional charge. Contact UMI directly to order.

UMI

A Bell & Howell Information Company
300 North Zeeb Road, Ann Arbor MI 48106-1346 USA
313/761-4700 800/521-0600



NOTE TO USERS

The original manuscript received by UMI contains pages with indistinct and/or slanted print. Pages were microfilmed as received.

This reproduction is the best copy available

UMI



UNIVERSITY OF ALBERTA

**Electrical Heating of Heavy Oil Reservoirs Using
Horizontal Wells**

by

Bruce C. W. McGee



A thesis submitted to the Faculty of Graduate Studies and Research in partial

fulfillment of the requirements for the degree of

Doctor of Philosophy

Department of Electrical Engineering

Edmonton, Alberta

Spring, 1998



National Library
of Canada

Acquisitions and
Bibliographic Services

395 Wellington Street
Ottawa ON K1A 0N4
Canada

Bibliothèque nationale
du Canada

Acquisitions et
services bibliographiques

395, rue Wellington
Ottawa ON K1A 0N4
Canada

Your file Votre référence

Our file Notre référence

The author has granted a non-exclusive licence allowing the National Library of Canada to reproduce, loan, distribute or sell copies of this thesis in microform, paper or electronic formats.

The author retains ownership of the copyright in this thesis. Neither the thesis nor substantial extracts from it may be printed or otherwise reproduced without the author's permission.

L'auteur a accordé une licence non exclusive permettant à la Bibliothèque nationale du Canada de reproduire, prêter, distribuer ou vendre des copies de cette thèse sous la forme de microfiche/film, de reproduction sur papier ou sur format électronique.

L'auteur conserve la propriété du droit d'auteur qui protège cette thèse. Ni la thèse ni des extraits substantiels de celle-ci ne doivent être imprimés ou autrement reproduits sans son autorisation.

0-612-29074-3

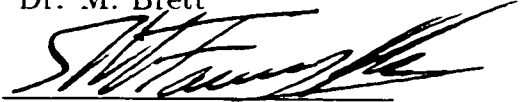
UNIVERSITY OF ALBERTA

FACULTY OF GRADUATE STUDIES AND RESEARCH

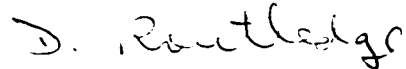
The undersigned certify that they have read, and recommend to the Faculty of Graduate Studies and Research for acceptance, a thesis entitled **Electrical Heating of Heavy Oil Reservoirs Using Horizontal Wells** submitted by Bruce C. W. McGee in partial fulfillment of the requirements for the degree of **Doctor of Philosophy**.



Dr. M. Brett



Dr. S. M. Farouq Ali

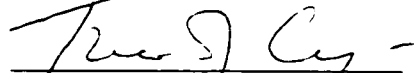


Dr. D. Routledge



Dr. F. Vermeulen

Supervisor



Dr. T. Cyr

External Examiner

Date: Jan 30. 1998

For my children Laura, Brandon, Meghan, and Frank.

Abstract

It is desirable to introduce heat into the production system of a horizontal well and the adjacent heavy oil reservoir. An increase in temperature can remove thermally alterable skin effects, which inhibit production, decrease oil viscosity to increase the productive length of the well, improve pumping efficiency, and reduce the energy requirements to lift the oil to surface. One way to create the heat is to use electricity.

The objective of this thesis is to solve the heat transfer problem for a horizontal well producing from a heavy oil reservoir where both the wellbore and reservoir are heated using low frequency electromagnetic energy. A semi-analytic model is thus developed that can be used to estimate the temperature distribution along the length of the horizontal well.

The problem consists of simultaneously solving for the effects of several concurrent heat transfer mechanisms occurring in different regions of the wellbore and reservoir. Electrical current flowing in the reservoir produces heat there because of the resistance of the reservoir. Significant heat is also generated as current flows in the horizontal well as a result of hysteresis and eddy current losses. As well, heat is produced from the reservoir with the fluids that flow into the wellbore and heat is conducted away from the well by thermal conduction. Thus, the heat transfer problem has to account for linear and non-linear electrical heat sources in several regions and heat transfer by thermal conduction and convection.

The horizontal well is constructed from commercial grade carbon steel pipe which is an electrically conducting ferromagnetic material. The hysteresis and eddy current losses in the steel pipe are determined using a finite difference time domain solution of Maxwell's equations. This numerical model, herein called the *EM Pipe Loss* model, is programmed to account for the non-linear magnetization process of the material using hysteresis loops. The hysteresis and eddy current losses in the pipe are calculated for a range of current values. A general polynomial is then fit to the calculated data so that the electrical losses can be interpolated for any value of current. The numerically derived polynomial is then incorporated into the equations

that describe the heat transfer problem, for which an analytic solution is then obtained.

It was found that for a long horizontal well, heat transfer to the adjacent reservoir by thermal conduction from the heated wellbore has a greater effect on the temperature achieved in the reservoir than heat transfer by convection and electrical heating by current flow in the reservoir. Also, it is shown that hysteresis and eddy current losses in the steel pipe cannot be ignored as was done previously [1], [2], and [3]. For a given current, hysteresis effects can more than triple the total power losses in the horizontal wellbore and other sections of the production system when compared to the power losses that would be present if hysteresis effects are ignored. This limits the magnitude and extent of electrical heating in the reservoir adjacent to the wellbore that can be achieved. The results obtained show that a significant volume of the reservoir and length of the horizontal well can be heated, which can substantially contribute to enhanced production rates from the reservoir.

Acknowledgments

The author wants to thank Dr. F. E. Vermeulen for his incredible support, mentorship, and friendship during this project.

Thanks are also due to Mr. Jim Fearn for his high standard of technical excellence in the construction of the experimental apparatus and Mr. Trent Loga for sharing his outstanding mathematical skills.

I want to thank those who have been an inspiration and motivation: John Howard, Julie Chan, Tom Harding, James Muldowney, Don Best, Homer Spencer, Leon Werenka, Ken O'Reilly, Robert Holt, Richard Schneider and of course my family.

I would like to thank to Dr. Kaz Vinsome for the use of his numerical simulation program TETRAD and Mr. Robert Isted for the use of his high current transformer.

This project is supported in part by research grants from the Natural Sciences and Engineering Research Council for which I am grateful.

Finally, I thank God.

BRUCE C. W. MCGEE

University of Alberta

Spring 1998

Contents

Chapter 1 Introduction	1
1.1 Overview	1
1.2 Background on Low Frequency Electrical Heating of Oil Reservoirs	7
1.3 Introduction to Magnetic Materials.	11
Chapter 2 Numerical Analysis of the Hysteresis and Eddy Current Losses in the Horizontal Well	14
2.1 Introduction	15
2.2 Finite Difference Time Domain Solution	19
2.2.1 Partial differential equation for the magnetic field strength.	20
2.2.2 Discretization of the partial differential equation for the magnetic field strength.	22
2.2.3 Numerical determination of the electric field strength.	30
2.2.4 The magnetization process for the steel pipe.	31
2.2.5 Distance factor method for constructing the hysteresis loops.	33
2.2.6 Determination of the power losses.	39
2.3 Analytic and Numerical Validations of the <i>EM Pipe Loss</i> Model.	42
2.3.1 Validation using the <i>Loga</i> analytic model.	42
2.3.2 Validation using the <i>Zakrzewski-Peitrás</i> numerical model.	45
2.4 Experimental Validation of the <i>EM Pipe Loss</i> model	53
2.4.1 Test setup and procedure.	54
2.4.2 Modifications of the test for collection of electrical data in the vicinity of strong electromagnetic fields.	59
2.4.3 Magnetic properties of the casing and tubing.	61
2.4.4 Determination of the electrical conductivity of the casing.	65

2.4.5	Validation of the <i>EM Pipe Loss</i> model using the <i>Electromagnetic Response Method</i>	70
2.4.6	Validation of the <i>EM Pipe Loss</i> model using the <i>Thermal Response Method</i>	72
2.5	Power Loss Interpolation Function for the Horizontal Wellbore	79
2.6	Analysis using the <i>EM Pipe Loss</i> Model	83
2.6.1	Impact of hysteresis on the distribution of the electromagnetic fields and power losses in steel pipe.	85
2.6.2	The hysteresis losses as a function of the current conducted in the centralized tubing.	87
2.6.3	The effect of the electrical conductivity of the pipe on the power losses in the casing.	90
2.6.4	Impact of the choice of hysteresis loop data on the calculation of the electromagnetic response of the steel pipe.	97
2.6.5	Calculation of the effective pipe resistance for the casing . . .	100
Chapter 3 Semi-Analytic Solutions of the Heat Transfer Problem		105
3.1	Introduction	105
3.1.1	Overview	105
3.1.2	Statement of the problem.	106
3.1.3	Numerical inversion of the Laplace transform.	110
3.2	Radial Semi-Analytic Heat Transfer Model	111
3.2.1	Radial heat transfer model in the wellbore.	112
3.2.2	Radial heat transfer model in the casing.	113
3.2.3	Radial heat transfer model in the reservoir.	116
3.2.4	Determination of unknown coefficients from the boundary conditions.	125
3.3	Validation of the Radial Semi-analytic Model	127
3.3.1	<i>Base Case</i> data set.	128
3.3.2	Validation using the <i>Killough and Gonzalez</i> analytic model. .	128
3.3.3	Validation using the <i>Conduction</i> model	132
3.3.4	Validation of the radial semi-analytic model using <i>TETRAD</i> .	135
3.4	The Axial Semi-Analytic Model	139

3.4.1	The axial heat transfer problem in the wellbore	139
3.4.2	Determination of $\hat{T}_2(r, s)$ and derivative.	144
3.4.3	Validation of the axial semi-analytic model using <i>TETRAD</i> .	150
3.4.4	The impact of temperature dependent electrical conductivity. .	169
Chapter 4 Conclusions and Recommendations for Further Study		179
4.1	Conclusions	179
4.2	Recommendations for Further Study	181
Bibliography		183

List of Tables

2.1	The input data for the steel pipe used in the validation of the <i>EM Pipe Loss</i> model with the <i>Loga Analytic Model</i>	43
2.2	The input data for the steel pipe used in the validation of the <i>EM Pipe Loss</i> model with the <i>Zakrzewski-Peitrzas</i> numerical model.	47
2.3	Comparison of the numerical power flow calculations carried out with the <i>EM Pipe Loss</i> model and the <i>Zakrzewski-Peitrzas</i> numerical model. The input data are summarized in Table 2.2	53
2.4	Physical dimensions of the casing and tubing used in the experiment.	54
2.5	Sampled data and measurement details for the thermal response test.	60
2.6	Summary of the <i>LDJ Electronics Inc.</i> tests.	61
2.7	Data used to determine the electrical conductivity of the 7" casing.	69
2.8	Pipe properties and input data for the <i>EM Pipe Loss</i> model used in the <i>electromagnetic validation</i>	70
2.9	Comparison of the measured surface electric field strengths in <i>mV/m</i> with the electric field strengths calculated by the <i>EM Pipe Loss</i> model.	72
2.10	Comparison of the measured surface phase angle θ in degrees with calculated values of θ by the <i>EM Pipe Loss</i> model.	72
2.11	Input data for the <i>EM Pipe Loss</i> model which is used to determine $\rho_s(z)$.	84
2.12	Pipe properties and runtime data for the <i>EM Pipe Loss</i> model.	85
2.13	Results for the 7" casing for the case <i>without</i> hysteresis when the current in the centralized tubing is 500 <i>A RMS</i> at 60 <i>Hz</i>	88
2.14	Results for the 7" casing for the case <i>with</i> hysteresis when the current in the centralized tubing is 500 <i>A RMS</i> at 60 <i>Hz</i>	89
2.15	Pipe properties of the 7" casing and input data used for evaluating the effect of electrical conductivity on the power losses in the casing.	91

2.16	Functional relationship for the 7" casing between total power, P_t , and current, I_t , for $I_t > 200$ A <i>RMS</i> and the three different values of electrical conductivity.	94
2.17	Effect of electrical conductivity on the depth of penetration of the electromagnetic field into the 7" casing.	95
2.18	Results for the 7" casing for the case with $\sigma_s = 7.3 \cdot 10^5$ S/m and a tubing current of $I_{rms} = 500$ A.	96
2.19	Results for the 7" casing for the case with $\sigma_s = 7.3 \cdot 10^6$ S/m and a tubing current of $I_{rms} = 500$ A.	97
2.20	Results for the 7" casing for the case with $\sigma_s = 7.3 \cdot 10^7$ S/m and a tubing current of $I_{rms} = 500$ A.	98
2.21	Pipe properties and runtime input data for comparing the effect of different hysteresis loops using the <i>EM Pipe Loss</i> model.	100
2.22	Comparison of the results for the two different hysteresis loops for the 7" casing and a tubing current of 367 A <i>RMS</i>	103
3.1	<i>Base Case</i> reservoir data.	128
3.2	<i>Base Case</i> thermal conductivity.	129
3.3	<i>Base Case</i> heat capacity (oil gravity of 12 °API)	129
3.4	<i>Base Case</i> operating data	130
3.5	Operating data for validation of the radial semi-analytic model using the <i>Killough and Gonzalez</i> model.	132
3.6	Operating data for comparison to the <i>Conduction</i> model.	135
3.7	Summary of the simulation runs used to validate the axial semi-analytic model.	156
3.8	<i>TETRAD</i> validation runs operating data. In all of the runs the initial reservoir temperature is 20 °C.	157
3.9	Electrical conductivity data for the reservoir as a function of temperature calculated using Equation 3.98 and the correlation shown in Equation 3.97.	171
3.10	Summary of the validation runs.	177

List of Figures

1.1	Organization of the thesis.	6
1.2	An electrically heated horizontal well.	10
1.3	Example of hysteresis loops over a range of different magnetic field strengths.	12
2.1	Electrically heated horizontal well showing the pipe configuration in the vertical and horizontal sections of the well.	15
2.2	The pipe configurations for the vertical and horizontal sections of the horizontal wellbore.	16
2.3	Description of the electromagnetic problem in the vertical section of the casing leading to the horizontal wellbore.	18
2.4	Grid system, consisting of node and grid points, adopted for the finite difference time domain numerical calculations.	23
2.5	Characteristics of the magnetization process within a grid cell.	32
2.6	The magnetization process during the transient period.	34
2.7	<i>Talukdar and Bailey</i> method for constructing hysteresis loops.	35
2.8	Method for constructing hysteresis loops used in this thesis and programmed into the <i>EM Pipe Loss</i> model. Note that the very first turn around point lies on the peak magnetization curve but subsequent turn around points generally do not until steady state is reached.	37
2.9	Comparison of the magnetic field strength, $H_\phi(r, t)$, calculated using the <i>EM Pipe Loss</i> model and the <i>Loga Analytic Model</i>	44
2.10	Comparison of the electric field strength, $E_z(r, t)$, calculated using the <i>EM Pipe Loss</i> model and <i>Loga Analytic Model</i>	45

2.11	Hysteresis loops for the magnetic material reproduced from Figure 4 of <i>Zakrzewski and Peitras</i> , Reference [86].	46
2.12	Comparison of the electric field strength at the surface of the ferromagnetic plate calculated using the <i>EM Pipe Loss</i> model, the <i>Zakrzewski-Peitras Numerical</i> numerical model, and their experimental data, [86].	49
2.13	Comparison of the electric field strength at the surface of the metal plate calculated using the <i>EM Pipe Loss</i> model, the <i>Zakrzewski-Peitras</i> numerical model and their experimental data, (Figure 5 of Reference [86]), with the maximum μ_r in the <i>EM Pipe Loss</i> model adjusted to match the measured electric field strength data.	50
2.14	Hysteresis loops at various depths from the surface of the solid steel sample calculated using the <i>EM Pipe Loss</i> model.	51
2.15	The electric field strength at various depths from the surface of the solid steel sample calculated using the <i>EM Pipe Loss</i> model.	52
2.16	End and system view of the equipment used in the thermal response test.	55
2.17	Side view of the equipment used in the thermal response test showing detailed dimensions.	56
2.18	The test apparatus as assembled in the Applied Electromagnetic Laboratory.	57
2.19	Hysteresis data for the 7" casing obtained using a hysteresigraph test as received from <i>LDJ Electronics Inc.</i>	62
2.20	Modification to the <i>LDJ Electronics Inc.</i> hysteresis data for the 7" diameter casing.	64
2.21	Several constructed hysteresis loops for the casing based on the <i>LDJ Electronics Inc.</i> tests and calculated using the <i>distance factor</i> method.	65
2.22	Comparison of the relative permeability μ_r calculated using raw and modified data.	66
2.23	Measurement locations of the surface electric field strengths and phase angles at various locations on the interior and exterior surfaces of the casing.	67

2.24	Measurement of the surface electric field strengths, (mV/m), and phase angles, (degrees) at various locations on the interior and exterior surfaces of the 7" casing for a sinusoidal excitation of 25 A (RMS) conducted in the centralized tubing.	68
2.25	Measurement of the surface electric field strengths (mV/m), and phase angles, (degrees) at various locations on the interior and exterior surfaces of the casing for a sinusoidal excitation of 50 A (RMS) conducted in the centralized tubing.	69
2.26	Comparison of the measured surface electric field strength, (mV/m), and phase angles, (degrees) at various locations on the interior and exterior surfaces of the 7" casing for currents of 100, 200 and 275 A (RMS) in the centralized tubing to calculated values using the <i>EM Pipe Loss</i> model.	71
2.27	Illustration of the <i>Thermal Response Method</i> using the temperature response of the 7" casing for a current of 500 A (RMS) in the centralized tubing.	75
2.28	Measured rate of temperature rise in the 7" casing as a function of the RMS current conducted in the centralized tubing.	75
2.29	Comparison of the experimental data and numerical calculation of the losses for the 4.0 meter long section of 7" casing used in the test as a function of the RMS current in the centralized tubing.	77
2.30	Percent hysteresis losses for the power losses shown in Figure 2.29 determined using the <i>EM Pipe Loss</i> model.	78
2.31	Comparison between the surface electric field strength derived from the test data and Equation 2.59 and calculated using the <i>EM Pipe Loss</i> model.	78
2.32	Resistivity as a function of the RMS current for the 7" K-55 steel casing, used in the horizontal wellbore.	83
2.33	The effect of hysteresis on the distribution of the electric field strength for the 7" steel casing for the case when the current in the centralized tubing is 500 A RMS at 60 Hz.	86

2.34	The effect of hysteresis on the distribution of the magnetic field strength for the 7" casing for the case when the current in the centralized tubing is 500 <i>A RMS</i> at 60 <i>Hz</i>	87
2.35	Analysis of the aggregate power losses per meter length of the 7" casing as a function of the magnitude of the current conducted in the tubing.	90
2.36	The phase angles on the interior and exterior surfaces of the 7" casing as a function of the magnitude of the current conducted in the tubing.	90
2.37	Hysteresis losses per meter of the 7" casing as a function of the magnitude of the current conducted in the tubing and for various values of electrical conductivity.	92
2.38	Eddy current losses per meter of the 7" casing as a function of the <i>RMS</i> current conducted in the 3½" tubing and various values of electrical conductivity.	92
2.39	Total losses per meter of the 7" casing as a function of the <i>RMS</i> current conducted in the tubing and various values of electrical conductivity.	93
2.40	The <i>RMS</i> value of the electric field strength in the 7" casing for various values of electrical conductivity and a current of 500 <i>A RMS</i> in the tubing.	94
2.41	The <i>RMS</i> value of the magnetic field strength distribution in the 7" casing for various values of electrical conductivity and a current of 500 <i>A RMS</i> in the tubing.	95
2.42	The 3,000 <i>A/m</i> and 1,000 <i>A/m</i> loops obtained from <i>LDJ Electronics Inc.</i> for the 7" diameter casing.	99
2.43	The <i>RMS</i> value of the electric field strength in the 7" casing calculated using the 3,000 <i>A/m</i> and 1,000 <i>A/m</i> hysteresis loops for a tubing current of 367 <i>A RMS</i>	101
2.44	The <i>RMS</i> value of the magnetic field strength in the 7" casing calculated using the 3,000 <i>A/m</i> and 1,000 <i>A/m</i> hysteresis loops for a tubing current of 367 <i>A RMS</i>	104
2.45	Comparison of the total effective resistance of the 7" casing calculated using the <i>EM Pipe Loss</i> model with data obtained experimentally by observing the temperature rise of the casing as a function of time.	104

3.1	Terminology and definition of the <i>regions</i> used in the semi-analytic models.	106
3.2	Depiction showing the determination of the heat flow into the wellbore from the casing using the radial semi-analytic model. Also shown is the use of the radial semi-analytic model at $z = Z_0$ to determine the Dirichlet boundary condition required for the derivation of the axial semi-analytic model.	108
3.3	Comparison of the temperature distribution obtained from the radial semi-analytic model to results obtained from the <i>Killough and Gonzalez</i> model, [3] for $\alpha_r = 3.54$	133
3.4	Comparison of the temperature distribution obtained from the radial semi-analytic model to results obtained from the <i>Killough and Gonzalez</i> model, [3] for $\alpha_r = 6.07$	134
3.5	Comparison of the temperature distribution obtained from Equation 3.49 to results obtained from the <i>Conduction</i> model for $r > r_w$ and $\alpha_r = 1.05$	136
3.6	Comparison of the temperature distribution obtained from Equation 3.49 to results obtained from the <i>Conduction</i> model for $0 \leq r \leq 2r_w$	136
3.7	Comparison of the temperature distribution obtained from Equation 3.49 to results obtained from the <i>Conduction Model</i> with convection ($\alpha_r = 1.51$).	137
3.8	Grid used for numerical validation of the radial semi-analytic model.	138
3.9	Comparison of the temperature distribution in the reservoir obtained from Equation 3.49 to results obtained from <i>TETRAD</i> with $\alpha_r = 1.51$	138
3.10	An element of the wellbore to describe the heat transfer problem in the wellbore.	141
3.11	Numerical calculation of the pressure drop between the reservoir and the wellbore along the length of a 1,000-meter long horizontal well. The wellbore is modeled using grid blocks that have a permeability of 100,000 Darcies.	153
3.12	Coarse grid used in <i>TETRAD</i> for validating the axial semi-analytic model.	154

3.13	Fine grid used in <i>TETRAD</i> for validating the axial semi-analytic model.	155
3.14	<i>Run 1.</i> Comparison of the axial temperature distribution obtained from the axial semi-analytic model to results obtained from numerical simulation for a 100-meter long well, same regional thermal properties, constant $\sigma_r(T)$, low fluid production rate of $Q_t = 0.5 m^3/day$, and after 30 days of heating.	158
3.15	<i>Run 2.</i> Comparison of the axial temperature distribution obtained from the axial semi-analytic model to results obtained from numerical simulation for a 100-meter long well, same regional thermal properties, constant $\sigma_r(T)$, moderate fluid production rate of $Q_t = 5.0 m^3/day$, and after 30 days of heating.	159
3.16	<i>Run 3.</i> Comparison of the axial temperature distribution obtained from the axial semi-analytic model to results obtained from numerical simulation for a 100-meter long well, same regional thermal properties, constant $\sigma_r(T)$, high fluid production rate of $Q_t = 10.0 m^3/day$, and after 30 days of heating.	160
3.17	<i>Run 4.</i> Comparison of the axial temperature distribution obtained from the axial semi-analytic model to results obtained from numerical simulation for a 100-meter long well, correct regional thermal properties, constant $\sigma_r(T)$, moderate fluid production rate of $Q_t = 5.0 m^3/day$, and after 30 days of heating.	162
3.18	<i>Run 4.</i> Comparison of the radial temperature distribution at the toe of the horizontal well obtained from the radial semi-analytic model to results obtained from numerical simulation for a 100-meter long well, correct regional thermal properties, constant $\sigma_r(T)$, moderate fluid production rate of $Q_t = 5.0 m^3/day$, and after 30 days of heating.	163
3.19	<i>Run 6.</i> Comparison of the axial temperature distribution obtained from the axial semi-analytic model to results obtained from numerical simulation for a 1,000-meter long well, same regional thermal properties, constant $\sigma_r(T)$, low fluid production rate of $Q_t = 10.0 m^3/day$, and after 30 days of heating.	164

3.20	<i>Run 7.</i> Comparison of the axial temperature distribution obtained from the axial semi-analytic model to results obtained from numerical simulation for a 1,000-meter long well, same regional thermal properties, constant $\sigma_r(T)$, moderate fluid production rate of $Q_t = 25.0 \text{ m}^3/\text{day}$, and after 30 days of heating.	165
3.21	<i>Run 8.</i> Comparison of the axial temperature distribution obtained from the axial semi-analytic model to results obtained from numerical simulation for a 1,000-meter long well, same regional thermal properties, constant $\sigma_r(T)$, high fluid production rate of $Q_t = 50.0 \text{ m}^3/\text{day}$, and after 30 days of heating.	166
3.22	<i>Run 9.</i> Comparison of the axial temperature distribution obtained from the axial semi-analytic model to results obtained from numerical simulation for a 1,000-meter long well, correct regional thermal properties, constant $\sigma_r(T)$, moderate fluid production rate of $Q_t = 25.0 \text{ m}^3/\text{day}$, and after 30 days of heating.	168
3.23	<i>Run 5.</i> Numerically calculated current distribution, $I(z)$, and electrical power losses, $\dot{q}_2(z)$, along the length of the 100-meter long horizontal well, for constant and temperature dependent $\sigma_r(T)$, same regional thermal properties, moderate fluid production rate of $Q_t = 5.0 \text{ m}^3/\text{day}$, and after 30 days of heating. The current is adjusted to maintain a maximum operating temperature of $100 \text{ }^\circ\text{C}$	172
3.24	<i>Run 5.</i> The effect of the temperature dependent $\sigma_r(T)$ on the numerical calculation of the axial temperature distribution and the electrical power losses in the casing, $\dot{q}_2(z)$, along the length of the 100-meter long horizontal well, for same regional thermal properties, moderate fluid production rate of $Q_t = 5.0 \text{ m}^3/\text{day}$, and after 30 days of heating. The current is adjusted to maintain a maximum operating temperature of $100 \text{ }^\circ\text{C}$	173

3.25	Run 5. Comparison of the numerically calculated temperature distribution along the length of a 100-meter long horizontal well for constant and temperature dependent $\sigma_r(T)$ with a constant total current of 500 A RMS, for same regional thermal properties, moderate fluid production rate of $Q_t = 5.0 m^3/day$, and after 30 days of heating.	174
3.26	Run 10. Comparison of the normalized temperature distribution for variable and constant $\sigma_r(T)$, along the length of a 1,000-meter long horizontal well, calculated using numerical simulation, with the same regional thermal properties, moderate fluid production rate of $Q_t = 25.0 m^3/day$, and after 30 days of heating.	175
3.27	Run 10. Comparison of the temperature distribution for variable and constant $\sigma_r(T)$, along the length of a 1,000-meter long horizontal well, calculated using numerical simulation and the axial semi-analytic model (constant $\sigma_r(T)$ only), with the same regional thermal properties, moderate fluid production rate of $Q_t = 25.0 m^3/day$, and after 30 days of heating.	176

Nomenclature

$\hat{T}(r, s)$ Laplace transform of $T(r, t)$

a_i, b_i, c_i, d_i i^{th} coefficient in the finite difference time domain equation , see equation (2.16), page 26

A_s surface area of a cross section of the casing, [m^2]

B magnetic induction vector, [$Tesla$], see equation (2.1), page 20

$d(B)$ distance factor as a function of the magnetic field strength, [$Tesla$] , see equation (2.31), page 39

d_1, d_2 upper and lower end point distance factors used in the construction of general hysteresis loops, [$Tesla$] , see equation (2.31), page 39

E electric field strength vector, [V/m], see equation (2.1), page 20

E_i electric field strength at grid i , [V/m], see equation (2.26), page 33

E_z electric field strength in the z direction, [V/m], see equation (2.9), page 22

E_{rms} RMS value of the electric field strength, [V/m]

H magnetic field strength vector, [A/m], see equation (2.1), page 20

H_ϕ magnetic field strength in the ϕ direction, [A/m], see equation (2.10), page 22

H_i magnetic field strength at node i , [A/m], see equation (2.13), page 25

H_{rms} RMS value of the magnetic field strength, [A/m]

i node location index

I_t total current in the casing or pipe, [A]

I_{rms} RMS value of the current, [A]

k_s wave number in steel, [m^{-1}] , see equation (2.50), page 46

L length of the pipe, [$meter$]

l length of the horizontal well, [meter]

n time level index , see equation (2.14), page 25

P_h hysteresis power losses, [W] , see equation (2.48), page 45

P_{ec} eddy current power losses, [W] , see equation (2.46), page 45

Q_t total fluid production rate, [m^3/day]

r radial coordinate, [meter]

r_i inside radius of the pipe, [meter]

r_i radius to node i , [meter]

r_w outside radius of the pipe, [m]

S normal surface vector, [m^2], see equation (2.11), page 23

T period of a sinusoidal wave, [second]

t time, [second]

T_0 initial temperature, [$^{\circ}C$]

u_i coefficients of the n^{th} order polynomial fitted to a plot of resistivity versus current, see equation (2.66), page 88

V volume, [m^3]

V_{rms} RMS value of the voltage, [V]

z z coordinate, [meter]

$\dot{q}_2(z)$ hysteresis and eddy current losses in the casing, [W/m^3] , see equation (2.67), page 88

$\dot{q}_3(r)$ electrical heating in the reservoir, [W/m^3], see equation (3.21), page 128

Greek

- δ skin depth, [meter] , see equation (2.69), page 92
- ΔP Poynting power flow, [W/m^2] , see equation (2.45), page 44
- Δr size of the grid block, [meter] , see equation (2.13), page 25
- Δt size of the time step, [second] , see equation (2.14), page 25
- ΔV elemental volume, [m^3]
- λ_f thermal conductivity of the fluid, [$W/(m^\circ C)$]
- λ_r thermal conductivity of the reservoir, [$W/(m^\circ C)$]
- λ_s thermal conductivity of the steel, [$W/(m^\circ C)$]
- μ magnetic permeability, [N/A^2], see equation (2.10), page 22
- μ_r relative permeability
- ω radian frequency, [sec^{-1}]
- ϕ angular coordinate
- ρ_r resistivity of the reservoir, [$\Omega \cdot m$]
- ρ_s resistivity of the steel, [$\Omega \cdot m$]
- ρC_f heat capacity of the fluid, [$J/(m^3^\circ C)$]
- ρC_r heat capacity of the reservoir, [$J/(m^3^\circ C)$]
- ρC_s heat capacity of the steel, [$J/(m^3^\circ C)$]
- σ electrical conductivity, [S/m]
- ε permittivity, [farad/m]

Chapter 1

Introduction

1.1 Overview

Using electrical heating in a long horizontal oil well can enhance the recovery of bitumen and heavy oil from the reservoir. Bitumen is a very viscous hydrocarbon with a specific gravity equal to or less than that of water. The oil viscosity is from 200,000 to 10,000,000 centipoise, which is much greater than the viscosity of water, which is one centipoise. Without the introduction of heat into the reservoir to lower the viscosity of the bitumen, the oil is immobile and cannot be recovered. Heavy oil has a specific gravity that is less than water but less than 22 °API (the specific gravity of water measured on the *American Petroleum Institute* scale is 10 °API). The oil can normally be produced from the reservoir without the aid of thermal stimulation. However, the introduction of heat can increase the productivity and recovery of oil from the reservoir.

The *National Task Force on Oil Sands Strategies of the Alberta Chamber of Resources* in their comprehensive report (1995), *The Oil Sands: A New Energy Vision for Canada*, Reference [4], stated that

Time is running out for our domestic conventional light and medium crude oil and something has to be done to make up the shortfall. There is only one major, relatively untapped source of petroleum left on the North American continent, the Alberta bitumen [*sic*] sands, [4].

The resource base for bitumen and heavy oil is immense. The *Alberta Energy and Utilities Board* estimates the total in place reserves for bitumen reservoirs at 1.7 trillion barrels with 300 billion barrels of these reserves estimated as being recoverable. The heavy oil reserves in the Western Canadian Sedimentary Basin of Alberta and Saskatchewan are estimated at 120 billion barrels, of which 5 to 8% is considered recoverable using present recovery methods. In comparison, the total remaining established *conventional* crude oil reserves in Western Canada are less than 4 billion barrels. At the present time, Canadian consumption averages 2.0 million barrels per day. The recoverable Alberta bitumen and heavy oil reserves can fulfil Canada's energy requirements for more than 160 years.

The task force recognizes the importance of horizontal well technology for the economic exploitation of bitumen and heavy oil reserves:

New Canadian technologies that use horizontal well *in situ* recovery processes are now being used commercially and are expected to more than double recovery rates, [4].

The task force also recognizes:

The direct benefit of a suitable technology for the exploitation of hard to recover bitumen and heavy oil resources will create additional employment opportunities and new prosperity unmatched by any business opportunity in Canada, [4].

The number of horizontal wells drilled in Western Canada has increased exponentially each year since 1988. Between 1988 and 1992 more than 500 horizontal wells were drilled in Alberta and Saskatchewan [5], with over 1,500 additional horizontal wells drilled from 1992 to 1994, [6]. For oil companies, horizontal well technology has become the primary exploitation strategy for heavy oil reservoirs. For example, in the Pelican Lake heavy oil area, located about 280 km north of Edmonton, Alberta, every oil well drilled since 1987 has been a horizontal well. Horizontal well technology has enabled economic viability for many heavy oil reservoirs where vertical well development was uneconomic, [7], [8].

The combined use of steam and horizontal well technology has greatly advanced the single and dual well steam-assisted gravity drainage process (SAGD),

[9], [10], [11], [12], [13], [14], and [15]. The SAGD technology was originally intended for tar sand reservoirs where primary production of fluids from the reservoir is not possible without first lowering the viscosity of fluids by heating. Recently SAGD has been applied to many heavy oil reservoirs, where there is primary production at initial reservoir conditions [16], [17], [18], [19], [20], [21], [22], [23], and [24].

In some instances steam is circulated to heat just the horizontal wellbore, as discussed by Best *et. al.* [25]. Best *et. al.* concluded that the transfer of heat away from the wellbore by thermal conduction is sufficient to thermally stimulate the reservoir, remove any thermally alterable skin effects, increase pump capacity, and reduce the viscosity of the oil in the wellbore to justify the incremental cost of steam injection facilities, lost oil production revenues during steaming, and increased operating costs. It is proposed in this thesis that a similar heating of the wellbore and reservoir can be accomplished using electrical energy. Electrical heating has the added advantages of direct heating in the reservoir, reduced total fluid handling requirements (thus reduced facilities costs), and simultaneous production of fluids and heating resulting in no lost oil revenues.

Additionally, it has been suggested that the use of electrical heating in bitumen reservoirs may be an effective way to thermally pre-condition the reservoir prior to implementation of SAGD, [26]. SAGD requires that a channel is established between two parallel horizontal wells of sufficient temperature that the oil is mobile within the channel. This is called the thermal channel. Once the thermal channel is established oil production can commence. Therefore it is desirable to establish the thermal channel as quickly as possible.

With conventional SAGD the thermal channel is formed as a result of thermal conduction into the reservoir while high temperature steam is circulated in the wellbore. This is a slow process and depending on the distance between the horizontal wells, may take up to a year to establish the thermal channel, [18]. Passing electrical current between the SAGD horizontal well pair can reduce the time it takes to establish the thermal channel. As current passes through the reservoir, electrical energy is converted to thermal energy by ohmic losses in accordance with the electrical properties of the reservoir. This heating process is *independent* of the mobility of the bitumen. As the horizontal well casing heats up

due to eddy current and hysteresis losses, the heat from the well is transferred to the reservoir by thermal conduction in a similar fashion as by circulating steam in the wellbore. Preliminary calculations indicate that the time to establish a thermal channel between a horizontal well pair in the presence of current passing through the reservoir between the wells, can be reduced from 12 months to three months, [26].

Electrical heating in SAGD processes may also allow the horizontal wells to be spaced farther apart, thus increasing the ultimate oil recovered from the reservoir. The reduction in time to pre-heat the reservoir and the potential for greater recovery of oil by increasing the distance between the wells are two factors that contribute significantly to the economic viability of a combined electrical heating and SAGD technology.

To properly determine the feasibility of using electrical heating technology in combination with horizontal wells requires a fundamental analysis of:

1. The electromagnetic problem associated with large currents conducted in the lossy ferromagnetic material used in the manufacture of the casing of the horizontal well. This problem requires the solution of the non-linear magnetization process of the ferromagnetic casing under the action of a sinusoidally varying excitation as governed by the hysteresis loops which are experimentally determined for the material,
2. The electrical current and fluid flow in the oil reservoir, and
3. The heat transfer dynamics between the regions consisting of the wellbore, casing, and reservoir and the resulting thermal response of the system.

This fundamental analysis of electrical heating technology for use with horizontal wells is the topic of this thesis.

Previous theoretical studies have ignored the combined hysteresis and eddy current losses in the casing and assumed that enormous currents can be used to heat the reservoir, [3], [27], [2], and [28]. In these studies, currents as large as 5,000 A *RMS* are passed through the reservoir from the horizontal well assuming no electrical losses in the casing. The fundamental determination of the electrical losses developed in this thesis indicates that currents of the order of 5,000 A *RMS* will cause the casing to overheat to unacceptable levels in *minutes*.

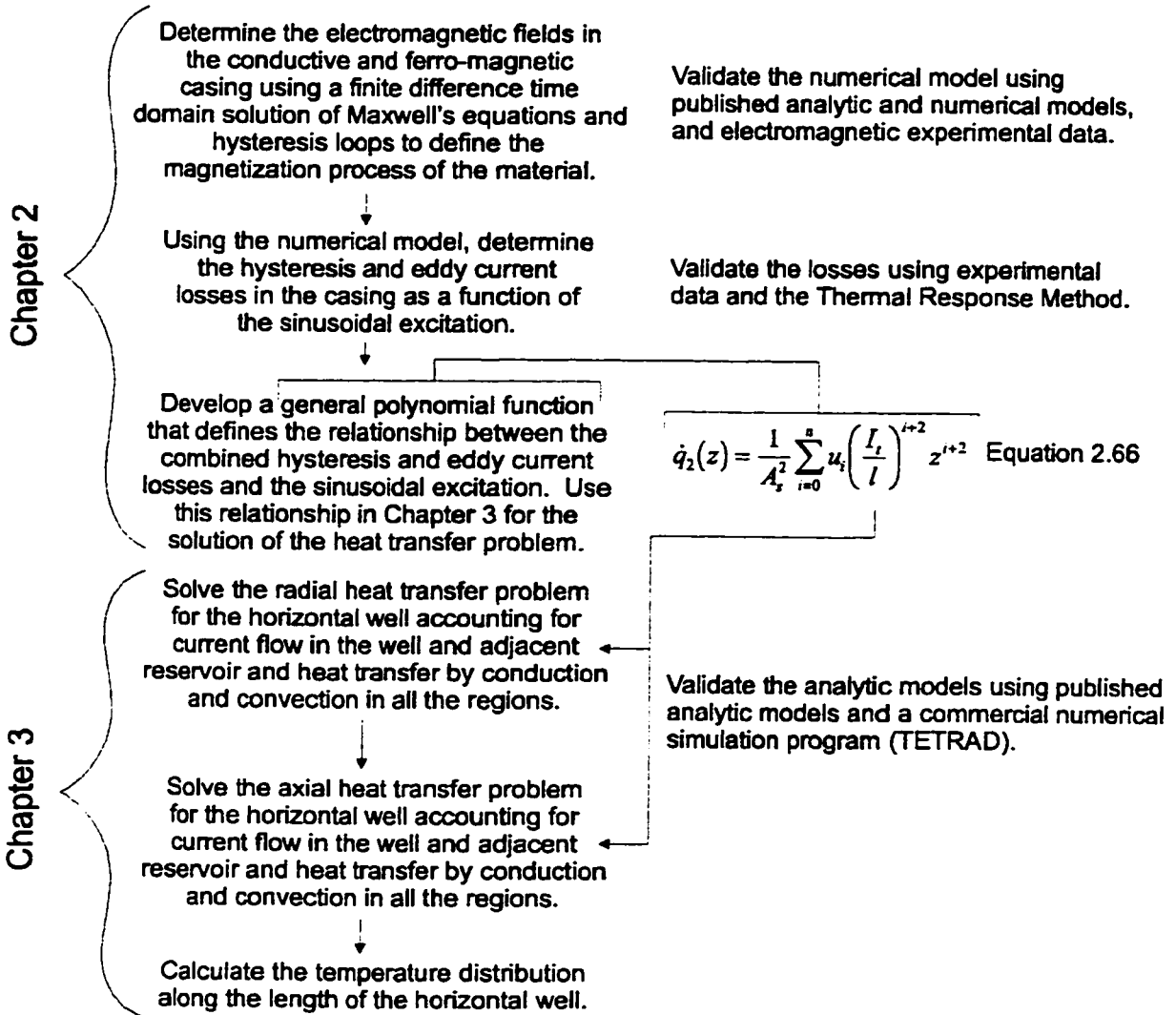
These previous studies determine the temperature rise in the reservoir from electrical heating using numerical simulation. The reported size of the grid block containing the horizontal well is of the order of several meters. Since the heat source distribution in the reservoir away from a horizontal well decreases as $1/r^2$, at a distance of less than one meter (for a typical well), the power density (*watt/m³*) has been reduced by over *100 times* from its value at the wellbore. To capture the electrical heating distribution in the reservoir, the size of the grid blocks near the well should be of the order of centimetres.

Other studies have developed models for the electrical losses in the casing and tubing that account only for the eddy current losses [1], and use indirectly related experimental data to account for the hysteresis losses, [29] and [30]. These studies have assumed that at lower currents, less than 250 A *RMS*, hysteresis losses are negligible and can be accounted for by an equivalent and linear magnetic permeability for the steel, [1]. The fundamental analysis of the hysteresis and eddy current losses developed in this thesis indicates that *hysteresis losses can account for up to 30 % of the total losses* at currents of 250 A *RMS*. The analysis also shows that the hysteresis effect on the eddy current distribution can result in total power losses that are *three times* greater than when hysteresis is not accounted for.

The thesis is organized as shown on Figure 1.1. The combined eddy current and hysteresis losses of the horizontal well are determined in *Chapter Two*. This is accomplished with a *finite difference time domain* solution of Maxwell's equations that incorporates the magnetization process of the casing using hysteresis loops. The numerical model which calculates the combined losses is called the *EM Pipe Loss* model. The model is validated using analytic, numerical, and experimental techniques.

Organization of the Thesis

Chapter 1 { Introduction



Chapter 4 { Conclusions and Recommendations for Further Study

Figure 1.1: Organization of the thesis.

A general polynomial function describing the relationship between the excitation current and the sum of the hysteresis and eddy current losses is then produced from the *EM Pipe Loss* model. The polynomial is in a suitable form that it can serve to describe a heat source term in the heat transfer problem, which is then solved, using analytic methods. This is accomplished in *Chapter Three*. In that chapter, the heat transfer problem between the wellbore, the casing, and the reservoir is solved. This is accomplished by taking the Laplace transform of the simultaneous partial differential equations that arise, and by subsequent numerical inversion of the Laplace transform solution into the time domain. The heat transfer problem accounts for the electrical losses in the casing characterized in *Chapter Two* and the electrical losses produced by current flow in the reservoir. Also accounted for are heat transfers by thermal conduction and convection.

The scope of the thesis is limited to the fundamental analysis of the electromagnetic, as well as the heat transfer problem, for the horizontal wellbore. Emphasis is placed on the validation of the analytic and numerical models developed in the thesis using experimental, analytic, and numerical approaches. The production performance of an electrically stimulated horizontal wellbore is not investigated here.

1.2 Background on Low Frequency Electrical Heating of Oil Reservoirs

This work is limited to electrical heating using low frequency, i.e. frequencies less than or equal to 60 Hz. Several publications involving high frequency methods, from several thousand to millions of Hz, are available in the literature, [31], [32], [33], [34], [35], [36], [37], [38], [39], [40], [41], [42], and [43].

Using electricity to increase the oil production rate from a well is not new technology. The oldest known means of using electricity to stimulate the oil production from a reservoir is the down-hole electric heater patented in 1865 under the patent, *Heating Oil Wells by Electricity*, [44]. Since then, there have been several reported applications of electrical heating designed to stimulate oil producing wells, [38], [45], [46], [47], [48], [49], [50], [51], [52], [53], [54], [55], [56],

[37], [57], [30],[58], [40], [59], [60], [61], [3], [62], [63], [64], [65], [66], [67], [68], [69], [70], [71], [72], [73], [74], [75], [27],[76], [2],[28],[77], [78], [79], [80], [81], [82], [83], [84],

The productivity increase of an electrically heated well can be substantial and is due to the

1. Removal of thermally alterable skin effects that are an obstacle to the flow of oil,
2. Reduction of the oil viscosity in the vicinity of the wellbore,
3. Reduced total pressure drop in the horizontal wellbore needed to produce the reservoir fluids, and
4. Improved efficiency of the down-hole pumping equipment in the well at the lowered oil viscosity.

Attractive features of the process are:

1. Electrical heating is operated as a continuous, not a cyclic process. Thus the heating occurs simultaneously with production of reservoir fluids as opposed to the *single well cyclic steam stimulation process* where the oil production from the well must be deferred until a predetermined volume of steam has been injected into the reservoir.
2. All the down-hole equipment to heat a well can be contained within a single wellbore. This allows for efficient use of rig and work-over time and generally reduces costs. Also, the capital costs of the electrical equipment and power supply are small compared to the capital costs for steam injection facilities.
3. There is no need to inject fluids into the reservoir, which can cause damage to the formation and reduce the preferential flow of oil in the reservoir.

The heavy oil reservoir consists of sand, oil, water, and gas. The sand matrix is electrically non-conductive. The reservoir derives the ability to conduct current from the conductive electrolytic connate water that partially fills the pore volume in the sand matrix. The pores are interconnected through the sand matrix by pore

throats. The connate water phase in the reservoir must be continuous if electrical current is to be pass through the formation.

The conductivity of the reservoir is determined by:

1. Shape, size, and number of the interstitial pore volumes and of the interconnecting passages,
2. Concentration of the dissolved electrolytes in the connate water,
3. Saturation of the water phase in the pore space, and
4. Temperature.

Figure 1.2 shows a simplified but representative example of an electrical heating system that uses combined horizontal and vertical wellbores. Several vertical wells are connected in series and all the current flowing from the vertical wells is collected at the horizontal well. This figure is extracted from References [83] and [81], which present the results of a recent field test by *Texaco Canada Petroleum Inc.* and the *Alberta Department of Energy*.

The production system consists of a tubing string concentrically located in a casing string. The tubing string extends to the pump and is used to facilitate the production of fluids. The pump is used to lift fluids from the reservoir to the surface. The casing string provides structural integrity in the vertical and horizontal sections of the wellbore. The horizontal portion of the wellbore is typically the vertical casing continuing on horizontally.

The current path is as follows. Electrical current flows from the power-conditioning unit to several vertical wells via power cables. In this example, current is conducted to the electrode using the tubing string. The tubing string is electrically isolated from the casing using non-conducting centralizers. Current flows from the electrodes in the vertical wells and into the reservoir.

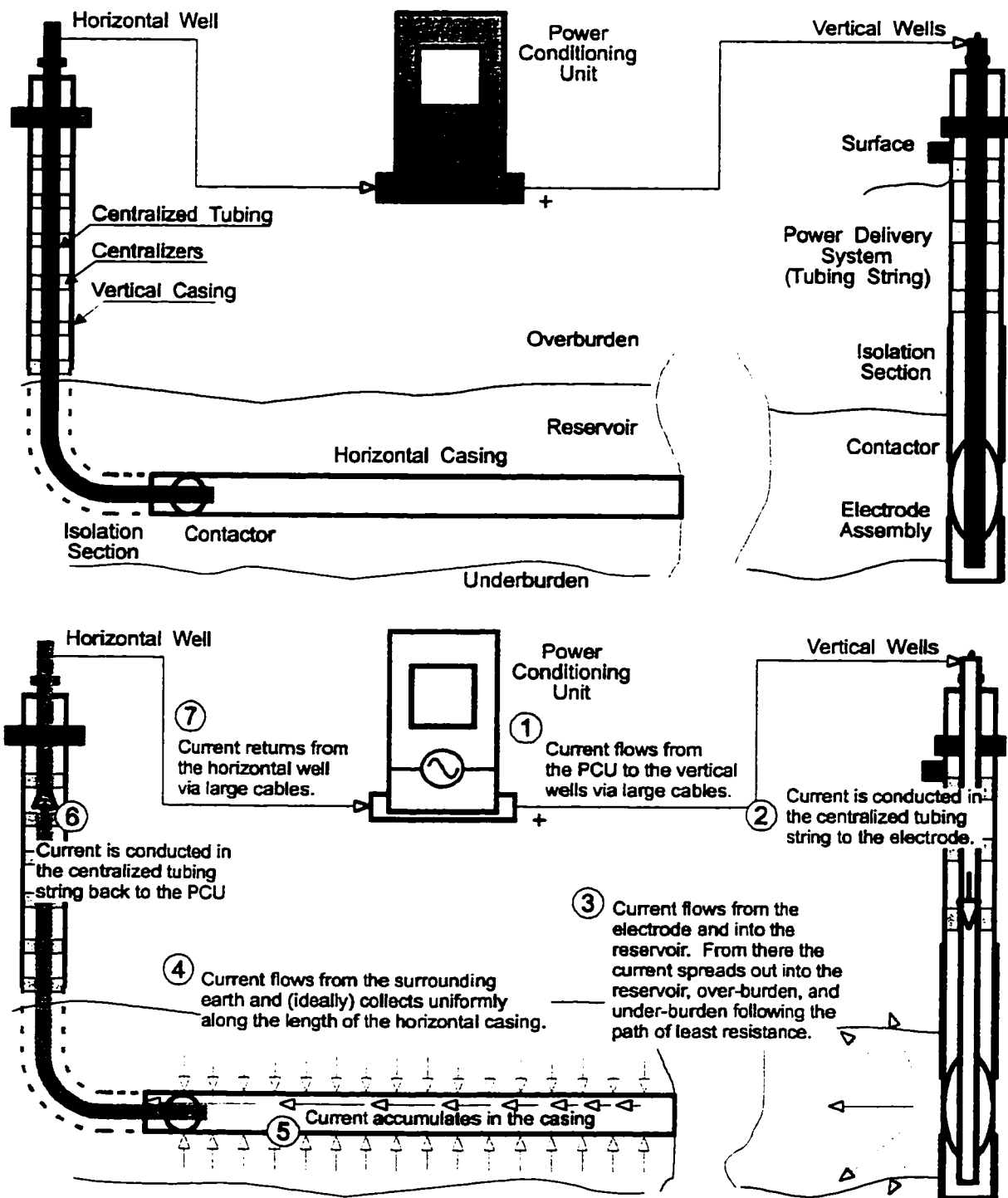


Figure 1.2: An electrically heated horizontal well.

The reservoir near the electrode is heated as a result of ohmic losses in the formation. From there, the current spreads out into the over- and under-burden, taking the path of least resistance to the horizontal well. At the horizontal well, current flows from the surrounding formation and is assumed to collect uniformly along the entire length of the casing. The current accumulates in the casing of the horizontal section of well and is conducted back to the surface by the centralized tubing in the vertical section of the wellbore. From here, current is returned to the power-conditioning unit via long cables on the surface.

The maximum allowable operating temperature of the system limits the amount of power that can be used to stimulate the well. The operating temperature of the system is determined by the interplay of fluid production rate and power losses in the tubulars. Fluids flow towards the well and increase in temperature since the formation temperature is higher near the well than elsewhere. As the production rate increases, more electrical power must be supplied to compensate for the increased rate of energy withdrawal from the formation by the produced fluids so that a desired temperature in the reservoir may be maintained. Power losses in the electrical conducting tubulars of the production system, such as the tubing and casing, will result in an increase in temperature. Depending on the cooling mechanism available at the location where these power losses are generated, excessive temperatures may limit the magnitude of the allowable current, and hence the power, that can be used to electrically heat the reservoir.

The goal of this thesis is to derive the mathematical models that can be used to determine the electromagnetic power losses in the conducting tubulars and to achieve the solution of the overall heat transfer problem so that the input power that can be used for electrical heating can be derived.

1.3 Introduction to Magnetic Materials

This section provides general background on the properties of magnetic materials. Specific details on the magnetization process for the casing and tubing are presented in *Chapter Two*.

Ferromagnetic material is characterized by a high magnetic permeability and by a non-linear and multi-valued relationship between the magnetic induction, \mathbf{B} , and magnetic field strength, \mathbf{H} . A basic measure of the magnetic properties of the material is the hysteresis loop. This shows the instantaneous relationship between the magnetic induction and the magnetic field strength over a complete cycle of operation. Each hysteresis loop has at its tips extremum values of magnetic induction and magnetic field strength. A plot of the extremum values of \mathbf{B} and \mathbf{H} is called the normal or *peak magnetization curve*. This curve then passes through the tips of a succession of \mathbf{B} - \mathbf{H} loops covering the range of magnetic induction such as shown in Figure 1.3

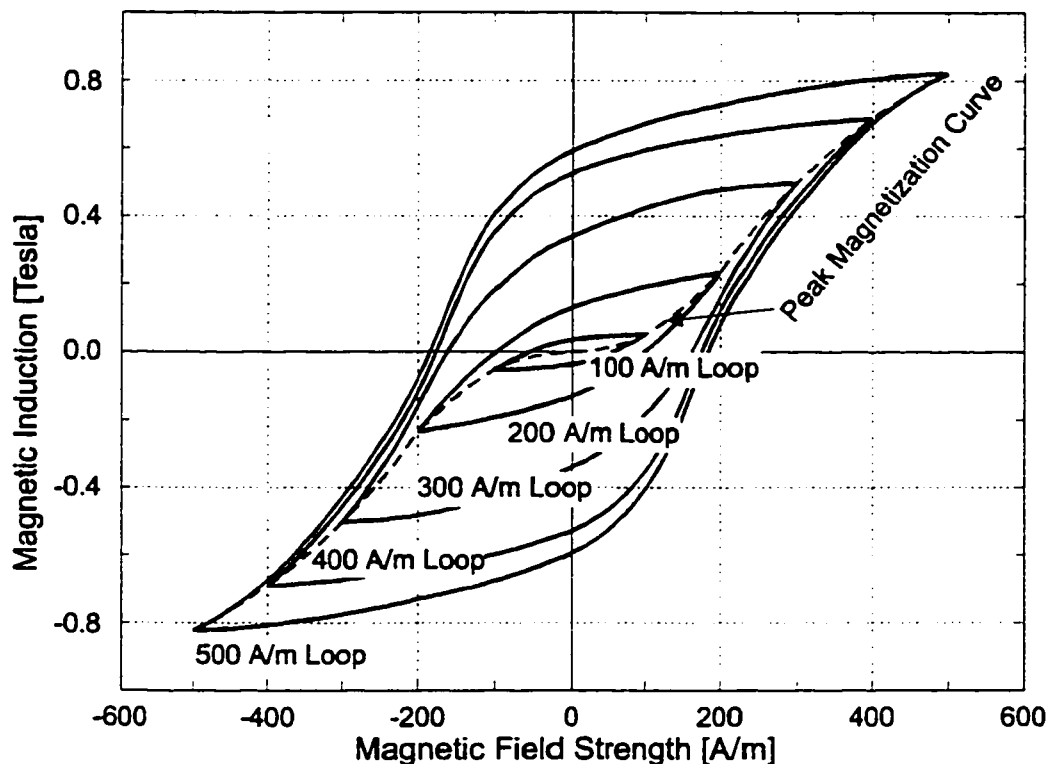


Figure 1.3: Example of hysteresis loops over a range of different magnetic field strengths.

Energy is dissipated in the magnetic material each time the material is subjected to one cycle of its \mathbf{B} - \mathbf{H} loop. The energy loss is separated into an eddy-current loss and hysteresis loss. The eddy-current loss is manifested by the I^2R loss due to currents that circulate in the steel pipe. The hysteresis loss is a manifestation of the energy expended in aligning the magnetic domains of the

material with the direction of the magnetic field strength. The losses depend upon the constituent components of the material, particularly the amount of silicon that is present, the frequency of excitation, the thickness of the material in a plane normal to the magnetic field strength, and the maximum magnetic induction, [85].

Most sheet-steel materials used in electro-magnetic circuits are manufactured to have preferred directions of magnetization so that the core loss is low and the magnetic permeability is high. Such materials are termed *grain-oriented steel*. By a suitable manufacturing technique, the grains are aligned in the rolling direction to make it the favoured direction of magnetization. When the direction of the magnetic field strength is parallel to the direction of the magnetic domains then these materials will have lower hysteresis losses than non-oriented steels, [85].

Silicon steel used to manufacture steel pipe has the desirable properties of low cost, high electrical conductivity, and high strength. However, the material is not optimized in the manufacturing process to minimize hysteresis losses. Therefore, hysteresis losses can and do contribute significantly to the total losses in an oil production system that utilizes electrical heating technology. Since hysteresis losses are generally significant in oil production tubulars, they must be accounted for in the thermal response of a well that is used for electrical heating. This can be done using the models developed in the thesis.

Chapter 2

Numerical Analysis of the Hysteresis and Eddy Current Losses in the Horizontal Well

This chapter presents a one-dimensional numerical solution in cylindrical coordinates of the electromagnetic field in a ferromagnetic electrically conducting cylindrical steel pipe. The solution uses hysteresis loops to account for variable magnetic permeability. Once the magnetic and electric field strengths have been obtained the combined eddy current and hysteresis power losses can be calculated. For the case with constant magnetic properties, (constant μ), the numerical model is compared to a simple analytic model. The numerical model is also compared to a similar numerical model that is solved in the Cartesian coordinate system. Validation of the numerical method with experimental data is presented.

The model is used to determine the losses in the steel pipe as a function of the magnetic excitation. The combined hysteresis and eddy current losses are then used to generate a polynomial expression for the effective resistivity as a function of current. This expression will then be used in *Chapter 3* for the solution of the heat transfer problem.

2.1 Introduction

The goal of this chapter is to derive a numerical model that can calculate the power losses for an electrically heated horizontal well. The numerical model is called the *EM Pipe Loss* model and is formulated to take into account both hysteresis and eddy current losses in pipe formed from ferromagnetic steel. Figure 2.1 shows the vertical and horizontal sections of the horizontal wellbore where the power losses are calculated. The power losses in the vertical section of the wellbore are associated with current flowing in the tubing string and the currents induced on the casing string. The power losses in the horizontal section of the wellbore are associated with current flow in the horizontal casing.

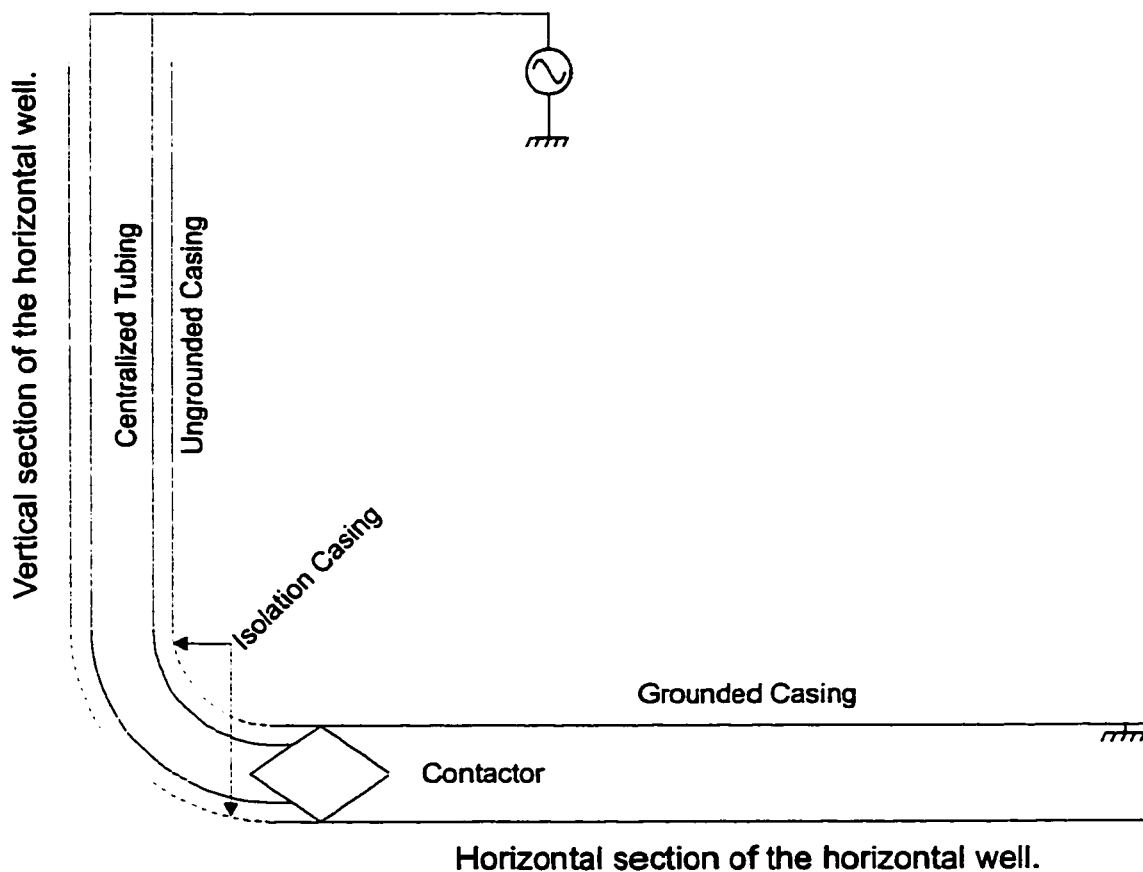


Figure 2.1: Electrically heated horizontal well showing the pipe configuration in the vertical and horizontal sections of the well.

Figure 2.2 shows the two pipe configurations considered here: 1) the casing-tubing pair in the vertical section of the wellbore and 2) the casing in the horizontal section of the wellbore (the dimensions for the pipes shown on the figure

are for the samples used to experimentally verify the numerical model). In the vertical section of the wellbore, current flows in the tubing and is distributed in the tubing as shown. This current produces a time varying magnetic field, which in turn induces current flow in the ungrounded casing. The current flows in a closed path around the length of the casing, in one direction on the interior surface and the opposite direction on the exterior surface, and is distributed within the casing as shown. Also shown is the current distribution in the horizontal well casing.

To determine the fraction of electrical power lost in the power delivery system and the temperature distribution along the length of the horizontal well requires a numerical model capable of calculating both the eddy current and hysteresis losses in the steel pipe.

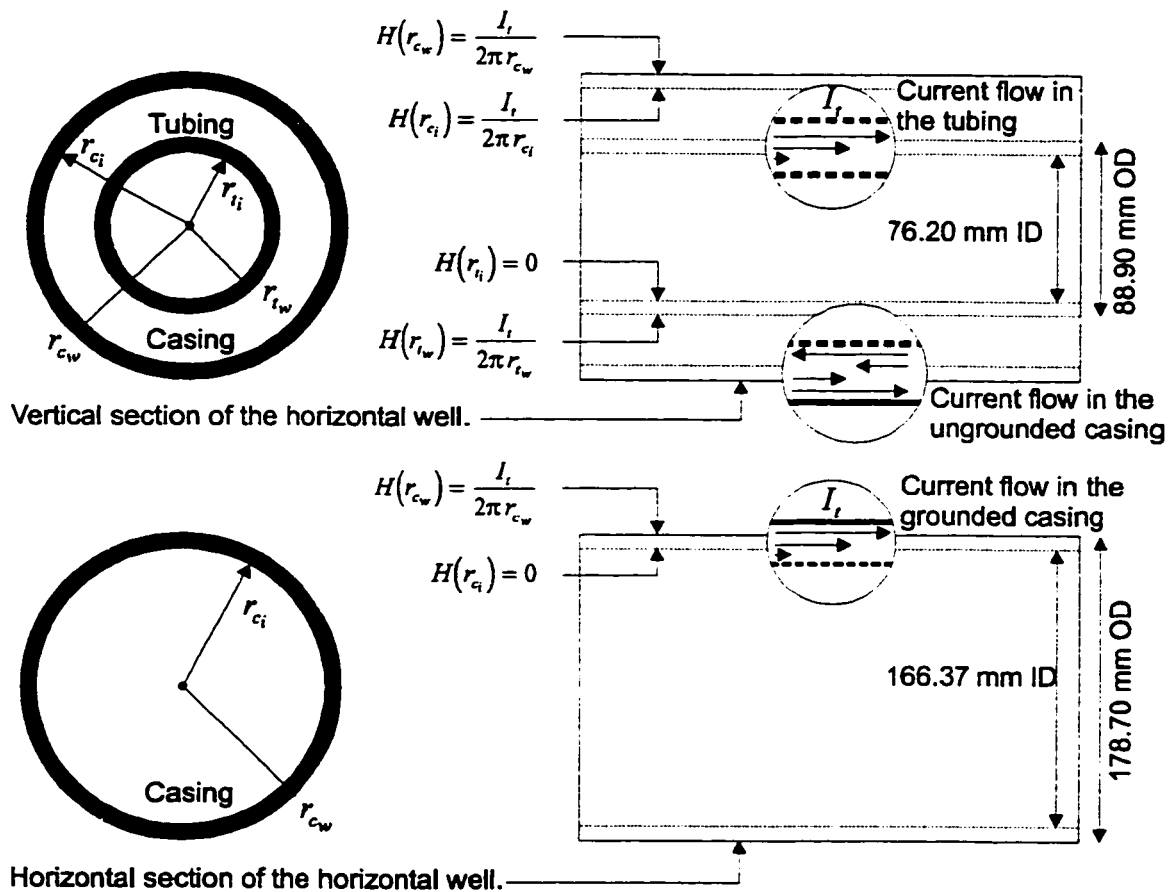


Figure 2.2: The pipe configurations for the vertical and horizontal sections of the horizontal wellbore.

The relative magnitudes of the eddy current and hysteresis losses depend on the frequency of the applied current. These losses can be of equal magnitude. It is

possible to measure the combined losses experimentally as in Reference [29]. However, analytical or numerical methods appear more practical given the uniqueness of each installation and variability of the magnetic properties in different pipe samples [29].

An analytical treatment of the calculation of the eddy current losses in steel pipe of constant relative permeability is documented by Loga [1]. Analytical determination of hysteresis losses in steel tubulars is not possible because of the extremely non-linear relationship between \vec{B} and \vec{H} as defined by hysteresis loops. The only approach to simultaneously calculate the eddy current and hysteresis losses in the conducting magnetic material is to solve Maxwells equations directly using numerical methods.

The finite difference time domain numerical method is used in this thesis. This method is capable of dealing with the transitory response of the magnetization process and also the fact that the steady state magnetization of the steel pipe is highly dependent on the history of magnetization from initial conditions [86].

The numerical solution presented here generally follows the work of *Zakrzewski and Peitras*. [86]. There are significant differences, however. These are:

1. The *EM Pipe Loss* model is developed for the cylindrical coordinate system rather than for the Cartesian coordinate system.
2. The method of geometrically constructing a family of hysteresis loops that is used in this thesis requires only a single experimentally derived hysteresis loop and the peak magnetization curve, rather than requiring extrapolation between data points of several experimentally derived hysteresis loops, as carried out in the work of *Zakrzewski and Peitras*, [86].
3. The electric field strength in the interior of the material is calculated using an integral form of Maxwell's equations rather than the point form of these equations. Rather than using a polynomial fit to the electric field strength in the interior to determine surface values by extrapolation, the surface values of the electric field strength are then calculated directly.

Figure 2.3 shows the magnetic and electric field strengths for an element of the casing in the vertical section of the wellbore. The current conducted in the

centralized tubing, I_t , is replaced by a current source located at $r = 0$. The interior and exterior surfaces of the casing are located at radii r_{ci} and r_{cw} , respectively. For simplicity in the work that follows, r_{ci} and r_{cw} are replaced by r_i and r_w .

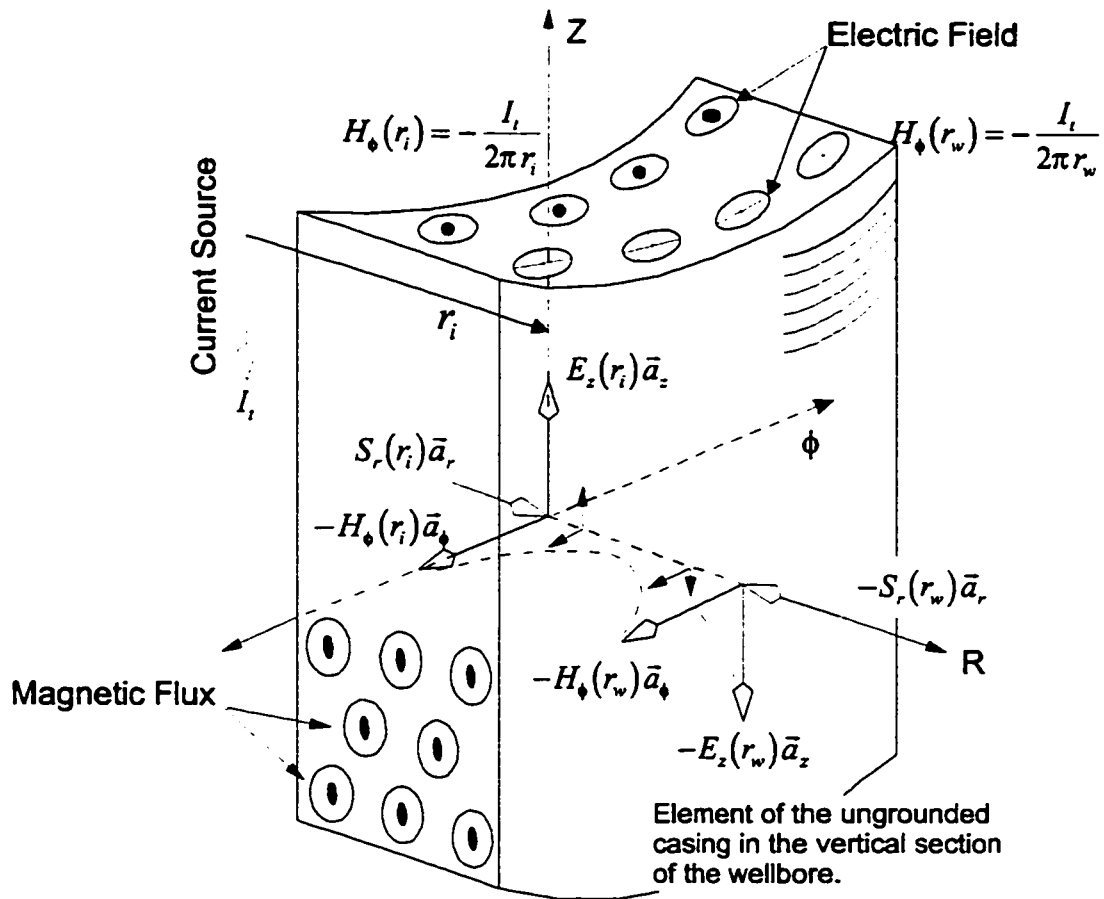


Figure 2.3: Description of the electromagnetic problem in the vertical section of the casing leading to the horizontal wellbore.

With reference to Figure 2.3, the following assumptions are made:

1. The pipe is sufficiently long so that end effects can be neglected.
2. The frequency of the excitation is sufficiently low that wavelength effects are negligible. From 1 it follows that there is no variation of any field quantity along the axial direction [1].
3. The magnetic field strength on the inner and outer boundaries of the casing is induced by an alternating current source centered on the axis of the casing. In the vertical section of the wellbore this is the tubing string. This assumption eliminates any variation of the field quantities in the ϕ direction.

4. The steel pipe is magnetically homogeneous along the length of the pipe.
5. The electrical conductivity of the pipe is constant.

The magnetic field strength, $H_\phi(r)$, is tangent to the inner and outer walls of the casing pipe and is in the negative ϕ direction. The electric field strength, $E_z(r)$, is in a direction parallel to the axial direction and is perpendicular to the magnetic field strength along the length of the pipe. Within the pipe, both the magnetic and electric field strengths vary in amplitude and phase in the radial direction. The Poynting vectors, $S_r(r_i)$ and $S_r(r_w)$, are in the directions of $\vec{\mathbf{E}} \times \vec{\mathbf{H}}$, and are directed into the pipe on both the interior and exterior surfaces. The magnetic field strengths on the interior and exterior surfaces of the pipe are obtained from Ampere's Law as shown in Figure 2.3.

Once a solution for the electric and magnetic field strengths has been derived, it is possible to use the values of these field qualities at the pipe surface to calculate the total power losses using Poynting's theorem. Separate values of the eddy current and hysteresis losses can be obtained using the equations, which are developed, in the next section.

2.2 Finite Difference Time Domain Solution

The finite difference time domain method is used to obtain the numerical solution of the magnetic field strength equation, which is a partial differential equation in terms of $H_\phi(r)$ only, and is derived from Maxwell's Equations. Finite differencing techniques are applied to the derivatives appearing in this equation, and the non-linear relationship between \mathbf{B} and \mathbf{H} is defined using hysteresis loops. The appropriate boundary conditions are invoked and the solution for the magnetic field strength is obtained. Then, using Ampere's Law, the electric field strength is derived from the magnetic field strength.

2.2.1 Partial differential equation for the magnetic field strength

All the information necessary to completely define the magnetic field strength as a function of time and space is contained within the differential form of Maxwell's equations. These equations are:

$$\nabla \times \vec{\mathbf{E}} = -\frac{\partial \vec{\mathbf{B}}}{\partial t} = -\frac{\partial f(\vec{\mathbf{H}})\vec{\mathbf{H}}}{\partial t} \quad (2.1)$$

$$\nabla \times \vec{\mathbf{H}} = \epsilon \frac{\partial \vec{\mathbf{E}}}{\partial t} + \sigma \vec{\mathbf{E}} \quad (2.2)$$

The term, $f(\vec{\mathbf{H}})$, on the right hand side of Equation 2.1 is contained within the partial derivative. This term cannot be directly removed from within the partial derivative since it is a function of $\vec{\mathbf{H}}$, which in turn is a function of time, t . Using the chain rule, the partial derivative can be rewritten as follows (the vector form of the variable is replaced by the scalar equivalent),

$$\frac{\partial f(H) H}{\partial t} = \frac{\partial B(H)}{\partial t} = \frac{dB(H)}{dH} \frac{\partial H}{\partial t} \quad (2.3)$$

Now define

$$\mu(H) \equiv \frac{dB(H)}{dH} \quad (2.4)$$

and directly substitute Equations 2.3 and 2.4 into Equation 2.1.

At low frequencies, less than 60 Hz, the magnitude of the conduction current is much greater than the magnitude of the displacement current, as indicated by

$$\frac{\sigma}{\epsilon \omega} \gg 1.$$

Therefore the term,

$$\epsilon \frac{\partial \vec{\mathbf{E}}}{\partial t}$$

in Equation 2.2 is eliminated. Equations 2.1 and 2.2 are rewritten as follows,

$$\nabla \times \vec{\mathbf{E}} = -\mu(\vec{\mathbf{H}}) \frac{\partial \vec{\mathbf{H}}}{\partial t} \quad (2.5)$$

$$\nabla \times \vec{\mathbf{H}} = \sigma \vec{\mathbf{E}} \quad (2.6)$$

Consider in detail the expanded form of Equation 2.6.

$$\begin{aligned} \left(\frac{1}{r} \frac{\partial H_z}{\partial \phi} - \frac{\partial H_\phi}{\partial z} \right) \vec{a}_r + \\ \left(\frac{\partial H_r}{\partial z} - \frac{\partial H_z}{\partial r} \right) \vec{a}_\phi + \\ \frac{1}{r} \left(\frac{\partial r H_\phi}{\partial r} - \frac{\partial H_r}{\partial \phi} \right) \vec{a}_z = \sigma \vec{\mathbf{E}} \quad (2.7) \end{aligned}$$

Based on the geometry and assumptions of the problem the electric field strength vector is in the axial or \vec{a}_z direction. Thus the coefficients of \vec{a}_r and \vec{a}_ϕ must be zero. The current source is located on the axis of the cylindrical casing and therefore H_r is independent of ϕ and any derivatives with respect to ϕ are zero. Based on the simplified geometry of the problem, Equation 2.7 becomes

$$\frac{1}{r} \frac{\partial r H_\phi}{\partial r} = \sigma E_z \quad (2.8)$$

Similarly, Equation 2.5 reduces to,

$$\frac{\partial E_z}{\partial r} = \mu \frac{\partial H_\phi}{\partial t} \quad (2.9)$$

Now substitute E_z from 2.8 directly into 2.9 to finally obtain the partial differential equation describing the magnetic field strength in the steel pipe,

$$\frac{\partial^2 H_\phi}{\partial r^2} + \frac{1}{r} \frac{\partial H_\phi}{\partial r} - \frac{H_\phi}{r^2} = \sigma \mu (H_\phi) \frac{\partial H_\phi}{\partial t} \quad (2.10)$$

Equation 2.10 is a diffusion type equation and describes the penetration of the magnetic field strength into the pipe. Equation 2.10 is discretized and numerically solved. Specification of the magnetic field strength at the boundaries determines

whether the solution is for the vertical section of the wellbore (tubing or ungrounded casing) or the horizontal section of the wellbore (grounded casing).

Once the magnetic field strength H_ϕ is defined, the electric field strength E_z can be derived directly from Equation 2.8. This is the approach used in the *Zakrzewski-Peitrás* numerical model, [86]. Numerically however, it may be desirable to use an integral approach to determine the electric field strength [87]. Thus Ampere's law is used to determine the electric field in the steel pipe,

$$\oint_C \vec{H} \cdot d\vec{l} = \int_S \sigma \vec{E} \cdot d\vec{S} \quad (2.11)$$

2.2.2 Discretization of the partial differential equation for the magnetic field strength

The partial differential equation 2.10 is solved numerically. The independent variables are discretized so that a solution can be found at nodes in space and at specific intervals of time. Figure 2.4 shows the solution space, which consists of the pipe volume between r_i and r_w , represented by a number of finite nodes. Fundamental to an accurate representation of the entire solution space are the choices for the size and number of time and space nodes. Often, the best techniques available for choosing the appropriate time and space increments rely on a trial and error approach, [88].

The method of discretizing the partial differential equation in both time and space, on a grid such as shown in Figure 2.4, is called the finite difference time domain method. The grid is designed so that there are calculations on the boundaries of the grid blocks, called node points and in the center of the grid blocks, called grid points. This is necessary since the grid for calculating the magnetic field strength at the node points is different from the grid required to calculate the electric field strength at the grid points when using Ampere's law.

Ideally the grid block size distribution can be designed according to the electromagnetic field distribution. Smaller grid blocks are used in regions near the source where the electromagnetic field changes rapidly in space, with larger grid blocks towards the interior of the pipe, where the electromagnetic field is attenuated

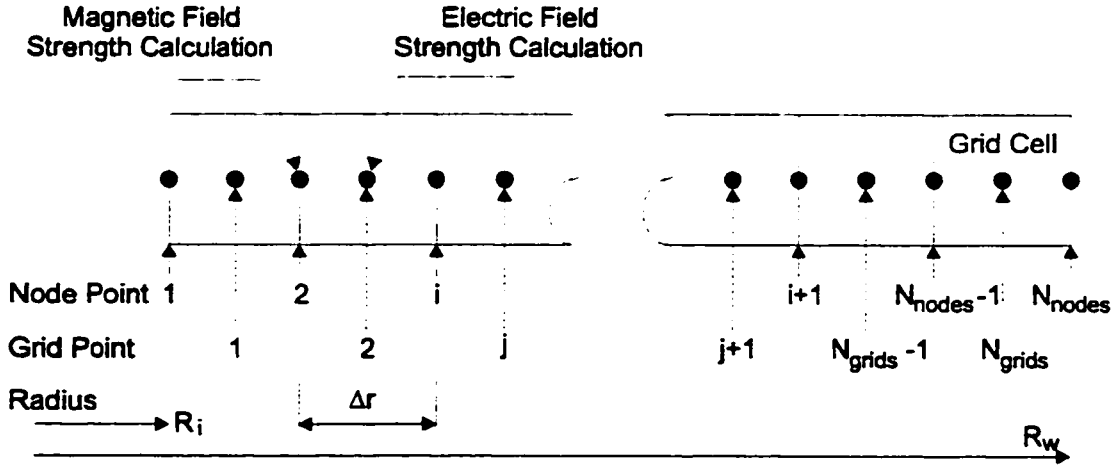


Figure 2.4: Grid system, consisting of node and grid points, adopted for the finite difference time domain numerical calculations.

and does not change rapidly in space. If a uniform grid distribution is used, it is important to ensure that the grids are sufficiently small so that the electromagnetic field is accurately calculated in all the regions. Otherwise the calculation of the electric field strength and of the power that is dissipated will be inaccurate. The computer program for solving the finite difference equations is programmed using a uniform grid distribution.

To arrive at the finite difference form of the partial differential equation, the common approach is to use a Taylor series expansion about an arbitrary node point i . Thus, the first and second order spatial derivatives can be written as follows [89];

$$\left. \frac{\partial H_\phi}{\partial r} \right|_i = \frac{H_{i+1} - H_{i-1}}{2\Delta r} + \mathcal{O}(\Delta r^2) \quad (2.12)$$

$$\left. \frac{\partial^2 H_\phi}{\partial r^2} \right|_i = \frac{H_{i-1} - 2H_i + H_{i+1}}{\Delta r^2} + \mathcal{O}(\Delta r^2) \quad (2.13)$$

The first order derivative, shown in Equation 2.12, is derived using the average of the forward and backward finite differences. This is referred to as the central finite difference and has the advantage of reduced error (second order truncation error) over the forward or backward finite difference. The overall truncation error for the spatial derivatives is second order, $\mathcal{O}(\Delta r^2)$.

The time derivative is obtained by a Taylor series expansion about time level $n + 1$,

$$\left. \frac{\partial H_\phi}{\partial t} \right|_{n+1} = \frac{H_i^{n+1} - H_i^n}{\Delta t} + O(\Delta t) \quad (2.14)$$

Equation 2.14 uses the backward finite difference rather than a central finite difference technique which could require two initial conditions. As well, a central difference technique in the time domain would be unconditionally unstable, ???. The order of truncation error is first order in time. However, a method will be used to diminish the size of the truncation error so that it is second order in time.

The finite difference representations of the continuous derivatives are substituted directly into Equation 2.10 with the following result,

$$a_i H_{i-1}^n + b_i H_i^n + c_i H_{i+1}^n = d_i^n H_i^n - d_i^n H_i^{n+1} \quad (2.15)$$

where,

$$\begin{aligned} a_i &= \frac{1}{\Delta r^2} - \frac{1}{2r_i \Delta r} \\ b_i &= -\frac{1}{r_i^2} - \frac{2}{\Delta r^2} \\ c_i &= \frac{1}{\Delta r^2} + \frac{1}{2r_i \Delta r} \\ d_i^n &= -\frac{\sigma_i \mu_i^n}{\Delta t} \end{aligned} \quad (2.16)$$

A discrete time level needs to be assigned for which the magnetic field strength on the left hand side of Equation 2.15 is calculated. If the current time level n is used, the magnetic field strength is known at every node and the magnetic field strength at the next time level, $n + 1$, is obtained directly using the following equation:

$$H_i^{n+1} = \left(1 - \frac{b_i}{d_i^n}\right) H_i^n - (a_i H_{i-1}^n + c_i H_{i+1}^n) \frac{1}{d_i^n} \quad (2.17)$$

This is known as the *explicit scheme*.

If the future time level $n + 1$ is used Equation 2.15 becomes

$$a_i H_{i-1}^{n+1} + (b_i + d_i^n) H_i^{n+1} + c_i H_{i+1}^{n+1} = d_i^n H_i^n \quad (2.18)$$

The magnetic field strength at every node is unknown and therefore the solution is obtained indirectly or implicitly from the known magnetic field strength at the previous timestep. This is known as the *implicit scheme*. As indicated in 2.18, the terms are rearranged so that the unknown magnetic field strength at time level $n + 1$ is on the left hand side of the equation and the known magnetic field strength at time level n is on the right hand side of the equation. Equation 2.18 is the basic structure that is adopted in this thesis for the development of the implicit numerical approximation of Equation 2.10.

The implicit scheme was chosen over the explicit scheme for reasons of efficiency, stability, and ease of computer programming. Although an explicit scheme apparently requires less effort to solve since it can be solved directly, the scheme suffers from the restriction that $\frac{a_i}{d_i^n} < \frac{1}{2}$ for stability. For typical properties of steel and a reasonable Δr of 1 mm this may require a time step of less than 0.1 μsec to ensure stability. This renders the technique cumbersome and impractical. Furthermore, it is impossible to know the maximum value of d_i^n throughout a computation since it depends on the slope of the hysteresis loop at the value of the magnetic field strength. The slope can vary from 10 to 10,000 over a single cycle of the hysteresis loop and therefore dramatically influence the size of the timestep required to obtain a stable solution. Therefore, some form of time step selection control would have to be programmed so that the explicit scheme remains stable throughout an entire calculation. On the other hand, the implicit scheme is unconditionally stable, for all values of Δt and Δr .

For the fully implicit scheme, it would seem that any value of Δt or Δr will result in a numerical solution. This is not the case. It is accepted that for given practical values of Δt and Δr , there will be a difference between the exact and numerical solution. This is known as the *discretization error*. The finite difference scheme is said to converge if the discretization error goes to zero as Δt and Δr approach zero. A practical approach to investigate the convergence of the numerical solution is to continuously reduce Δt and Δr and monitor changes in the numerical

solution. If reductions in Δt and Δr result in minor changes in the numerical solution, it is reasonable to conclude that the solution has converged to a value within the discretization error [89].

The accuracy (discretization error) to which the solution converges can be estimated from the *truncation error*. The truncation error is the difference between the partial differential equation and its finite difference representations. The truncation errors have been indicated in Equations 2.12 and 2.13 by the notation $O(\Delta r^2)$ and $O(\Delta t)$, describing a second order truncation error in space and a first order truncation error in time. Greater accuracy in the numerical solution is implied if the truncation error is of higher order. If the truncation error tends to zero as Δt and Δr tend to zero, and the solution is stable, then convergence of the solution is also implied.

Up to this point, the finite difference equations have a truncation error that is $O(\Delta t + \Delta r^2)$. It is desirable to increase the order of the truncation error of the time variable so that it is of the same order as that of the spatial variable. Incorporation of the *Crank-Nicholson* method into the finite difference equation achieves this objective. Basically, the *Crank-Nicholson* equation is developed by alternately applying the explicit and implicit equations at different time levels. The final finite difference formulation remains unconditionally stable.

To develop the *Crank-Nicholson* method for this specific problem, consider again the implicit method shown in 2.18 and advance the time level of the entire equation by a single time step,

$$a_i H_{i-1}^{n+2} + (b_i + d_i) H_i^{n+2} + c_i H_{i+1}^{n+2} = d_i^n H_i^{n+1} \quad (2.19)$$

For the term H_i^{n+1} in the above equation, substitute H_i^{n+1} from equation 2.17. The size of the time step between the known and unknown magnetic field strengths is now increased by a factor of two. To reduce the difference to a single time step, the *Crank-Nicholson* method decreases the size of the time step by a factor of two and shifts the time level for the magnetic field strength in 2.19 from $n + 2$ to $n + 1$. The resulting form of the *Crank-Nicholson* method is as follows

$$a_i H_{i-1}^{n+1} + (b_i + 2d_i^n) H_i^{n+1} + c_i H_{i+1}^{n+1} = -a_i H_{i-1}^n + (2d_i^n - b_i) H_i^n - c_i H_{i+1}^n \quad (2.20)$$

The *Crank-Nicholson* equation has a truncation error of $O(\Delta t^2 + \Delta r^2)$. The method is also unconditionally stable and has the advantage of a significant gain in accuracy over other methods. Hence the time step size can be increased so that the total computation time is reduced.

In Equation 2.20 d_i depends on the value of the relative permeability, μ_i , which in turn is calculated from the magnetic field strength as defined by Equation 2.4. To this point it is assumed that d_i is calculated using values for the known magnetic field strength at time level n . The simplest procedure is to retain the *Crank-Nicholson* method and use H_i^n to calculate d_i^n and assume d_i^n does not vary rapidly between time steps. However, there are several schemes, such as the DuFort-Frankel scheme [89], which attempts to manipulate equation 2.20 so that $H_i^{n+\frac{1}{2}}$ is used to determine $d_i^{n+\frac{1}{2}}$. These are classified as predictor-corrector or hopscotch methods and for multi-dimensional problems these methods can improve the accuracy of the numerical method. However, numerical tests have shown that the *Crank-Nicholson* method is marginally better for one-dimensional non-linear problems with consideration for the selection of Δr and Δt than methods which use the predictor corrector modification [89]. For extension to two-dimensional problems, this may not be the case. The approach used in this thesis is to simply use the *Crank-Nicholson* method and ensure that d_i^n , or μ_i , do not vary rapidly between time steps by suitable selection of the size of Δt .

Equation 2.20 is applied to every node within the spatial domain, excluding the boundary nodes. What results is a matrix of coefficients \mathbf{A} , a solution matrix \mathbf{x} , and a matrix of known quantities \mathbf{b} , also referred to as the forcing matrix,

$$\mathbf{A}^n \cdot \mathbf{x}^{n+1} = \mathbf{b}^n \quad (2.21)$$

The goal is to determine \mathbf{x}^{n+1} , the solution matrix, using

$$\mathbf{x}^{n+1} = (\mathbf{A}^n)^{-1} \cdot \mathbf{b}^n \quad (2.22)$$

The time level is shown to indicate at what time each of these matrices is calculated. It is important to note that the forcing matrix is calculated at time level $n + 1$ only at the boundaries. Closer inspection of \mathbf{A} is instructional for understanding the solution procedure. \mathbf{A} is the matrix of coefficients and in terms of Equation 2.20 is as follows,

$$\begin{array}{ccccccc}
 b_2 + 2d_2^n & c_2 & 0 & 0 & 0 & 0 & 0 \\
 a_3 & b_3 + 2d_3^n & c_3 & 0 & 0 & 0 & 0 \\
 0 & a_4 & b_4 + 2d_4^n & c_4 & 0 & 0 & 0 \\
 0 & 0 & a_{i+1} & \ddots & c_{i+1} & 0 & 0 \\
 0 & 0 & 0 & a_{N-3} & b_{N-3} + 2d_{N-3}^n & c_{N-3} & 0 \\
 0 & 0 & 0 & 0 & a_{N-2} & b_{N-2} + 2d_{N-2}^n & c_{N-2} \\
 0 & 0 & 0 & 0 & 0 & a_{N-1} & b_{N-1} + 2d_{N-1}^n
 \end{array} \quad (2.23)$$

The first row shows the finite difference equation applied to the second node, the second row applies to the third node, and so on to the $N-1$ th node. The equation is not applied to nodes 1 and N since these are the boundary nodes and the value of the magnetic field strength is specified there. The a_i , b_i , c_i , and d_i coefficients are defined in equation 2.16. The subscripts that appear in the coefficients apply to the node number.

The matrix is a special case of a system of linear equations that is tridiagonal and appears frequently in the solution of one-dimensional finite difference problems. Using the Thomas algorithm for solving tridiagonal systems of equations, the necessary computer code is only a few lines long and the solution matrix \mathbf{x} is calculated very efficiently.

zero and the initial value of μ_r is set to the initial relative permeability of the material. The matrix of coefficients is calculated at time level n and the forcing matrix is then calculated at time level n and at time level $n + 1$ at the boundary nodes. Using the Thomas algorithm for solving tridiagonal systems of equations, the solution matrix is solved thus updating the magnetic field strength. Using the updated value of the magnetic field strength, μ_i^n is appropriately updated and the coefficient matrix and forcing matrix are also updated. At the end of the specified calculation time, the electric field strength and magnetic induction are calculated from the magnetic field strength. The magnetic induction at each node is calculated directly using the equation $B(r, t)_\phi = \mu H(r, t)_\phi$. Once all the electromagnetic fields are known, the power losses in the magnetic material can be determined.

The following sections describe in detail the numerical methods used to determine the electric field strength, the magnetization process and determination of μ_i , and the eddy current and hysteresis power losses. These methods are programmed into the *EM Pipe Loss* model.

2.2.3 Numerical determination of the electric field strength

Calculation of the electric field strength is achieved using Ampere's Law. This approach can be used directly because of cylindrical symmetry. Consider Ampere's law applied at the inner boundary of the steel tube, $r = r_i$,

$$\oint H_1^{n+1} \cdot d\vec{l} = I \quad (2.25)$$

Now apply Ampere's law at the next node inside the steel pipe,

$$\oint H_2^{n+1} \cdot d\vec{l} = I + \sigma \int_0^{2\pi} \int_{R_1}^{R_2} E_{3/2}^{n+1} r dr d\phi \quad (2.26)$$

Directly substitute Equation 2.25 into Equation 2.26, carry out the integration, and solve for the electric field strength to obtain

$$E_{3/2}^{n+1} = -\frac{2(H_2^{n+1} R_2 - H_1^{n+1} R_1)}{\sigma \cdot (R_2^2 - R_1^2)} \quad (2.27)$$

Continue this process until the electric field strength is calculated at each grid point. The general equation for determining the electric field strength is

$$E_{i+1/2}^{n+1} = -\frac{2(H_{i+1}^{n+1}R_{i+1} - H_i^{n+1}R_i)}{\sigma \cdot (R_{i+1}^2 - R_i^2)} \quad 1 \leq i \leq N-1 \quad (2.28)$$

The electric field strength at the inner and outer boundary nodes can be calculated using

$$E_1^{n+1} = \frac{1}{2} \left(3E_{3/2}^{n+1} - E_{5/2}^{n+1} \right) \quad (2.29)$$

$$E_{N+1}^{n+1} = \frac{1}{2} \left(3E_{N-1/2}^{n+1} - E_{N-3/2}^{n+1} \right) \quad (2.30)$$

2.2.4 The magnetization process for the steel pipe

This section describes the magnetization process for the magnetic material used in the steel pipe. Consider the periodic magnetization process for the magnetic material. It is assumed that the thickness (Δr_i) of material is sufficiently small so that the magnetization process is uniform within Δr_i . Therefore, within Δr_i , the material is assumed to be magnetized according to a static hysteresis loop such as shown in Figure 2.5.

The presence of eddy currents will attenuate the electromagnetic wave in the material and as a result the magnetic field strength, H_ϕ , is not uniform throughout the steel pipe. *Thus, at each node position r_i within the magnetic material, a unique hysteresis loop to describe the magnetization process within Δr_i is required. At steady state conditions, N_{nodes} hysteresis loops will be necessary to describe the magnetization of the steel pipe at every grid node.*

Initially, it is assumed that the material is demagnetized and the magnetic field strength, $H_\phi(r)$, is zero everywhere. This corresponds to the point of initial conditions as shown on Figure 2.5. $H_\phi(r) = 0$ is an essential initial condition since the magnetization of each grid cell depends on the history of magnetization. Therefore a transient period is necessary to define the magnetization characteristics of a grid cell at steady state.

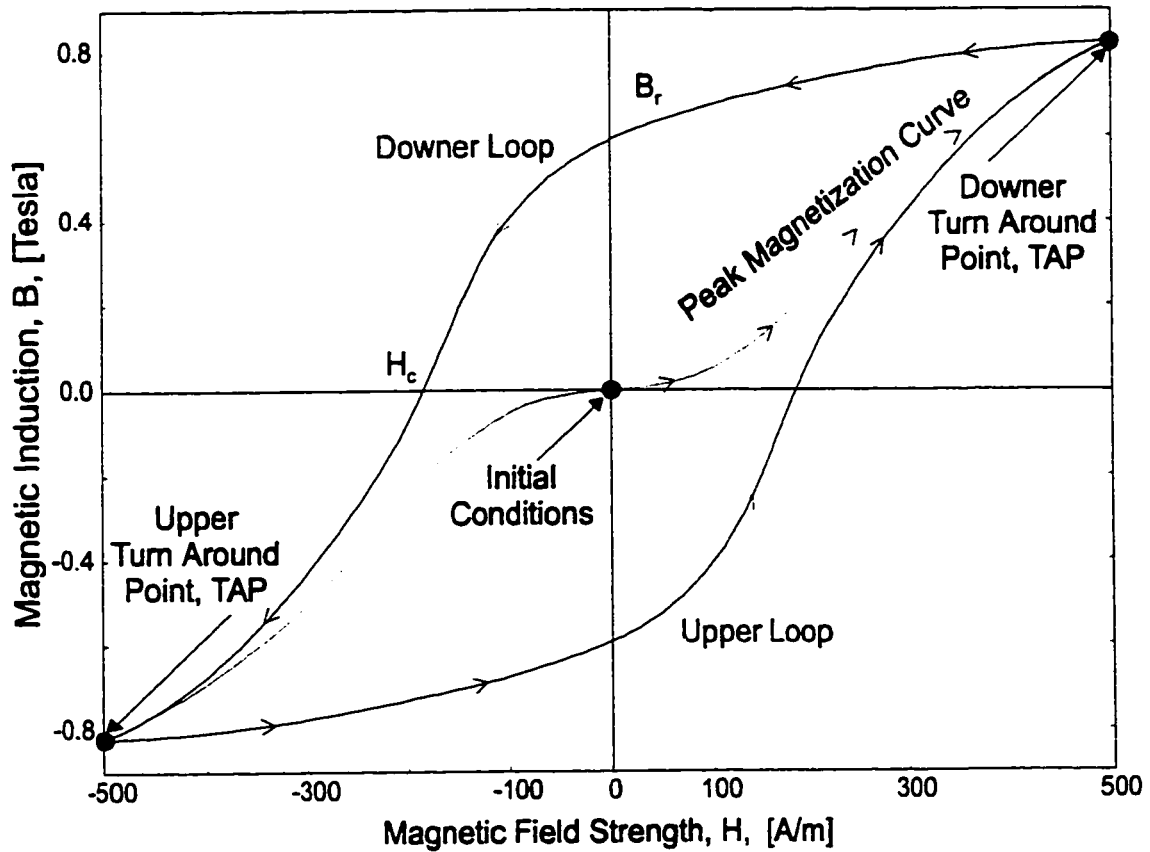


Figure 2.5: Characteristics of the magnetization process within a grid cell.

As the magnetic field strength increases with increasing time, the magnetization initially follows the *peak magnetization curve* as shown in Figure 2.5. This curve is referred to as the *peak magnetization curve* since the end points or tips of symmetric hysteresis loops of different magnitudes lie on the curve. When the magnetic field strength reaches a maximum, demagnetization occurs along the curve called the *downer loop*. The point where the magnetic field strength peaks at a positive maximum is called the *downer turn around point* and is defined numerically by the condition $H_{\phi_i}^{n+1} < H_{\phi_i}^n$. The term *downer* is used to emphasize that the magnetic field strength is decreasing and the magnetization process proceeds *down* the hysteresis loop. Similar reasoning is used to explain the use of the term *upper*.

The demagnetization process continues along the *downer loop*. When the magnetic field strength is reduced to zero a residual magnetic induction, B_r , remains in the magnetic steel pipe. The coercive magnetic field strength, H_c , is the value of the magnetic field strength necessary to reduce the magnetic induction in

the material to zero and is shown on Figure 2.5 at the intersection of the *downer loop* and the \mathbf{H} axis.

The demagnetization process continues along the *downer loop* until the magnetic field strength reaches a minimum. This point is called the *upper turn around point* and is defined numerically by the condition, $H_{\phi_i}^{n+1} > H_{\phi_i}^n$. Re-magnetization of the material occurs along the *upper loop* until the *downer turn around point* is reached again, completing a single cycle of magnetization. The magnetization process continues along the *downer* and *upper* loops for each cycle of the applied magnetic field strength. Magnetization along the *peak magnetization curve* only occurs once from the initial condition of zero magnetization.

During the transient period, the magnitudes of $\vec{\mathbf{B}}$ and $\vec{\mathbf{H}}$ at the *upper turn around point* and *downer turn around point* are usually different. At steady state, the magnitudes of $\vec{\mathbf{B}}$ and $\vec{\mathbf{H}}$ are the same and the *downer loop* and *upper loop* are symmetrical. For the model developed here, the *upper turn around point* and *downer turn around point* always lie on the *peak magnetization curve* once steady state is reached.

The process just described is repeated several times until steady state is reached. The transient period exists for four to five cycles of the periodic magnetic field strength. This is exemplified in Figure 2.6. This figure shows the transient period of magnetization calculated for a grid cell using the *EM Pipe Loss* model and ten cycles of the applied magnetic field strength. As the figure shows, the transients disappear after about four cycles of magnetization.

To determine the magnetization for each grid cell requires a general method of generating hysteresis loops, so that for any value of the peak magnetic field strength a corresponding hysteresis loop describing the magnetization can be defined. The method for constructing hysteresis loops is described in the next section.

2.2.5 Distance factor method for constructing the hysteresis loops

This section presents the procedure for constructing the general hysteresis loops needed for the solution of Equation 2.10. The method is an extension of a method developed by *Talukdar and Bailey*, [90]. They developed a procedure to

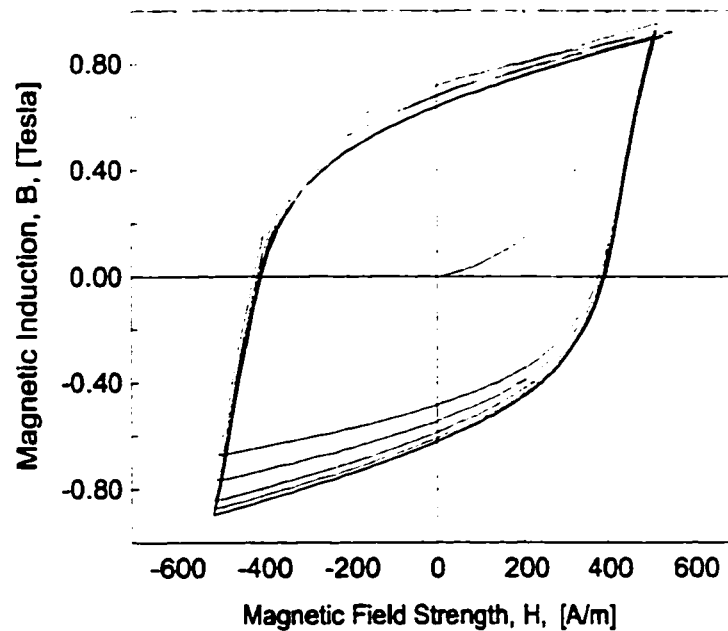


Figure 2.6: The magnetization process during the transient period.

scale a maximum hysteresis loop using a *distance factor* so that a hysteresis loop can be constructed for any applied magnetic field strength.

The *Talukdar and Bailey* method is described first. Then the extensions to their method developed in this thesis are presented. Using this approach to describe the *distance factor* method will illustrate the method and explain the differences between the two approaches.

The *distance factor* approach requires a maximum hysteresis loop for the magnetic material which is usually obtained experimentally. For the *Talukdar and Bailey* approach the maximum hysteresis loop *must* extend to the saturation points, as shown in Figure 2.7. This condition is not necessary for the *distance factor* method developed in this thesis. Our only requirement is that the extremum of the maximum hysteresis loop be greater than the maximum value of the applied magnetic field strength. It will be demonstrated in a following section that the ability to use a maximum hysteresis loop that closely follows the applied magnetic field strength results in a more accurate solution of the electromagnetic problem. This is especially true if the maximum applied magnetic field strength is much less than the magnetic field strength at saturation conditions.

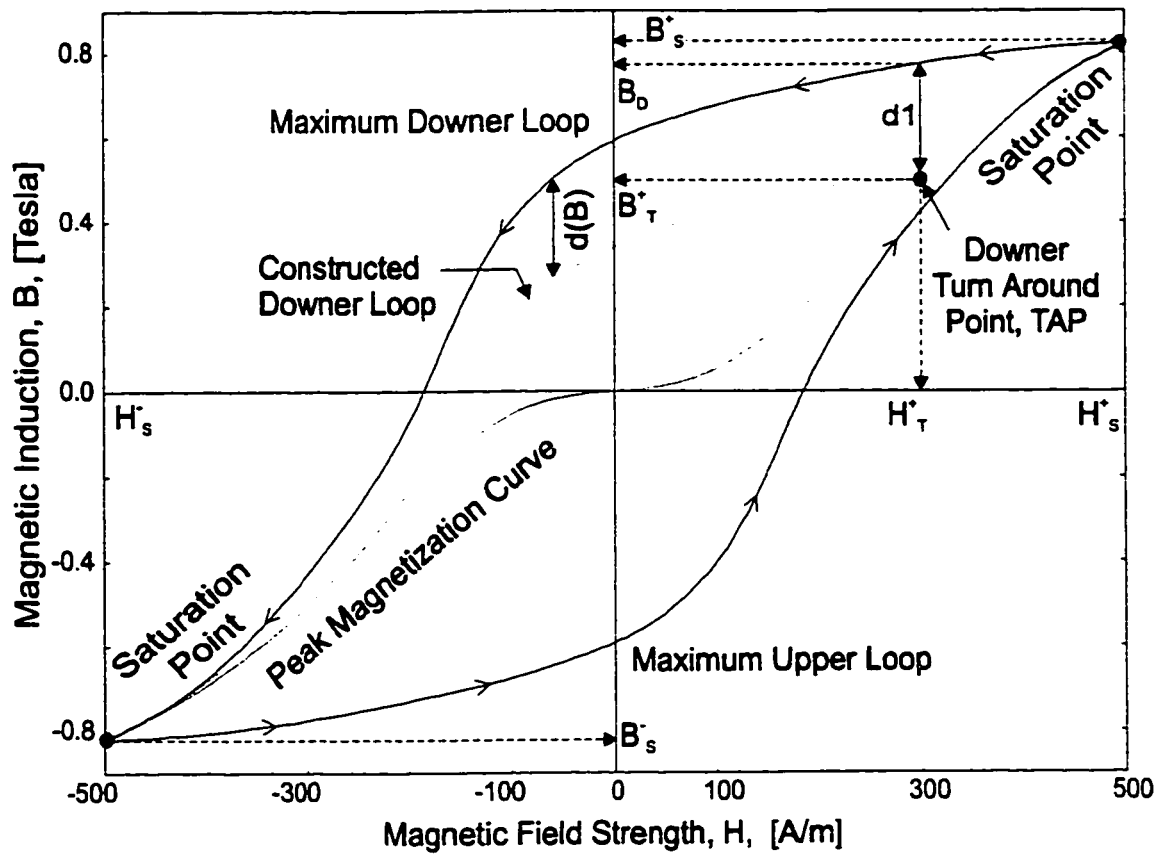


Figure 2.7: *Talukdar and Bailey* method for constructing hysteresis loops.

With reference to Figure 2.7, the *Talukdar and Bailey* approach for constructing a hysteresis loop for an arbitrary value of the applied magnetic field strength is described as follows:

1. The *downer turn around point* is defined by the coordinate, (H_T^+, B_T^+) and is located on the *peak magnetization curve*. When the magnetic field strength reaches the *downer turn around point*, determine the vertical distance from the *maximum downer loop* to the *downer turn around point*. This distance is d_1 and is equal to $B_D - B_T^+$.
2. For any value of the magnetic field strength decreasing from the *downer turn around point*, the *constructed downer loop* is derived by translating the *maximum downer loop* by a variable displacement that is defined by $d(B)$. The relationship for d that is used by *Talukdar and Bailey* is to make d vary linearly from $d(B_T^+) = d_1$ to $d(B_s^-) = 0$. This relationship is then used to define the *constructed downer loop*.

3. *Talukdar and Bailey* assume symmetry between the *constructed downer loop* and *constructed upper loop*, so that the *constructed upper loop* is derived using the previous two steps beginning at the *upper turn around point* which they define by the coordinate, $(-H_T^+, -B_T^+)$.

The *distance factor* resulting from the second step of the above procedure and which is used to determine the *constructed downer loop* is,

$$d(B) = d_1 \frac{B - B_s^-}{B_T^+ - B_s^-} \quad (2.31)$$

The approach used in this thesis is similar to the approach of *Talukdar and Bailey* except for the relationship defining $d(B)$. In this approach, d is made to vary linearly from $d(B_T^+) = d_1$ to $d(B_T^-) = d_2$. The distance d_2 is determined at the *upper turn around point*. The *upper turn around point* is defined by the coordinate, (H_T^-, B_T^-) , as shown on Figure 2.8. Thus, the distance d_2 between the *maximum downer loop* and the *constructed downer loop* is equal to $B_D^- - B_T^-$. To distinguish between the two turn around points, the distance d_1 is defined slightly differently than was defined by *Talukdar and Bailey* and is equal to $B_D^+ - B_T^+$. In this thesis, B_D^+ is not restricted to the saturation hysteresis loop.

Note that both d_1 and d_2 are always positive when defined as the distance from the *maximum downer loop* to the *constructed downer loop*. The distances d_1 and d_2 have exactly the same meaning for determining the *constructed upper loop*. However, so that the same equation can be used to define the variable displacement for the upper loops, d_1 and d_2 are redefined as the distance from the *constructed upper loop* to the *maximum upper loop* so that they are also always positive. This results in the following equation for the *distance factor*, $d(B)$, which can be used for determining both the *constructed downer loop* and *constructed upper loop*,

$$d(B) = d_2 + \frac{d_1 - d_2}{B_T^+ - B_T^-} (B - B_T^-) \quad (2.32)$$

The *constructed downer loop* is calculated for decreasing values of magnetic field strength from the *downer turn around point* and is

$$B_{cd}(H) = B_d(H) - d(B)$$

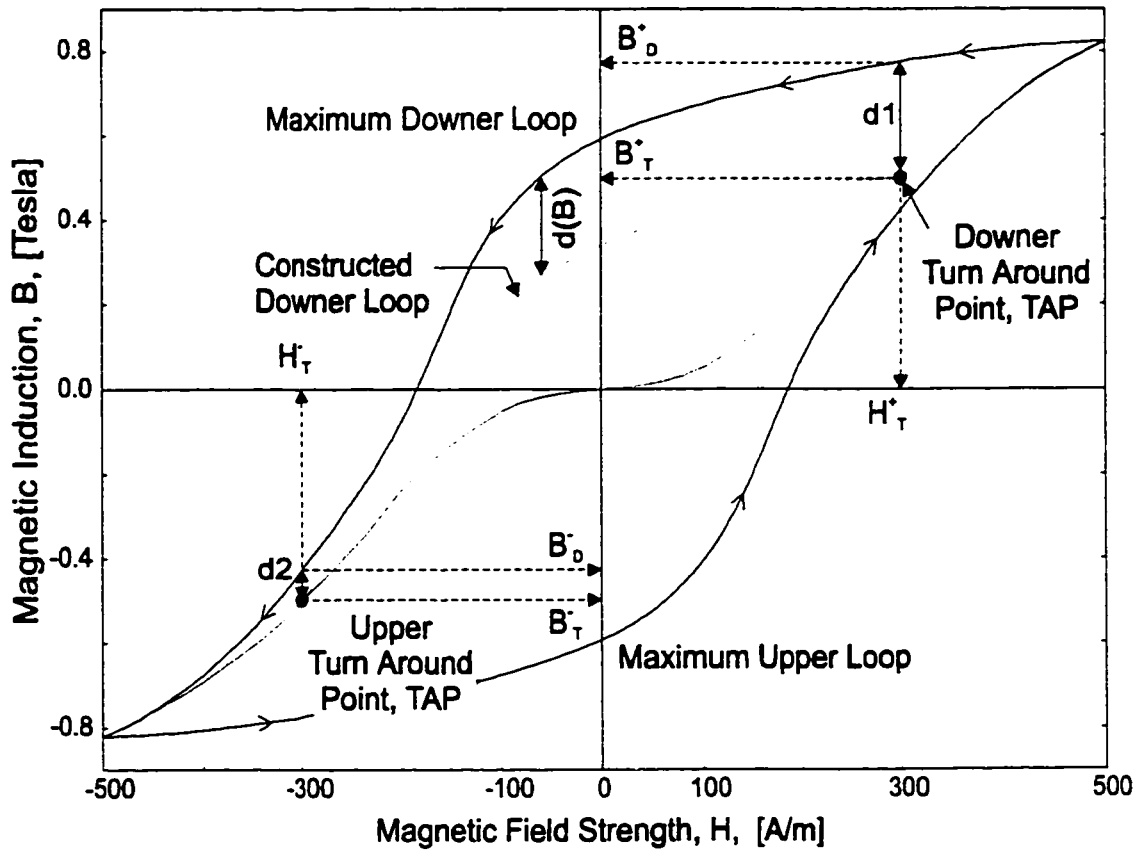


Figure 2.8: Method for constructing hysteresis loops used in this thesis and programmed into the *EM Pipe Loss* model. Note that the very first turn around point lies on the peak magnetization curve but subsequent turn around points generally do not until steady state is reached.

where $B_{cd}(H)$ is the magnetic induction for the *constructed downer loop* and $B_d(H)$ is the magnetic induction corresponding to the *maximum downer loop*. The *distance factor* is determined from Equation 2.32.

Similarly, the *constructed upper loop* is calculated for increasing values of magnetic field strength from the *upper turn around point* and is

$$B_{cu}(H) = B_u(H) + d(B)$$

where $B_{cu}(H)$ is the magnetic induction for the *constructed upper loop* and $B_u(H)$ is the magnetic induction corresponding to the *maximum upper loop*. The *distance factor* is determined from Equation 2.32 just as in the previous case.

It is important to note that the condition for symmetry required by the

Talukdar and Bailey approach is relaxed with the introduction of d_2 at the *upper turn around point*. Therefore, $(H_T^-, B_T^-) \neq (-H_T^+, -B_T^+)$ and the magnetization process through the transient period can be properly modeled. Otherwise, the hysteresis loops are forced to be symmetrical upon completion of the first cycle of the applied magnetic field strength, which is normally associated with a steady state condition.

As previously mentioned, an advantage of using the *distance factor* method developed in this thesis, is that it is not necessary to obtain a maximum hysteresis loop that extends to the magnetic saturation of the material. This is an important experimental consideration since magnetic saturation for oil-field steel tubulars typically occur at very large magnetic field strengths. Also, practical values for the applied magnetic field strength are much less than at saturation conditions. Since it is desirable to use a maximum hysteresis loop that is close to the applied magnetic field strength to improve on the accuracy of the electromagnetic field calculations, the *distance factor* method used in this thesis was developed.

There are other methods for constructing hysteresis loops as summarized by Macki *et. al.*, Reference [91]. Many of these methods are based on an approach called Preisach's theory [92], [93]. Using the Preisach approach it is possible to expand the characterization of the magnetization process to include magnetization paths that are not restricted to the peak magnetization curve and include hysteresis loops that are asymmetrical. The hysteresis loops for the oil-field steel tubulars used in the experimental phase of this thesis are symmetrical and the magnetization process closely follows the *peak magnetization curve*. These criteria being met, the *distance factor* method is capable of accurately constructing hysteresis loops for the electromagnetic problem solved in this thesis.

In summary, a general approach is introduced to construct a family of hysteresis loops that define the relationship between the magnetic field strength and magnetic induction for a magnetic material. It is now possible to solve the numerical problem and determine the electromagnetic fields in the steel pipe. Once the electric and magnetic field strengths are determined, the power losses can be calculated directly. The determination of the power losses is the topic of the next section.

2.2.6 Determination of the power losses

The total electromagnetic power flow into the pipe can be obtained from Poynting's vector, which is valid despite the *highly non-linear* response of the ferromagnetic material. Poynting's theorem can be derived from Maxwell's equations (Equations 2.1 and 2.2). Maxwell's equations, in a good conductor, assuming negligible displacement currents, are restated as follows,

$$\nabla \times \vec{\mathbf{E}} = -\frac{\partial \mu(\vec{\mathbf{H}})\vec{\mathbf{H}}}{\partial t} = -\frac{\partial \vec{\mathbf{B}}}{\partial t} \quad (2.33)$$

$$\nabla \times \vec{\mathbf{H}} = \sigma \vec{\mathbf{E}} \quad (2.34)$$

Using the equivalence of vector operations,

$$\nabla \cdot (\vec{\mathbf{E}} \times \vec{\mathbf{H}}) = \vec{\mathbf{H}} \cdot \nabla \times \vec{\mathbf{E}} - \vec{\mathbf{E}} \cdot \nabla \times \vec{\mathbf{H}} \quad (2.35)$$

and applying this to Equations 2.33 and 2.34 results in

$$\nabla \cdot (\vec{\mathbf{E}} \times \vec{\mathbf{H}}) = -\vec{\mathbf{H}} \cdot \frac{\partial \vec{\mathbf{B}}}{\partial t} - \sigma \vec{\mathbf{E}} \cdot \vec{\mathbf{E}} \quad (2.36)$$

Equation 2.36 is integrated throughout volume V ,

$$-\int_V \nabla \cdot (\vec{\mathbf{E}} \times \vec{\mathbf{H}}) dV = \int_V \left[\vec{\mathbf{H}} \cdot \frac{\partial \vec{\mathbf{B}}}{\partial t} + \sigma \vec{\mathbf{E}} \cdot \vec{\mathbf{E}} \right] dV \quad (2.37)$$

The divergence theorem states that

$$-\int_V \nabla \cdot (\vec{\mathbf{E}} \times \vec{\mathbf{H}}) dV = -\oint_S (\vec{\mathbf{E}} \times \vec{\mathbf{H}}) \cdot d\vec{\mathbf{S}} \quad (2.38)$$

Thus Equation 2.37 can be restated as follows,

$$-\oint_S (\vec{\mathbf{E}} \times \vec{\mathbf{H}}) \cdot d\vec{\mathbf{S}} = \int_V \left[\vec{\mathbf{H}} \cdot \frac{\partial \vec{\mathbf{B}}}{\partial t} + \sigma \vec{\mathbf{E}} \cdot \vec{\mathbf{E}} \right] dV \quad (2.39)$$

Equation 2.39 is *Poynting's theorem*. This is a general equation that applies to any conducting material since no assumptions are necessary with respect to the linearity of the material [94]. The units of Equation 2.39 are in watts. The Poynting vector, $\vec{\mathbf{E}} \times \vec{\mathbf{H}}$, represents the rate of energy flow or power across a surface (W/m^2). The term $\vec{\mathbf{H}} \cdot \frac{\partial \vec{\mathbf{B}}}{\partial t}$ represents the time rate of increase of the stored energy in the magnetic field strength and, when integrated over one cycle, determines the hysteresis losses, and $\sigma \vec{\mathbf{E}} \cdot \vec{\mathbf{E}}$ represents the eddy-current losses.

Given that the electric and magnetic field strengths are solved for in the time domain, the time average power flow outward toward surface S , over one cycle, is

$$\frac{1}{T} \oint_S \int_0^T \left(\vec{\mathbf{E}}(t) \times \vec{\mathbf{H}}(t) dt \right) \cdot d\vec{\mathbf{S}} \quad (2.40)$$

If the magnetic field strength exists on the interior and exterior surfaces of the pipe, then the time average power that flows into the pipe through the interior surface of the pipe at $r = r_i$ is

$$\Delta P_{r=r_i} = \frac{2\pi r_i L}{T} \int_0^T E_z(r_i, t) H_\phi(r_i, t) dt \quad (2.41)$$

where L is the length of the pipe. At $r = r_w$ the time average power that flows into the pipe through the exterior surface of the pipe is

$$\Delta P_{r=r_w} = \frac{2\pi r_w L}{T} \int_0^T E_z(r_w, t) H_\phi(r_w, t) dt \quad (2.42)$$

The numerical equivalent to Equation 2.41 is

$$\Delta P_{r=r_i} = 2\pi r_i L \frac{\Delta t}{T} \sum_{n=0}^{N_{time}} \frac{E_{z_{0,n+1}} H_{\phi_{0,n+1}} + E_{z_{0,n}} H_{\phi_{0,n}}}{2} \quad (2.43)$$

where N_{time} is the number of time steps per cycle of the wave and both E_z and H_ϕ are calculated on the surface node of the grid.

The numerical equivalent to Equation 2.42 is

$$\Delta P_{r=r_w} = -2\pi r_w L \frac{\Delta t}{T} \sum_{n=0}^{N_{time}} \frac{E_{z_{N_{grids}+2,n+1}} H_{\phi_{N_{nodes},n+1}} + E_{z_{N_{grids}+2,n}} H_{\phi_{N_{nodes},n}}}{2} \quad (2.44)$$

Since the direction of power flow, as defined by Poynting's vector, is into the pipe at both the inner and outer surfaces for the general problem solved in this thesis, the total time average input power (losses) is given by,

$$\Delta P = \Delta P_{r=r_i} - \Delta P_{r=r_w} \quad (2.45)$$

When the magnetic field strength is present only on the outer boundary of the steel pipe, (the condition for the horizontal section of the wellbore), the power flow determined from Poynting's vector is zero at the inner boundary and Equation 2.45 remains valid.

The only losses assumed in the steel pipe are eddy-current and hysteresis losses. The total power losses, Equation 2.45, must equal the sum of these losses. The time averaged eddy-current losses are calculated using

$$P_{ec} = \frac{2\pi L}{T} \int_{r_i}^{r_w} \int_0^T \sigma E_z^2(r, t) r dr dt \quad (2.46)$$

and are determined numerically using

$$P_{ec} = \frac{\sigma L}{T} \sum_{i=1}^{N_{grids}} \left[\pi (r_{i+1}^2 - r_i^2) \sum_{n=0}^{N_{time}} E_{z_i,n}^2 \Delta t \right] \quad (2.47)$$

The time averaged hysteresis losses over a cycle of the applied magnetic field strength within a volume of steel pipe is calculated using

$$P_h = \frac{2\pi L}{T} \int_{r_i}^{r_w} \int_{B_\phi(0)}^{B_\phi(T)} H_\phi(r, B_\phi) dB_\phi r dr \quad (2.48)$$

and is determined numerically using

$$P_h = \frac{L}{T} \sum_{i=1}^{N_{grids}} \left[\pi (r_{i+1}^2 - r_i^2) \sum_{n=0}^{N_{time}} (\bar{B}_{\phi_{i,n+1}} - \bar{B}_{\phi_{i,n}}) \bar{H}_{\phi_{i,n+1}} \right] \quad (2.49)$$

where $\bar{H}_{\phi_{i,n}}$ and $\bar{B}_{\phi_{i,n}}$ are the magnetic field strength and magnetic induction at the grid point at time level n . These are calculated averages using adjacent node points at the same time level. N_{time} is the number of time steps per cycle.

In summary, the total power flow into the pipe, per unit area, is derived using Poynting's vector (Equation 2.40). Then the power losses due to eddy-currents are calculated using Equation 2.49. Finally, the power losses due to hysteresis effects are calculated using Equation 2.48. As a test of the numerical model, the sum of the eddy-current and hysteresis losses must equal the total power flow into the pipe volume calculated from Poynting's vector.

2.3 Analytic and Numerical Validations of the *EM Pipe Loss* Model.

In this section, the *EM Pipe Loss* model is validated using an analytical solution of the magnetic and electric field strengths in a cylindrical pipe for the special case where the steel has a constant relative permeability μ_r , [1]. Validation is also obtained by comparing results from the *EM Pipe Loss* model with results obtained from a numerical model solved in the Cartesian coordinate system [86].

2.3.1 Validation using the *Loga* analytic model

Loga solves Maxwell's equations to obtain analytical solutions for the electric and magnetic field strengths in steel pipe without magnetic hysteresis (constant relative permeability μ_r). The detailed derivation of these solutions can be obtained from Reference [1]. The equation for the electric field strength is

$$E_z(r) = A \mathbf{H}_0^{(2)}(k_s r) + B \mathbf{H}_0^{(1)}(k_s r) \quad (2.50)$$

and the equation for the magnetic field strength is

$$H_\phi(r) = -\frac{A}{j\eta_s} \mathbf{H}_1^{(2)}(k_s r) - \frac{B}{j\eta_s} \mathbf{H}_1^{(1)}(k_s r) \quad (2.51)$$

where the wave number is denoted by k_s , and for $\sigma_s \gg \omega\epsilon_s$, may be approximated by the expression, $k_s \cong \sqrt{-j\omega\mu_r\sigma_s}$. Similarly,

$$\eta_s \cong \sqrt{\frac{j\omega\mu_r}{\sigma_s}}.$$

The subscript s is used to signify that the properties are for steel pipe. Thus k_s and η_s are the *wave number* and *intrinsic impedance* of the steel pipe.

$\mathbf{H}_0^{(1)}(k_s, r)$ and $\mathbf{H}_0^{(2)}(k_s, r)$ are zero order Hankel functions of the first and second kind, and $\mathbf{H}_1^{(1)}(k_s, r)$ and $\mathbf{H}_1^{(2)}(k_s, r)$ are first order Hankel functions. The constants A and B are determined from the boundary conditions of the problem.

In order to compare the analytical and finite difference methods, it is important that the finite difference solution reach steady state. This is accomplished by running the solution through several cycles of the applied magnetic field strength. It is noted that although the analytical solution is exact in theory, the actual calculations of the Hankel functions are approximated and are therefore subject to minor numerical error.

Data	Symbol	Value	Units
Inner radius	r_i	83.185	<i>mm</i>
Outer radius	r_o	89.345	<i>mm</i>
Frequency	f	60.0	<i>Hz</i>
Current	I	300.0	<i>A</i>
Electrical conductivity	σ_s	7,300,000	<i>S/m</i>
Relative permeability	μ_r	200	
Relative dielectric constant	ϵ_s	1	
Calculated Constants			
	Wave Number, k_s	427 - j 427	
	Intrinsic Impedance, η_s	$(1.1 + j 1.1) \cdot 10^{-4}$	

Table 2.1: The input data for the steel pipe used in the validation of the *EM Pipe Loss* model with the *Loga Analytic Model*.

Table 2.1 summarizes the base case input data used in the comparison. Figure 2.9 compares the steady state calculations of the magnetic field strength distribution in the steel pipe made of a linear magnetic material using Loga's analytic model and the results produced from the *EM Pipe Loss* model. The two different calculation methods yield almost identical results. Also shown on the graph is the percentage

difference between the calculations, which is given by the following equation,

$$\xi = \left| \frac{H_{Loga} - H_{EMPL}}{H_{Loga}} \cdot 100 \right| \quad (2.52)$$

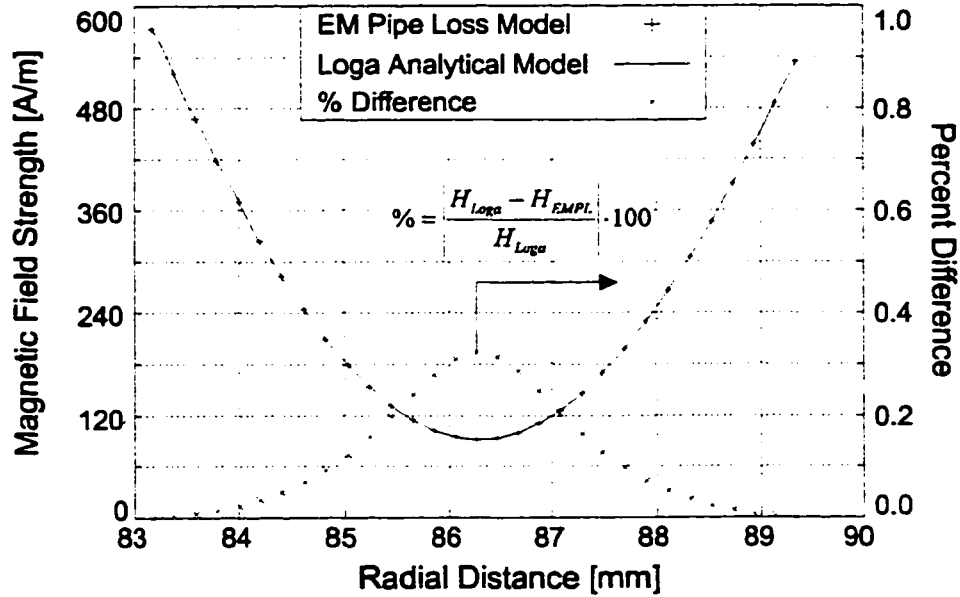


Figure 2.9: Comparison of the magnetic field strength, $H_{\phi}(r, t)$, calculated using the *EM Pipe Loss* model and the *Loga Analytic Model*.

At the boundaries of the problem there is no error since the boundary conditions determine the magnetic field strength there a priori. However, for calculations of the magnetic field strength in the interior of the pipe, there is an accumulation of error. This is expected since the calculation of the field at r_{i+1} away from the boundary depends on the calculation of the field at r_i and the numerical error at r_i feeds into the calculation at r_{i+1} . This accumulation of error is referred to as *numerical dispersion* and is common in the numerical solution of many physical problems. The percentage difference ξ does not exceed 0.4%.

Figure 2.10 compares the calculations of the electric field strength in the steel pipe between Loga's analytic model and the *EM Pipe Loss* model. Again, the two different calculation methods yield almost identical results.

Since the electric field strength is determined using an integral method that computes the difference of adjacent magnetic field strengths (see Equation 2.28), the error in the electric field strength is *smoothed* and subtracted out, and numerical

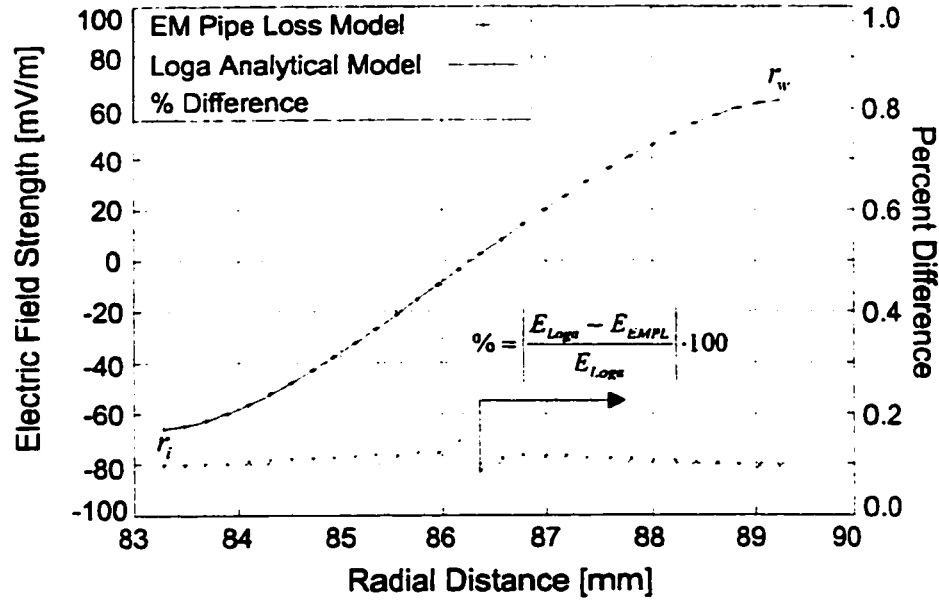


Figure 2.10: Comparison of the electric field strength, $E_z(r, t)$, calculated using the *EM Pipe Loss* model and *Loga Analytical Model*.

dispersion is not evident in the error. The magnitude of the maximum error is less than the numerical error for the calculation of the magnetic field strength by nearly a factor of two, thus demonstrating the benefit of using an integral approach to calculate the electric field strength.

2.3.2 Validation using the *Zakrzewski-Peitras* numerical model

This section validates the *EM Pipe Loss* model by comparing results obtained with it with the model developed by *Zakrzewski and Peitras*. They present a numerical model for calculating the one-dimensional electromagnetic field in conducting magnetic material in the Cartesian coordinate system, (Reference [86]). Like the model developed in this thesis, their model considers the magnetic non-linearity of the material using hysteresis loops. The equation they solve is

$$\frac{\partial^2 H_z}{\partial x^2} = \sigma \mu(H_z) \frac{\partial H_z}{\partial t} \quad (2.53)$$

which is equivalent to the equation solved in this thesis,

$$\frac{\partial^2 H_\phi}{\partial r^2} + \frac{1}{r} \frac{\partial H_\phi}{\partial r} - \frac{H_\phi}{r^2} = \sigma \mu(H_\phi) \frac{\partial H_\phi}{\partial t} \quad (2.54)$$

As $r \rightarrow \infty$ in Equation 2.54, Equation 2.54 approaches Equation 2.53 and the results obtained with the two numerical methods can be compared.

Data for the family of experimentally obtained hysteresis loops presented in the *Zakrzewski and Peitras* paper are obtained from Figure 4 of Reference [86] and are input into the *EM Pipe Loss* model. The family of hysteresis loops for the material used by *Zakrzewski and Peitras* are reproduced in Figure 2.11. Some error is unavoidable when the graphical data of *Zakrzewski and Peitras* are used to derive numerical values, and this error will be reflected when comparing our results to those obtained with the *Zakrzewski-Peitras* numerical model.

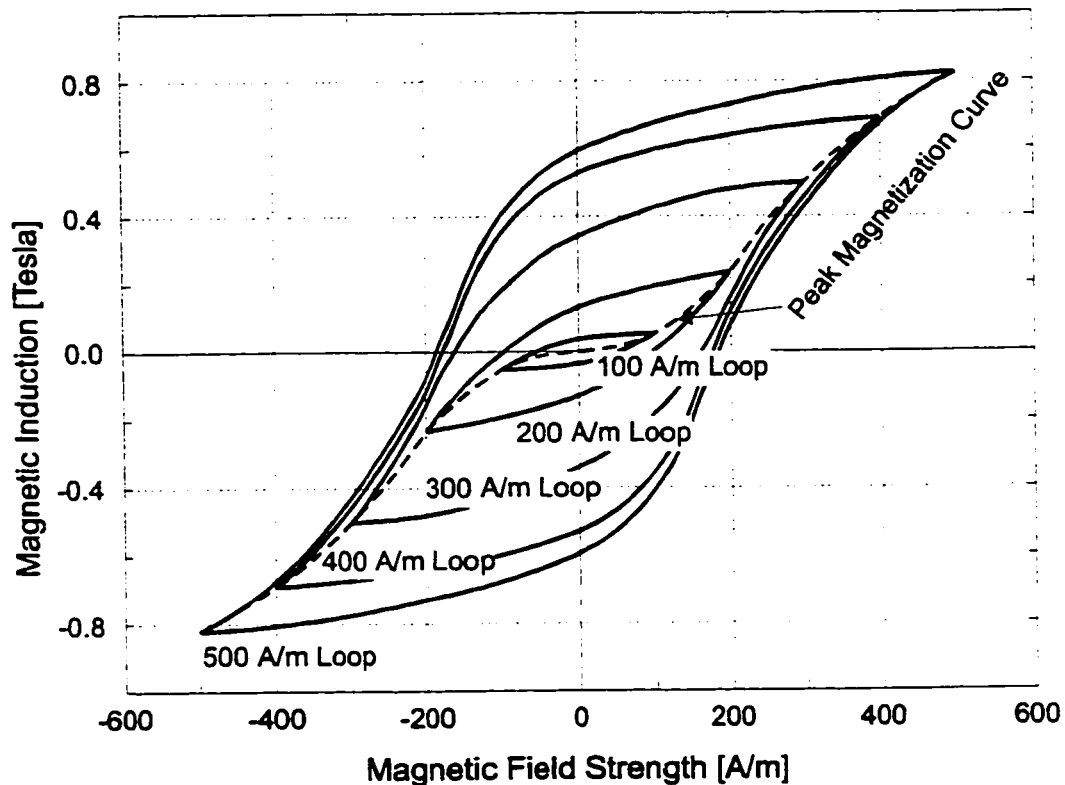


Figure 2.11: Hysteresis loops for the magnetic material reproduced from Figure 4 of *Zakrzewski and Peitras*, Reference [86].

For the validation, the radius r is set to 500 *mm*, a value much greater than the 3.875 *mm* thickness of the steel sample used in the calculation. The magnitude

of the current is selected so that the magnetic field strength at the surface of the iron is sinusoidal with a peak amplitude of 410 A/m . The values of Δr and Δt are set to 0.125 mm and 83 μs , as in the paper by *Zakrzewski and Peitras*.

The *EM Pipe Loss* model has an optional provision so that the maximum value of the relative permeability that will occur during the calculation can be limited to a value set in the input data set. The relative permeability calculated from the hysteresis loops, μ_r , is compared to the desired maximum value. If it is greater, the maximum value of the relative permeability is set to μ_r and used in subsequent calculations. The maximum value of the relative permeability is generally approximated from the experimentally determined hysteresis loop corresponding to the magnetic field strength at the boundary of the problem (location of the maximum magnetic field strength). For this example, the maximum magnetic field strength corresponds to a peak value of 410 A/m . From the hysteresis loops on Figure 4 of Reference [86], the maximum μ_r is about 4,000.

For this problem, the magnetic field strength impinges from one side onto the surface of the steel plate. The thickness of the plate is much greater than the skin depth so that the outer boundary condition can be set to $H_o(r_o) = 0.0 A/m$. Additional input data are summarized in Table 2.2.

Data	Symbol	Value	Units
Inner radius	r_i	500.000	mm
Outer radius	r_o	503.875	mm
Frequency	f	50.0	Hz
Magnitude of sinusoidal			
Magnetic field strength	H_o	410.0	A/m
Electrical conductivity	σ_s	5,440,000	S/m
Maximum $dB/(\mu dH)$		4000	

Table 2.2: The input data for the steel pipe used in the validation of the *EM Pipe Loss* model with the *Zakrzewski-Peitras* numerical model.

Before comparing results of the calculations between the two models, it is noted that the *Zakrzewski-Peitras* numerical model calculates the electric field at

the nodes using the point form of Ampere's Law,

$$E_i = -\frac{1}{\sigma} \frac{H_{i+1}^n - H_i^n}{\Delta x} \quad (2.55)$$

Once the electric field strengths at the interior nodes are calculated, a polynomial expression is fit to the data to obtain extrapolated values for the electric field strength on the surface of the steel. In this thesis, the electric field strength is calculated using the integral form of Ampere's Law as stated in Equation 2.28 and the field on the surface is calculated directly using Equations 2.29 and 2.30.

Figure 2.12 shows a comparison between the electric field strength calculated with the *EM Pipe Loss* model and the electric field strength calculated with the *Zakrzewski-Peitras* numerical model. The two calculations show good agreement. The difference in the *calculated* peak value of the electric field strength obtained with the *Zakrzewski-Peitras* numerical model and that obtained with *EM Pipe Loss* model is 9.3%. The difference between the electrical field calculated using the *EM Pipe Loss* model and the peak value of the electrical field *measured* by *Zakrzewski and Peitras* is 16.8 %.

The phase angle between the magnetic and the electric field strength is 0.55 radians (the electric field strength leading the magnetic field strength), calculated using the *Zakrzewski-Peitras* numerical model. The *EM Pipe Loss* model calculates a phase angle of 0.54 radians, resulting in a difference of less than .01 radians in the phase angles. The numerical data for the *Zakrzewski-Peitras* numerical model and their experimental data are reproduced from graphical figures in their paper. This procedure is subject to an inherent error of as much as 5.0%.

By adjusting the maximum value of μ_r that is allowed to occur in the numerical calculations, a closer match between the *EM Pipe Loss* model calculations and those of *Zakrzewski-Peitras* numerical model can be obtained. Figure 2.13 shows a comparison of the *EM Pipe Loss* model to the *Zakrzewski and Peitras* data with the adjustments. A good match was achieved with $\mu_r=2,000$. The difference in the calculated peak value of the electric field strength obtained from the *Zakrzewski-Peitras* numerical model and the calculated peak value of the electric field strength from the *EM Pipe Loss* model is 4.1%. The difference between the peak value obtained from the *EM Pipe Loss* model and the peak value from the

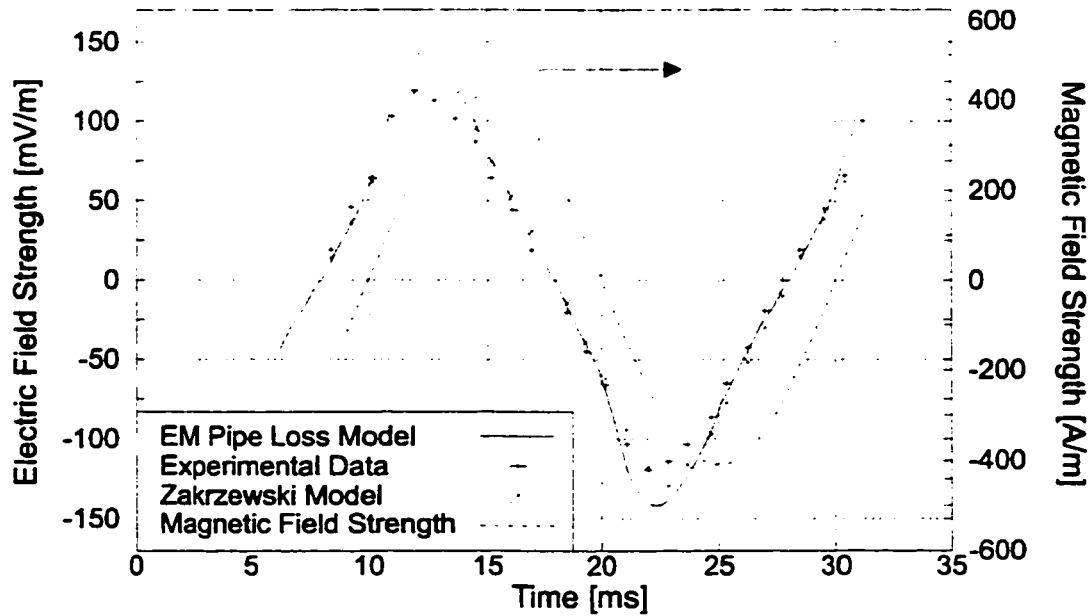


Figure 2.12: Comparison of the electric field strength at the surface of the ferromagnetic plate calculated using the *EM Pipe Loss* model, the *Zakrzewski-Peitras Numerical* numerical model, and their experimental data, [86].

Zakrzewski-Peitras experimental data is 4.2 %. It is also observed on Figures 2.12 and 2.13 that the *shape* of the electric field strength calculated using the *EM Pipe Loss* model more closely follows the experimental data than that of the electrical field strength calculated with the *Zakrzewski-Peitras* numerical model. The peak values are placed closer to each other and the distortions in the sinusoidal curves are more congruent.

The value for the maximum μ_r can be used as a *history matching* parameter to scale the calculation of the non-linear magnetic hysteresis loops so that the calculation of the electric field strength matches observed data. This is a convenient feature since determining derivatives from experimental data, which is necessary for the calculation of μ_r , can result in large variations in the calculation if proper care is not taken to ensure good data. This practical approach is a simple way of ensuring the calculations can be matched with actual results. However, since the maximum μ_r is usually associated with hysteresis loops near the boundaries, error in calculating the input power can result.

Figure 2.14 shows the hysteresis loops at various depths from the surface of the steel sample, as calculated with the *EM Pipe Loss* model. This figure represents

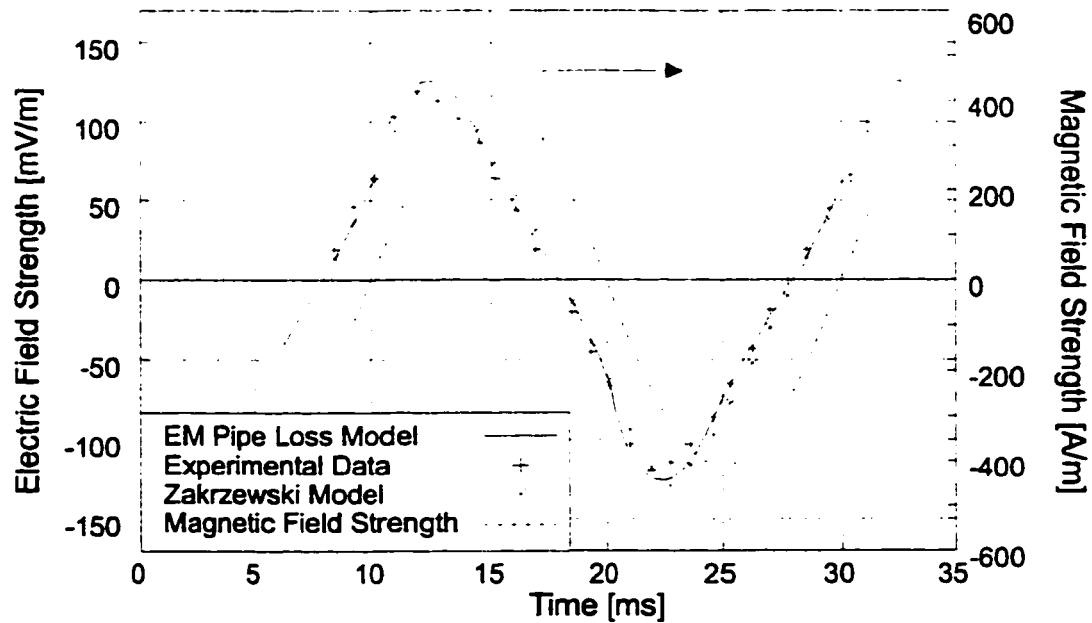


Figure 2.13: Comparison of the electric field strength at the surface of the metal plate calculated using the *EM Pipe Loss* model, the *Zakrzewski-Peitras* numerical model and their experimental data, (Figure 5 of Reference [86]), with the maximum μ_r in the *EM Pipe Loss* model adjusted to match the measured electric field strength data.

the process of magnetization within the steel at steady state conditions. From the surface, the magnetic field strength decreases with increasing depth. For example, at a depth of 0.75 mm the amplitude of the time varying magnetic field strength is 185 A/m , and as a result the corresponding hysteresis loop encloses a much smaller area than the loop at the surface of the steel.

Figure 2.15 shows the electric field strength at various depths from the surface of the steel. The figure shows that as the electromagnetic wave penetrates into the steel, the electric field strength is attenuated (and thus the eddy-currents) and the peak value of the electric field strength occurs at later times than at the surface. The shape of the electric field strength is distorted by the non-linear magnetization characteristics of the steel. The distortion increases with depth and is controlled by the shape of the hysteresis loops throughout the material.

As a final validation of the *EM Pipe Loss* model, the calculation of the eddy current, hysteresis, and total power losses using the *EM Pipe Loss* model are compared to the corresponding values calculated with the *Zakrzewski-Peitras* numerical model. For these calculations, the maximum μ_r is set to the maximum

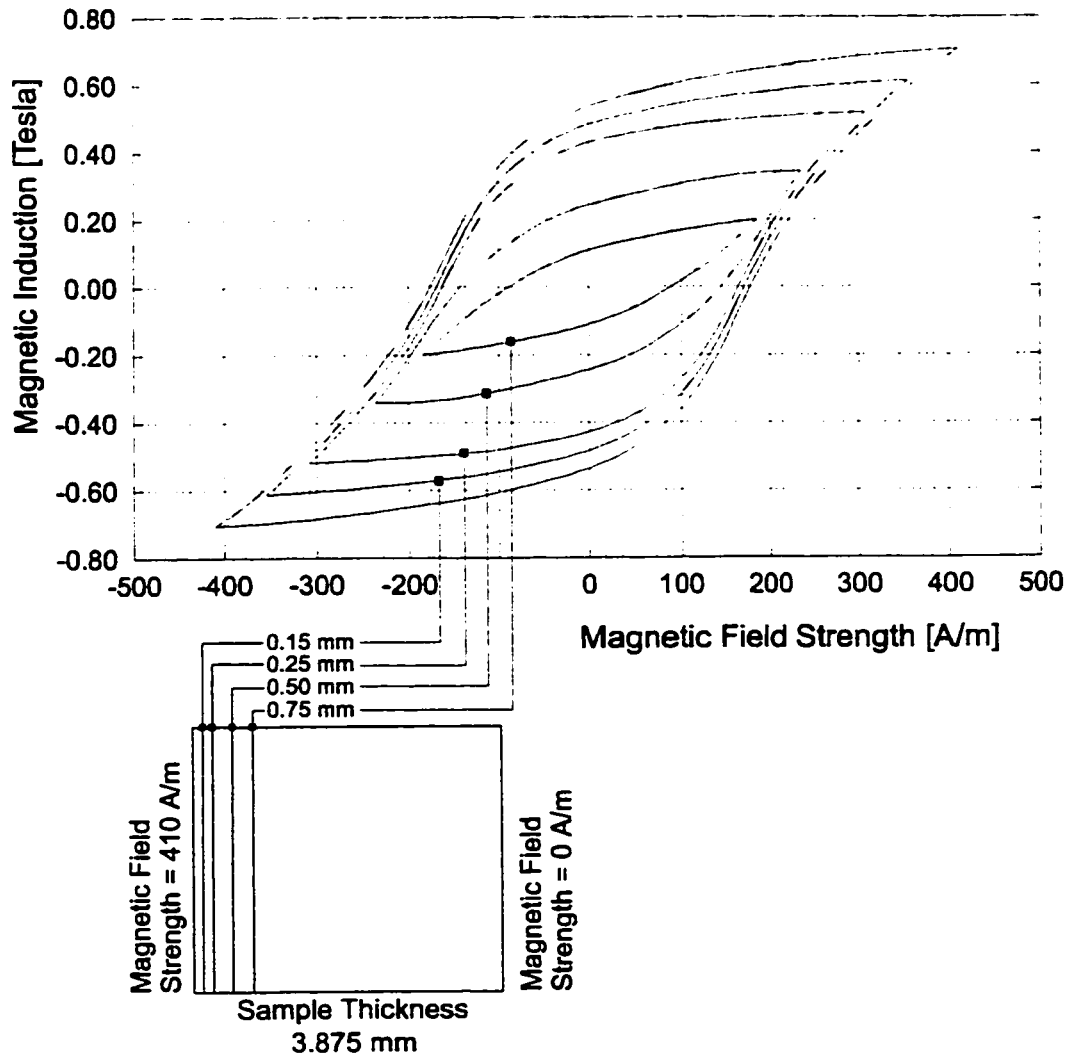


Figure 2.14: Hysteresis loops at various depths from the surface of the solid steel sample calculated using the *EM Pipe Loss* model.

value as estimated from the *Zakrzewski and Peitras* hysteresis loops, which is about 4,000. It is noted that using this value does not exactly match the surface electric field as shown in Figure 2.12. The interpretation of the hysteresis loop data from the figures in Reference [86] likely contributes significantly to the differences. The results are summarized in Table 2.3.

Note that in Table 2.3 the sum of the eddy-current and hysteresis losses does not equal the total power losses. The total power losses are calculated using Poynting's vector. The eddy current and hysteresis losses are calculated separately. The total power calculated from Poynting's vector for the *EM Power Loss* model is 22.41 W/m^2 which is within 2.2 % of the sum of the hysteresis and eddy current

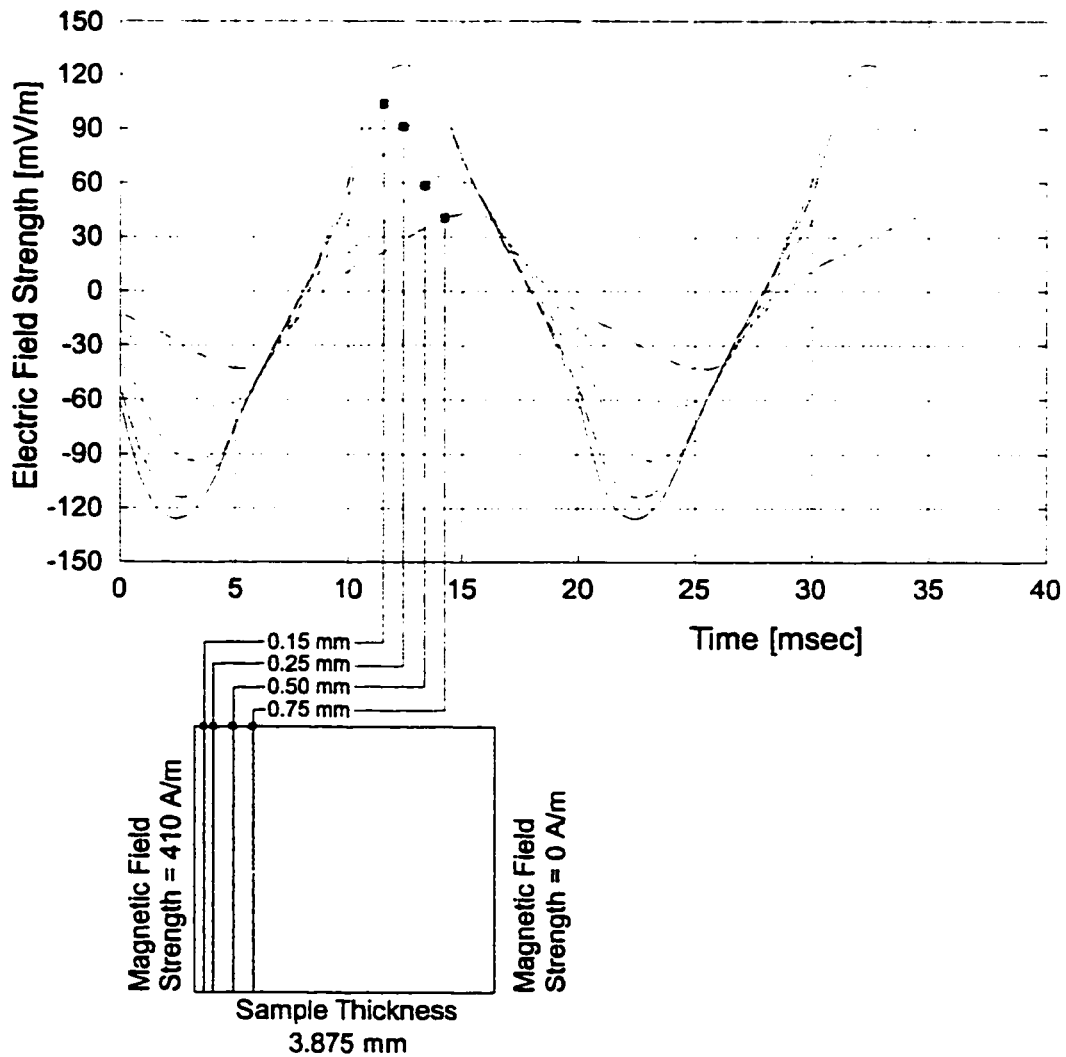


Figure 2.15: The electric field strength at various depths from the surface of the solid steel sample calculated using the *EM Pipe Loss* model.

losses calculated by *Zakrzewski and Peitras*.

Zakrzewski and Peitras do not calculate the hysteresis and eddy current losses simultaneously while hysteresis is taken into account, and this is clearly stated in their paper. First, they determine the eddy current losses without the effects of hysteresis. Then they use their model to determine the total power loss from Poynting's vector. From these total power losses they subtract the eddy current losses to obtain an estimate of the losses that are due to hysteresis effects.

Since hysteresis has a strong influence on the distribution of the eddy currents, their approach is only approximately valid. The *EM Pipe Loss* model determines both the hysteresis and eddy current losses while hysteresis effects are accounted

Data	<i>EM Power Loss Model</i>	Zakrzewski-Peitras	Units
Total power losses	22.41	20.20	W/m^2
Eddy current losses	13.05	15.00	W/m^2
Hysteresis losses	8.87	5.20	W/m^2
Fraction eddy current losses	59.43	67.00	percent
Fraction hysteresis losses	40.46	33.00	percent

Table 2.3: Comparison of the numerical power flow calculations carried out with the *EM Pipe Loss* model and the *Zakrzewski-Peitras* numerical model. The input data are summarized in Table 2.2

for. The different approaches produce different results as indicated in Table 2.3. The *EM Pipe Loss* model calculates that the hysteresis losses are actually 7% greater and the eddy current losses are 7% less than estimated by the *Zakrzewski-Peitras* numerical model.

The *EM Power Loss* model has been compared to the numerical model developed by *Zakrzewski and Peitras* (Reference [86]). The results obtained with these two models demonstrate the sensitivity of the calculations to the hysteresis loops used for the material. Hysteresis can make a major contribution to the total power losses. The next section compares and validates the *EM Pipe Loss* model to data obtained from experiments that were conducted as part of this thesis.

2.4 Experimental Validation of the *EM Pipe Loss* model

In this section the *EM Pipe Loss* model is validated using data obtained from experiments that were conducted during the course of this thesis. The validation consists of two components. For the first validation, the electrical field strength measured at the interior and exterior surfaces are compared to the electric field strength and phase angle calculations determined with the numerical model. For the second validation, the power losses in the casing as a function of the excitation are experimentally determined from the thermal response of the system. These power losses are compared to the total hysteresis and eddy current losses calculated using

the *EM Pipe Loss* model.

The second validation is consistent with the purpose of the numerical model, which is to determine the power losses in a pipe made from lossy ferromagnetic material conducting current. Thus, the second approach is a *direct* validation of the numerical model with regards to the capability of the model to reasonably determine the power losses in the pipe taking into account all power loss mechanisms.

This section is organized as follows: the test procedure, experimental determination of the electrical properties of the pipe, and finally the validation of the *EM Pipe Loss* model using electric field strength measurements and the thermal response of the system.

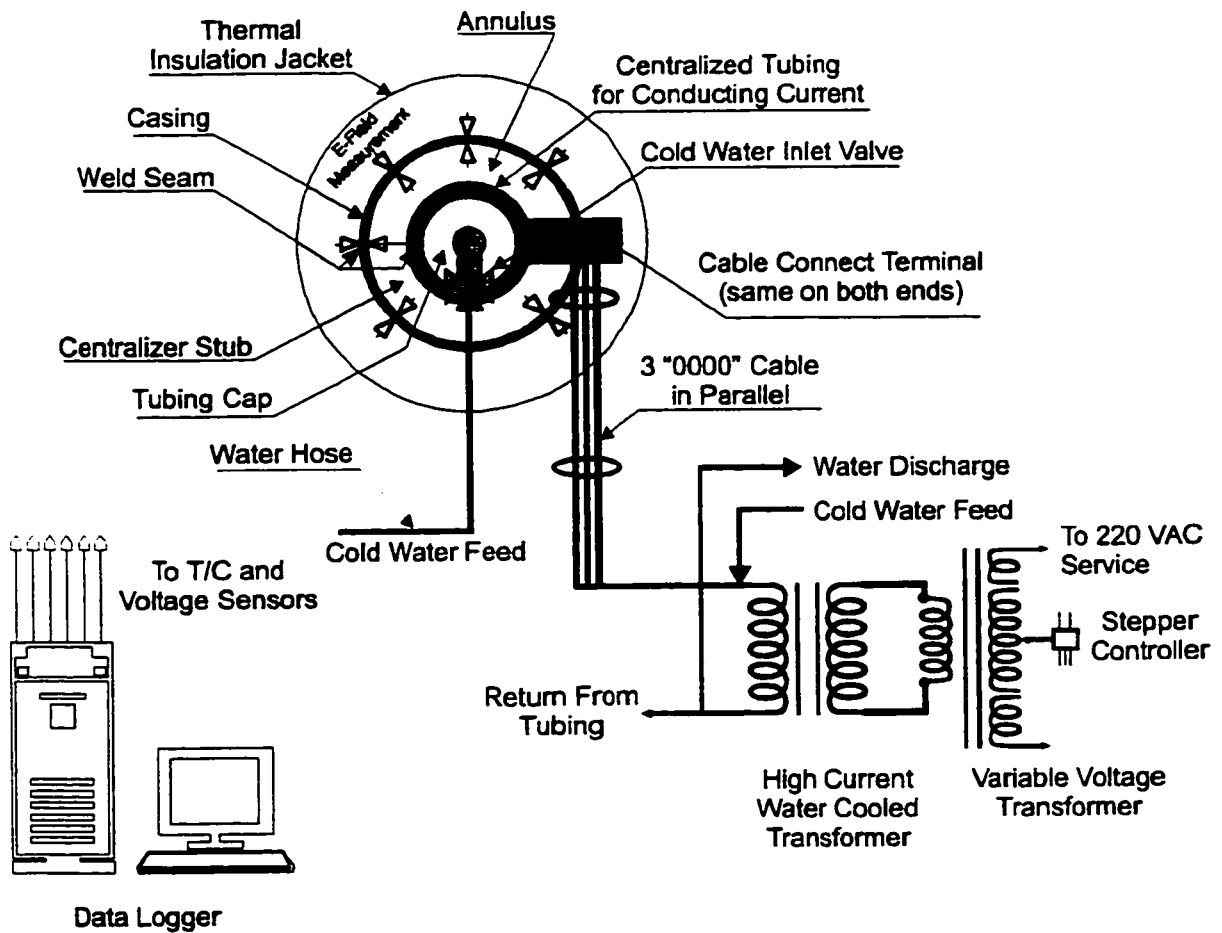
2.4.1 Test setup and procedure

The equipment used in the test is illustrated in Figures 2.16 and 2.17. Figure 2.16 shows the end and overall system view and Figure 2.17 shows the side view and dimension details. A photo of the test set-up is shown in Figure 2.18

The tubing and casing are both oilfield tubular type K-55 and were donated to the Applied Electromagnetics Laboratory by *Texaco Canada Petroleum Inc.* The physical dimensions of the casing and tubing are summarized in Table 2.4, and are the precise dimensions used in all associated numerical calculations.

Dimension	Value
Casing Dimensions	
Inside Radius, R_i	83.185 [mm]
Outside Radius R_w	89.345 [mm]
Length L	4.007 [m]
Tubing Dimensions	
Inside Radius R_{t_i}	38.100 [mm]
Outside Radius R_{t_w}	44.260 [mm]
Length L	4.988 [m]

Table 2.4: Physical dimensions of the casing and tubing used in the experiment.



End and System View

Figure 2.16: End and system view of the equipment used in the thermal response test.

The tubing was centralized in the casing using a centralizer stub at both ends of the tubing string. The centralizer stub was manufactured so that the location of the tubing was concentric within the casing with a high degree of precision. The length of the centralizer stub was limited to approximately 7.5 cm to minimize any interference with the heat transfer mechanisms along the axial length of the casing and tubing.

As a result of the process used to manufacture the pipe, a weld seam is produced along the axial length of the tubing and casing. This is shown on Figure 2.16. The impact of the weld seam on the results was minor. However, it is noted for completeness.

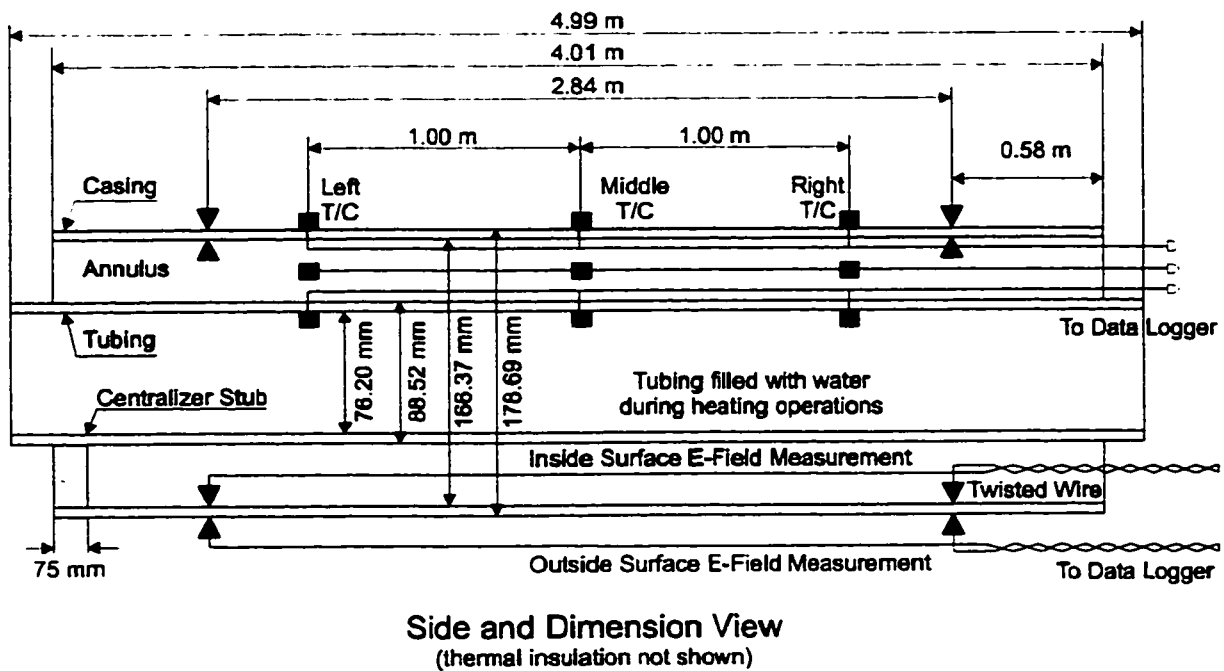


Figure 2.17: Side view of the equipment used in the thermal response test showing detailed dimensions.

Cable connect terminals with uniform circumferential contact on the tubing (at both ends of the tubing) were used so that the current uniformly entered and exited the pipe. The tubing was also fitted with low pressure end caps and valves to accommodate a cooling system so that the system could be efficiently cooled down at the end of a thermal test. Also, during a thermal test, the tubing was filled with water and the temperature of the water was closely monitored. If the temperature reached $90\text{ }^{\circ}\text{C}$ the test was terminated.

Thermal insulation of the casing was necessary so that the temperature response could be related to the total electromagnetic power losses in the casing. Fiberglass insulation was placed around the exterior of the casing for this purpose. The fiberglass insulation had a rating of R-40, which was adequate for the purposes of this experiment. The annular region between the tubing and the casing was filled with stagnant air, which has a thermal conductivity of less than $0.09\text{ W}/(\text{m}^{\circ}\text{C})$. Since the tubing was increasing in temperature at approximately the same rate as the casing, convection currents were minimized and thermal insulation was

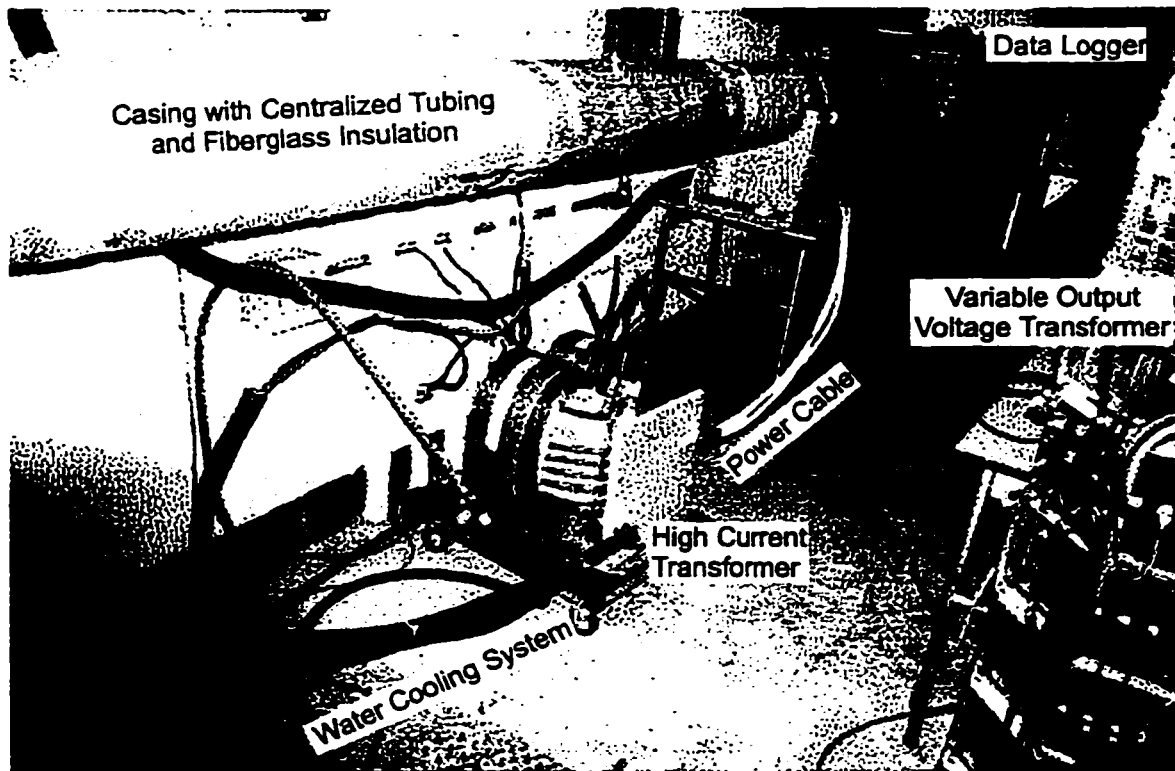


Figure 2.18: The test apparatus as assembled in the Applied Electromagnetic Laboratory.

effectively provided at the interior casing wall by the annular region filled with air.

The power system consisted of a variable voltage transformer connected to a water-cooled high current transformer. A composite cable consisting of three 0000 cables in parallel was connected to both ends of the centralized tubing. This large cable was used to minimize the resistance of the system and thus maximize the current that could be delivered by the transformer. The three No. 4 cables connected in parallel have a maximum current capacity in air of 1,300 A (National Electrical Code) [95].

The purpose of the variable voltage transformer is to step down and control the voltage input to the high current transformer. The small combined resistance of the cable and tubing connected to the output of the high current transformer requires that the voltage is stepped down to limit the current to a range of predetermined values. The variable turns ratio feature of the voltage transformer made it possible for the current transformer to be set to a constant turns ratio for convenient and safe operation.

The input of the variable voltage transformer was connected to the 220 VAC single phase electrical service in the Electrical Engineering building. The transformer was equipped with a stepper control module designed specifically for the experiment. The control module was designed so that the turns ratio of the transformer could be changed in very small increments, thus allowing accurate regulation of the current flow into the system to within ± 0.1 A.

The high current transformer was custom manufactured by *Madis Engineering Limited* of Calgary, Alberta, Canada, and was lent to the Applied Electromagnetics Laboratory for the duration of the experiments. It was modified so that cooling of the output windings using a cold water circulation system was possible. The modified transformer was capable of a continuous output current of 1,000 A *RMS*.

The *RMS* value of the axial electric field strength was measured on the interior and exterior surfaces of the casing at eight equally spaced locations around the circumference of the pipe as shown on Figure 2.16 and in more detail on Figure 2.23. Twisted wires were used to connect the measurement points to the data logger to minimize any electromagnetic interference with measurements. The axial distance between the measurement points was 2.84 meters and the distance from the measurement points to either end of the casing was 0.58 meters. This distance is equivalent to seven radii of the casing and is of sufficient length that end effects are not noted [29]. It was desirable to have the axial measurement points as far apart as possible so that a maximum voltage was measured and the measurement error was kept to a minimum. The *RMS* value of the electric field strength is the *RMS* potential drop between the measurement points divided by the distance between them.

The temperature responses of the casing, the annular region between the tubing and casing, and the tubing were measured at three equally spaced locations along the length of the tubing-casing apparatus as shown in Figure 2.16. The thermocouples in the casing and tubing were attached so that any thermal contact resistance between the thermocouples and the tubing was minimized. An adjustable metal band was used to hold the thermocouples firmly in place. The thermocouples were located sufficiently far from the ends of the casing and tubing so that end effects were not noted.

The procedure for conducting the experiment is as follows:

1. Fill the tubing string with water.
2. Connect the water cooling system to the high current transformer and power up the system at minimum voltage and current levels.
3. Using the stepper controller for the variable voltage transformer, adjust the output current from the high current transformer to the desired operating level.
4. Turn on the data logger and begin recording the electrical and temperature data.
5. Monitor the temperature of the water in the tubing string. When the temperature reaches $90\text{ }^{\circ}\text{C}$ or when the system has reached a thermal steady state so that there is no further increase in temperature (the latter will occur for currents less than 200 A RMS), terminate power to the system.
6. Cool the system down by flowing cold water through the tubing. Once the temperature of the system has decreased to approximately room temperature, repeat the test at a different current level.

The data was monitored continuously using a computer controlled data logger. The current and voltages were all measured using true *RMS* meters. Table 2.5 summarizes the data measurement details.

2.4.2 Modifications of the test for collection of electrical data in the vicinity of strong electromagnetic fields

The test setup and procedure just described were designed to collect both electrical and temperature data simultaneously for subsequent analysis. A review of the electrical data indicated that the proximity of the transformer and the location of the equipment relative to the electrical distribution panels and cables that supply power to the laboratory resulted in excessive electromagnetic interference with the voltage that is measured along the length of the casing. It was necessary to have the

Measurement Points	Comments
Casing Axial Electric Field	Measured on the casing. Voltage sensors 2.84 m apart and circumferentially placed around the casing every $\pi/4$ radians. Twisted wire used to reduce EM interference. Data recorded by data logger.
Tubing, Casing, and Annulus Temperature	Three thermocouples (T/C) placed 1.00 m apart axially, one in the middle and the others at one meter to either side. Sensors set and held firmly in place with adjustable straps. Data recorded by data logger.
Water Temperature in the tubing	Thermocouple placed in a thermowell in contact with the water. Data recorded by data logger.
Current Transformer V-I Output	Output current measured with current probe connected to true <i>RMS</i> DVM. Current value recorded by hand. Output voltage recorded by data logger.
Current Transformer Temperature	Thermocouple placed into transformer core and input to a portable thermocouple meter. Data recorded by hand.

Table 2.5: Sampled data and measurement details for the thermal response test.

high current transformer located near the tubing, since using longer cables introduced additional resistance that severely compromised the output current capacity of the transformer. As a practical matter, the space allocated for the test was not sufficient to configure both the variable output voltage transformer and high current transformer, as well as the test equipment, in a manner such that the proximity effects could be satisfactorily reduced. To solve the proximity problem, the test equipment was re-located away from the electrical service distribution system to a distance that proved to be satisfactory. A smaller transformer was then used and located two meters from the test equipment and positioned so that the leakage of magnetic field strength from the transformer core had minimum interference with the test. Longer cables of the same capacity were connected to the ends of the tubing and positioned to minimize interference.

The trade off in relocating the test equipment and using a smaller transformer in order to obtain more accurate electrical data was that the maximum magnitude of the current was reduced from 1,000 A to 275 A *RMS*. The impact of limited current capacity on the test results was minimal. The relative hysteresis effects at 275 A *RMS* are of a similar magnitude as at 1,000 A, and thus adequate test data

was obtained to validate the *EM Pipe Loss* model.

2.4.3 Magnetic properties of the casing and tubing

The casing used in the experiment is type K-55 with an inner radius of 83.185 mm and outer radius of 89.345 mm, commonly referred to as 7" casing. The thickness of the pipe is 6.160 mm. The density of the steel is 7.66 g/cm^3 . A sample of the casing and tubing pipe, commonly referred to as 3.5" tubing was sent to *LDJ Electronics, Inc.* in Troy, Michigan, USA, for hysteresigraph testing. The purpose of the hysteresigraph test is to obtain several maximum hysteresis loops that can be used to construct general hysteresis loops using the *distance factor* method described in Section 2.2.5. Both AC and DC measurements were taken although only the DC data is needed for the numerical model.

Table 2.6 summarizes the hysteresigraph tests performed by *LDJ Electronics Inc.* on the casing and tubing.

DC Loop Tests					
Sample	Hysteresis Loop Peak Field <i>A/m</i>	Coercive Force <i>A/m</i>	Saturation Induction Tesla	Relative Permeability	
				$\mu_{initial}$	μ_{max}
				3½" Tubing	1,000
3½" Tubing	8,000	575	1.747	416	1,233
7" Casing	1,000	452	1.092		
7" Casing	500	274	0.392		
7" Casing	8,000	564	1.747	477	1,699
AC Loop Tests at 60 Hz					
Sample	Peak Induction Tesla		Core Loss <i>W/kg</i>		
3½" Tubing	1.0		60		
7" Casing	1.0		59		

Table 2.6: Summary of the *LDJ Electronics Inc.* tests.

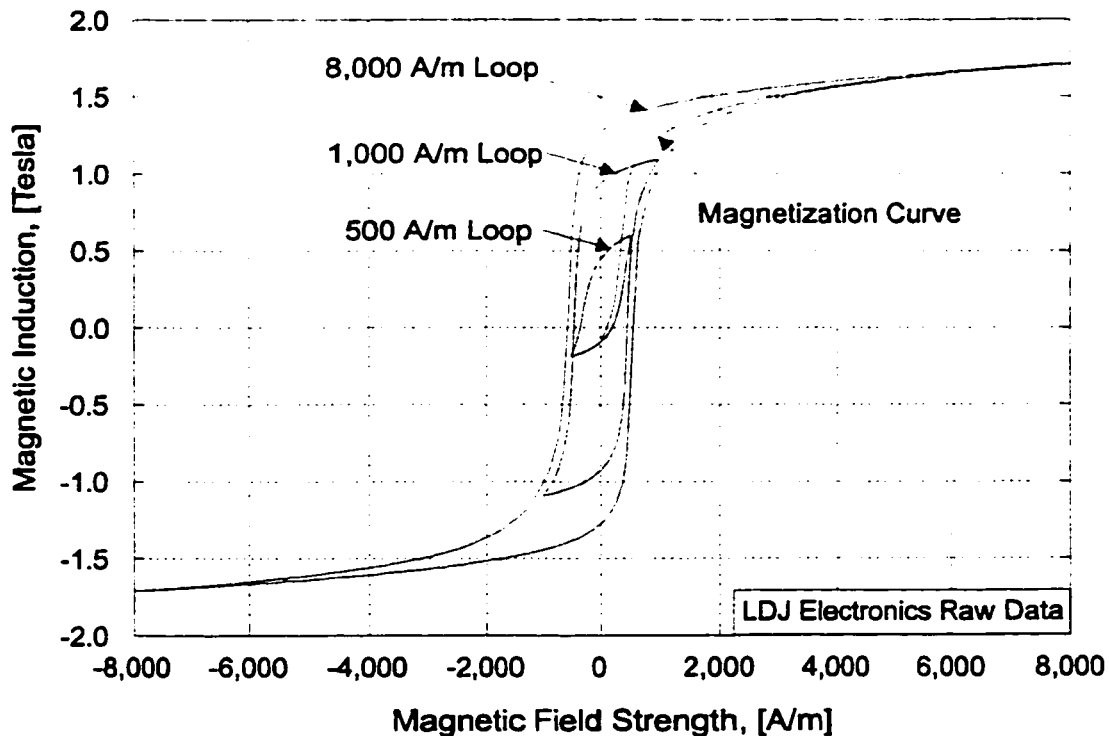


Figure 2.19: Hysteresis data for the 7" casing obtained using a hysteresigraph test as received from *LDJ Electronics Inc.*

Figure 2.19 shows the hysteresis loops for the 7" casing. The hysteresis loops are virtually symmetrical and very little correction to make them symmetrical is required. The minor corrections that are required are to ensure that the *upper maximum loop* and *downer maximum loop* are exactly symmetrical about the origin, that the ends or peaks of the loops coincide with the *peak magnetization curve*, and the *peak magnetization curve* begins at the origin and is also symmetrical.

The data must be filtered to ensure that the magnetic induction is monotonically increasing for the upper loop and monotonically decreasing for the downer loop. Otherwise the numerical calculation of μ_r may be negative which is physically unrealistic. For the 500 A/m loop, the sample is far from saturation and as shown in Figure 2.19 the loop is very asymmetrical about the origin and the peaks of the loop do not follow the *peak magnetization curve*. This loop was discarded.

Notable characteristics of the raw data are

1. All but the 500 A/m curves are approximately symmetrical about the origin.
2. The 500 A/m is not symmetrical, since according to *LDJ Electronics Inc.* at

500 A/m the test is conducted so far from the magnetic saturation of the material that the casing is cycling in a minor loop and is likely in error. The 500 A/m data are not used in the construction of general hysteresis loops for the *EM Pipe Loss* model.

3. The end points or peaks of the 1,000 A/m loop do not lie on the *peak magnetization curve* for the material. The data is scaled a minor amount so that the end points of the loop exactly coincide with the *peak magnetization curve*.
4. The *peak magnetization curve* does not begin exactly at the origin. The data is shifted upwards a small amount so that the initial data point is located exactly at the origin.
5. Although not visible on Figure 2.19, several of the adjacent data points are not all either monotonically increasing or decreasing. These data are *filtered*.
6. Also not visible on Figure 2.19 is that the loops do not lie entirely between the maximum and minimum magnetic field strength for the loop. The loops are scaled a minor amount so that the peaks exactly correspond to the peak values of the field.

In summary then, the following modifications to the raw data were done so that the curves can be used by the *distance factor* method to generate a hysteresis loop for any applied magnetic field strength.

1. Filter the data for the *peak magnetization curve*, *downer loops*, and the *upper loops* to eliminate any magnetic induction data that is not increasing or decreasing with increasing or decreasing magnetic field strength.
2. Shift the 1,000 and 8,000 A/m loops by the necessary $\pm\Delta B$ and $\pm\Delta H$ so that they are symmetrical about the origin.
3. Shift the *peak magnetization curve* by the necessary magnetic induction, B so that the curve intersects the origin at $H = 0$ A/m.
4. Scale the 1,000 A/m data so that the end points or peaks of the hysteresis loop coincide with the *peak magnetization curve* at $H = 1,000$ A/m.

- Finally, smooth the data using cubic spline interpolation so that the derivatives between adjacent data points are smooth and the $B - H$ data can be used for small values of ΔH .

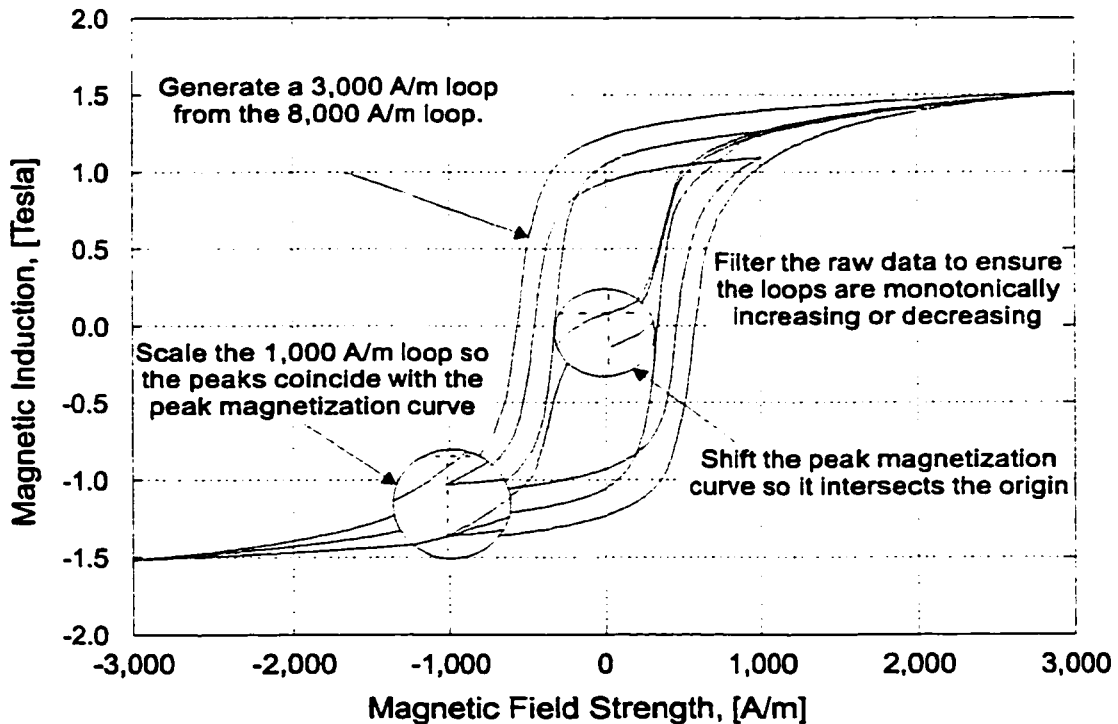


Figure 2.20: Modification to the *LDJ Electronics Inc.* hysteresis data for the 7" diameter casing.

Since the magnetic field strength in our experiment at no time exceeded 2,000 A/m , a 3,000 A/m loop was constructed from the 8,000 A/m data using the *distance factor* method described in Section 2.2.5. This reduced the number of data points needed to define the hysteresis loops in the model.

The modified 3,000 A/m and 1,000 A/m hysteresis loops are input into the *EM Pipe Loss* model and are used to construct a hysteresis loop for any value of the magnetic field strength using the methods described in Section 2.2.5. A comparison of the corrected hysteresis loops and the raw data for the casing are shown in Figure 2.20. It is evident from the figure that very little correction of the raw data was necessary.

Several hysteresis loops for the casing constructed using the *distance factor* method are shown in Figure 2.21. The constructed loops range in value from 250 A/m to 3,000 A/m .

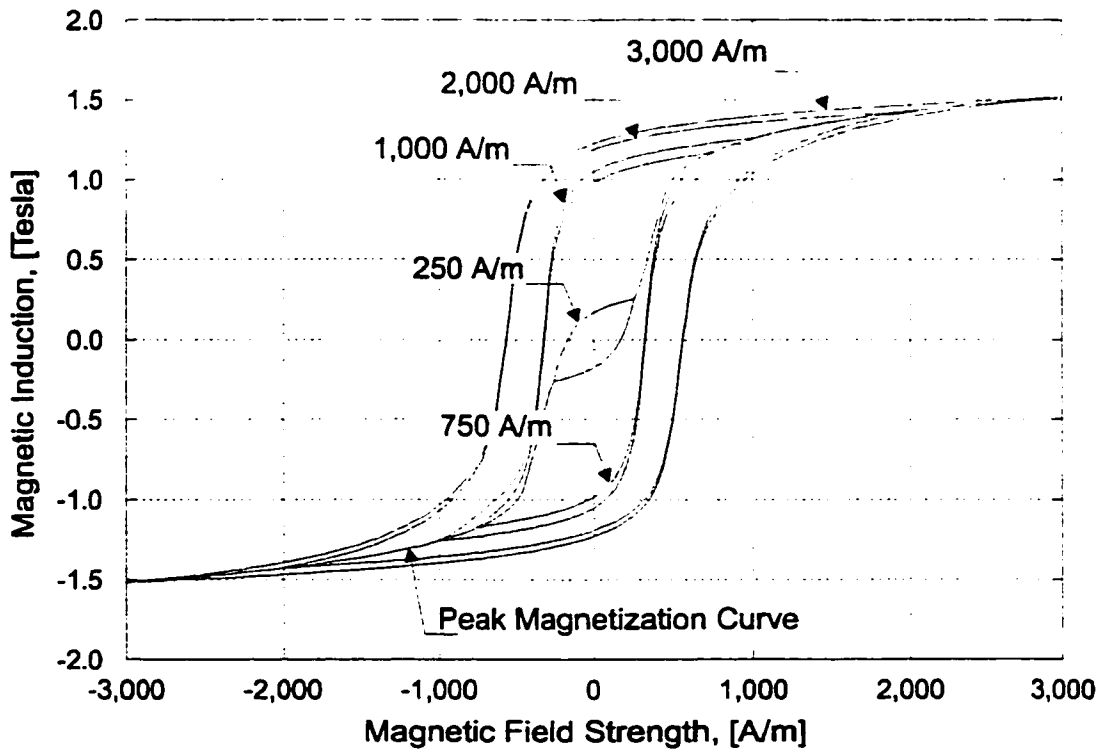


Figure 2.21: Several constructed hysteresis loops for the casing based on the *LDJ Electronics Inc.* tests and calculated using the *distance factor* method.

The need to filter and adjust the raw data can be demonstrated by comparing the relative permeability μ_r determined using raw data and the same raw data after it has been appropriately modified. Figure 2.22 shows this comparison for the 1,000 A/m hysteresis loop.

It is evident that unless care is taken to modify the raw data, it cannot be used in the numerical program. Since the adjustments made to the raw data are minimal, they do not undermine the integrity of the calculated results.

2.4.4 Determination of the electrical conductivity of the casing

The electrical conductivity of the casing is too large to measure using direct methods. Alternatively, the electric field strength on the surface of the casing is measured and the electrical conductivity is indirectly calculated using the *Loga* analytic model which is described by Equations 2.50 and 2.51, [1].

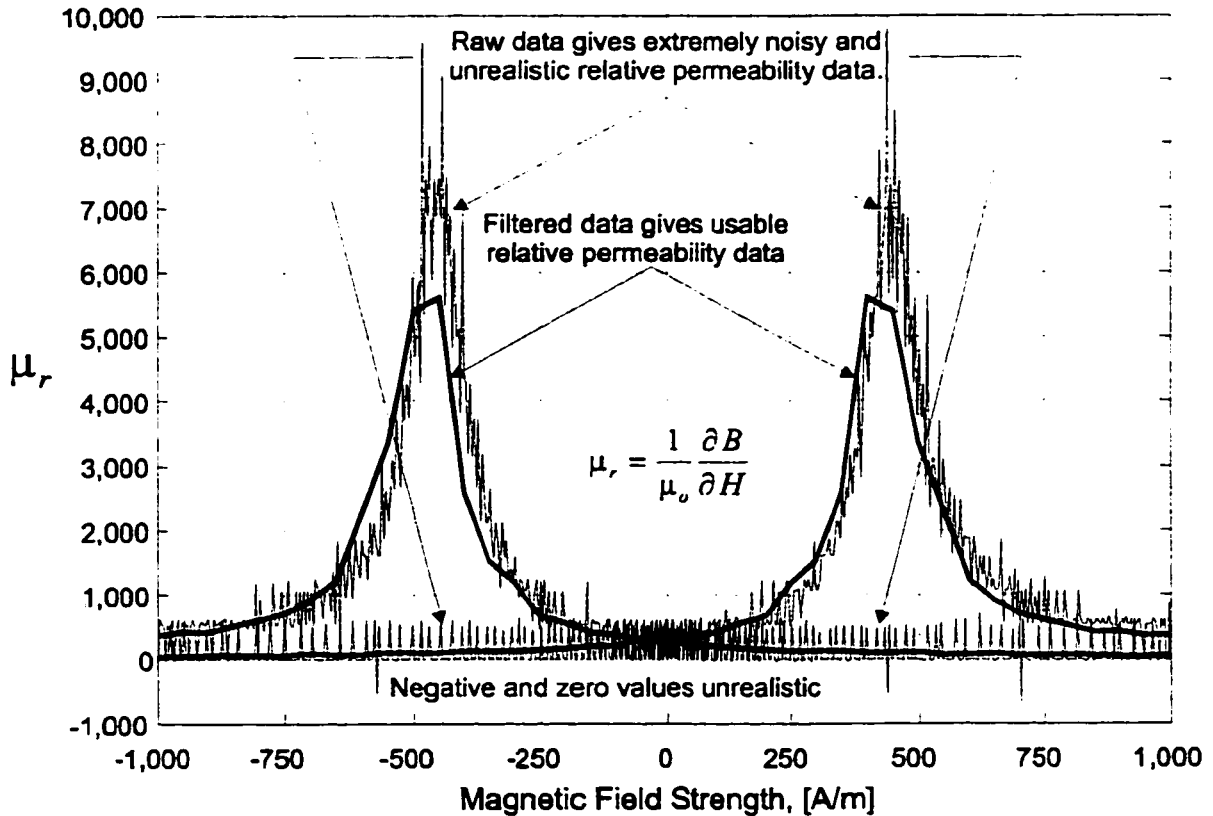


Figure 2.22: Comparison of the relative permeability μ_r calculated using raw and modified data.

The electric field strength on the surface of the casing is intentionally kept small so that hysteresis effects are negligible. Under these conditions, the fields are linear and the *Loga* analytic model can be used to determine the electromagnetic response of the pipe under sinusoidal excitation. The electrical conductivity is adjusted until the calculated electric field strength equals the electric field strength measured on the surfaces of the pipe. When the fields match, the electrical conductivity for the steel pipe has been determined indirectly. Figure 2.23 shows the locations where the electric field strength is measured.

The electric field strengths and phase angles with respect to the sinusoidal excitation on the interior and exterior surfaces are measured at eight locations circumferentially around the perimeter of the pipe as shown in Figure 2.23. The measured data are summarized on Figures 2.24 and 2.25 for currents of 25 and 50 A *RMS*.

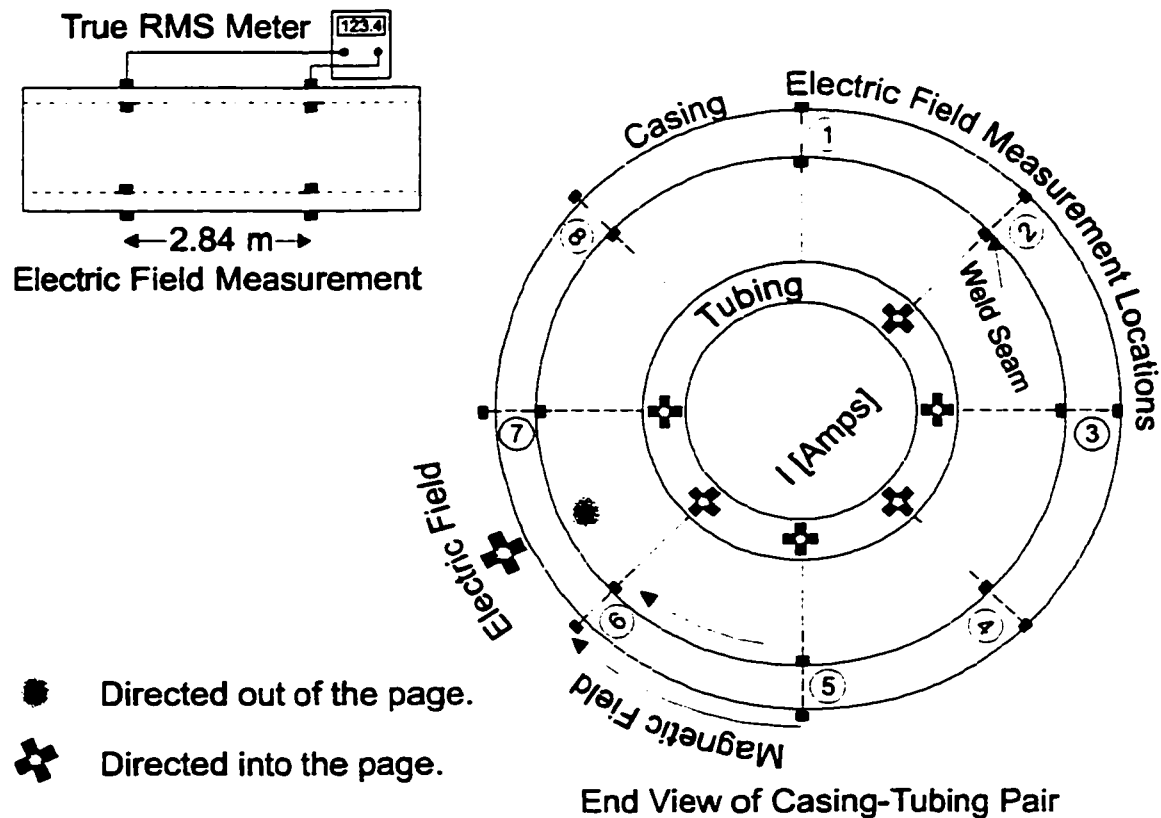


Figure 2.23: Measurement locations of the surface electric field strengths and phase angles at various locations on the interior and exterior surfaces of the casing.

The data shows that the electric field strength is not uniform around the perimeter of the casing as might be expected for a steel pipe with homogeneous electrical properties. It is conceivable that the variation of the electric field strength may be a result of non-homogeneous electrical properties created by the manufacturing process for the steel pipe. Also, electromagnetic interference from the transformer and power distribution system may affect the uniformity of the electromagnetic field distribution in the pipe.

The pipe is fabricated from a large steel sheet that is rolled at high temperature and welded along a seam to form a closed cylinder. Along the welded seam, the electrical conductivity is expected to be different than elsewhere due to the introduction of different materials to form the welding process. The location where the minimum electric field strength on the outside surface and maximum on the interior surface is measured, as shown on Figures 2.24 and 2.25, consistently coincides with the location of the welded seam (Point 2).

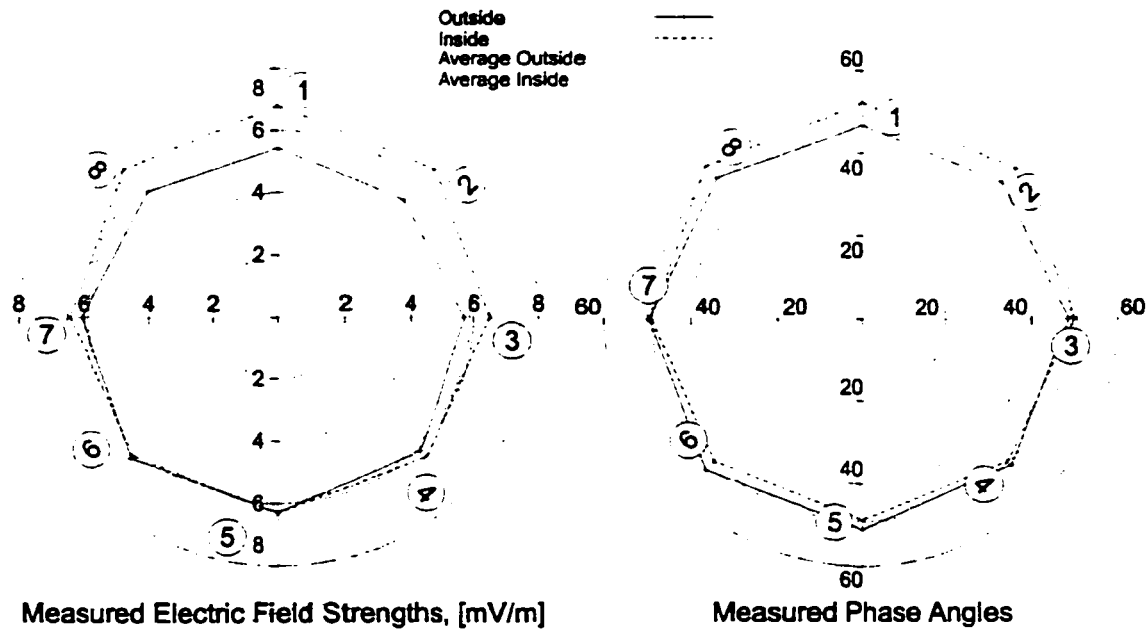


Figure 2.24: Measurement of the surface electric field strengths, (mV/m), and phase angles, (degrees) at various locations on the interior and exterior surfaces of the 7" casing for a sinusoidal excitation of 25 A (RMS) conducted in the centralized tubing.

For both the 25 and 50 amp RMS sinusoidal excitation, the average values of the electric field strength on the interior and exterior surfaces are matched respectively to the analytic model, one average electric field strength at a time, by adjusting two respective electrical conductivities, σ_i and σ_w . Specifically, the electrical conductivity σ_i is calculated to match the electric field strengths measured on the interior surface of the pipe, and σ_w is calculated to match the measurements on the outside surface. An average electrical conductivity for the steel pipe is obtained from the average of σ_i and σ_w . The average values of the electrical conductivity are shown in Table 2.7.

The relative permeability for the casing, μ_r , used in the matching procedure was measured by *LDJ Electronics Inc.* and is 269. This value of μ_r is larger than the measured values for similar steel pipe published by Stroemich *et. al.* and Chute and Vermeulen, [29] and [96]. However, it is generally observed that the magnetic properties of the steel can vary between samples by as much as 200 to 300% , [29].

From Table 2.7 the electrical conductivity for the steel casing is between $6.46 \cdot 10^6$ and $7.31 \cdot 10^6$ S/m . The electrical conductivity measured at the two different currents is not the same. The lower conductivity at 50 A could be a result

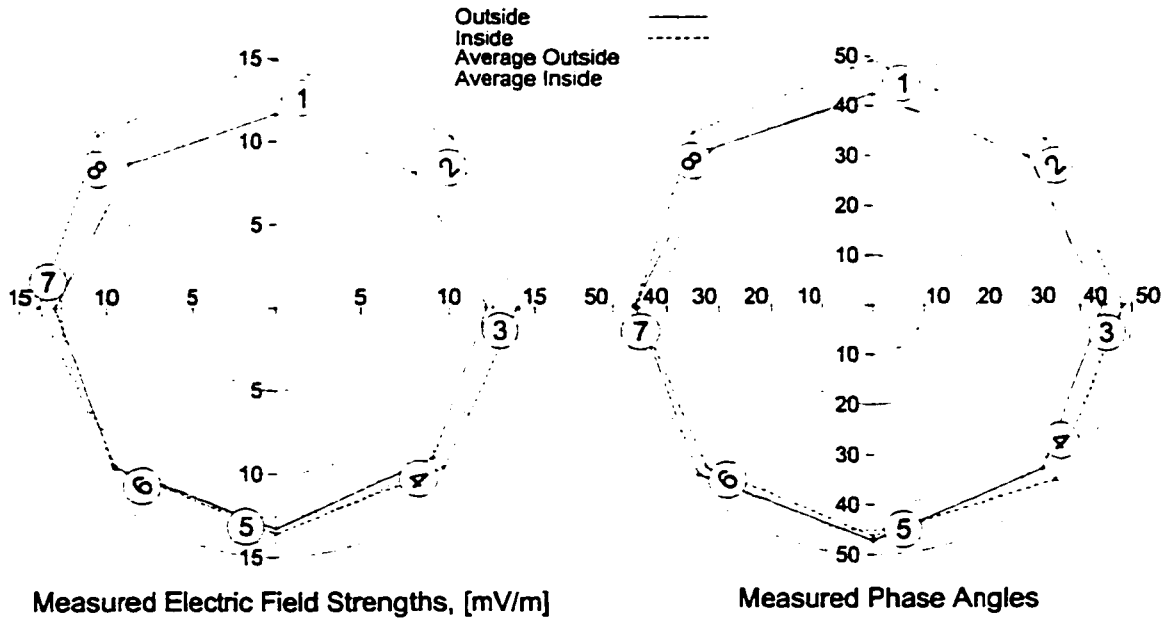


Figure 2.25: Measurement of the surface electric field strengths (mV/m), and phase angles, (degrees) at various locations on the interior and exterior surfaces of the casing for a sinusoidal excitation of 50 A (RMS) conducted in the centralized tubing.

Low Current Tests					
Current	Average Measured E-Field		Calculated σ		Average σ
I	$\bar{E}(R_w)$	$\bar{E}(R_i)$	$\sigma(R_w)$	$\sigma(R_i)$	$\bar{\sigma}$
A RMS	mV/m	mV/m	S/m	S/m	S/m
25	5.87	6.51	$7.57 \cdot 10^6$	$7.05 \cdot 10^6$	$7.31 \cdot 10^6$
50	12.56	14.12	$6.76 \cdot 10^6$	$6.16 \cdot 10^6$	$6.46 \cdot 10^6$

Table 2.7: Data used to determine the electrical conductivity of the 7" casing.

of non-linear magnetic effects in the steel pipe that are more significant at higher currents and are not accounted for in the analytic model used to determine the electrical conductivity. A value of $7.3 \cdot 10^6 S/m$ was used as the bulk electrical conductivity for the steel pipe since at the lower current, the effect of non-linear hysteresis is minimal. This value is similar to the electrical conductivity for K-55 type pipe measured by Stroemich *et. al.* of $5.6 \cdot 10^6 S/m$, Reference [29].

2.4.5 Validation of the *EM Pipe Loss* model using the *Electromagnetic Response Method*

Figure 2.26 shows the measured electric field strengths and phase angles for currents of 100, 200 and 275 A *RMS* conducted in the centralized tubing. Also shown are the electric field strengths and phase angles calculated using the *EM Pipe Loss* model. The 1000 A/m hysteresis loop was used as the maximum hysteresis loop for the calculations. Additional input data are summarized in Table 2.8.

The measurement locations are indicated on Figure 2.26. The location indicated by Point 2 coincides with the weld along the axial length of the pipe, which is a result of the manufacturing process. This location consistently shows the greatest variance in the measured data.

Data	Symbol	Value	Units
Pipe Properties			
Inner radius	r_i	83.185	<i>mm</i>
Outer radius	r_w	89.345	<i>mm</i>
Length	L_p	4.010	<i>m</i>
Initial relative permeability	μ_r	269.00	
Electrical conductivity	σ_s	7.30	10^6 S/m
Run Time Data			
<i>RMS</i> excitation current	I_t	100	<i>A</i>
	I_t	200	<i>A</i>
	I_t	275	<i>A</i>
Frequency	f	60.00	<i>Hz</i>
Size of time step	ΔT	34.7220	μsec
Size of grid block	Δr	0.1027	<i>mm</i>
Number of grid nodes	N_{nodes}	61	
Time steps per cycle	N	480	

Table 2.8: Pipe properties and input data for the *EM Pipe Loss* model used in the *electromagnetic validation*.

Electric Field Strengths, [mV/m]

Surface Phase Angles

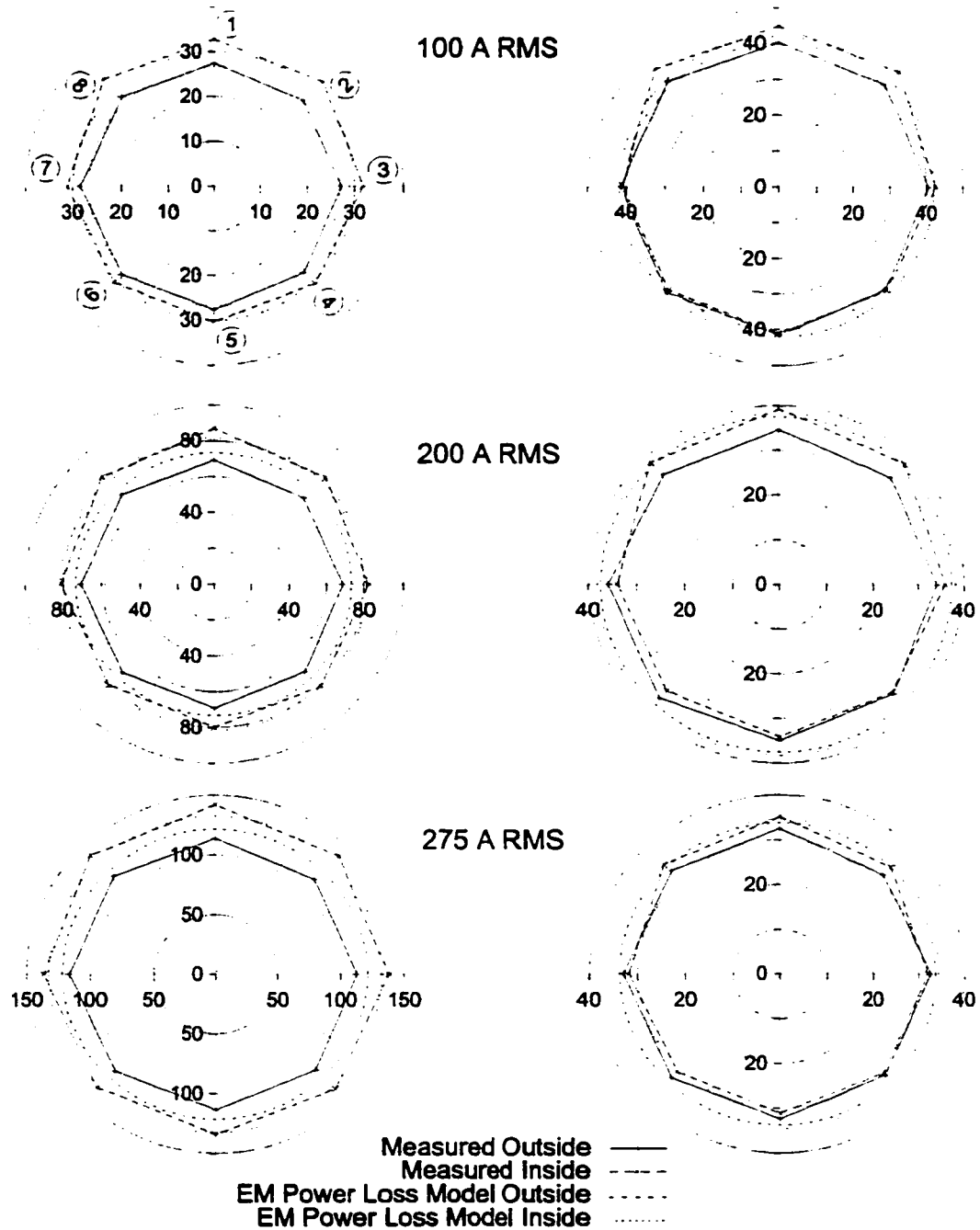


Figure 2.26: Comparison of the measured surface electric field strength, (mV/m), and phase angles, (degrees) at various locations on the interior and exterior surfaces of the 7" casing for currents of 100, 200 and 275 A (RMS) in the centralized tubing to calculated values using the *EM Pipe Loss* model.

Total Current	Measured E-Field		Calculated E-Field		% Difference	
I_t	$\bar{E}(R_w)$	$\bar{E}(R_i)$	$E_c(R_w)$	$E_c(R_i)$	ξ_w	ξ_i
A RMS	mV/m	mV/m	mV/m	mV/m	ξ_w	ξ_i
25	5.87	6.51	5.00	6.38	-2.16	+2.06
50	12.56	13.12	11.00	12.76	+4.49	+2.78
100	27.64	31.72	26.78	28.80	+3.08	+9.21
200	69.23	82.35	73.27	81.54	-5.85	+0.98
275	114.04	137.59	121.57	132.39	-6.60	+3.78

Table 2.9: Comparison of the measured surface electric field strengths in mV/m with the electric field strengths calculated by the *EM Pipe Loss* model.

RMS Current	Measured θ		Calculated θ		% Difference	
A	$\bar{\theta}(R_w)$	$\bar{\theta}(R_i)$	$\theta_c(R_w)$	$\theta_c(R_i)$	ξ_w	ξ_i
50	44.71	45.12	43.25	43.50	+3.27	+3.60
100	40.99	42.88	41.00	41.00	-2.04	+2.04
200	34.79	35.98	37.50	38.25	-7.80	-6.32
275	32.39	32.58	33.75	34.50	-4.21	-5.91

Table 2.10: Comparison of the measured surface phase angle θ in degrees with calculated values of θ by the *EM Pipe Loss* model.

Overall, there is good agreement between the measured and numerical data for electric field strengths and phase angles. Tables 2.9 and 2.10 summarize the results for the electromagnetic validation shown in Figure 2.26. The results obtained with the *EM Pipe Loss* model differ by less than 4° from the measured surface electric field strength or phase angle data.

2.4.6 Validation of the *EM Pipe Loss* model using the *Thermal Response Method*

In this section the power losses calculated using the *EM Pipe Loss* model are compared to the power losses that are derived from the measured thermal response

of the casing. This approach is called the *thermal response method* for determining the power losses. The approach follows the work of Stroemich *et. al.*, [29]. They measure the time rate of change of temperature of a current carrying thermally insulated casing and determine from it the power that is absorbed to generate the measured temperature response.

Stroemich *et. al.* compared the results obtained from the *thermal response method* to the power calculated indirectly from the measured electric and magnetic field strengths and demonstrated that the results from the two methods compare to within 5% of each other. The *thermal response method* is preferred over the indirect method for calculating power from measured electric and magnetic field strengths because the measurements that are conducted are less likely to be affected by electrical interference. Also, the purpose of the *EM Pipe Loss* model is to determine the power losses in the pipe. Since the *thermal response method* is a direct measure of the conversion of electrical energy to heat, it is important that the calculations made using the *EM Pipe Loss* model agree with the losses that are determined experimentally.

During the initial heating of the casing while its temperature is very close to room temperature, heat transfer from the thermally insulated casing by conduction and natural convection is assumed negligible and the thermal response may be defined by the following equation,

$$P = \rho C_s \Delta V \frac{\partial T}{\partial t} \quad (2.56)$$

In Equation 2.56 P is the power loss in volume ΔV of the pipe and must be equal to the power flow into the pipe through the interior and exterior surfaces determined using Poynting's Theorem,

$$\frac{P}{\Delta L} = E_{rms}(r_i) I_{rms} \cos(\theta_i) + E_{rms}(r_w) I_{rms} \cos(\theta_w) \quad (2.57)$$

In Equation 2.57, I_{rms} is the current flowing in the centralized tubing and is measured using a true *RMS* meter. The heat capacity, ρC_s , of the steel 7" casing is obtained from Reference [97] and is $3.7 \cdot 10^6 J/(m^3 \cdot ^\circ C)$. The rate of temperature rise, $\frac{\partial T}{\partial t}$ is approximated from the slope of the temperature versus time data, $\frac{\Delta T}{\Delta t}$

during the early time region of the experimental data as shown in Figure 2.27. Once the slope is known, P can be calculated directly from Equation 2.56 and compared to the calculation of the power losses calculated using the *EM Pipe Loss* model.

The slope of the temperature versus time data, $\frac{\Delta T}{\Delta t}$ is determined from the experimental data as follows:

1. The initial measured temperatures at the three thermocouples located on the casing are averaged to provide an estimate of the initial temperature of the casing, $T_o = (T_{left} + T_{centre} + T_{right})/3$.
2. The three temperature data are averaged at each sample time. The several averaged sampled data from $t = 0$ to $t = t_f$ are then fit to a linear equation $T(t) = T_o + mt$ using a least squares method and a value for m is determined. The slope m is the time rate of temperature rise $\frac{\Delta T}{\Delta t}$.
3. The value of t_f is decreased (the number of samples fit to the linear equation are reduced) until a reduction in t_f does not change the value of m .
4. The smallest value of t_f obtained in the previous step defines the *early time region* since the temperature response during $0 < t < t_f$ can be defined by Equation 2.56. During this period, $\frac{\partial T}{\partial t} \approx m$ and the power converted to heat can be calculated directly and compared to the power losses calculated using the *EM Pipe Loss* model.

Figure 2.28 summarizes the measured rate of temperature rise in the 7" casing for the range of currents used in the experiment. The data for Figure 2.28 was determined using the above procedure.

It was observed that the temperature response of the thermocouples is highly dependent on the integrity of the contact of the thermocouple at the point of measurement. When a small pressure was applied to the thermal thermocouple it was observed that the measured temperature increased by as much as 5 to 10 °C. This can be seen in Figure 2.27 where the *right* thermocouple is in poor contact at the point of measurement. In most of the calculations the *right* thermocouple data could not be used.

Additionally, it is possible to compare electric fields deduced from the measured power losses with numerically calculated values. This is not a true

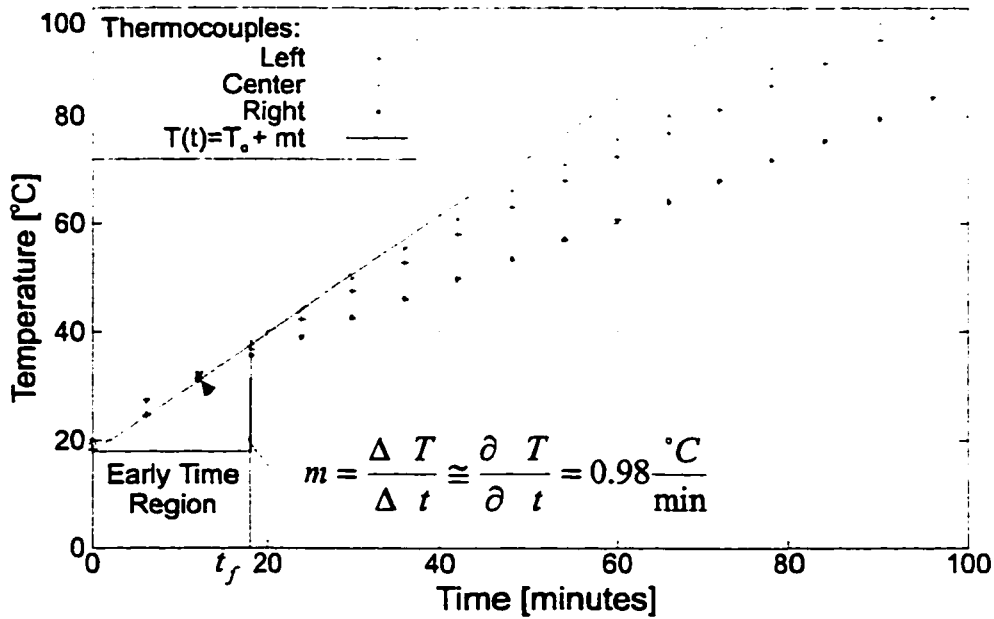


Figure 2.27: Illustration of the *Thermal Response Method* using the temperature response of the 7" casing for a current of 500 A (*RMS*) in the centralized tubing.

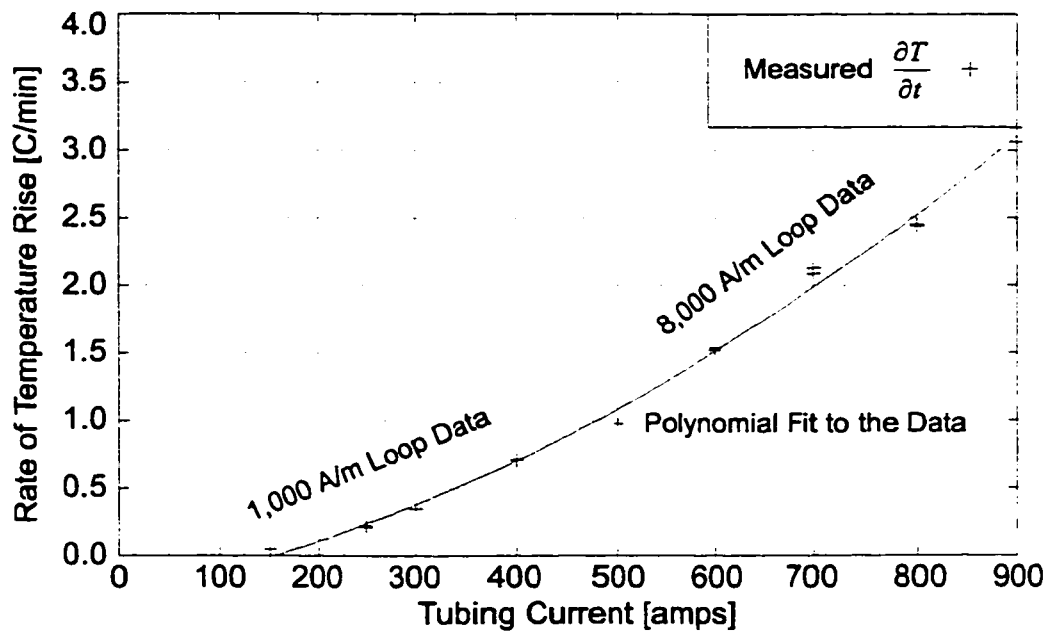


Figure 2.28: Measured rate of temperature rise in the 7" casing as a function of the *RMS* current conducted in the centralized tubing.

validation of the numerical model since the electric field strengths thus deduced are not measured directly but are derived from the measured power losses using Equation 2.57 and approximations for the value of the phase angles, θ_i and θ_w .

The surface electric field strengths are determined from the measured power losses as follows. Once the power is calculated the unknowns in Equation 2.57 are $E_{rms}(r_i)$, $E_{rms}(r_w)$, θ_i , and θ_w . For a linear magnetic material, Loga's analytic model (Reference [1]) shows that,

$$E_{rms}(r_w) \approx E_{rms}(r_i) \frac{r_i}{r_w} \quad (2.58)$$

Also, the phase angle between the magnetic and electric field strengths on the interior and exterior surfaces, θ_i and θ_w , are approximately the same so $\theta_w \approx \theta_i$. Values for θ_i are obtained from measured data for a similar sample of pipe published by Stroemich *et. al.*, [29]. This combined with Equation 2.58 leads to an approximate value for the electric field strength,

$$E_{rms}(r_i) = \frac{P}{1 + \frac{r_i}{r_w}} \frac{\pi(r_w^2 - r_i^2)}{I_{rms} \cos\theta_i} \quad (2.59)$$

Values for both the experimentally measured power and for the electric field strengths obtained using Equations 2.56 and 2.59 respectively are compared to values calculated using the *EM Pipe Loss* model. In the numerical calculations, the 1,000 A/m hysteresis loop is used when the magnetic field strength is less than 1,000 A/m, and for values of the magnetic field strength greater than 1,000 A/m the 8,000 A/m hysteresis loop is used. This approach was recommended by technical specialists at *LDJ Electronics Inc.*, the firm engaged to obtain the hysteresis loop data [98].

Figure 2.29 compares the total power losses in the pipe obtained experimentally from Equation 2.56 with the power losses calculated by the *EM Pipe Loss* model. Figure 2.30 shows the percent of the losses shown in Figure 2.29 that are attributed to hysteresis losses, as calculated using the *EM Pipe Loss* model. The results compare favourably as indicated by the percentage difference ranging from just less than 1.0% to about 6.0%.

Figure 2.29 suggests closer agreement between the two calculations at higher current levels. This may be due to two factors. At the higher current levels the early time slope of the temperature versus time data can be obtained in a shorter period of time, reducing the influence of heat losses through the thermal insulation.

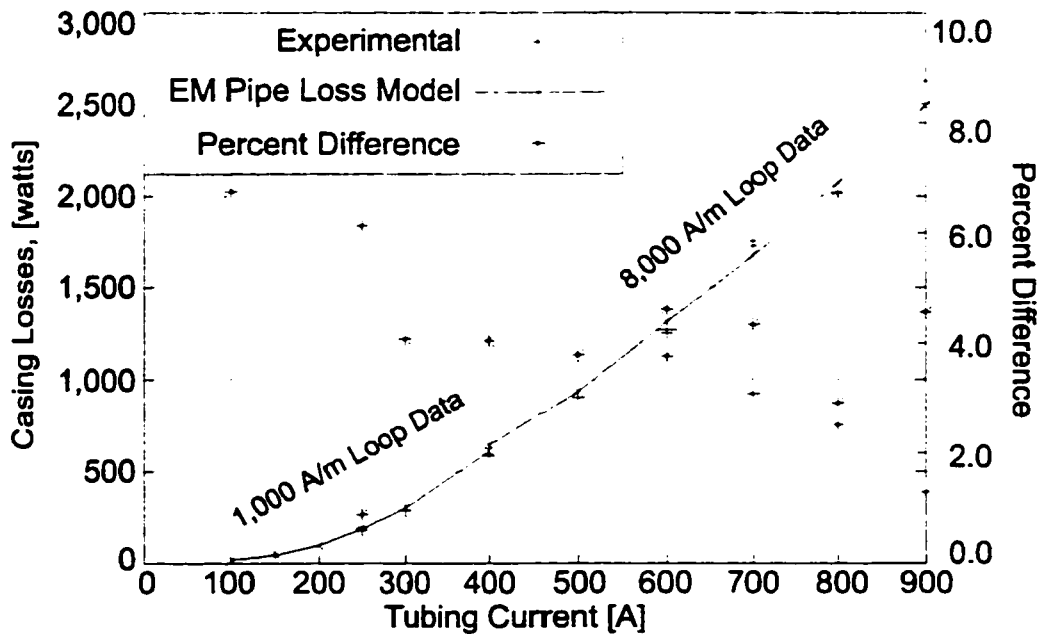


Figure 2.29: Comparison of the experimental data and numerical calculation of the losses for the 4.0 meter long section of 7" casing used in the test as a function of the *RMS* current in the centralized tubing.

As well, the accuracy of the numerical model may improve at the higher currents since more data points are used to define the hysteresis loops at greater values of the magnetic field strength.

The results shown in Figure 2.30 show that the portion of the losses attributed to hysteresis achieves a maximum at relatively low currents. This result is not intuitively obvious. Previous studies have ignored the effects of hysteresis on the basis that the current in the pipe was sufficiently small, [1], [29]. A method to determine at what maximum magnitude the current had to be for which hysteresis effects could be ignored was never quantified until now. Figure 2.30 shows that for the sample of pipe used in this thesis, the effects of hysteresis should not be ignored for total currents greater than 100 A *RMS*.

As a final confirmation, Equation 2.59 is used to compare the surface electric fields derived from the test data with those calculated using the *EM Pipe Loss* model. This is not a validation of the model for reasons already stated, but it does provide an indication of the *consistency* of the numerical model. The comparison is shown Figure 2.31.

The results shown in Figure 2.29 experimentally validate the *EM Pipe Loss*

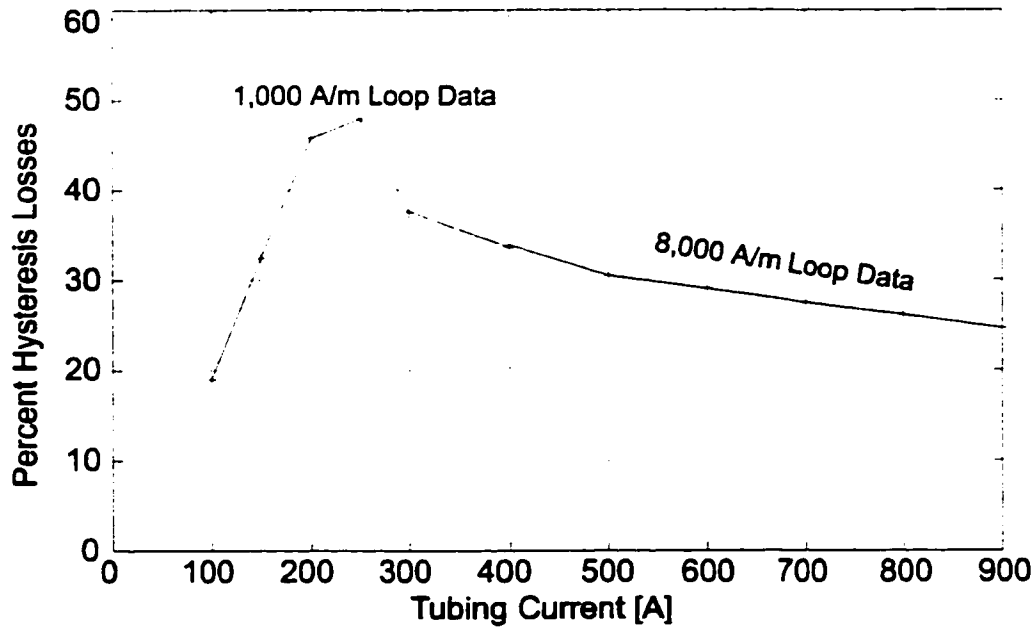


Figure 2.30: Percent hysteresis losses for the power losses shown in Figure 2.29 determined using the *EM Pipe Loss* model.

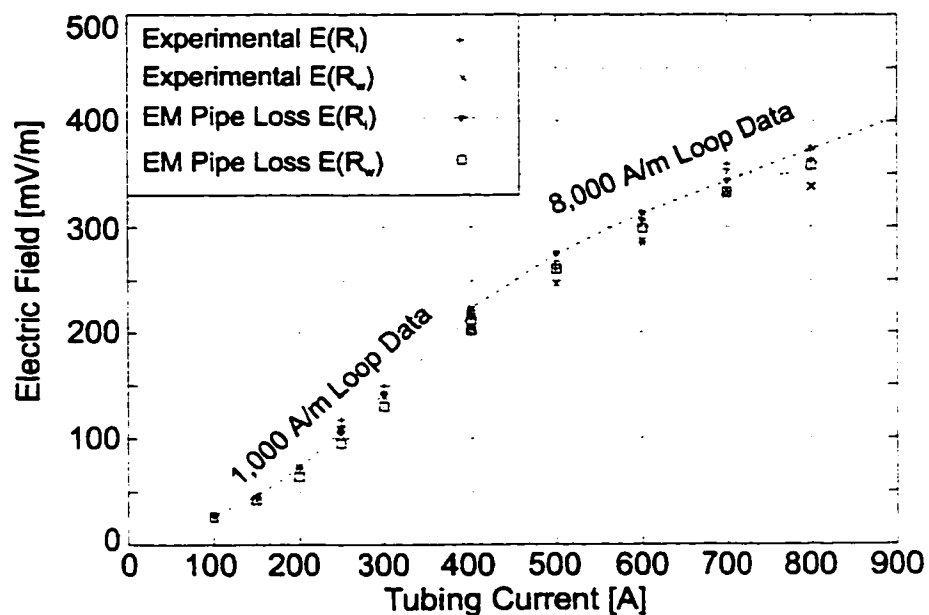


Figure 2.31: Comparison between the surface electric field strength derived from the test data and Equation 2.59 and calculated using the *EM Pipe Loss* model.

model as a tool for determining the combined hysteresis and eddy current losses in pipe made of non-linear magnetic material. Up to this point, the *EM Pipe Loss* model has been successfully validated using an analytic model, [1], and by comparison to the *Zakrzewski-Peitras* numerical model which is a similar problem in

the Cartesian coordinate system, [86], and finally by using experimental data from the test conducted as part of this thesis. The following section uses the *EM Pipe Loss* model to generate the power loss function that is needed in the next chapter to solve the heat transfer problem for an electrically heated horizontal well.

2.5 Power Loss Interpolation Function for the Horizontal Wellbore

For the heat transfer problems that are solved in the next chapter, an energy source must be developed as a function of z , the axial coordinate along the length of the horizontal well, that accounts for both eddy current and hysteresis losses. The primary goal of the *EM Pipe Loss* model is to assemble the information required to define such an energy source function for the pipe. This function is constructed in terms of the power losses per unit volume and is defined as $\dot{q}_2(z)$, where the subscript 2 indicates Region 2, and the dot over the q indicates a *rate* of energy consumption, i.e., power. Region 2 refers to the cylindrical region occupied by the steel of the horizontal casing, and is so designated for later convenience in conducting the work described in Chapter 3 of this thesis. For a more detailed description of the *regions* please refer to Figure 3.1 in Chapter 3.

The approach used in this thesis to arrive at a suitable $\dot{q}_2(z)$ is similar to that developed by Stroemich *et. al.*, [29]. They experimentally obtain the effective impedance as a function of the current flowing in the casing. The significant difference between the work of Stroemich *et. al.* and the work described in this thesis is that the effective impedance of the casing is not constant along the length of the casing but varies with axial position on the casing. This is due to the non-uniform axial distribution of current that flows in the casing.

It is important to characterize the electromagnetic problem for the casing in the horizontal section of the wellbore in order to appreciate the development of $\dot{q}_2(z)$. The casing in the horizontal section of the wellbore is a long, single, and continuous piece of pipe that is in direct contact with the reservoir over a length of several hundred meters, as shown in Figure 2.1. The current source is located in the reservoir a large distance from the horizontal wellbore, and current is assumed to

collect uniformly on the surface of the horizontal pipe. For brevity, we now replace r_{ci} and r_{cw} shown for the casing in Figure 2.2 by r_i and r_w . Since there are no current sources in the interior of the pipe, and since there is cylindrical symmetry, then from Ampere's law, the magnetic field strength on the interior surface at $r = r_i$ is $H_\phi(r_i, z, t) = 0.0$. The magnetic field strength at the outer surface is determined by the current flowing axially in the casing and from Ampere's law is $H_\phi(r_w, z, t) = I(z)/(2\pi r_w)$, where $I(z)$ is the axial current in the casing at location z . The origin, $z = 0$, is located at the far end of the horizontal well, away from the vertical casing. Since current from the reservoir is assumed to collect uniformly on the casing, $I(z) = I_t(z/l)$, where l is the length of the horizontal casing. These two boundary conditions for the magnetic field strength,

$$\begin{aligned} H_\phi(r_i, z, t) &= 0.0 \\ H_\phi(r_w, z, t) &= \frac{I_t}{2\pi r_w} \frac{z}{l} \end{aligned} \quad (2.60)$$

are used in the *EM Pipe Loss* model to determine the effective impedance of the pipe from the calculated surface electric field strength.

Following Stroemich's approach, the effective pipe impedance per unit length is defined using the surface electric field strength as

$$\mathbf{Z} = \frac{E_{rms}(z)}{I_{rms}(z)} e^{j\theta(z)} \left[\frac{\Omega}{m} \right] \quad (2.61)$$

where E_{rms} is the *RMS* phasor magnitude of the z -directed electric field calculated at the outer surface of the casing, and $I_{rms}(z)$ is the *RMS* magnitude of the excitation current flowing in the casing at z . Here $I_{rms}(z) = 2\pi r_w H_{rms}(z)$ where $H_{rms}(z)$ is the ϕ directed magnetic field strength at the outer surface of the casing. The angle θ represents the phase angle by which the electric field strength leads the magnetic field strength. Values for $E_{rms}(z)$, $H_{rms}(z)$, and $\theta(z)$ are calculated by use of the *EM Pipe Loss* model.

The effective impedance can be represented by an effective series resistance, R , and series reactance, X . In terms of the *RMS* values of the electric field strength

and current these are expressed as,

$$\begin{aligned} R(z) &= \frac{E_{rms}(z)}{I_{rms}(z)} \cos \theta(z) \\ X(z) &= \frac{E_{rms}(z)}{I_{rms}(z)} \sin \theta(z) \end{aligned} \quad (2.62)$$

Using the approach adopted by Stroemich, the effective resistance, R , of the casing yields the power losses per meter of pipe from

$$P(z) = I_{rms}(z)^2 R(z) \quad (2.63)$$

In this thesis the power losses in the casing, $\dot{q}_2(z) = P(z)/V_s$, are expressed in terms of losses per cubic meter of pipe material, V_s . The effective resistance can be expressed in terms of an effective resistivity, ρ_s . Equations 2.62 and 2.63 now lead to an expression for the power losses per m^3 of casing material as a function of z ,

$$\dot{q}_2(z) = \rho_s \frac{I_{rms}(z)^2}{A_s^2} \quad (2.64)$$

where $I_{rms}(z) = I_t \frac{z}{l}$, and I_t is the total rms current flowing in the casing at $z = l$, and A_s is the the cross-sectional area of the casing.

To describe the non-linear dependence of the resistivity on current requires that ρ_s be expressed as a function of the current flowing in the pipe at z . Thus, the definition of the heat source term in Equation 2.64 must be restated as

$$\begin{aligned} \dot{q}_2(z) &= \rho_s(I_{rms}(z)) \frac{I_{rms}(z)^2}{A_s^2} \\ &= \rho_s(z) \frac{I_t^2}{A_s^2} \left(\frac{z}{l}\right)^2 \end{aligned} \quad (2.65)$$

A plot of ρ_s versus I_{rms} is generated using the *EM Pipe Loss* model. An n^{th} order polynomial is then fitted to the plot of ρ_s versus I_{rms} to generate a suitable $\rho_s(I_{rms})$. Since $I_{rms}(z) = I_t \frac{z}{l}$, it is possible to directly substitute z as the independent variable and determine a general polynomial curve fit for the

resistivity, $\rho_s(z)$, as follows

$$\begin{aligned}\rho_s(I_{rms}(z)) &= \rho_s\left(I_t \frac{z}{l}\right) \\ \rho_s(z) &= \sum_{i=0}^n u_i \left(\frac{I_t}{l}\right)^i z^i\end{aligned}\tag{2.66}$$

where u_i are the coefficients of the n^{th} order polynomial fitted to a plot of resistivity versus current.

Substituting Equation 2.66 into Equation 2.65 results in an equation for the electrical losses in the pipe

$$\begin{aligned}\dot{q}_2(z) &= \frac{I_{rms}(z)^2}{A_s^2} \sum_{i=0}^n u_i \left(\frac{I_t}{l}\right)^i z^i \\ &= \frac{1}{A_s^2} \left(z \frac{I_t}{l}\right)^2 \sum_{i=0}^n u_i \left(\frac{I_t}{l}\right)^i z^i \\ &= \frac{1}{A_s^2} \sum_{i=0}^n u_i \left(\frac{I_t}{l}\right)^{i+2} z^{i+2}\end{aligned}\tag{2.67}$$

Equation 2.67 conveniently expresses the non-linear relationship between current and electrical losses. All that is necessary is to determine the dependence of the effective resistivity on current, which is a linear function of z . Then, using a curve fitting method, the coefficients u_i can be determined.

A plot of resistivity versus the *RMS* current for the sample of 7" K-55 casing is shown in Figure 2.32. The input data to the *EM Pipe Loss* model are summarized in Table 2.11. The data calculated using the *EM Pipe Loss* model have been fitted to a third order polynomial.

Finally, the u_i coefficients are obtained using the *Marquardt-Levenberg* algorithm packaged in the mathematical graphing program called *Gnuplot* and are,

$$\begin{aligned}u_0 &= 0.393886 \\ u_1 &= 0.00350495 \\ u_2 &= -2.15843 \cdot 10^{-6} \\ u_3 &= -3.15483 \cdot 10^{-10}\end{aligned}\tag{2.68}$$

Any positive order polynomial may be used. However, Figure 2.32 shows that

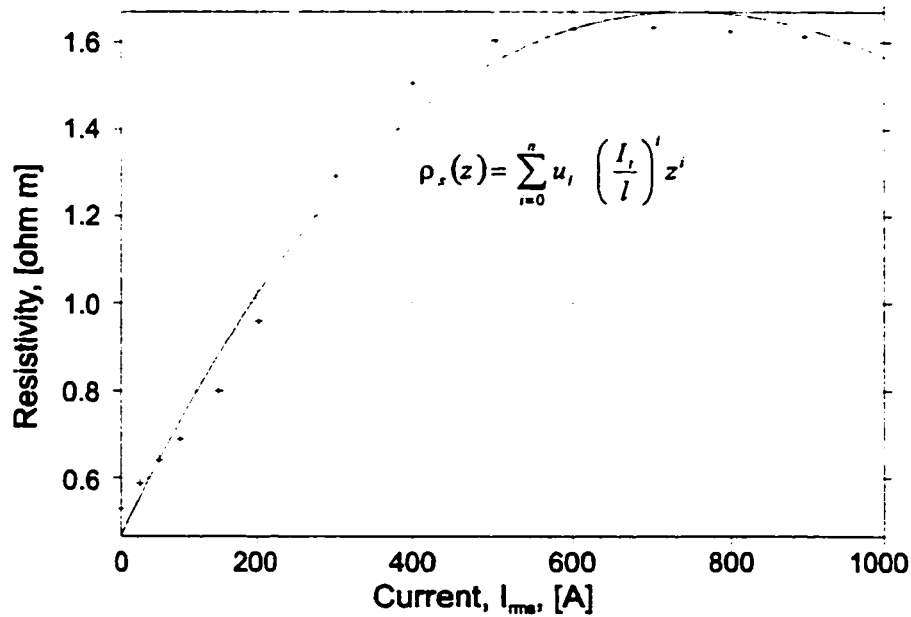


Figure 2.32: Resistivity as a function of the *RMS* current for the 7" K-55 steel casing, used in the horizontal wellbore.

the third order polynomial provides adequate interpolation of the data.

The effect of temperature on the resistivity is not accounted for in the calculation of $\dot{q}_2(z)$. To include temperature effects will result in a non-linear heat transfer equation that cannot be solved analytically. Stroemich *et. al.*, [29], observed that the overall increase in power dissipation due to temperature effects for oil field tubulars was minimal. With constant current, an increase in temperature of 50 °C in the pipe resulted in an increase in power dissipation of only 12.0%. Thus, the *EM Pipe Loss* model will calculate a slightly conservative $\dot{q}_2(z)$ for a given operating current. The polynomial equation defined by the coefficients of Equation 2.68 will be employed in solving the heat transfer problems addressed in Chapter 3.

2.6 Analysis using the *EM Pipe Loss* Model

In this final section the *EM Pipe Loss* Model is used as a numerical tool to analyse various electromagnetic problems. Some of the problems that can be analysed using the *EM Pipe Loss* Model are:

1. The impact of hysteresis on the distribution of the electromagnetic fields and power losses in steel pipe.

Data	Symbol	Value	Units
Pipe Properties			
Inner radius	r_i	83.185	<i>mm</i>
Outer radius	r_w	89.345	<i>mm</i>
Length	L_p	4.007	<i>m</i>
Initial relative permeability	μ_r	269.00	
Electrical conductivity	σ_s	7.30	10^6 <i>S/m</i>
Run Time Data			
Peak excitation current	I_t	<i>variable</i>	<i>A</i>
Peak magnetic field strength.	$H_\phi(r_w)$	<i>variable</i>	<i>A/m</i>
	$H_\phi(r_i)$	0.0	<i>A/m</i>
Frequency	f	60.00	<i>Hz</i>
Size of time step	ΔT	34.7222	<i>μsec</i>
Size of grid block	Δr	0.1027	<i>mm</i>
Number of grid nodes	N_{nodes}	61	
Time steps per cycle	N	480	

Table 2.11: Input data for the *EM Pipe Loss* model which is used to determine $\rho_s(z)$.

2. The significance of hysteresis losses in the casing in relation to the resistive losses as a function of the current conducted in the centralized tubing.
3. The effect of the electrical conductivity of the steel pipe on the significance of hysteresis losses in relation to the resistive losses.
4. The impact of the hysteresis loop data on the calculation of the electromagnetic response of the steel pipe.
5. The calculation of the effective pipe resistance for the casing.

Unless otherwise specified the example problems that are considered below are for the ungrounded casing in the vertical section that supplies power to the horizontal wellbore. Also, only the 8000 *A/m* hysteresis loop data are used in these examples. This means that a large range of the excitation magnetic field strengths can be accommodated and that the complexity of the problem is minimized since only the data for a single experimentally measured hysteresis loop is utilized. In a following subsection, the impact of using different hysteresis loop data for the same

material will be analysed.

2.6.1 Impact of hysteresis on the distribution of the electromagnetic fields and power losses in steel pipe

The effects of hysteresis on the distribution of eddy currents and losses in the casing in the vertical section of the wellbore are analysed. The input data for the problem are summarized in Table 2.12. The current in the centralized tubing is 500 *A RMS*. The current produces $H_\phi(r_i) = 1,352.88 \sin(\omega t)$ on the interior surface of the pipe and $H_\phi(r_w) = 1,259.60 \sin(\omega t)$ on the exterior surface of the pipe.

Data	Symbol	Value	Units
Pipe Properties			
Inner radius	r_i	83.185	<i>mm</i>
Outer radius	r_w	89.345	<i>mm</i>
Length	L_p	4.007	<i>m</i>
Initial relative permeability	μ_r	269.00	
Electrical conductivity	σ_s	7.30	10^6 <i>S/m</i>
Run Time Data			
Peak excitation current	I_p	707.11	<i>A</i>
Peak magnetic field strength.	$H_\phi(r_i)$	1352.88	<i>A/m</i>
Frequency	f	60.00	<i>Hz</i>
Size of time step	Δt	34.7222	μsec
Size of grid block	Δr	0.2053	<i>mm</i>
Number of grid nodes	N_{nodes}	31	
Time steps per cycle	N	480	

Table 2.12: Pipe properties and runtime data for the *EM Pipe Loss* model.

Figures 2.33 and 2.34 compare the *RMS* values of electric and magnetic field strengths in the 7" casing with and without hysteresis effects. Tables 2.13 and 2.14 summarize the results of the calculations.

The redistribution of the electric field strength towards the interior and exterior surfaces when hysteresis is present results in an eddy current loss that is nearly twice as large as when no hysteresis is present. In addition, the magnitude of the hysteresis loss is comparable to the eddy current loss in the pipe when hysteresis

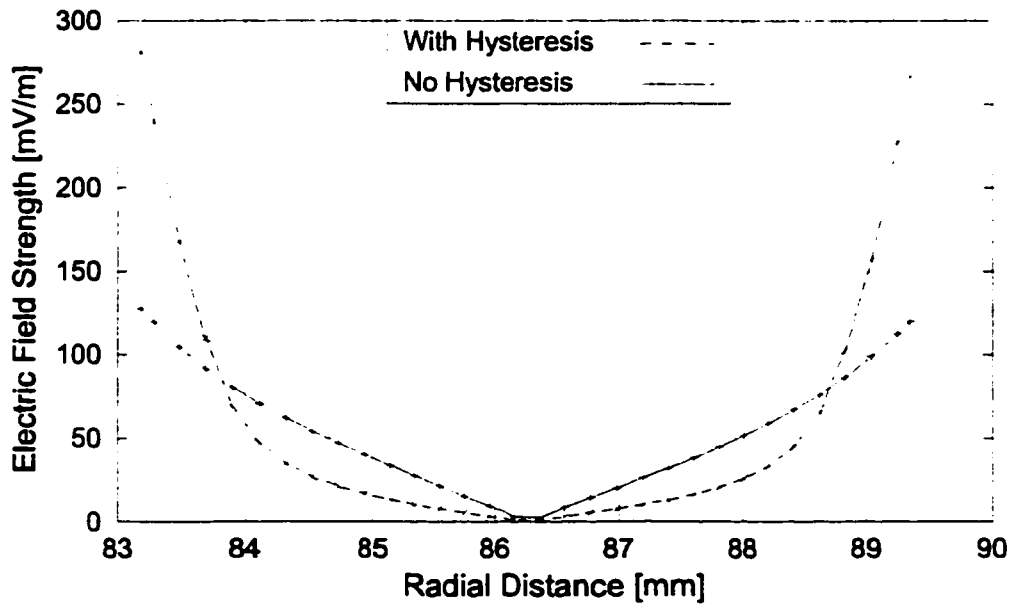


Figure 2.33: The effect of hysteresis on the distribution of the electric field strength for the 7" steel casing for the case when the current in the centralized tubing is 500 A RMS at 60 Hz.

is not considered. Thus, for this typical example, where the current in the centralized tubing is 500 A RMS the overall impact of hysteresis is to increase the total power losses by a factor of about three.

As shown in Figure 2.33, hysteresis forces the current to flow near the surfaces through a smaller effective area and therefore the current density, J , and losses are greater than when hysteresis is not present. The effective area depends on the depth of penetration of the electromagnetic fields, termed the *skin depth* δ . The skin depth is the distance the electromagnetic wave penetrates into the material before being attenuated in magnitude by a factor equal to e^{-1} . For a plane wave it is given by the equation,

$$\delta = \frac{1}{\sqrt{\pi f \mu_r \mu_o \sigma_s}} \quad (2.69)$$

where f is the frequency, μ_r is the relative permeability, μ_o is $4\pi \cdot 10^{-7}$ and σ_s is the electrical conductivity of the steel. The units for δ are meters.

The skin depth δ for the cylindrical 7" casing, for the case with no hysteresis, is estimated from Figures 2.33 and 2.34 and is 1.54 mm. The value calculated for a plane wave from Equation 2.69 is 1.47 mm. The skin depth when hysteresis is

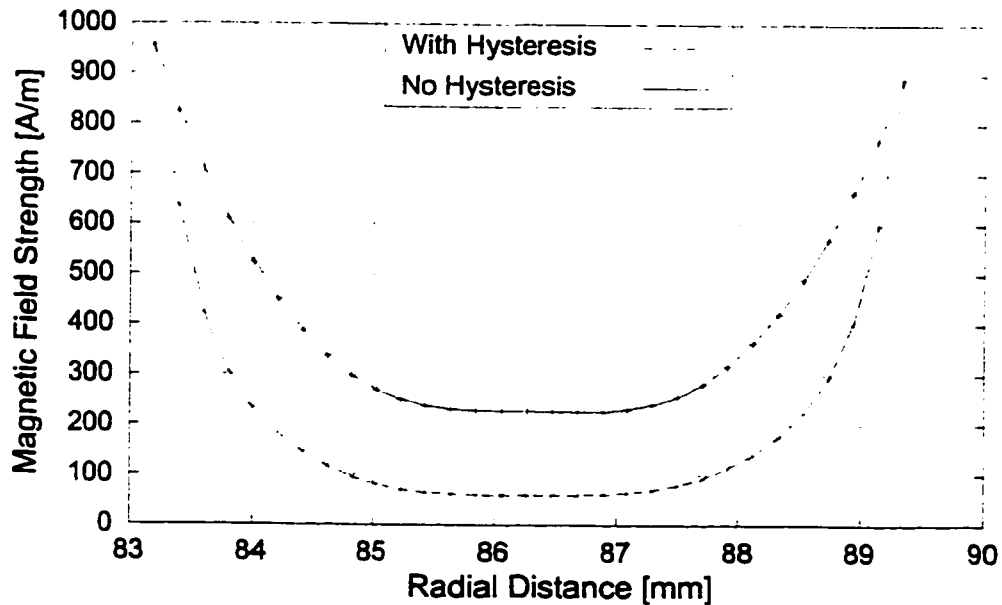


Figure 2.34: The effect of hysteresis on the distribution of the magnetic field strength for the 7" casing for the case when the current in the centralized tubing is 500 A RMS at 60 Hz.

present is approximately 0.54 mm. Using this value of skin depth in Equation 2.69 an *effective relative permeability* μ_r of the magnetic material can be calculated. Here μ_r is the value of relative permeability that a fictitious material which does not possess hysteresis would have to exhibit to lead to the same skin depth as that shown by the actual steel of the pipe. For a skin depth of 0.54 mm, μ_r for the material is 2,421.

Referring to Tables 2.13 and 2.14, the power loss for the case with hysteresis is approximately three times greater than when hysteresis is not present (exactly 2.75 times). This example calculation clearly demonstrates that hysteresis effects cannot be overlooked in the design of an electrical heating system for oil field or environmental applications when calculating the power losses.

2.6.2 The hysteresis losses as a function of the current conducted in the centralized tubing

The purpose of this section is to analyse the relative importance of hysteresis as a function of current magnitude and thus indirectly as a function of the magnetic field strength. Figures 2.35 and 2.36 show the losses and phase angles as a function

Data	Symbol	Value	Units
Power Calculations			
Poynting Power	$P(r_i)$	46.58	[W/m]
	$P(r_w)$	44.20	[W/m]
Total Poynting Power	P_t	90.78	[W/m]
Eddy Current Losses	P_{ec}	89.34	[W/m]
Hysteresis Losses	P_h	0.00	[W/m]
$P_{ec} + P_h$ losses	P_{ec+h}	89.34	[W/m]
Percent Hysteresis Losses		0.00	Percent
Electro-Magnetic Calculations			
RMS Electric Field	$E_z(r_i)$	127.4640	[mV/m]
	$E_z(r_w)$	119.8634	[mV/m]
Skin Depth	δ	1.53	[mm]
Phase Angle	$\theta(r_i)$	42.75	[degrees]
	$\theta(r_w)$	42.00	[degrees]

Table 2.13: Results for the 7" casing for the case *without* hysteresis when the current in the centralized tubing is 500 A RMS at 60 Hz.

of current magnitude. Also plotted on each of the figures are the contributions of the hysteresis losses to the total losses as a function of current magnitude.

Figure 2.19 shows the family of hysteresis loops for the sample of 7" casing used in the experimental tests. At larger values of magnetic field strength, an incremental change in the magnetic field strength does not change the area enclosed by the hysteresis loop as much as the same incremental change at lower values of magnetic field strength. The area of the hysteresis loop is directly related to the hysteresis loss. Thus for a given incremental change in magnetic field strength, the larger changes in hysteresis losses will occur at lower values of the magnetic field strength. Also, at the higher values of the magnetic field strength, which corresponds to greater excitation current, the eddy current losses, which are proportional to the square of the current density, increase at a greater rate than the hysteresis losses. This is evident on Figure 2.35.

Data	Symbol	Value	Units
Power Calculations			
Poynting Power	$P(r_i)$	125.64	[W/m]
	$P(r_w)$	119.56	[W/m]
Total Poynting Power	P_t	245.20	[W/m]
Eddy Current Losses	P_{ec}	164.86	[W/m]
Hysteresis Losses	P_h	68.84	[W/m]
$P_{ec} + P_h$ losses	P_{ec+h}	233.70	[W/m]
Percent Hysteresis Losses		29.46	Percent
Electro-Magnetic Calculations			
RMS Electric Field	$E_z(r_i)$	281.23	[mV/m]
	$E_z(r_w)$	267.10	[mV/m]
Skin Depth	δ	0.54	[mm]
Phase Angle	$\theta(r_i)$	23.25	[°]
	$\theta(r_w)$	24.00	[°]

Table 2.14: Results for the 7" casing for the case *with* hysteresis when the current in the centralized tubing is 500 A RMS at 60 Hz.

In summary, the relative importance of hysteresis does not always increase with the strength of the magnetic field strength as might be expected. On the contrary, the largest contribution of the hysteresis losses to the total power losses may actually occur at a much lower magnetic field strength than the saturation magnetic field strength, as shown in Figure 2.35. These results are consistent with experimental results presented by Stroemich *et. al.* [29].

The phase angles shown in Figure 2.36 represent the phase angles by which the electric field leads the magnetic field strength on the interior and exterior surfaces of the pipe. As the magnetic field strength increases little change in the phase angle is observed until the percentage of losses due to hysteresis is greater than 10%. At this point, the phase angle decreases very rapidly, leveling off at higher values of magnetic field strength. Again, these results are consistent with experimental results obtained by Stroemich *et. al.*, [29].

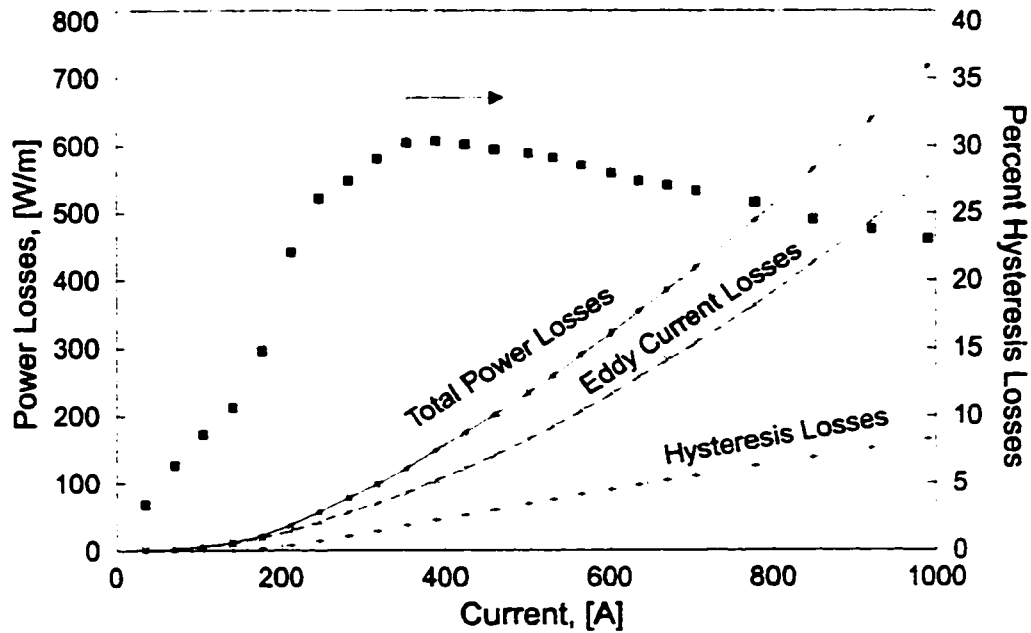


Figure 2.35: Analysis of the aggregate power losses per meter length of the 7" casing as a function of the magnitude of the current conducted in the tubing.

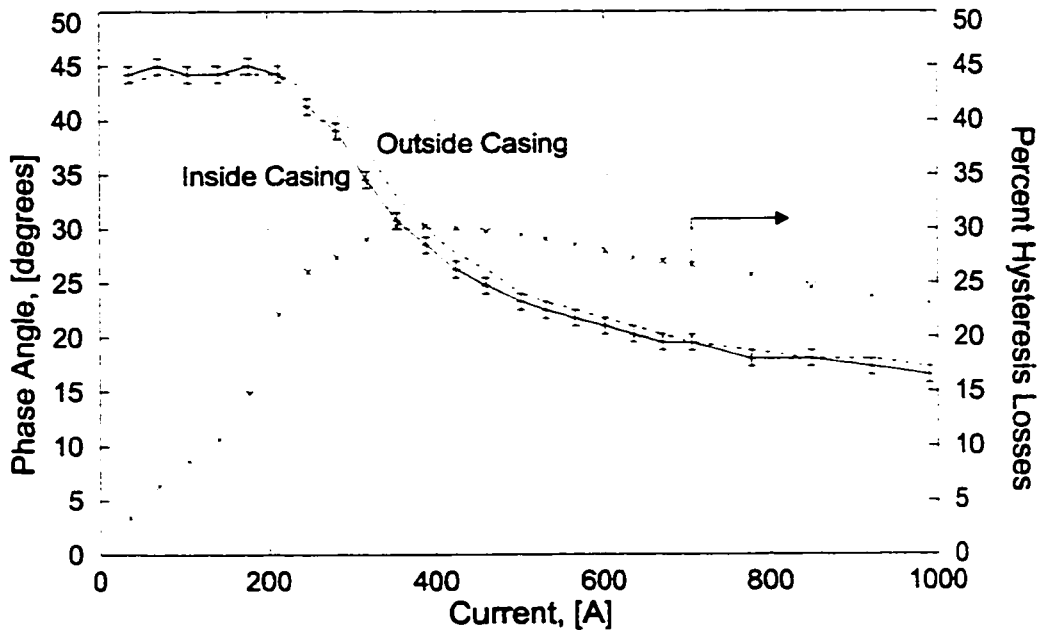


Figure 2.36: The phase angles on the interior and exterior surfaces of the 7" casing as a function of the magnitude of the current conducted in the tubing.

2.6.3 The effect of the electrical conductivity of the pipe on the power losses in the casing

The effect of the electrical conductivity of the steel on the power losses is investigated in this section. Three scenarios are presented: casing with low electrical

conductivity steel, casing with the measured conductivity of the steel (the base case), and a high conductivity casing. Each incremental change in electrical conductivity is an order of magnitude, as summarized in Table 2.15. For the high conductivity case, the size of the grid blocks had to be reduced since the skin depth is very small. The number of grid nodes was increased from 31 to 61.

Data	Symbol	Value	Units
Pipe Properties			
Inner radius	r_i	83.190	<i>mm</i>
Outer radius	r_w	89.340	<i>mm</i>
Length	L_p	4.007	<i>m</i>
Initial relative permeability	μ_r	269.00	
Electrical conductivity	σ_s		
Low Case		0.73	10^6 <i>S/m</i>
Base Case		7.30	10^6 <i>S/m</i>
High Case		73.00	10^6 <i>S/m</i>
Run Time Data			
Peak excitation current	I_p	Variable	<i>A</i>
Peak magnetic field strength.	$H_\phi(r_i)$	Variable	<i>A/m</i>
Frequency	f	60.00	<i>Hz</i>
Size of time step	ΔT	34.7222	μ <i>sec</i>
Size of grid block	Δr	0.1027	<i>mm</i>
Number of grid nodes	N_{nodes}	61	
Time steps per cycle	N	480	

Table 2.15: Pipe properties of the 7" casing and input data used for evaluating the effect of electrical conductivity on the power losses in the casing.

Figure 2.37 shows the relative increase in hysteresis losses as the electrical conductivity of the material is decreased. The increase in hysteresis losses is consistent with the increasing depth of penetration of the electromagnetic wave into the material as the electrical conductivity is decreased. This can be deduced from the equation for skin depth, Equation 2.69, which states that the depth of penetration is inversely proportional to the square root of the electrical conductivity. On the other hand, as the electrical conductivity increases, the penetration of the wave into the material decreases. Thus, the volume of material that is significantly exposed to the magnetization process and associated hysteresis losses is diminished.

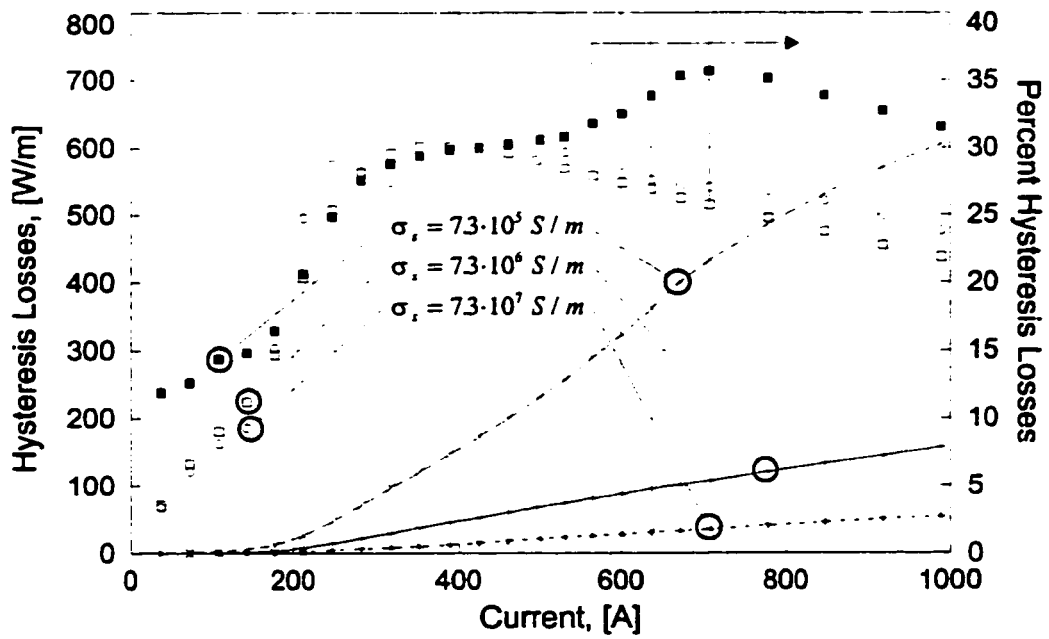


Figure 2.37: Hysteresis losses per meter of the 7" casing as a function of the magnitude of the current conducted in the tubing and for various values of electrical conductivity.

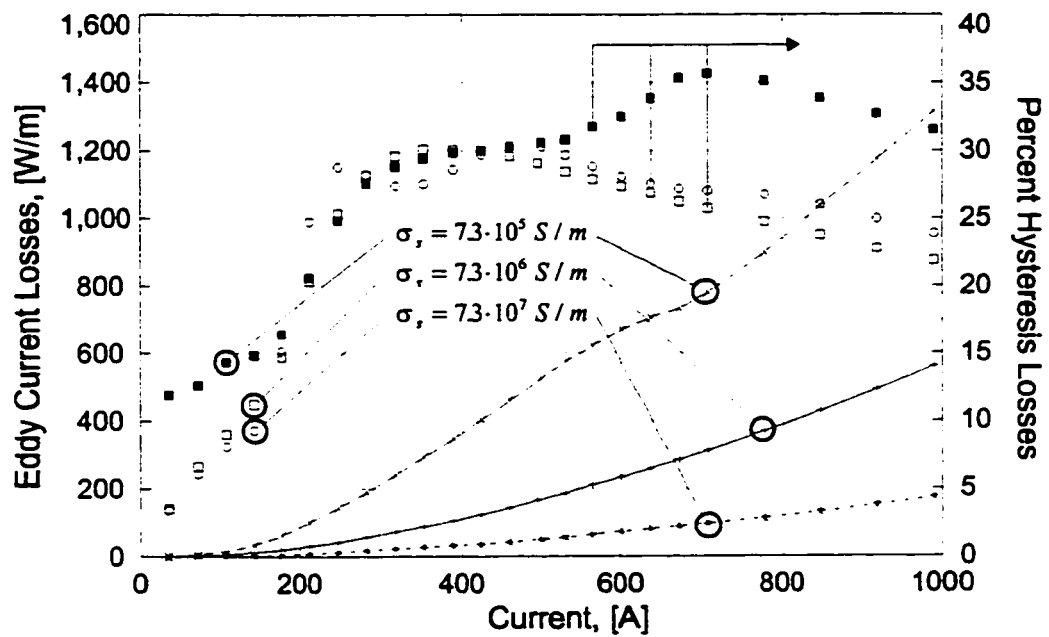


Figure 2.38: Eddy current losses per meter of the 7" casing as a function of the *RMS* current conducted in the 3½ tubing and various values of electrical conductivity.

Figure 2.38 shows the increase in eddy current losses as the electrical conductivity of the material is decreased. This increase is consistent with the resulting overall increase in resistance of the material, and thus greater losses are

expected. However, the increase in eddy current losses is not proportional to the decrease in electrical conductivity, which is especially evident for the higher conductivity calculations. The argument for limited depth of penetration of the electromagnetic field into the material is valid for both eddy current and hysteresis losses. At the higher electrical conductivity, the electric field strength is concentrated on the two surfaces of the material and, therefore, the current density and associated losses are greater. Therefore, as shown on Figure 2.38, a ten fold increase in electrical conductivity, from $\sigma_s = 7.3 \cdot 10^6$ to $\sigma_s = 7.3 \cdot 10^7$ results in a power loss at 1000 A *RMS* that is diminished to approximately 1/3 or $1/\sqrt{10}$.

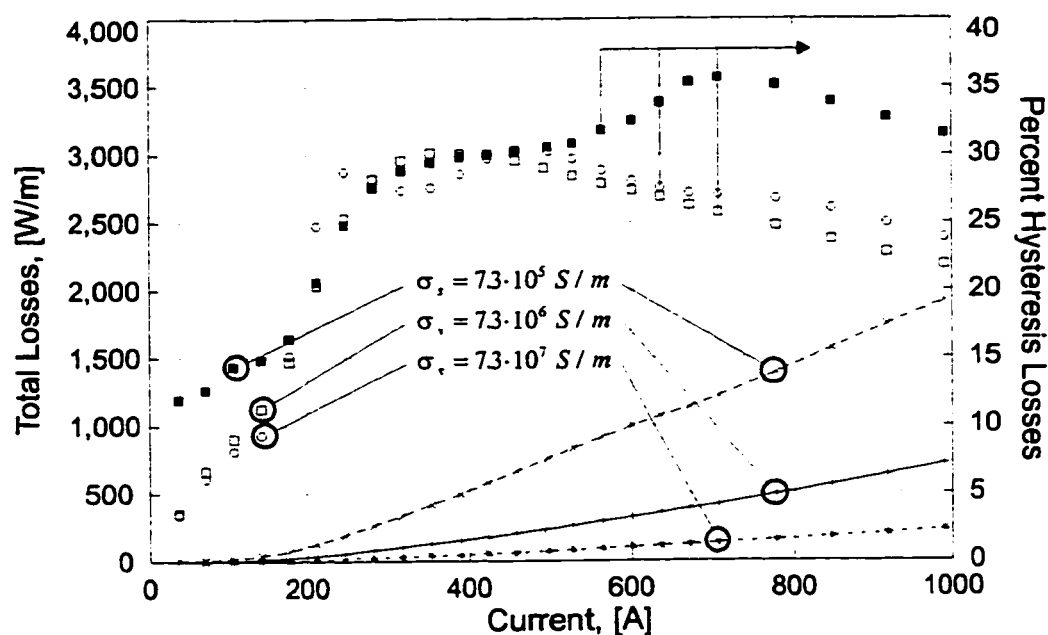


Figure 2.39: Total losses per meter of the 7" casing as a function of the *RMS* current conducted in the tubing and various values of electrical conductivity.

Figure 2.39 shows the total power losses as a function of current. The relationship between total power losses and current is investigated for the three cases. For a linear material, the total power losses are proportional to the square of the current, $P_t \propto I_t^2$. However, the presence of hysteresis in the material changes the relationship dramatically. The total power loss as a function of current is fit to the curve $P_t = a I_t^b$ for values of current where the contribution of hysteresis losses exceeds 15%. This occurs for $I_t > 200$ A *RMS*. The curves are fit to the calculations using the *Marquardt-Levenberg* algorithm for non-linear least squares curve fitting. Table 2.16 summarizes the results.

σ_s [S/m]	
$7.3 \cdot 10^5$	$P_t = 1.54 \cdot (I_t)^{1.0601}$
$7.3 \cdot 10^6$	$P_t = 0.19 \cdot (I_t)^{1.2295}$
$7.3 \cdot 10^7$	$P_t = 0.04 \cdot (I_t)^{1.2768}$

Table 2.16: Functional relationship for the 7" casing between total power, P_t , and current, I_t , for $I_t > 200$ A *RMS* and the three different values of electrical conductivity.

Referring to Figure 2.39, the plots of the percent hysteresis losses for the three cases indicate that for the lowest conductivity case the overall contribution of the hysteresis losses is about 70% greater than hysteresis losses found in the higher conductivity cases. The results presented here permit an estimate of the power losses in the casing in the vertical section of the horizontal wellbore to be made. These losses *do not* increase as the square of the current as would be the case if hysteresis were not present.

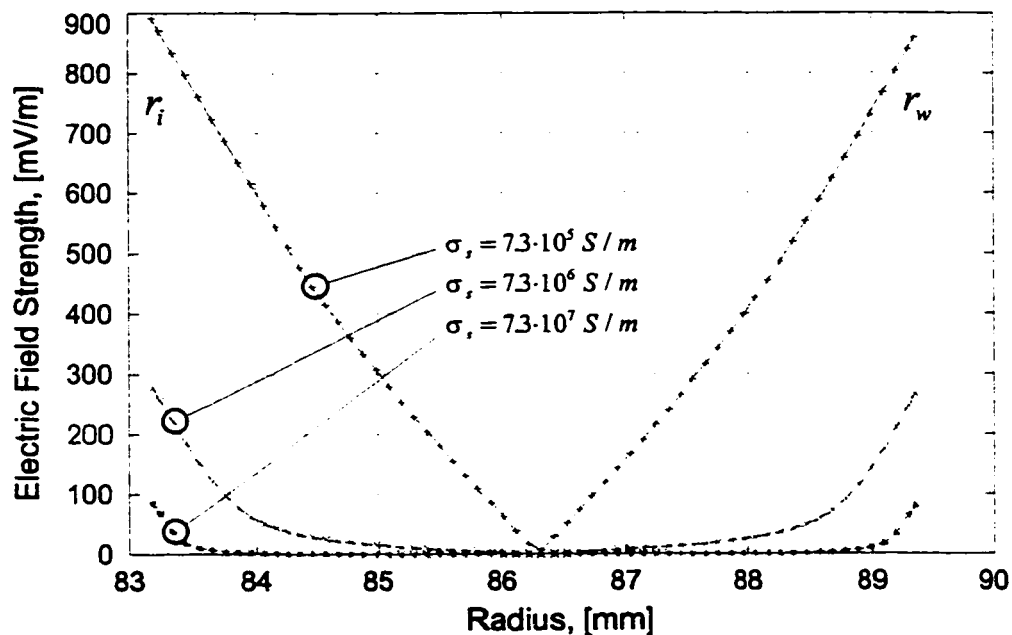


Figure 2.40: The *RMS* value of the electric field strength in the 7" casing for various values of electrical conductivity and a current of 500 A *RMS* in the tubing.

The electromagnetic field distributions in the casing for the various values of electrical conductivity are shown in Figures 2.40 and 2.41. The fields are calculated

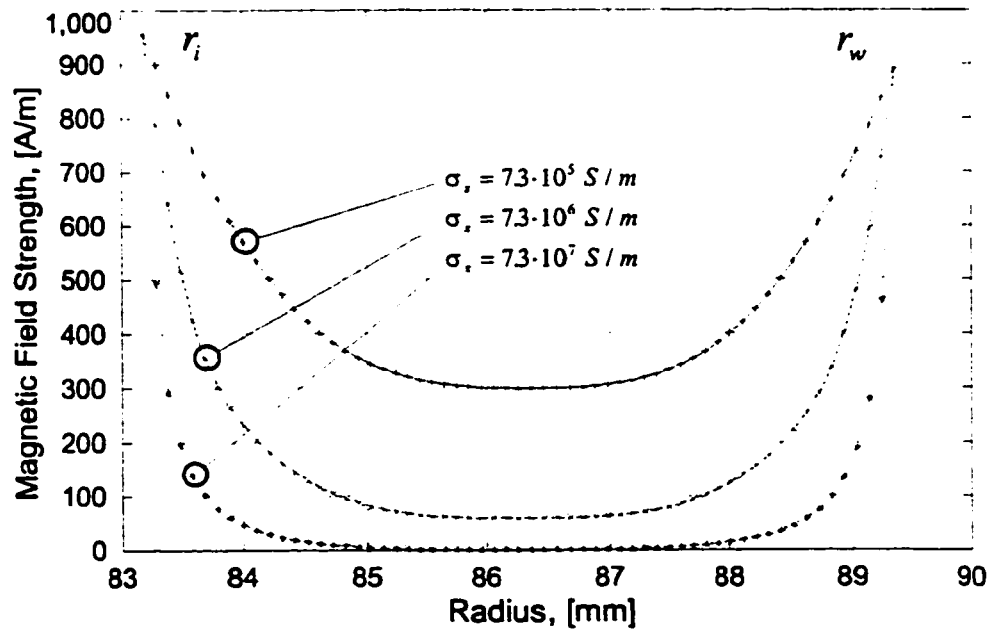


Figure 2.41: The *RMS* value of the magnetic field strength distribution in the 7" casing for various values of electrical conductivity and a current of 500 A *RMS* in the tubing.

for an excitation current of 500 A *RMS* conducted in the concentrically located tubing. These figures show the attenuation of the electromagnetic fields as the electrical conductivity of the material increases. The depths of penetration as defined by the skin depth, δ , for the three cases are compared to the theoretical values for the case of no hysteresis, using the value of $\mu_r = 269$, as measured by *LDJ Electronics Inc.*, for the casing, and using Equation 2.69. The results are summarized in Table 2.17.

σ_s [S/m]	Calculated δ [mm] With Hysteresis	Theoretical δ [mm] Without Hysteresis	Ratio
$7.3 \cdot 10^5$	1.7140	4.6367	2.7052
$7.3 \cdot 10^6$	0.5460	1.4662	2.6853
$7.3 \cdot 10^7$	0.1829	0.4637	2.5353

Table 2.17: Effect of electrical conductivity on the depth of penetration of the electromagnetic field into the 7" casing.

The effect of hysteresis on the distribution of the electromagnetic field in the material is significant. The distance the wave penetrates into the material is reduced by a factor of almost three leading to a corresponding redistribution of the eddy currents.

Tables 2.18, 2.19, and 2.20 summarize the power loss and electro-magnetic results for the calculations using three different electrical conductivities and a current of 500 A *RMS*. The effect of electrical conductivity on the power losses in the pipe when hysteresis effects are taken into account show that the relationship between power loss and current is not as predictable as for a magnetically linear material. The hysteresis losses have to take into account the magnetic properties of the pipe or extreme errors in the estimate of the losses will result.

Data	Symbol	Value	Units
Power Calculations			
Poynting Power	$P(r_i)$	386.09	[W/m]
	$P(r_w)$	374.09	[W/m]
Total Poynting Power	P_t	760.18	[W/m]
Eddy Current Losses	P_{ec}	527.36	[W/m]
Hysteresis Losses	P_h	230.72	[W/m]
$P_{ec} + P_h$ losses	P_{ec+h}	758.08	[W/m]
Percent Hysteresis Losses		30.43	Percent
Electro-Magnetic Calculations			
<i>RMS</i> Electric Field	$E_z(r_i)$	891.25	[mV/m]
	$E_z(r_w)$	859.88	[mV/m]
Skin Depth	δ	1.71	[mm]
Phase Angle	$\theta(r_i)$	24.75	[°]
	$\theta(r_w)$	25.50	[°]

Table 2.18: Results for the 7" casing for the case with $\sigma_s = 7.3 \cdot 10^5$ S/m and a tubing current of $I_{rms} = 500A$.

Data	Symbol	Value	Units
Power Calculations			
Poynting Power	$P(r_i)$	122.43	[W/m]
	$P(r_w)$	117.17	[W/m]
Total Poynting Power	P_t	239.60	[W/m]
Eddy Current Losses	P_{ec}	168.16	[W/m]
Hysteresis Losses	P_h	68.45	[W/m]
$P_{ec} + P_h$ losses	P_{ec+h}	236.62	[W/m]
Percent Hysteresis Losses		28.93	Percent
Electro-Magnetic Calculations			
RMS Electric Field	$E_z(r_i)$	278.56	[mV/m]
	$E_z(r_w)$	266.56	[mV/m]
Skin Depth	δ	0.54	[mm]
Phase Angle	$\theta(r_i)$	23.25	[°]
	$\theta(r_w)$	24.0	[°]

Table 2.19: Results for the 7" casing for the case with $\sigma_s = 7.3 \cdot 10^6$ S/m and a tubing current of $I_{rms} = 500A$.

2.6.4 Impact of the choice of hysteresis loop data on the calculation of the electromagnetic response of the steel pipe

In this example, the impact of the hysteresis loop on the loss calculations is investigated. Several hysteresis loops were obtained for the 7" casing sample sent to *LDJ Electronics Inc.* The first test was for a loop that ranged to the saturation magnetic field strength of the material, $H_{loop} = H_{sat} = \pm 8,000$ A/m. Then a second test was done to generate data for a loop that ranged to a magnetic field strength of $H_{loop} = \pm 1,000$ A/m, and the last test was for a loop that ranged to $H_{loop} = \pm 500$ A/m. Only the first two loops provided data that can be used in the numerical model. These loops and associated *peak magnetization curves* are reproduced in Figure 2.42.

Data	Symbol	Value	Units
Power Calculations			
Poynting Power	$P(r_i)$	40.12	[W/m]
	$P(r_w)$	37.36	[W/m]
Total Poynting Power	P_t	77.48	[W/m]
Eddy Current Losses	P_{ec}	50.08	[W/m]
Hysteresis Losses	P_h	21.74	[W/m]
$P_{ec} + P_h$ losses	P_{ec+h}	71.83	[W/m]
Percent Hysteresis Losses		30.27	Percent
Electro-Magnetic Calculations			
RMS Electric Field	$E_z(r_i)$	85.56	[mV/m]
	$E_z(r_w)$	79.77	[mV/m]
Skin Depth	δ	0.18	[mm]
Phase Angle	$\theta(r_i)$	22.50	[°]
	$\theta(r_w)$	24.75	[°]

Table 2.20: Results for the 7" casing for the case with $\sigma_s = 7.3 \cdot 10^7$ S/m and a tubing current of $I_{rms} = 500A$.

Figure 2.42 shows that a difference in the magnetization processes for the same material, as indicated by the different *peak magnetization curves*, takes place for the two tests. Clearly, the first test, which was conducted to the saturation conditions of the material, *altered* the magnetic characteristics of the material. This demonstrates that the history of magnetization for the material is important in determining the magnetic response of the material to sinusoidal excitation. This is consistent for a material that exhibits magnetic hysteresis. As a result, the calculations for power and the electromagnetic response of the material will be different, depending on which loop is used in the calculation.

The calculations are restricted to a peak excitation current, I_p , ranging from $0 \leq I_t \leq 368A$ RMS. For currents exceeding this range, the 1,000 A/m data cannot be used since the *distance factor* method can only generate hysteresis loops that are *less than* the maximum hysteresis loop. Additional input data for the calculations are summarized in Table 2.21.

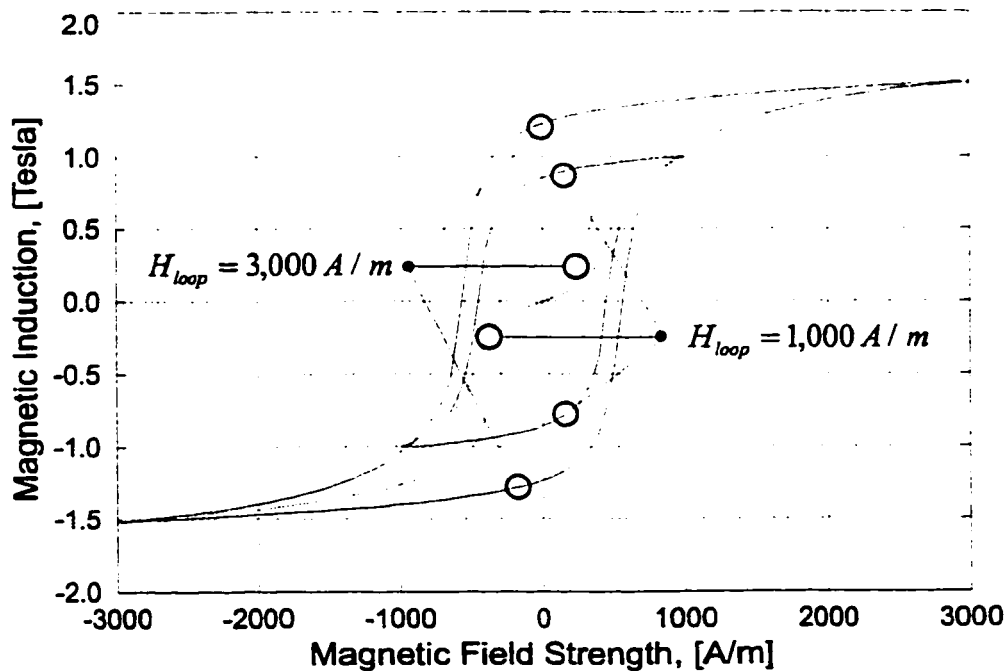


Figure 2.42: The 3,000 A/m and 1,000 A/m loops obtained from *LDJ Electronics Inc.* for the 7" diameter casing.

Figures 2.43 and 2.44 show the electric and magnetic field strengths for the 3,000 A/m and 1,000 A/m loop cases. The figures show a noticeable difference in the electromagnetic response of the material for the two different characterizations of the magnetization process. Of particular interest are the differences in the magnitudes of the surface electric field strengths. The surface electric field strength calculated with the 3,000 A/m loop is about 25% greater than that calculated for the 1,000 A/m loop. This will have a notable impact on the calculation of the power losses since the surface electric field strength is used to determine power flow into the material by application of the Poynting vector.

A comparison between the results of the calculations using the two different hysteresis loops is summarized in Table 2.22. The greatest differences arise as a result of the differences in distribution of the electric fields for the two different loops. Therefore, the eddy current losses and consequently total power losses are affected significantly.

It is difficult to know what curves should be used in the simulation of the magnetization process. Experts at *LDJ Electronics Inc.* recommend the use of the curves that are obtained near the operating conditions for which the calculation is

Data	Symbol	Value	Units
Pipe Properties			
Inner radius	r_i	83.185	<i>mm</i>
Outer radius	r_w	89.345	<i>mm</i>
Length	L_p	4.007	<i>m</i>
Initial relative permeability	μ_r	269.00	
Electrical conductivity	σ_s	7.30	10^6 <i>S/m</i>
Run Time Data			
Peak excitation current	I_p	520.00	<i>A</i>
Peak magnetic field strength	$H_\phi(r_i)$	994.90	<i>A/m</i>
Frequency	f	60.00	<i>Hz</i>
Size of time step	ΔT	34.7222	μ <i>sec</i>
Size of grid block	Δr	0.1027	<i>mm</i>
Number of grid nodes	N_{nodes}	61	
Time steps per cycle	N	480	

Table 2.21: Pipe properties and runtime input data for comparing the effect of different hysteresis loops using the *EM Pipe Loss* model.

intended. Thus for current levels less than 520 A (368 A *RMS*), the 1,000 *A/m* loops should be used. Their advice was adhered to in this thesis, and resulted in good agreement between numerical calculation and experimental results.

This example calculation emphasizes the significant effect that hysteresis loops have on the results of numerical modeling of the magnetization process. It is important, therefore, that representative and accurate hysteresis loops are obtained for a sample, and that the loops are obtained at the operating conditions of interest.

2.6.5 Calculation of the effective pipe resistance for the casing

Calculation of the effective pipe resistance for the casing in the vertical section of the horizontal well, or for any pipe in the production system of the horizontal well, can be carried out using the *EM Pipe Loss* model.

For the ungrounded casing in the vertical section of the wellbore, the current circulates up the interior of the casing and down the exterior of the casing in the

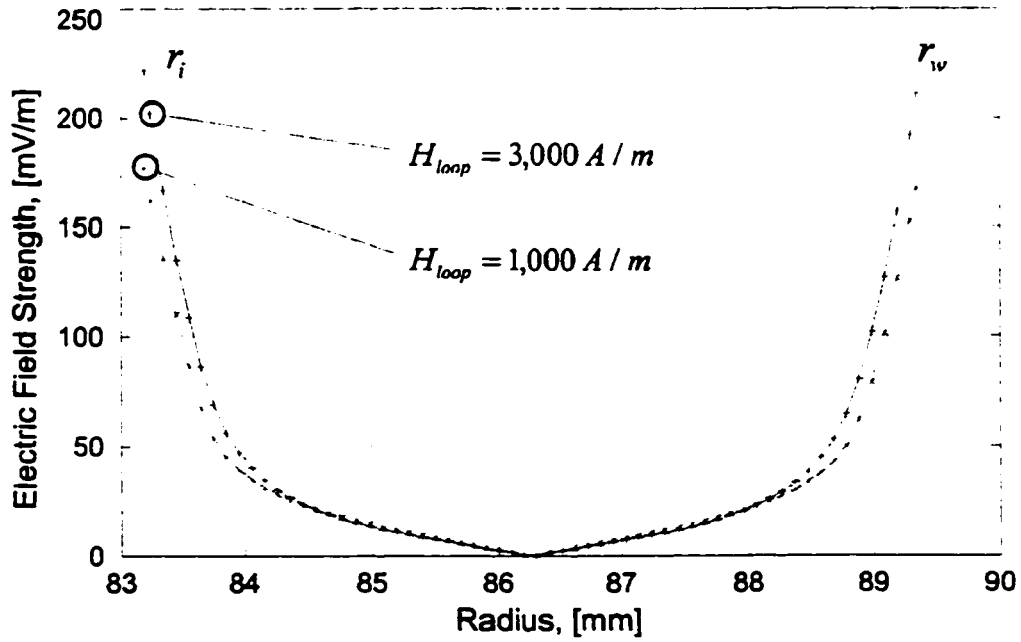


Figure 2.43: The *RMS* value of the electric field strength in the 7" casing calculated using the 3,000 A/m and 1,000 A/m hysteresis loops for a tubing current of 367 A *RMS*.

same direction as that of the electric field strength. In the center of the casing at $r_m = \frac{r_w - r_i}{2}$, the electric field strength and current density are equal to zero. Thus the power losses for the inside section of the casing, $r_i < r < r_m$ can be calculated by integrating $\vec{E} \times \vec{H}$ over the surface at r_i . Similarly, the power losses for the outside section of the casing can be calculated by integrating $\vec{E} \times \vec{H}$ over the surface at r_w . The resistance can be determined directly from the power losses and since the current is circulating, the interior and exterior resistance, (R_i and R_o) are in series and the effective resistance per meter of casing is the sum of these resistances. The interior and exterior power losses per meter of casing are thus

$$\begin{aligned} P_i &= E_{rms}(r_i) I_{rms} \cos(\theta_i) \\ P_o &= E_{rms}(r_w) I_{rms} \cos(\theta_w) \end{aligned} \quad (2.70)$$

From Equation 2.70 the interior and exterior resistance per unit length of casing are determined directly using,

$$R_i = \frac{P_i}{I_{rms}^2} \quad R_o = \frac{P_o}{I_{rms}^2} \quad (2.71)$$

The total resistance R_{casing} is thus, $R_{casing} = R_i + R_o$.

For example, the total resistance per meter is calculated for a current of 300 A *RMS*. For the 300 A *RMS* case, $E_{rms}(r_i) = 142.68 \text{ mV/m}$, $E_{rms}(r_w) = 130.18 \text{ mV/m}$, and $\theta_i = \theta_w = 21^\circ$.

Using Equation 2.70, the calculated power losses on the interior are 39.96 *W/m* and on the exterior are 36.46 *W/m*. Using Equation 2.71 the interior and exterior resistance are 444.01 $\mu\Omega/m$ and 405.11 $\mu\Omega/m$. Thus the total resistance per meter of ungrounded casing is 849.12 $\mu\Omega/m$.

It is of interest to compare the calculated resistance with the total effective resistance obtained experimentally by Stroemich *et. al.* for a *grounded* casing of the same size. In the grounded casing, the current is not circulating but flows on the interior of the pipe only and thus travels only half the distance it would have in an ungrounded casing. They obtain a value of 387.07 $\mu\Omega/m$, for K-55 casing, less than approximately half of that of the ungrounded casing.

These calculations are consistent with expectations since for an ungrounded casing, the current must flow through twice the distance it has to flow through in the grounded casing. Also, for the ungrounded casing of the current is confined to flow closer to the surface of the pipe because the current density must diminish to zero at r_m . Similar results are presented by *Newbold and Perkins*, [99] where they concluded that the power losses in a system using cables inside an ungrounded casing results in about twice the power losses that would occur if tubing was used to conduct the current and the casing is grounded.

Plots of the total casing resistance per unit length are shown on Figure 2.45. The figure compares the total effective resistance per meter obtained using the *EM Pipe Loss* model with experimental values obtained by measuring the temperature rise of the casing with time. As the plot shows, the experimental data coincides closely with the numerical calculations. The maximum percentage difference in the results of the calculations is less than 10%. The phase angles θ_i and θ_w were not measured during the experiments and are approximated from Stroemich *et. al.*, [29].

This concludes Chapter Two. In this chapter, a finite difference time domain numerical model, called the *EM Pipe Loss* model, which solves the appropriate form of Maxwell's equations in a non-linear magnetic material, has been developed. The

model has the capability to determine the combined eddy current and hysteresis losses in a piece of pipe fabricated from magnetic material that exhibits hysteresis under the influence of a time varying magnetic field strength. The model has been tested against an analytic solution published by *Loga*, [1] and a similar numerical model published by *Zakrzewski and Peitras*, [86] with satisfactory results. The model has been compared to experimental results involving the power losses in a piece of pipe, again with acceptable results.

The *EM Pipe Loss* model is employed in the next chapter to characterize a heat source in the heat transfer problem associated with a long horizontal well producing liquids from an oil reservoir.

Data	Symbol	1,000 A/m loop	3,000 A/m loop	Units
Power Calculations				
Poynting Power	$P(r_i)$	57.29	70.96	[W/m]
	$P(r_w)$	54.35	67.09	[W/m]
Total Poynting Power	P_t	111.64	138.05	[W/m]
Eddy Current Losses	P_{ec}	62.13	94.68	[W/m]
Hysteresis Losses	P_h	48.18	40.96	[W/m]
$P_{ec} + P_h$ losses	P_{ec+h}	110.31	135.64	[W/m]
Percent Hysteresis Losses		43.68	30.20	Percent
Electro-Magnetic Calculations				
RMS Electric Field	$E_z(r_i)$	177.43	221.79	[mV/m]
	$E_z(r_w)$	167.66	210.74	[mV/m]
Skin Depth	δ	0.48	0.49	[mm]
Phase Angle	$\theta(r_i)$	21.00	28.50	[°]
	$\theta(r_w)$	21.75	30.00	[°]

Table 2.22: Comparison of the results for the two different hysteresis loops for the 7" casing and a tubing current of 367 A RMS.

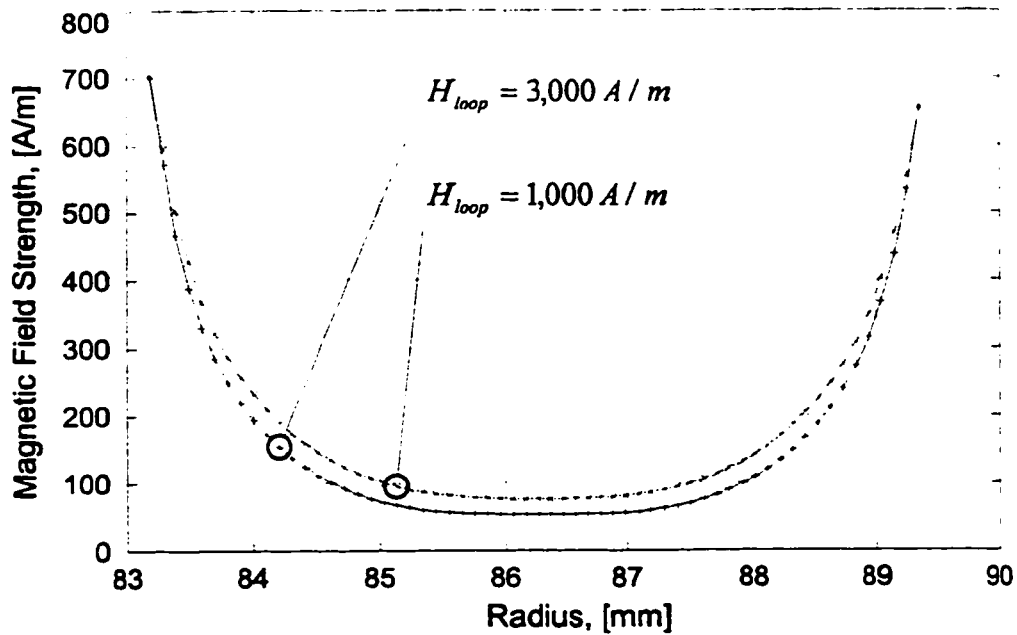


Figure 2.44: The *RMS* value of the magnetic field strength in the 7" casing calculated using the 3,000 A/m and 1,000 A/m hysteresis loops for a tubing current of 367 A *RMS*.

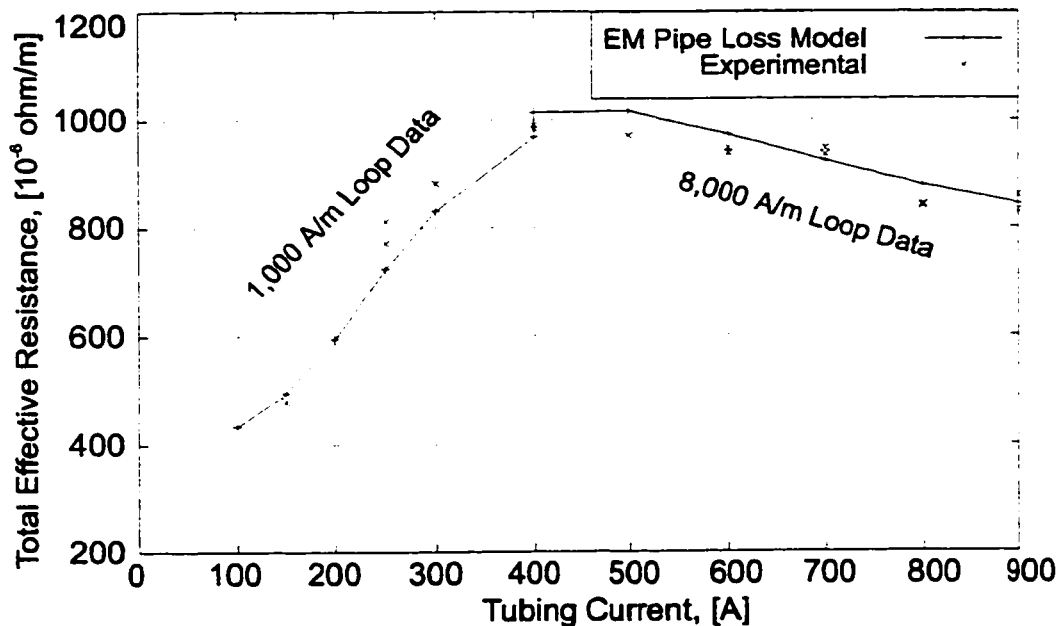


Figure 2.45: Comparison of the total effective resistance of the 7" casing calculated using the *EM Pipe Loss* model with data obtained experimentally by observing the temperature rise of the casing as a function of time.

Chapter 3

Semi-Analytic Solutions of the Heat Transfer Problem

3.1 Introduction

3.1.1 Overview

In this chapter, radial and axial semi-analytic equations are developed to calculate the heat flow in a horizontal well using electrical heating to enhance the production of oil from a heavy oil reservoir. The semi-analytic model uses the results of the previous chapter to determine the heat losses in the casing as a result of hysteresis and eddy current losses. The radial semi-analytic heat transfer model calculates the temperature distribution from the center of the wellbore, through the casing, and throughout the reservoir. The axial semi-analytic model calculates the temperature distribution along the length of the horizontal wellbore. The two models are effectively combined to provide the temperature distribution throughout the entire problem domain.

The solution of the heat transfer problem in the wellbore is important. A model that accounts for the fluid production rate and input power and determines the resulting peak temperature in the well is necessary to design a system that will have thermal stability and can be operated safely. These models can be used to determine the maximum length of the horizontal well for a specified heating strategy. Also, these models can be used to estimate the input power requirements

to electrically heat a long horizontal well and thereby allow estimation of operating expenses and equipment specifications for an electrical heating strategy.

The development of the semi-analytic models is presented in detail. The mathematical approach to solving the problems is novel. The equations presented herein can be modified to solve a general suite of boundary value problems, such as heating the horizontal well by circulating steam.

3.1.2 Statement of the problem

Figure 3.1 depicts the horizontal wellbore. The terminology used to define the regions for the heat transfer problem is described in this figure.

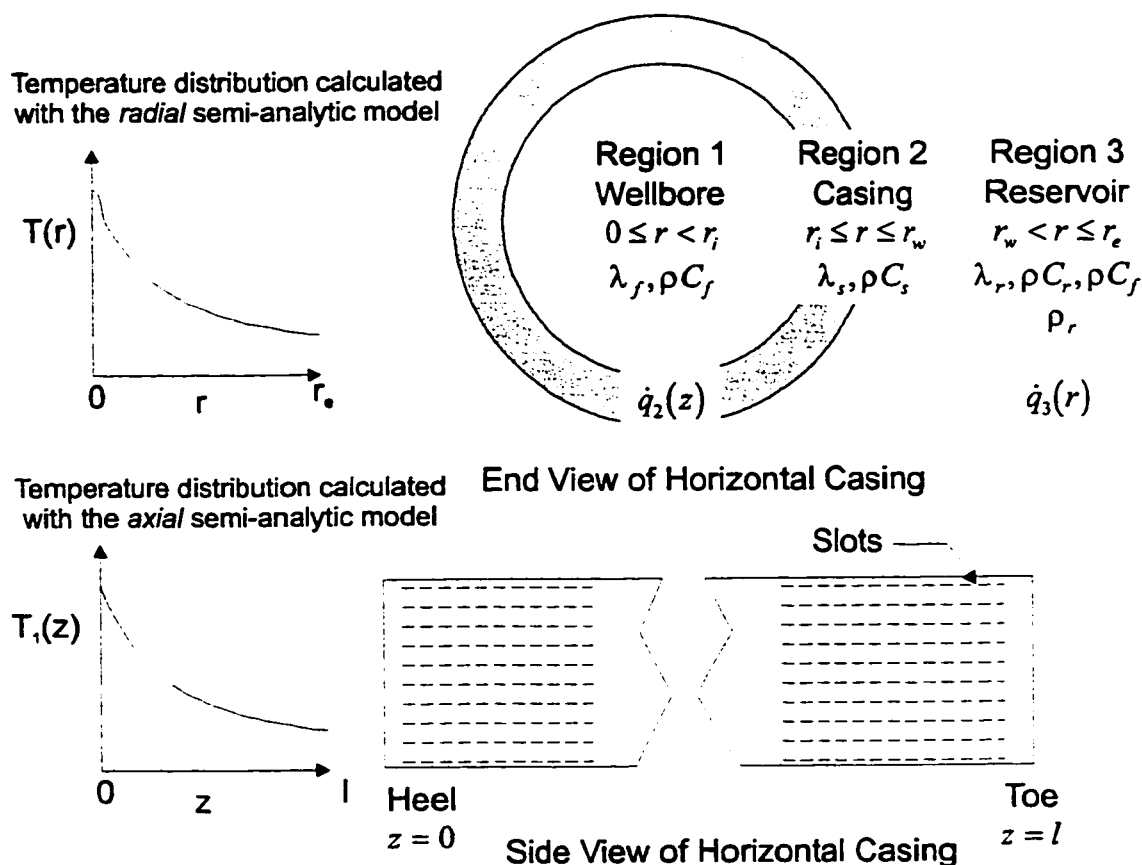


Figure 3.1: Terminology and definition of the *regions* used in the semi-analytic models.

Region 1 is the wellbore and extends from $0 \leq r < r_i$. The wellbore is filled with a fluid mixture of oil and water. The fluid is characterized by a thermal conductivity of λ_f and heat capacity of ρC_f . The fluids flow in the axial direction

from the toe, $z = l$, to the heel, $z = 0$, in the wellbore. Heat transfer in the axial direction is with the movement of the fluids. Heat transfer by thermal conduction in the axial direction is insignificant in comparison to the flow of heat by convection and is ignored in the axial semi-analytic model. Heat transfer by thermal conduction in the radial direction is accounted for in the radial semi-analytic model but not in the axial model.

Region 2 is the casing and extends from $r_i \leq r \leq r_w$. The casing conducts current resulting in the creation of heat due to hysteresis and eddy current losses. The heat generation is specified by $\dot{q}_2(z)$, which is defined in Equation 2.67. The casing has the thermal conductivity, λ_s , and heat capacity, ρC_s , of steel. Heat flows very efficiently in the casing by thermal conduction due to the very high thermal conductivity of the steel.

Region 3 is the reservoir and extends from $r_w < r \leq r_e$. Current flows in the reservoir, in the radial direction, and produces heat as a result of ohmic losses. The reservoir has a bulk thermal conductivity of λ_r , heat capacity of ρC_r , and electrical resistivity of ρ_r . Fluid is produced from the reservoir into the wellbore through *slots* or *perforations*. The movement of fluids radially into the wellbore results in the transfer of heat by convection. Heat transfer by convection depends on the fluid velocity, ν_f , and the heat capacity of the flowing fluid, ρC_f . Heat transfer by conduction in the reservoir is due to the thermal conductivity of the reservoir, λ_r .

The solution of the heat transfer problem in the radial direction is the first step in the derivation of the axial semi-analytic model as depicted in Figure 3.2.

It is assumed that radial flow into the wellbore is entirely due to thermal conduction, and hence, any radial heat flow into the wellbore by thermal convection can be neglected. With these assumptions the Neumann boundary condition at the boundary between *Regions* 1 and 2

$$\lambda_s \frac{\partial T_2(r, t)}{\partial r} \Big|_{r=r_i} = \lambda_f \frac{\partial T_1(r, t)}{\partial r} \Big|_{r=r_i}$$

governs the radial heat flow into the wellbore in the radial semi-analytic model shown in Figure 3.2.

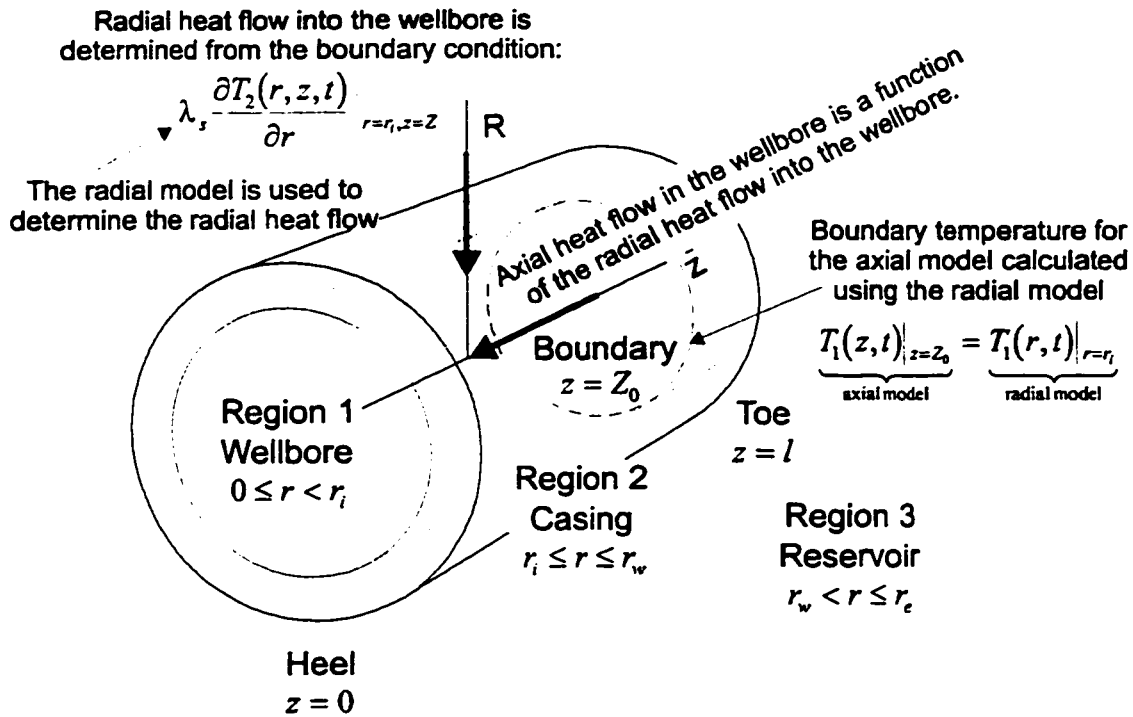


Figure 3.2: Depiction showing the determination of the heat flow into the wellbore from the casing using the radial semi-analytic model. Also shown is the use of the radial semi-analytic model at $z = Z_0$ to determine the Dirichlet boundary condition required for the derivation of the axial semi-analytic model.

To derive the axial semi-analytic model requires a boundary condition at $z = Z_0$. There are two obvious boundaries in the problem, one at $z = 0$ and the other at the toe of the well, $z = l$. The temperature at $z = l$ cannot be set to a constant value since electrical heating in the adjacent reservoir and the flow of fluids into the wellbore modify the temperature at $z = l$ as time passes. In this thesis, as depicted in Figure 3.2, the radial semi-analytic model is used to provide the boundary condition at Z_0 required for solution of the axial model. Thus

$$\underbrace{T_1(z, t)|_{z=Z_0}}_{\text{axial model}} = \underbrace{T_1(r, t)|_{r=r_i}}_{\text{radial model}} \quad (3.1)$$

The boundary, Z_0 , is located where the total fluid production in the wellbore is effectively zero and thus there is no heat transfer in the axial direction. *The temperature in the wellbore at the boundary Z_0 can therefore be determined using the radial semi-analytic model.*

The semi-analytic models are based on the application of the principle of conservation of energy to a system with heat transfer by thermal conduction and convection due to a single flowing phase and containing energy sources. Stated in terms of the temperature of the system this principle results in the following general equation [100],

$$\nabla \cdot (\lambda \nabla T) - \nabla (\rho C_f v_f T) + \dot{q} = \frac{\partial (\rho C_b T)}{\partial t} \quad (3.2)$$

In the above equation λ is the thermal conductivity, ρC_f is the heat capacity of the flowing phase, ρC_b is the bulk heat capacity of the system, v_f is the velocity of the flowing phase, and \dot{q} is the energy source. All these elements normally vary in space and with temperature, resulting in a non-linear equation. The necessary assumptions for any analytic work to progress are that:

1. all physical properties are constant in space and time, and
2. the heat source may vary spatially but not with temperature.

Various assumptions are used to reduce Equation 3.2 so that it can be solved analytically. These assumptions are presented in detail in the specific sections pertaining to the solution of the radial and axial semi-analytic models.

Once the partial differential equation for describing the heat transfer problem in each of the regions is determined, the Laplace transform method is employed to obtain a solution in Laplace space. Properties of the Laplace transform that are used to transform the partial differential equations are,

$$\begin{aligned} \mathcal{L}\{T(r, t)\} &= \int_{t_0}^{\infty} e^{-st} T(r, t) dt \\ &= \hat{T}(r, s) \\ \mathcal{L}\left\{\frac{\partial T(r, t)}{\partial t}\right\} &= s\hat{T}(r, s) - T(r, t_0) \\ \mathcal{L}\left\{\frac{\partial^n T(r, t)}{\partial r^n}\right\} &= \frac{d^n \hat{T}(r, s)}{dr^n} \\ \mathcal{L}\left\{\frac{t^{n-1}}{(n-1)!} \cdot h(r)\right\} &= \frac{h(r)}{s^n} \end{aligned} \quad (3.3)$$

where s is the variable of transformation and t_0 is the time at which the initial conditions are specified. For these properties of the Laplace transform to apply there must be absolute convergence of $T(r, t)$ at the limits of integration.

The inversion of the Laplace transform solution must be completed numerically. This is accomplished using a method called the *Stehfest Inversion Algorithm*, [101].

3.1.3 Numerical inversion of the Laplace transform

Numerical inversion of the Laplace transform is accomplished using a calculation method published by H. Stehfest, Reference [101]. This numerical inversion method has been used to solve many types of reservoir engineering problems, in particular for well test pressure analysis, [102], [103], [104], and [105].

The method is simple to use and program into computer code. In Equation 3.4, F_a is the inverse of $\hat{T}(r, s)$, the Laplace transform of the temperature distribution $T(r, t)$, at the instant of time t . Equation 3.4 must be evaluated for each time t that a solution is desired.

$$F_a = T(r, t) = \frac{\ln 2}{t} \sum_{i=1}^N V_i \hat{T} \left(r, \frac{\ln 2}{t} i \right) \quad (3.4)$$

The coefficients in Equation 3.4, V_i , are defined in Equation 3.5 and are independent of the Laplace transform being inverted.

$$V_i = (-1)^{\frac{N}{2}+i} \sum_{k=\text{floor}(\frac{i+1}{2})}^{\min(i, \frac{N}{2})} \frac{k^{\frac{N}{2}} (2k)!}{(\frac{N}{2} - k)! k! (k-1)! (i-k)! (2k-i)!} \quad (3.5)$$

There are some practical issues that need to be considered when using the *Stehfest Inversion Algorithm*:

1. N in Equations 3.4 and 3.5 is arbitrary. It must, however, be an even number. It is *the* parameter that controls the accuracy of the numerical inversion. Theoretically, the larger N , the more accurate the inversion.
2. For N too large, the solution can become unstable because of round off errors

or numerical limitations in the computer's ability to determine V_i , which involves the multiplication and division of factorial terms.

3. The best way to select an optimum N is to apply the Stehfest inversion algorithm to the problem and increase N until a solution is obtained which does not change when N is increased further. As a guideline, the optimum N is approximately equal to the number of significant figures used by the computer, [101].

For the axial and radial semi-analytic models, a value of N ranging from 6 to 12 (even integers only) provided satisfactory results.

3.2 Radial Semi-Analytic Heat Transfer Model

In this section the multi-region, radial heat transfer model is developed. For a given set of conditions, the temperature distribution from the center of the wellbore through the casing and into the reservoir can be calculated.

The radial semi-analytic model is developed using the following procedure:

1. Determine the partial differential equations that define the heat transfer model in each of the regions, (see Equations 3.6, 3.12, and 3.21).
2. Obtain the Laplace Transform of Equations 3.6, 3.12, and 3.21, (see Equations 3.7, 3.14, and 3.22). The partial differential equations obtained in *Step 1* are transformed into ordinary differential equations.
3. Solve the ordinary differential equations obtained in *Step 2*.
4. Using the boundary conditions of the problem, construct a system of linear equations and solve the unknown coefficients of the general solutions in Laplace space.
5. Obtain the radial temperature distribution in the time domain by numerical inversion of the Laplace transforms obtained in *Step 4* using the Stehfest Inversion Algorithm.

3.2.1 Radial heat transfer model in the wellbore

The heat transfer model in the wellbore is developed in this section. The following assumptions are made:

1. A liquid occupies the entire wellbore.
2. Heat transfer is in the radial direction.
3. The dominant heat transfer mechanism in the radial direction is thermal conduction. The effects of natural and forced convection mechanisms are assumed to be negligible.
4. The heat flow from the casing into the liquid occupying the wellbore is by thermal conduction.

With these simplifying assumptions, the general heat transfer model, Equation 3.2, can be simplified to the following equation,

$$\lambda_f \frac{\partial^2 T_1}{\partial r^2} + \frac{\lambda_f}{r} \frac{\partial T_1}{\partial r} = \rho C_f \frac{\partial T_1}{\partial t} \quad (3.6)$$

where λ_f is the thermal conductivity of the fluids in $W/(m \text{ } ^\circ C)$ and ρC_f is the heat capacity of the fluids with units $J/(m^3 \text{ } ^\circ C)$. The Laplace Transform of Equation 3.6 is determined directly using Equations 3.3 and is

$$\frac{d^2 \hat{T}_1}{dr^2} + \frac{1}{r} \frac{d\hat{T}_1}{dr} - s\beta_f \hat{T}_1 = -\beta_f T_0 \quad (3.7)$$

where, $\beta_f = \frac{\rho C_f}{\lambda_f}$.

The solution of Equation 3.7, is known, [106] and is

$$\hat{T}_1(r, s) = A(s) \mathbf{I}_0 \left(r \sqrt{s\beta_f} \right) + B(s) \mathbf{K}_0 \left(r \sqrt{s\beta_f} \right) + \frac{T_0}{s} \quad (3.8)$$

where \mathbf{I}_0 is the modified Bessel function of the first kind of zero order and \mathbf{K}_0 is the modified Bessel function of the second kind of zero order.

In summary, the partial differential equation that defines the radial heat transfer model in the wellbore, Equation 3.6, the Laplace transform of this equation,

Equation 3.7, and the solution of the Laplace transform, Equation 3.8, have been developed in this section. The unknown coefficients $A(s)$ and $B(s)$ will be determined by matching boundary conditions and will be functions of the axial coordinate z .

3.2.2 Radial heat transfer model in the casing

The heat transfer model for the casing will now be determined. The following assumptions are made:

1. Heat transfer in the casing by thermal conduction in the radial direction is much greater than in the axial direction and the latter is neglected.
2. A localized electrical heating rate resulting from hysteresis and eddy current losses occurs within the casing.
3. Eddy current and hysteresis losses are accounted for using the methods developed in *Chapter Two*.
4. Radial heat transfer by convection in the steel casing, due to the fluids flowing through the slots or perforations, is assumed to be negligible.
5. The electrical properties of the casing do not vary with temperature.

The assumption of radial thermal conduction being *the* dominant heat transfer mechanism in the casing is critically tested at a later point by comparing the semi-analytic solution that is obtained for the temperature distribution with a more exact solution obtained with a numerical simulation program.

Heat transfer by convection in the casing is insignificant since the velocity of the fluids, (ν_f) , into the wellbore along the length of the casing is small and the thermal conductivity of the steel casing is large, $(\lambda_r > 50 \text{ W}/(m^\circ\text{C}))$. It is possible to calculate the relative importance of conduction and convection heat transfer in the casing using α_s , as defined in Equation 3.9, [107]. For a value of α_s which approaches unity, heat transfer by conduction is dominant. For a value of α_s which is greater than two, the dominant heat transfer mechanism is convection [107]. For

typical thermal properties of steel casing and a nominal production rate of 50 m^3/day , α_s is

$$\begin{aligned}\alpha_s &= 1 + \frac{\rho C_f Q_t}{2\pi l \lambda_s} \\ &= 1 + \frac{(2,809,968 J/(m^3 \cdot ^\circ C)) \cdot (50 m^3/day)}{2\pi \cdot (1,000 m) \cdot (50 W/(m \cdot ^\circ C))} \\ &\approx 1.005\end{aligned}\tag{3.9}$$

where ρC_f is the heat capacity of the produced fluid, λ_s is the thermal conductivity of the casing, $\nu_f = Q_t/(2\pi l)$, Q_t is the total fluid production rate, and l is the length of the horizontal well. As the calculated value of Equation 3.9 indicates, heat transfer by convection can be ignored.

Incorporating these assumptions into Equation 3.2 results in a heat transfer model for the casing as follows:

$$\lambda_s \frac{\partial^2 T_2}{\partial r^2} + \frac{\lambda_s}{r} \frac{\partial T_2}{\partial r} + \dot{q}_2(z) = \rho C_s \frac{\partial T_2}{\partial t}\tag{3.10}$$

The heat source term, $\dot{q}_2(z)$, in Equation 3.10 was derived in the previous chapter. It arises from the hysteresis and eddy current losses produced by the current flowing in the casing at location z . Figure 1.2 shows the flow of current in the horizontal well. As depicted, current is assumed to collect uniformly along the length of the horizontal well and flow in the casing on a return path to the *Power Conditioning Unit*.

Since the current collects uniformly on the well, the magnitude of the current in the casing increases linearly along the length of the well, being zero at the toe of the well, and equal to the total current, I_t , at the heel of the well. Therefore in Equation 3.10, \dot{q}_2 is defined as a function of z . The equation for $\dot{q}_2(z)$ which was

developed in the previous chapter is repeated here for convenience:

$$\begin{aligned}
\dot{q}_2(z) &= \frac{I(z)^2}{A_s^2} \sum_{i=0}^n u_i \left(\frac{I_t}{l}\right)^i z^i \\
&= \frac{1}{A_s^2} \left(z \frac{I_t}{l}\right)^2 \sum_{i=0}^n u_i \left(\frac{I_t}{l}\right)^i z^i \\
&= \frac{1}{A_s^2} \sum_{i=0}^n u_i \left(\frac{I_t}{l}\right)^{i+2} z^{i+2}
\end{aligned} \tag{3.11}$$

The final form of the heat transfer model for the casing is:

$$\lambda_s \frac{\partial^2 T_2}{\partial r^2} + \frac{\lambda_s}{r} \frac{\partial T_2}{\partial r} = \rho C_s \frac{\partial T_2}{\partial t} - \frac{1}{A_s^2} \sum_{i=0}^n u_i \left(\frac{I_t}{l}\right)^{i+2} z^{i+2} \tag{3.12}$$

It is noted that the power loss in the casing, *Region 2*, is determined directly from Equation 3.11 and is

$$\begin{aligned}
P_2 &= \int_V \dot{q}_2(z) dV \\
&= \int_0^l \dot{q}_2(z) \pi (r_w^2 - r_i^2) dz \\
&= \frac{1}{A_s} \sum_{i=0}^n \frac{u_i}{i+3} \left(\frac{I_t}{l}\right)^{i+2} l^{i+3}
\end{aligned} \tag{3.13}$$

The Laplace Transform of Equation 3.12 is determined by using Equations 3.3

$$\frac{d^2 \hat{T}_2}{dr^2} + \frac{1}{r} \frac{d\hat{T}_2}{dr} - s\beta_s \hat{T}_2 = -\beta_s T_0 - \frac{1}{s\lambda_s} \frac{1}{A_s^2} \sum_{i=0}^n u_i \left(\frac{I_t}{l}\right)^{i+2} z^{i+2} \tag{3.14}$$

where $\beta_s = \frac{\rho C_s}{\lambda_s}$. The solution for Equation 3.14 is known from [106] and is

$$\hat{T}_2(r, s) = C(s) \mathbf{I}_0 \left(r \sqrt{s\beta_s}\right) + D(s) \mathbf{K}_0 \left(r \sqrt{s\beta_s}\right) + \frac{T_0}{s} + \sum_{i=0}^n \eta_i(s) z^{i+2} \tag{3.15}$$

where

$$\eta_i(s) = \frac{u_i}{s^2 \beta_s \lambda_s A_s^2} \left(\frac{I_t}{l}\right)^{i+2} \tag{3.16}$$

The derivative of Equation 3.15 will be required. It is

$$\frac{d\hat{T}_2(r, s)}{dr} = C(s) \mathbf{I}_1 \left(r\sqrt{s\beta_s} \right) \sqrt{s\beta_s} - D(s) \mathbf{K}_1 \left(r\sqrt{s\beta_s} \right) \sqrt{s\beta_s} \quad (3.17)$$

The unknown coefficients $C(s)$ and $D(s)$ will be determined by matching the boundary conditions and will be functions of the axial coordinate z .

3.2.3 Radial heat transfer model in the reservoir

The heat transfer model for the reservoir, *Region 3*, is developed in this section. The following assumptions are made:

1. Heat, current, and fluid flow are in the radial direction.
2. The electrical conductivity of the reservoir does not change with temperature.
3. Heat transfer by conduction in the axial direction can be neglected in comparison to the combined effects of the heat transfer mechanisms of conduction and convection in the radial direction.
4. Fluid production rate is uniform along the length of the horizontal well. Thus, the total production rate (i.e. the total fluid flow), in the wellbore at any location z is $Q(z) = Q_t \frac{z}{l}$.
5. The current flowing from the reservoir into the horizontal wellbore is collected uniformly along the length of the horizontal well. Thus, the current in the casing at any location z is $I(z) = I_t \frac{z}{l}$.

With these assumptions, Equation 3.2 can be simplified and the heat transfer model for the reservoir is stated as

$$\lambda_r \frac{\partial^2 T_3}{\partial r^2} + \left(\lambda_r + \rho C_f \frac{Q_t}{2\pi l} \right) \frac{1}{r} \frac{\partial T_3}{\partial r} + \dot{q}_3(r) = \rho C_r \frac{\partial T_3}{\partial t} \quad (3.18)$$

where Q_t is the total fluid production rate in m^3/day and l is the length of the horizontal well, measured from the toe to the heel.

The heat source term in Equation 3.21, $\dot{q}_3(r)$, originates from ohmic losses as a result of current flow in the reservoir. The term $\dot{q}_3(r)$ is derived from the electrical properties of the reservoir and radial distribution of current.

The electrical properties of the reservoir are assumed to be constant with temperature. In actuality, the electrical conductivity varies with temperature which is not normally ignored [108]. However, it may be ignored here since electrical heating in the *reservoir* (not the casing) has a relatively small effect on the overall heat transfer problem for a long horizontal well, as will be demonstrated in a later section. Thus, the variation of electrical conductivity with temperature is neglected.

It is assumed that the current collects uniformly along the length of the wellbore. For this assumption to hold, it is necessary that the largest dimension of the system is much less than the wavelength of the electromagnetic field in the reservoir.

The wavelength can be calculated from the following equation, [34],

$$\lambda = \frac{2\pi}{\omega \sqrt{\left[\frac{\mu\epsilon}{2}\right] \left[\sqrt{1 + \left(\frac{\sigma}{\omega\epsilon}\right)^2} + 1\right]}} \quad (3.19)$$

where $\omega = 2\pi f$ is the applied frequency, $\frac{\sigma}{\omega\epsilon}$ is the ratio of conduction to displacement current, ϵ is the permittivity and μ is the relative permeability of the material. Using typical values for σ and ϵ of the formation from Reference [34], the electromagnetic wavelength in the reservoir at an applied frequency of 60 Hz is calculated to be of the order of several thousand meters. The wavelength increases as the frequency of operation is lowered, and hence can always be selected to be much longer than the length of the horizontal well.

The heat source, \dot{q}_3 , is determined using Ohm's law:

$$\dot{q}_3(r) = \rho_r |J(r)|^2 = \rho_r \left(\frac{I_t}{2\pi rl}\right)^2 \quad (3.20)$$

where ρ_r is the electrical resistivity of the reservoir and I_t is the total current.

It is noted that the value of $\dot{q}_3(r)$ diminishes as $1/r^2$ and also decreases in proportion to the square of the length of the well, $1/l^2$. These observations

emphasize that only near wellbore heating can be achieved with electrical heating and that the the magnitude of the current required to achieve electrical heating of a given magnitude increases in proportion to the square of the horizontal well length.

The final form of the heat transfer model for Region 3 is:

$$\lambda_r \frac{\partial^2 T_3}{\partial r^2} + \left(\lambda_r + \rho C_f \frac{q_f}{2\pi l} \right) \frac{1}{r} \frac{\partial T_3}{\partial r} = \rho C_r \frac{\partial T_3}{\partial t} - \rho_r \left(\frac{I_t}{2\pi l} \right)^2 \frac{1}{r^2} \quad (3.21)$$

The Laplace transform of Equation 3.21 is,

$$\frac{d^2 \hat{T}_3}{dr^2} + \left(1 + \frac{\rho C_f Q_t}{\lambda_r 2\pi l} \right) \frac{1}{r} \frac{d\hat{T}_3}{dr} - s\beta_r \hat{T}_3 = -\beta_r T_0 - \frac{\rho_r}{s\lambda_r} \left(\frac{I_t}{2\pi l} \right)^2 \frac{1}{r^2} \quad (3.22)$$

where $\beta_r = \frac{\rho C_r}{\lambda_r}$.

The solution of Equation 3.22 is not readily available and is developed in detail as part of this thesis. Since Equation 3.22 is non-homogeneous, the solution will be separated into two parts: the complementary solution, $\hat{T}_{3,c}(r, s)$, which is the solution to the homogeneous form of Equation 3.22, and a particular solution $\hat{T}_{3,p}(r, s)$. Thus the solution consists of

$$\hat{T}_3(r, s) = \hat{T}_{3,c}(r, s) + \hat{T}_{3,p}(r, s) \quad (3.23)$$

The complementary solution $\hat{T}_{3,c}(r, s)$ is known from Reference [106] and is

$$\hat{T}_{3,c}(r, s) = E(s) \frac{\mathbf{I}_p(r\sqrt{s\beta_r})}{r^p} + F(s) \frac{\mathbf{K}_p(r\sqrt{s\beta_r})}{r^p} \quad (3.24)$$

where p is defined as follows:

$$p = \sqrt{\frac{1}{4}(1 - \alpha_r)^2} \quad (3.25)$$

$$\alpha_r = 1 + \frac{\rho C_f Q_t}{\lambda_r 2\pi l}$$

The *Method of Variation of Parameters* is used to obtain the particular solution in Equation 3.23. This method can be used to determine the complete solution of any linear differential equation for which the general homogeneous solution is known. In this case, the variation of parameters is applied to a second

order linear differential equation of the form

$$\frac{d^2T(r)}{dr^2} + a_1(r) \frac{dT(r)}{dr} + a_2(r) T(r) = h(r) \quad (3.26)$$

The complementary solution of the equation is known and in the form

$$T_c(r) = c_1 u_1(r) + c_2 u_2(r) \quad (3.27)$$

where the u_1 and u_2 are the independent homogeneous solutions and the c_1 and c_2 are arbitrary constants or parameters. The particular solution can be obtained by replacing the constant parameters c_1 and c_2 by appropriate functions of r . It is assumed that the particular solution has the form

$$T_p(r) = C_1(r, s) u_1(r) + C_2(r, s) u_2(r) \quad (3.28)$$

and is a solution of Equation 3.26. The last step is to determine appropriate functions for $C_1(r, s)$ and $C_2(r, s)$. The independent variable s is retained in the function to indicate that the equations are solved in Laplace space.

When $T(r, s) = T_p(r, s) + T_c(r, s)$ is substituted into Equation 3.26, the following set of equations is generated

$$\begin{aligned} \frac{dC_1(r, s)}{dr} u_1(r, s) + \frac{dC_2(r, s)}{dr} u_2(r, s) &= 0 \\ \frac{dC_1(r, s)}{dr} \frac{du_1(r, s)}{dr} + \frac{dC_2(r, s)}{dr} \frac{du_2(r, s)}{dr} &= h(r, s) \end{aligned} \quad (3.29)$$

Since u_1 and u_2 satisfy Equation 3.26 when $h(r, s)$ is replaced by zero, the set of equations in Equation 3.29 can be solved for C_1' and C_2' directly

$$\begin{aligned} \frac{dC_1(r)}{dr} &= -\frac{h(r)u_2(r)}{\mathbf{W}[u_1(x, s), u_2(x, s)]} \\ \frac{dC_2(r)}{dr} &= \frac{h(r)u_1(r)}{\mathbf{W}[u_1(x, s), u_2(x, s)]} \end{aligned} \quad (3.30)$$

The parameters $C_1(r, s)$ and $C_2(r, s)$ are finally determined from the following integrals,

$$C_1(r, s) = - \int_{r_w}^r \frac{u_2(x, s) \cdot h(x, s)}{\mathbf{W}[u_1(x, s), u_2(x, s)]} dx$$

$$C_2(r, s) = \int_{r_w}^r \frac{u_1(x, s) \cdot h(x, s)}{\mathbf{W}[u_1(x, s), u_2(x, s)]} dx$$
(3.31)

where $h(x, s)$ and the Wronskian of the complementary solutions, $\mathbf{W}[u_1(x, s), u_2(x, s)]$, are as follows:

$$h(x, s) = -\frac{\rho_r}{s} \frac{1}{\lambda_r} - \rho C_r T_0 \left(\frac{I_t}{2\pi l} \right)^2 \frac{1}{x^2}$$

$$\mathbf{W}[u_1(x, s), u_2(x, s)] = -\frac{E(s)F(s)}{x^{2p+1}}$$
(3.32)

Thus, in Equation 3.23 the particular solution is

$$\hat{T}_{3,p}(r, s) = u_1(r, s)C_1(r, s) + u_2(r, s)C_2(r, s)$$
(3.33)

The functions $u_1(r, s)$ and $u_2(r, s)$ are the independent homogeneous solutions defined in Equation 3.24,

$$u_1(r, s) = E(s) \frac{\mathbf{I}_p(r\sqrt{s\beta_r})}{r^p}$$

$$u_2(r, s) = F(s) \frac{\mathbf{K}_p(r\sqrt{s\beta_r})}{r^p}$$
(3.34)

It is noted that the limits of integration in Equation 3.31 may be arbitrarily selected, [106]. For mathematical convenience, the integration is taken from r_w to r , the domain of Region 3, where $r_w \leq r \leq r_e$.

Explicit expressions for $u_1(r, s) \cdot C_1(r, s)$ and $u_2(r, s) \cdot C_2(r, s)$ are now derived. This requires that the following integral expressions are solved:

$$u_1(r, s) \cdot C_1(r, s) = -\frac{I_p(r\sqrt{s\beta_r})}{r^p} \left\{ \frac{\gamma_b}{s} \int_{r_w}^r \frac{K_p(x\sqrt{s\beta_r})}{x^{1-p}} dx + \beta_r T_0 \int_{r_w}^r \frac{K_p(x\sqrt{s\beta_r})}{x^{1+p}} dx \right\} \quad (3.35)$$

$$u_2(r, s) \cdot C_2(r, s) = \frac{K_p(r\sqrt{s\beta_r})}{r^p} \left\{ \frac{\gamma_b}{s} \int_{r_w}^r \frac{I_p(x\sqrt{s\beta_r})}{x^{1-p}} dx + \beta_r T_0 \int_{r_w}^r \frac{I_p(x\sqrt{s\beta_r})}{x^{1+p}} dx \right\} \quad (3.36)$$

It is convenient to break the particular solution $\hat{T}_{3,p}(r, s)$ into two parts.

$$\hat{T}_{3,p}(r, s) = \hat{T}_{3,p1}(r, s) + \hat{T}_{3,p2}(r, s) \quad (3.37)$$

where $\hat{T}_{3,p1}(r, s)$ contains the $\beta_r T_0$ term and $\hat{T}_{3,p2}(r, s)$ contains the $\frac{\gamma_b}{s}$ term.

First, consider the expressions in Equations 3.35 and 3.36, which have the $\beta_r T_0$ term and obtain an explicit equation for $\hat{T}_{3,p1}(r, s)$. These expressions can be integrated using the following identities,

$$\int x^{p+1} I_p(\alpha x) dx = \frac{1}{\alpha} x^{p+1} I_{p+1}(\alpha x) \quad (3.38)$$

$$\int x^{p+1} K_p(\alpha x) dx = -\frac{1}{\alpha} x^{p+1} K_{p+1}(\alpha x), p \neq 0, \text{ integer} \quad (3.39)$$

Thus,

$$\beta_r T_0 \int_{r_w}^r \frac{\mathbf{K}_p(x\sqrt{s\beta_r})}{x^{1+p}} dx = -\frac{\beta_r T_0}{r\sqrt{s\beta_r}} r_w^{p+1} \mathbf{I}_p(r\sqrt{s\beta_r}) \mathbf{K}_{p+1}(r_w\sqrt{s\beta_r}) + \frac{1}{2} \frac{T_0}{s} \quad (3.40)$$

and

$$\beta_r T_0 \int_{r_w}^r \frac{\mathbf{I}_p(x\sqrt{s\beta_r})}{x^{1+p}} dx = -\frac{\beta_r T_0}{r\sqrt{s\beta_r}} r_w^{p+1} \mathbf{K}_p(r\sqrt{s\beta_r}) \mathbf{I}_{p+1}(r_w\sqrt{s\beta_r}) + \frac{1}{2} \frac{T_0}{s} \quad (3.41)$$

These terms are added together to give

$$\hat{T}_{3,p1}(r, s) = -\frac{\beta_r T_0}{r\sqrt{s\beta_r}} r_w^{p+1} \left\{ \mathbf{I}_p(r\sqrt{s\beta_r}) \mathbf{K}_{p+1}(r_w\sqrt{s\beta_r}) + \mathbf{K}_p(r\sqrt{s\beta_r}) \mathbf{I}_{p+1}(r_w\sqrt{s\beta_r}) \right\} + \frac{T_0}{s} \quad (3.42)$$

The derivative of Equation 3.42 will be required in subsequent calculations and is presented now:

$$\frac{d\hat{T}_{3,p1}(r, s)}{dr} = -\beta_r T_0 \frac{r_w^{p+1}}{r^p} \left\{ \mathbf{I}_{p+1}(r\sqrt{s\beta_r}) \mathbf{K}_{p+1}(r_w\sqrt{s\beta_r}) - \mathbf{K}_{p+1}(r\sqrt{s\beta_r}) \mathbf{I}_{p+1}(r_w\sqrt{s\beta_r}) \right\} \quad (3.43)$$

There are no direct analytical solutions for the other integral terms in Equations 3.35 and 3.36. The series representation of the modified Bessel function of the first kind,

$$\mathbf{I}_p(z) = \sum_{k=0}^{\infty} \frac{(z)^{2k+p}}{2^{2k+p} k! \Gamma(k+p+1)} \quad (3.44)$$

and the identity

$$\mathbf{K}_p(z) = \frac{\pi}{2} \frac{\mathbf{I}_{-p}(z) - \mathbf{I}_p(z)}{\sin(p\pi)} \quad (3.45)$$

are therefore used and integrated term by term. The result of this approach is

$$\begin{aligned}
& - \frac{\mathbf{I}_p(r\sqrt{s\beta_r})}{r^p} \frac{\gamma_b}{s} \int_{r_w}^r \frac{\mathbf{K}_p(x\sqrt{s\beta_r})}{x^{1-p}} dx = \\
& - \frac{\gamma_b \pi \mathbf{I}_p(r\sqrt{s\beta_r})}{2s \sin(p\pi)} \cdot \left(\frac{2}{r\sqrt{s\beta_r}} \right)^p \left\{ \frac{\ln\left(\frac{r}{r_w}\right)}{\Gamma(1-p)} + \right. \\
& \quad \sum_{k=1}^{\infty} \frac{(r\sqrt{s\beta_r})^{2k} - (r_w\sqrt{s\beta_r})^{2k}}{2k \cdot k! \cdot \Gamma(k-p+1)} \frac{1}{2^{2k}} - \\
& \quad \left. \sum_{k=0}^{\infty} \frac{(r\sqrt{s\beta_r})^{2k+2p} - (r_w\sqrt{s\beta_r})^{2k+2p}}{2^{2k+2p+1} (k+p) k! \Gamma(k+p+1)} \right\} \quad (3.46)
\end{aligned}$$

and,

$$\begin{aligned}
& \frac{\mathbf{K}_p(r\sqrt{s\beta_r})}{r^p} \frac{\gamma_b}{s} \int_{r_w}^r \frac{\mathbf{I}_p(x\sqrt{s\beta_r})}{x^{1-p}} dx = \\
& \quad \frac{\gamma_b \mathbf{K}_p(r\sqrt{s\beta_r})}{s} \left(\frac{2}{r\sqrt{s\beta_r}} \right)^p \\
& \quad \sum_{k=0}^{\infty} \frac{(r\sqrt{s\beta_r})^{2k+2p} - (r_w\sqrt{s\beta_r})^{2k+2p}}{2(k+p) \cdot k! \cdot \Gamma(k+p+1)} \frac{1}{2^{2k+2p}} \quad (3.47)
\end{aligned}$$

where for convenience $\gamma_b = \frac{\rho_r I_t^2}{4\pi^2 l^2} \frac{1}{\lambda_r}$.

It is noted that in using this approach, the following identity for the modified Bessel function of the second kind of real order p ,

$$\mathbf{K}_p(z) = \frac{\pi}{2} \frac{\mathbf{I}_{-p}(z) - \mathbf{I}_p(z)}{\sin(p\pi)} \quad (3.48)$$

requires that p is non-zero and cannot be a positive integer.

The solution to Equation 3.22, the Laplace transform of the heat transfer model with conduction, convection, and electrical heating in the reservoir is therefore,

$$\begin{aligned}
\hat{T}_3(r, s) = & E(s) \frac{\mathbf{I}_p(r\sqrt{s\beta_r})}{r^p} + F(s) \frac{\mathbf{K}_p(r\sqrt{s\beta_r})}{r^p} + \frac{T_0}{s} - \\
& \frac{\gamma_b \pi \mathbf{I}_p(r\sqrt{s\beta_r})}{2s \sin(p\pi)} \cdot \left(\frac{2}{r\sqrt{s\beta_r}} \right)^p \left\{ \frac{\ln\left(\frac{r}{r_w}\right)}{\Gamma(1-p)} + \right. \\
& \left. \sum_{k=1}^{\infty} \frac{(r\sqrt{s\beta_r})^{2k} - (r_w\sqrt{s\beta_r})^{2k}}{2k \cdot k! \cdot \Gamma(k-p+1)} \frac{1}{2^{2k}} - \sum_{k=0}^{\infty} \frac{(r\sqrt{s\beta_r})^{2k+2p} - (r_w\sqrt{s\beta_r})^{2k+2p}}{2^{2k+2p+1} (k+p)k! \Gamma(k+p+1)} \right\} + \\
& \frac{\gamma_b}{s} \mathbf{K}_p(r\sqrt{s\beta_r}) \left(\frac{2}{r\sqrt{s\beta_r}} \right)^p \sum_{k=0}^{\infty} \frac{(r\sqrt{s\beta_r})^{2k+2p} - (r_w\sqrt{s\beta_r})^{2k+2p}}{2(k+p) \cdot k! \cdot \Gamma(k+p+1)} \frac{1}{2^{2k+2p}} \\
& - \frac{\beta_r T_0}{r\sqrt{s\beta_r}} r_w^{p+1} \left\{ \mathbf{I}_p(r\sqrt{s\beta_r}) \mathbf{K}_{p+1}(r_w\sqrt{s\beta_r}) + \right. \\
& \left. \mathbf{K}_p(r\sqrt{s\beta_r}) \mathbf{I}_{p+1}(r_w\sqrt{s\beta_r}) \right\} + \frac{T_0}{s} \quad (3.49)
\end{aligned}$$

The unknown coefficients $E(s)$ and $F(s)$ will be obtained by matching boundary conditions, and will be functions of the axial coordinate z . To obtain these coefficients it will be necessary to have an expression for the derivative of Equation 3.49. Again, the series representation of the Bessel functions is used and the derivative on a term by term basis is evaluated so that,

$$\begin{aligned}
\frac{d\hat{T}_p(r, s)}{dr} = & \frac{\gamma_b}{s} \left(\frac{2}{r\sqrt{s\beta_r}} \right)^p \left[\frac{-\pi\sqrt{s\beta_r} \mathbf{I}_{p+1}(r\sqrt{s\beta_r})}{2 \sin(p\pi)} \left\{ \frac{\ln\left(\frac{r}{r_w}\right)}{\Gamma(1-p)} + \right. \right. \\
& \left. \left. \sum_{k=1}^{\infty} + \frac{(r\sqrt{s\beta_r})^{2k} - (r_w\sqrt{s\beta_r})^{2k}}{2^{2k+1} k k! \Gamma(k-p+1)} - \sum_{k=0}^{\infty} \frac{(r\sqrt{s\beta_r})^{2k+2p} - (r_w\sqrt{s\beta_r})^{2k+2p}}{2^{2k+2p+1} (k+p)k! \Gamma(k+p+1)} \right\} + \right. \\
& \left. \sqrt{s\beta_r} \mathbf{K}_{p+1}(r\sqrt{s\beta_r}) \sum_{k=0}^{\infty} \frac{(r\sqrt{s\beta_r})^{2k+2p} - (r_w\sqrt{s\beta_r})^{2k+2p}}{2^{2k+2p+1} (k+p)k! \Gamma(k+p+1)} \right] + \\
& \beta_r T_0 \frac{r_w^{p+1}}{r^p} \left\{ \mathbf{I}_{p+1}(r\sqrt{s\beta_r}) \mathbf{K}_{p+1}(r_w\sqrt{s\beta_r}) - \right. \\
& \left. \mathbf{K}_{p+1}(r\sqrt{s\beta_r}) \mathbf{I}_{p+1}(r_w\sqrt{s\beta_r}) \right\} \quad (3.50)
\end{aligned}$$

Up to this point, *Steps 1 to 3* in the solution procedure are completed for all the regions. Remaining are *Step 4*, the determination of the unspecified coefficients from the boundary conditions and *Step 5*, the numerical inversion of the final Laplace transform.

3.2.4 Determination of unknown coefficients from the boundary conditions

In this section, the unknown coefficients, $A(s)$, $B(s)$, $C(s)$, $D(s)$, $E(s)$ and $F(s)$ are determined from the boundary conditions applied at $r = r_i$, $r = r_w$, and $r = r_e$. This is *Step 4* of the solution process. For reference please note that $r = r_i$ is the inside radius of the casing, $r = r_w$ is the outside radius of the casing, and $r = r_e$ is the external radius of the problem domain.

The temperature distribution is assumed to be continuous at all the boundaries and the following Dirichlet boundary conditions are valid,

$$\hat{T}_1(r_i, s) = \hat{T}_2(r_i, s) \quad \hat{T}_2(r_w, s) = \hat{T}_3(r_w, s) \quad (3.51)$$

Furthermore, the heat flux across the boundaries is also assumed to be continuous and the following Neumann boundary conditions apply,

$$\begin{aligned} \lambda_f \frac{d\hat{T}_1(r, s)}{dr} \Big|_{r=r_i} &= \lambda_s \frac{d\hat{T}_2(r, s)}{dr} \Big|_{r=r_i} \\ \lambda_s \frac{d\hat{T}_2(r, s)}{dr} \Big|_{r=r_w} &= \lambda_r \frac{d\hat{T}_3(r, s)}{dr} \Big|_{r=r_w} \end{aligned} \quad (3.52)$$

At the external boundary of the problem, $r = r_e$, there are two choices for the boundary condition. In one case, the heat flux at the boundary is set to zero and in the other case, the temperature is fixed to the initial reservoir temperature. These are stated as follows:

$$\begin{aligned} \lambda_r \frac{d\hat{T}_3(r, s)}{dr} \Big|_{r=r_e} &= 0 \\ \hat{T}_3(r_e, s) &= \frac{T_0}{s} \end{aligned} \quad (3.53)$$

In this thesis the radial semi-analytic model is solved for both of the above conditions so that r_e can be determined. The distance to r_e , which is unknown, is assumed to be determined when the two solutions converge. This approach to estimate the boundary of a problem is commonly used in the pressure analysis of oil

and gas wells, [109]. Only the solution for the constant temperature boundary condition is presented.

Since a solution must exist at $r = 0$, $K_0(r\sqrt{s\beta_s})$ must vanish and thus the value of $A(s)$ must equal zero.

Applying these boundary conditions to Equations 3.8, 3.15, and 3.49 results in the following system of linear equations in matrix form. The coefficients $B(s)$ through $F(s)$ can be readily determined using elementary linear algebra techniques.

$$\begin{array}{l}
 \left. \begin{array}{l}
 I_0(r_i\sqrt{s\beta_f}) \quad -I_0(r_i\sqrt{s\beta_s}) \quad -K_0(r_i\sqrt{s\beta_s}) \\
 I_1(r_i\sqrt{s\beta_f}) \quad -\frac{\lambda_r}{\lambda_f}\sqrt{\frac{\beta_r}{\beta_f}}I_1(r_i\sqrt{s\beta_s}) \quad \frac{\lambda_r}{\lambda_f}\sqrt{\frac{\beta_r}{\beta_f}}K_1(r_i\sqrt{s\beta_s}) \\
 0 \quad I_0(r_w\sqrt{s\beta_s}) \quad K_0(r_w\sqrt{s\beta_s}) \\
 0 \quad I_1(r_w\sqrt{s\beta_s}) \quad -K_1(r_w\sqrt{s\beta_s}) \\
 0 \quad 0 \quad 0 \\
 \\
 0 \quad 0 \\
 0 \quad 0 \\
 -\frac{1}{r_w^p}I_p(r_w\sqrt{s\beta_r}) \quad -\frac{1}{r_w^p}K_p(r_w\sqrt{s\beta_r}) \\
 -\frac{1}{r_w^p}\frac{\lambda_r}{\lambda_s}\sqrt{\frac{\beta_r}{\beta_s}}I_{p+1}(r_w\sqrt{s\beta_r}) \quad \frac{1}{r_w^p}\frac{\lambda_r}{\lambda_s}\sqrt{\frac{\beta_r}{\beta_s}}K_{p+1}(r_w\sqrt{s\beta_r}) \\
 \frac{1}{r_e^p}I_p(r_e\sqrt{s\beta_r}) \quad \frac{1}{r_e^p}K_p(r_e\sqrt{s\beta_r})
 \end{array} \right| \\
 \\
 \left(\begin{array}{l}
 B(s) \\
 C(s) \\
 D(s) \\
 E(s) \\
 F(s)
 \end{array} \right) = \left(\begin{array}{l}
 \frac{\dot{q}_2(z)}{s^2\beta_s\lambda_s} \\
 0 \\
 \hat{T}_p(r_w, s) - \frac{\dot{q}_2(z)}{s^2\beta_s\lambda_s} - \frac{T_0}{s} \\
 \frac{1}{\sqrt{s\beta_s}}\frac{\lambda_r}{\lambda_s}\frac{dT_p(r_w, s)}{dr} - \frac{T_0}{s} \\
 -\hat{T}_p(r_e, s)
 \end{array} \right) \quad (3.54)
 \end{array}$$

Equation 3.54 has the form

$$\mathbf{A}_{i,j} \cdot \mathbf{x}_i = \mathbf{B}_i \quad (3.55)$$

where i and j are the row and column index respectively.

The solution vector \mathbf{x}_i is obtained directly from,

$$\mathbf{x}_i = \mathbf{A}_{i,j}^{-1} \cdot \mathbf{B}_i \quad (3.56)$$

The expressions for each component of the vector \mathbf{x} are lengthy and are not presented here. It is important, however, to recognize that $\mathbf{x}_1 = B(s)$, $\mathbf{x}_2 = C(s)$ and so forth. The final solutions for the heat transfer models in each of the regions in Laplace space are obtained by replacing the unknown coefficients in Equations 3.8, 3.15, and 3.49 with the appropriate \mathbf{x}_i obtained from Equation 3.56.

Explicit expressions for the temperature distributions in all three regions have been derived. These solutions are all in Laplace space and must be inverted into the time domain as a final step in the solution procedure. These expressions are too complex for an analytic inversion into the time domain. Thus a numerical approach using the *Stehfest Inversion Algorithm* [101] is used to obtain the final time domain solution.

3.3 Validation of the Radial Semi-analytic Model

In this section, calculations obtained using the radial semi-analytic model are compared to

1. The *Killough and Gonzalez* analytic model, Reference [3],
2. A semi-analytic model that accounts for all the heat transfer mechanisms of the radial semi-analytic model, except for convection heat transfer and electrical heating in the reservoir, (this model is called the *conduction* semi-analytic model for convenience), and
3. Numerical simulation.

These comparisons are used to validate the radial semi-analytic model.

The computer program *TETRAD* is used for the numerical simulation validation, the last one of the three validations enumerated above. *TETRAD* is commercial numerical model that is commonly used by oil and gas companies to

model reservoir processes. More information on *TETRAD* can be obtained from References [82], [110], and [111].

3.3.1 *Base Case* data set

The data used for defining the *Base Case*, i.e. the standard case used in all of the three comparisons, are obtained from the public record [112]. An effort was made to use data that was representative of a Sparky oil formation in the Frog Lake area of North Eastern Alberta [77]. The various data for the *Base Case*, presented with the units used in the numerical simulator *TETRAD*, are summarized in Tables 3.2, 3.3, 3.4, and 3.9.

Data	Symbol	Value	Units
Thickness	h_t	5.0	m
Oil Saturation	S_o	0.75	
Water Saturation	S_w	0.25	
Initial Temperature	T_o	20	$^{\circ}C$
Oil Gravity	$^{\circ}API$	12	
Permeability	k	5000	md
Porosity	ϕ	0.30	<i>fraction</i>
Reservoir resistivity	ρ_r	40.00	$\Omega \cdot m$

Table 3.1: *Base Case* reservoir data.

In addition to these data, the electrical resistivity of the steel casing as a function of the *RMS* current was fitted to a third order polynomial whose coefficients are given in Equation 2.68.

3.3.2 Validation using the *Killough and Gonzalez* analytic model

The purpose of this validation is to determine if the temperature distribution in the reservoir calculated using the radial semi-analytic model and resulting from the heat transfer problem consisting of electrical heating and heat transfer by only

Component	Symbol	Thermal Conductivity	
		$\frac{W}{m^{\circ}C}$	$\frac{KJ}{m^{\circ}C Day}$
Oil	λ_o	0.14	12.00
Water	λ_w	0.67	57.96
Rock	λ_r	2.80	241.85
Steel casing	λ_q	50.00	4320.00
Fluid	λ_f	0.27	23.49
Reservoir	λ_r	2.04	176.34

Table 3.2: *Base Case* thermal conductivity.

Component	Symbol	Heat Capacity	
		$\frac{MJ}{m^3 \cdot ^{\circ}C}$	$\frac{KJ}{m^3 \cdot ^{\circ}C}$
Oil	$\rho_o C_o$	2.40	2400
Water	$\rho_w C_w$	4.05	4050
Rock	$\rho_q C_q$	2.21	2210
Steel casing	$\rho_s C_s$	3.56	3560
Fluid	$\rho_f C_f$	2.81	2810
Reservoir	$\rho_r C_r$	2.40	2400

Table 3.3: *Base Case* heat capacity (oil gravity of 12 °API)

convection compares to the results calculated using a fully analytic model specifically developed to solve that type of problem.

The *Killough and Gonzalez* analytic model was developed to validate a fully-implicit numerical model for electrically enhanced oil recovery developed by *Killough and Gonzalez*, Reference [3]. The analytic model takes into account heat transfer by convection and electrical heating in a single cylindrically symmetric region consisting of the reservoir and calculates the temperature distribution as a function of time and radius from the wellbore. The model assumes a constant voltage at the wellbore and zero voltage at r_e . The *Killough and Gonzalez* analytic model does not take into account heat transfer in the reservoir by thermal conduction or heat losses in the casing resulting from hysteresis and eddy current

Data	Symbol	Value	Units
Total current	I_t	500 to 1000	<i>A RMS</i>
Fluid production rate	Q_t	5 to 50	m^3/day
Produced Water cut	W_{cut}	0.25	<i>fraction</i>
Inner radius of steel casing	r_i	8.3185	<i>cm</i>
Outer radius of steel casing	r_w	8.9345	<i>cm</i>
Horizontal Well Length	l	100 or 1000	<i>m</i>

Table 3.4: *Base Case* operating data

losses. It is, however, a suitable model for situations where heat transfer by convection is the dominating heat transfer mechanism and the losses in the casing (electrode) can be ignored. This may be the case for short vertical wells but not for long horizontal wells where the heat transfer problem in the casing and wellbore is significant. Constant electrical properties are assumed. For a detailed mathematical development of the *Killough and Gonzalez* analytic model refer to Reference [3] or [73].

Assuming heat transfer by only convection in the reservoir and electrical heating in the reservoir results in the following energy equation:

$$\rho C_r \frac{\partial T_3}{\partial t} - \frac{\rho C_r Q_t}{2\pi l} \frac{\partial T_3}{\partial t} = \rho \frac{I_t^2}{4\pi^2 l^2} \frac{1}{r^2} \quad (3.57)$$

The following constants are defined,

$$\begin{aligned} c_1 &= \frac{Q_t \rho C_f}{2\pi l \rho C_r} \\ c_2 &= \frac{\rho}{\rho C_r} \frac{I_t^2}{4\pi^2 l^2} \end{aligned} \quad (3.58)$$

and the solution to Equation 3.57 is given by the following,

$$T_3(r, t) = T^*(r, t) + \frac{c_2}{c_1} \ln\left(\frac{r_e}{r}\right) + T_0 \quad (3.59)$$

where,

$$T^*(r, t) = \begin{cases} -\frac{c_2}{c_1} \ln \left(\frac{r_e}{\sqrt{r^2 + 2c_1 t}} \right) & \text{for } r \leq \sqrt{r_e^2 - 2c_1 t} \\ 0 & \text{for } r > \sqrt{r_e^2 - 2c_1 t} \end{cases} \quad (3.60)$$

The input data used in the radial semi-analytic model are selected so that the assumptions from the *Killough and Gonzalez* model are approximated. The length of the electrode, l , and fluid production rate, Q_t , are chosen so that heat transfer by conduction can be neglected. In the first case

$$\alpha_r = 1 + \frac{\rho C_f Q_t}{2\lambda_r \pi l}$$

is set to 3.5361 and then increased to 6.0722 for the second comparison. As a practical matter, for $\alpha_r \geq 2.0$, heat transfer by conduction can usually be neglected and heat transfer by convection is the dominant heat transfer mechanism [107]. The electrical properties of the steel casing are chosen so that there is no heat produced in the casing, effectively creating a single region model. These data are summarized in Table 3.5.

Figure 3.3 shows a comparison of the temperature distribution in the reservoir obtained with the *Killough and Gonzalez* model with results obtained from the radial semi-analytic model, which is the numerical inversion of Equation 3.49. The maximum difference between the calculated temperatures at any value of the radius after 30 days of heating is 4.6%, indicating good agreement between the two models.

Although the input data for the radial semi-analytic model were selected so that convection was the dominant heat transfer mechanism, Figure 3.3 shows a minor amount of heat transfer by conduction calculated with the radial semi-analytic model. This is indicated by the invasion of heat further into the reservoir. As the temperature gradient decreases at a greater distance away from the well, heat transfer by conduction also decreases.

For *Case 2* the flow rate, Q_t , is doubled causing the value of α_r to increase to 6.07. The larger value of α_r reduces the importance of conduction as a heat transfer mechanism and thus the two models should more closely match in the calculation of

Data	Symbol	Case 1	Case 2	Units
Total current	I_t	85.27	120.75	A
Fluid production rate	Q_t	10.00	20.00	m^3/day
Heating time	t	30.00	30.00	days
Produced Water cut	W_{cut}	0.25	0.25	fraction
Outer radius of steel casing	r_w	8.9345	8.9345	cm
Exterior Radius	r_e	$100 r_w$	$100 r_w$	cm
Electrode Length	l	10.00	10.00	m
Resistivity of the casing	ρ_s	small	small	$\Omega \cdot m$
$1 + \frac{\rho C_f Q_t}{2\lambda_r \pi l}$	α_r	3.53610	6.07220	
$\frac{1}{2} \sqrt{(1 - \alpha_r)^2}$	p	1.26805	2.53610	

Table 3.5: Operating data for validation of the radial semi-analytic model using the *Killough and Gonzalez* model.

the temperature distribution. These results are shown in Figure 3.4. The maximum difference between the calculations of the temperature at any value of the radius after 30 days of heating, as shown in Figure 3.4 has decreased to 3.7%.

3.3.3 Validation using the *Conduction* model

The *Conduction* model is a reduced form of the radial semi-analytic model. The *Conduction* model does not take into account electrical heating in the reservoir or heat transfer by convection in the reservoir as does the radial semi-analytic model. Otherwise, the *Conduction* model is developed in exactly the same way as the radial semi-analytic model.

The purpose of this validation is to determine if the radial semi-analytic model *reduces* to the much simpler problem of heat transfer in the reservoir with only thermal conduction. With heat transfer by conduction in the reservoir the following heat transfer model applies

$$\lambda_r \frac{\partial^2 T_3}{\partial r^2} + \frac{\lambda_r}{r} \frac{\partial T_3}{\partial r} = \rho C_r \frac{\partial T_3}{\partial t} \quad (3.61)$$

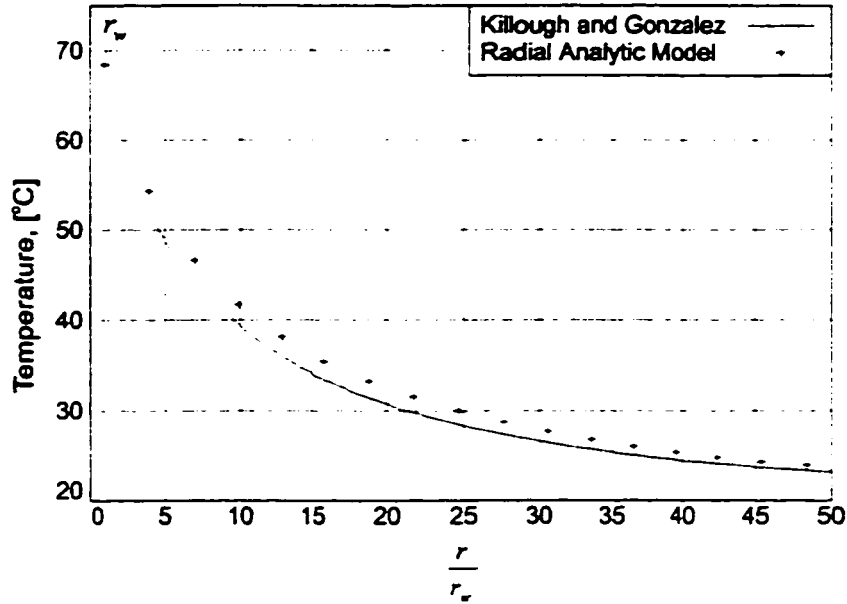


Figure 3.3: Comparison of the temperature distribution obtained from the radial semi-analytic model to results obtained from the *Killough and Gonzalez* model, [3] for $\alpha_r = 3.54$.

The Laplace transform of this equation is

$$\frac{d^2 \hat{T}_3}{dr^2} + \frac{1}{r} \frac{d\hat{T}_3}{dr} - s\beta_r \hat{T}_3 = -\beta_r T_0 \quad (3.62)$$

and has the following solution,

$$\hat{T}_3(r, s) = E(s)I_0(r\sqrt{s\beta_r}) + F(s)K_0(r\sqrt{s\beta_r}) \quad (3.63)$$

The temperature distribution with the isolated mechanism of thermal conduction is obtained following the same procedure that was used to solve the radial semi-analytic model, except that Equation 3.49 is replaced with 3.63.

The input data for the radial semi-analytic model are selected so that the assumptions for heat transfer by the isolated mechanism of thermal conduction in the reservoir is closely approximated. Current flows just in the casing and creates the only source of heating in the problem. The input data is selected so that α_r in Equation 3.49 is close to unity and thus eliminates convection as an important heat transfer mechanism. It is noted that α_r *cannot* be unity because of various limitations imposed on the series representation of the Bessel functions. The

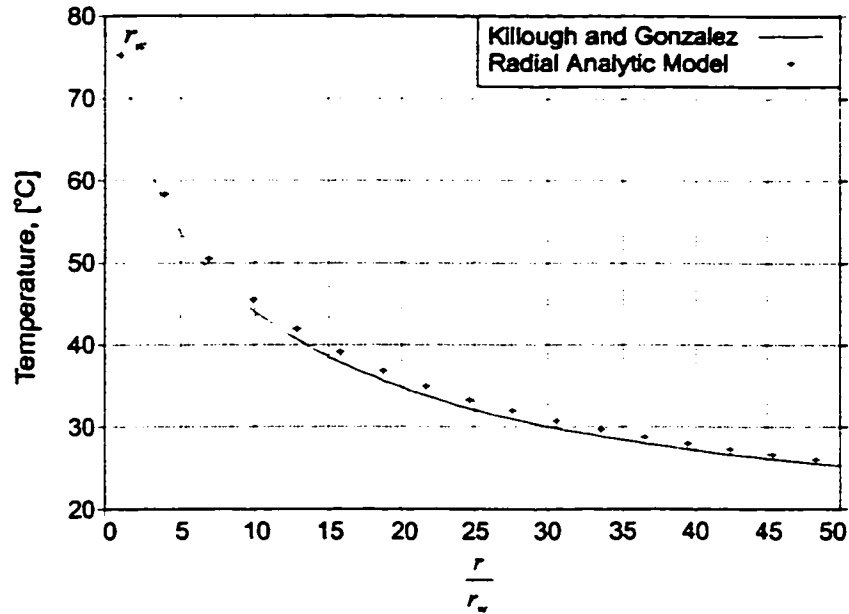


Figure 3.4: Comparison of the temperature distribution obtained from the radial semi-analytic model to results obtained from the *Killough and Gonzalez* model, [3] for $\alpha_r = 6.07$.

electrical resistivity of the reservoir is set to a small value so that electrical heating approaches zero.

An additional comparison between the models is made where α_r is increased by increasing the fluid production rate Q_t , so that the effects of convection can be observed when comparing the *Conduction* model to the radial semi-analytic model. The *Conduction* model cannot account for convection so the comparison is useful only to determine if the effects of convection are being modeled in the radial semi-analytic model. The input data for these comparisons are summarized in Table 3.6. *Case 1* has no convection and *Case 2* has some convection. There is no electrical heating in the reservoir in either of the two cases.

A comparison of the temperature distribution in the reservoir calculated using the *Conduction* model and the radial semi-analytic model is shown in Figure 3.5. The maximum percent difference between the calculations of the temperature at any radius using the input data defined for *Case 1* is less than 2.0 %.

Figure 3.6 shows plots of the temperature distribution calculated using the *Conduction* model and the radial semi-analytic model for the input data defined for *Case 1*. These plots show the temperature distribution in all of the three regions for

Data	Symbol	Case 1	Case 2	Units
Total current (Region 2)	I_t	750.00	750.00	A
Fluid production rate	Q_t	2.00	20.00	m^3/day
Heating time	t	30.00	30.00	$days$
Produced Water cut	W_{cut}	.25	.25	$fraction$
Outer radius of steel casing	r_w	8.9345	8.9345	cm
Exterior Radius	r_e	$100 r_w$	$100 r_w$	cm
Electrode Length	L	100.00	100.00	m
Resistivity of the casing	ρ_s	Eq. 2.66	Eq. 2.66	$\Omega \cdot m$
Resistivity of the reservoir	ρ_r	1.00	1.00	$\Omega \cdot m$
$1 + \frac{\rho C_f Q_t}{2\lambda_r \pi l}$	α_r	1.05072	1.50722	
$\frac{1}{2} \sqrt{(1 - \alpha_r)^2}$	p	0.02536	0.71219	

Table 3.6: Operating data for comparison to the *Conduction* model.

radii defined by $0 \leq r \leq 2r_w$. There is good agreement between the two calculations in all three regions. It is noted that for no axial fluid flow in the wellbore, the change in temperature with radial position in both the wellbore and casing is small.

Figure 3.7 shows the calculation of the temperature distribution in the reservoir with convection as calculated with the radial semi-analytic model and compares these results to the case with only heat transfer by conduction in the reservoir as calculated with the *Conduction* model. As expected, the production of fluids from the reservoir, and thus heat transfer by convection resulting in the removal of energy from the reservoir, reduces the distance that heat penetrates away from the wellbore.

3.3.4 Validation of the radial semi-analytic model using *TETRAD*

The temperature distributions obtained using the radial semi-analytic model are compared to the temperature distribution calculated from numerical simulation using a computer program called *TETRAD*. The purpose of this comparison is to

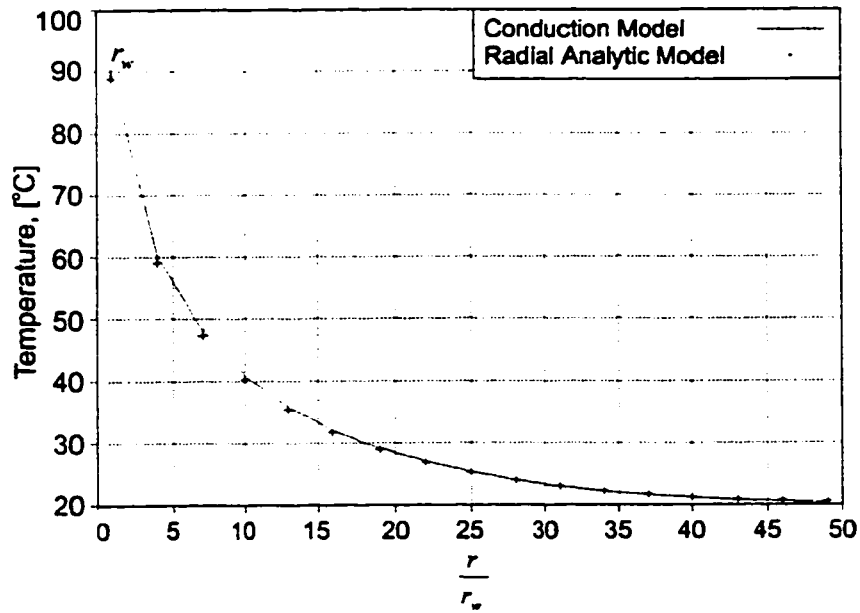


Figure 3.5: Comparison of the temperature distribution obtained from Equation 3.49 to results obtained from the *Conduction* model for $r > r_w$ and $\alpha_r = 1.05$.

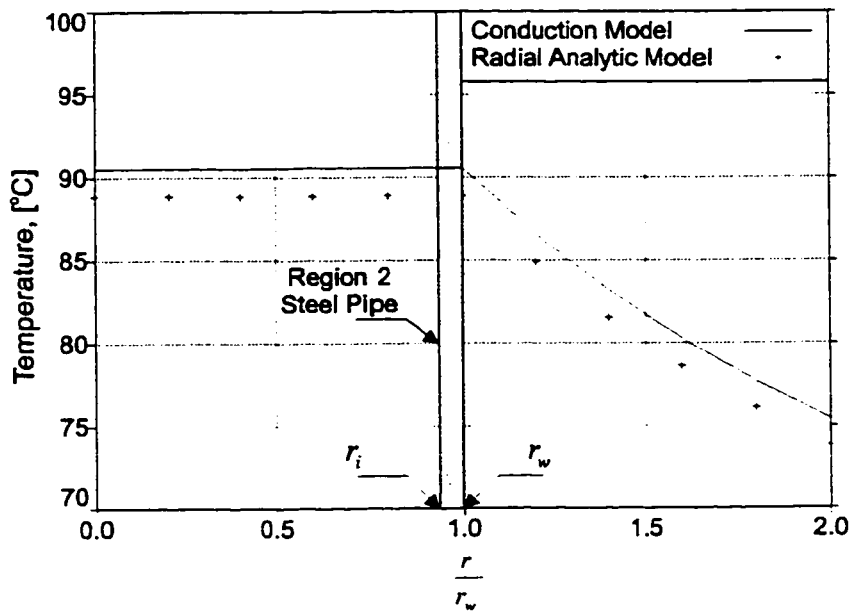


Figure 3.6: Comparison of the temperature distribution obtained from Equation 3.49 to results obtained from the *Conduction* model for $0 \leq r \leq 2r_w$.

demonstrate that the radial semi-analytic model agrees with the numerical simulation program for the condition where all heat transfer mechanisms are present in the reservoir.

The input data is the same as for *Case 2* of the previous validation with the

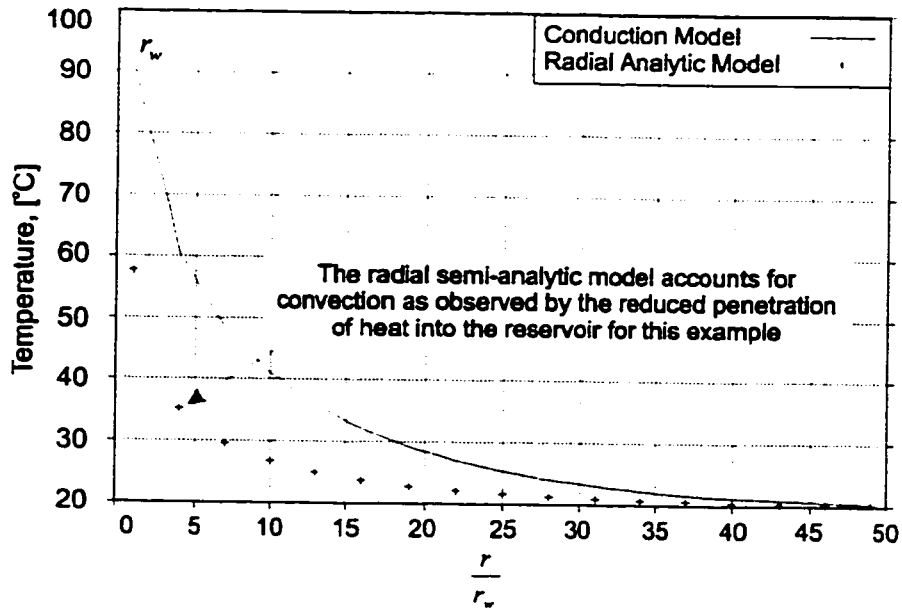


Figure 3.7: Comparison of the temperature distribution obtained from Equation 3.49 to results obtained from the *Conduction Model* with convection ($\alpha_r = 1.51$).

resistivity of the reservoir set to $\rho_r = 40 \Omega \cdot m$. The current is limited to 500 A *RMS* so that the temperature at the wellbore does not exceed 100 °C.

The grid used to model the problem domain using *TETRAD* is shown in Figure 3.8. The results obtained by using the radial semi-analytic and *TETRAD* are shown in Figure 3.9. The maximum difference between the results obtained is less than 1.0 %, indicating very good agreement between the radial semi-analytic model and *TETRAD*. Further detailed comparisons between the semi-analytic models and numerical calculations are presented in a later section of this thesis.

In this section, several validations of the radial semi-analytic model have been presented. Calculations of the temperature distribution obtained using the radial semi-analytic model compare favourably to the calculations made using the *Killough and Gonzalez* analytic model, the *Conduction* model and numerical calculations obtained using *TETRAD*. The next sections in this Chapter are dedicated to the development of the axial semi-analytic model. Much of the development of the radial semi-analytic model is incorporated into the development of the axial model as previously discussed.

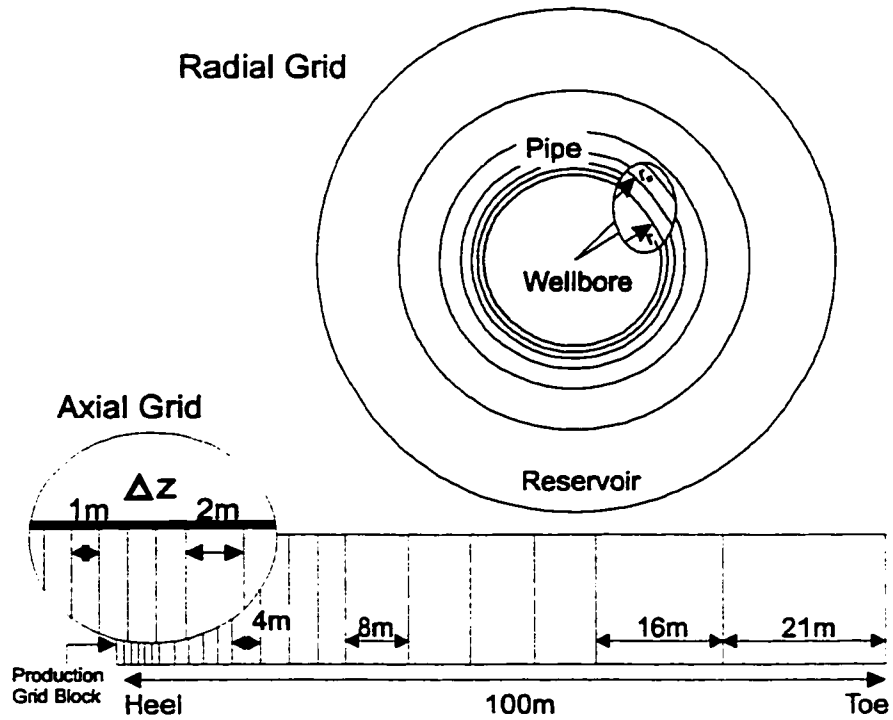


Figure 3.8: Grid used for numerical validation of the radial semi-analytic model.

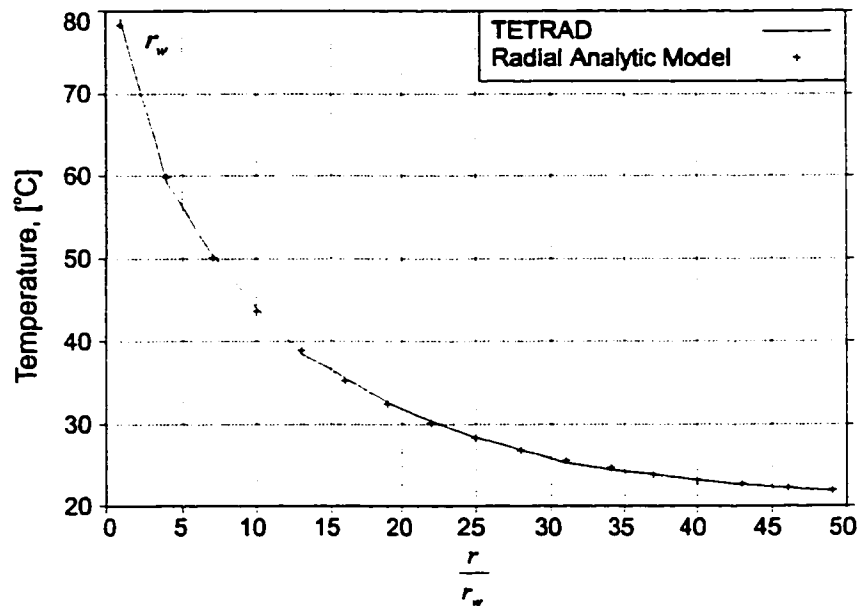


Figure 3.9: Comparison of the temperature distribution in the reservoir obtained from Equation 3.49 to results obtained from *TETRAD* with $\alpha_r = 1.51$.

3.4 The Axial Semi-Analytic Model

In this section the axial semi-analytic model is derived. The mathematical derivation of the axial model incorporates the radial model derived in the previous section. The radial model is mathematically decoupled from the axial heat transfer problem using a heat flow boundary condition between the wellbore and the casing as shown in Figure 3.2 and described in detail Sections 3.1.2 and 3.4.1.

The process followed to derive the axial semi-analytic model is similar to the process previously used to obtain the radial model. The approach is to:

1. Determine the partial differential equation that defines the heat transfer problem in the wellbore.
2. Define the heat flow into the wellbore from the casing in terms of the radial semi-analytic model.
3. Obtain the Laplace transform of the heat transfer model in the wellbore. In this step, the partial differential equations obtained in *Step 1* and *Step 2* are transformed into ordinary differential equations.
4. Solve the ordinary differential equations obtained in *Step 3*.
5. Using the boundary condition of the problem, solve for the unknown coefficient $G(s)$ (whose meaning will be made clear in the work that follows) to obtain a solution in Laplace space.
6. Obtain the axial temperature distribution in the time domain by numerical inversion of the Laplace transforms obtained in *Step 5* using the *Stehfest Inversion Algorithm*.

Using this approach a 2D problem is reduced to two 1D problems, one in the radial coordinate system, and the other in the axial direction, the latter of which is solved in this section.

3.4.1 The axial heat transfer problem in the wellbore

The heat transfer problem for the wellbore is solved in this section resulting in an equation that can be used to calculate the axial temperature distribution along

the length of the horizontal well. The following assumptions are necessary to proceed with the axial semi-analytic solution to the problem:

1. The temperature distribution in the radial direction from the center of the wellbore at $r = 0$ to the interior radius of the casing at $r = r_i$ does not vary with r . In the *radial* semi-analytic model this situation corresponds to a *constant* temperature in *Region 1*. Thus, the work that follows involves a simplified version of the radial semi-analytic model.
2. Fluid flow is laminar. Thus, heat transfer between the inside surface of the casing and adjacent fluid layers in the wellbore is by thermal conduction, [97].
3. The flow of heat from the casing into the wellbore is determined by the radial temperature gradient in the casing and is defined by Fourier's law of conduction between the two regions.
4. Heat transfer in the axial direction is by convection only.
5. The production of fluids from the reservoir into the wellbore is uniform along the length of the horizontal well.
6. The fluid production rate and electrical current are constant with time.
7. The thermal and electrical properties are independent of temperature in all the regions.

The development of the mathematical model to describe temperature as a function of the axial direction follows Welty *et. al.*, page 346, Reference [97]. Figure 3.10 shows a control volume in the wellbore where the first law of thermodynamics is applied. This law requires that the net rate of energy flow into the control volume must equal the rate of energy accumulation at any moment in time. An increase in energy in the control volume will result in an increase in temperature.

The first law of thermodynamics applied to the control volume shown in Figure 3.10 is

$$\dot{q}_f \Big|_{z=z-\frac{\Delta z}{2}} - \dot{q}_f \Big|_{z=z+\frac{\Delta z}{2}} + \dot{q}_s \Big|_z = \rho C_f \frac{\partial T_1}{\partial t} A_f \Delta z \quad (3.64)$$

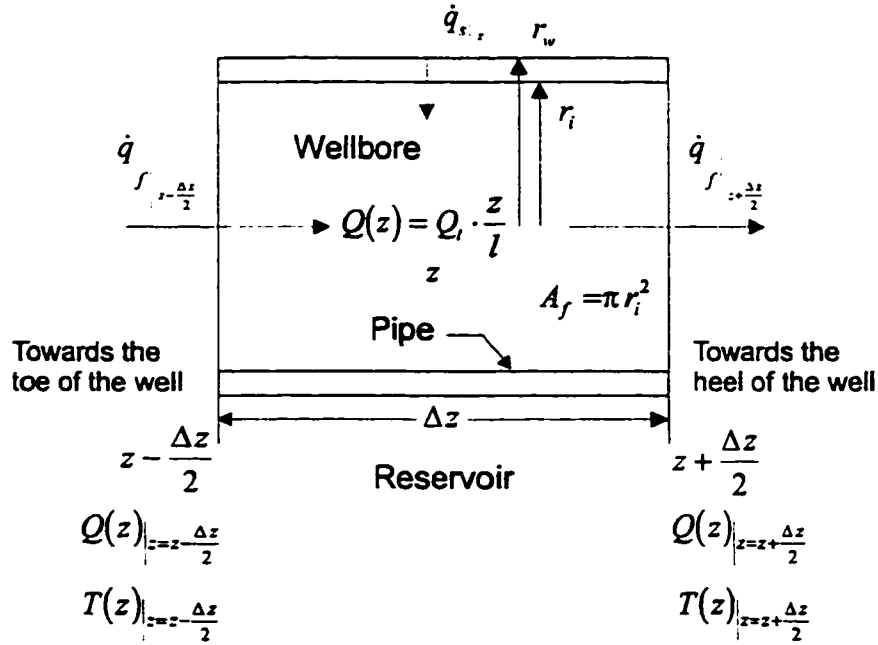


Figure 3.10: An element of the wellbore to describe the heat transfer problem in the wellbore.

where

$$\dot{q}_f \Big|_{z=z-\frac{\Delta z}{2}} = \rho C_f Q(z) T_1(z, t) \Big|_{z=z-\frac{\Delta z}{2}} \quad (3.65)$$

and

$$\dot{q}_f \Big|_{z=z+\frac{\Delta z}{2}} = \rho C_f Q(z) T_1(z, t) \Big|_{z=z+\frac{\Delta z}{2}} \quad (3.66)$$

The total production of fluid at z is $Q(z)$. The heat capacity of the fluid is ρC_f and \dot{q}_s is the heat flow from the casing into the wellbore. The heat transfer mechanism associated with \dot{q}_s is developed forthwith.

One approach to determine the heat flow from the surface of the casing into the wellbore, \dot{q}_s , is to define an *overall heat transfer coefficient* such that, [97],

$$\dot{q}_s = 2\pi U_t r_i \Delta z (T_2(r_i, t) - T_\infty) \quad (3.67)$$

In Equation 3.67 U_t is the *overall heat transfer coefficient* and T_∞ is defined as the temperature of the fluid on the axis of the casing ($r = 0$).

The overall heat transfer coefficient represents the net thermal resistance to the flow of heat from the casing to the wellbore fluids. The determination of U_t is difficult as it is dependent on the mechanism of flow, (laminar or turbulent), the radial temperature gradient in the wellbore, the radial and axial velocity components of fluid flow, the physical properties of the fluids in the wellbore, and the geometry of the problem, [113], [114].

For this problem, the axial velocity of the fluids in the casing increases as the heel of the well is approached. When this effect is combined with the increasing temperature of the casing over time, a U_t results that is a complex function of location and time. Using the *overall heat transfer coefficient* approach to determine the transfer of heat between the casing and the wellbore fluids will render a semi-analytic solution to the problem an impossibility.

Since axial fluid flow in the wellbore is assumed to be laminar, the energy transfer between the surface of the casing and the wellbore fluids will occur by thermal conduction [97]. Under these conditions, the heat transfer rate determined using Equation 3.67 must equal the heat transfer rate by conduction [97]. Applying Fourier's law of thermal conduction at $r = r_i$ results in,

$$2\pi U_t r_i \Delta z (T_2 - T_\infty) = 2\pi r_i \Delta z \lambda_f \left. \frac{\partial T_1}{\partial r} \right|_{r=r_i} \quad (3.68)$$

Equation 3.68 requires that the temperature distribution in the radial direction in the wellbore is known. This necessitates a two-dimensional solution of the heat transfer problem in the wellbore, which would be unattainable given the non-linear heating in the casing due to hysteresis and eddy current losses. However, since the heat flow in the wellbore is essentially axial we approximate the radial heat flow into the wellbore from the casing by using continuity of thermal conduction at the inner surface of the casing,

$$\lambda_s \left. \frac{\partial T_2}{\partial r} \right|_{r=r_i} = \lambda_f \left. \frac{\partial T_1}{\partial r} \right|_{r=r_i} \quad (3.69)$$

The flow of heat from the casing into the wellbore due to thermal conduction alone can then be stated as

$$2\pi r_i \Delta z \lambda_s \frac{\partial T_2}{\partial r} \Big|_{r=r_i} \quad (3.70)$$

Use of Equation 3.69 to replace the radial heat flow into the wellbore at $r = r_i$ by the radial heat flow at $r = r_i$ due to thermal conduction in the casing is the *key step* that is taken to reduce the single two-dimensional problem into two one-dimensional problems. This *decoupling* of the two-dimensional problem makes it possible to solve the two one-dimensional problems using analytic methods.

Fluid also flows into the control volume from the reservoir. Accounting for both the radial flow of heat due to heat transfer by conduction from the casing, (Equation 3.70), and the production of fluids from the reservoir, results in the following expression for the radial heat flow into the control volume,

$$\dot{q}_s \Big|_z = 2\pi r_i \Delta z \lambda_s \frac{\partial T_2}{\partial r} \Big|_{r=r_i} + \rho C_f Q_t \frac{\Delta z}{l} T_2 \Big|_{r=r_i} \quad (3.71)$$

Substituting Equations 3.65, 3.66, and 3.71 into Equation 3.64, dividing through by $A_f \Delta z$ and ρC_f , and taking the limit as Δz goes to zero results in,

$$-\frac{1}{A_f} \frac{\partial \{Q(z)T_1(z, t)\}}{\partial z} = \frac{\partial T_1(z, t)}{\partial t} - 2 \frac{\lambda_s}{\rho C_f r_i} \frac{1}{\partial r} \frac{\partial T_2}{\partial r} \Big|_{r=r_i} - \frac{Q_t}{2\pi r_i l} T_2 \Big|_{r=r_i} \quad (3.72)$$

Expanding the partial derivatives and substituting $Q(z) = Q_t \cdot \frac{z}{l}$ results in the following equation.

$$z \frac{\partial T_1(z, t)}{\partial z} + T_1(z, t) = -\alpha \frac{\partial T_1(z, t)}{\partial t} + \frac{2\alpha \lambda_s}{\rho C_f r_i} \frac{1}{\partial r} \frac{\partial T_2(r, t)}{\partial r} \Big|_{r=r_i} + T_2(r, t) \Big|_{r=r_i} \quad (3.73)$$

where $\alpha = \frac{A_f l}{Q_t}$.

This is the final form of the mathematical model for the heat transfer problem in terms of $T_1(z, t)$ in the wellbore. To solve Equation 3.73 requires explicit

expressions for $T_2(r, t) \Big|_{r=r_i}$ and $2\alpha \frac{\lambda_s}{\rho C_f r_i} \frac{1}{\partial r} \frac{\partial T_2(r, t)}{\partial r} \Big|_{r=r_i}$

To accomplish this task, the solutions for the heat transfer models in the casing and the reservoir are required. These solutions were developed in a previous section, Section 3.2, where no axial flow of fluids was assumed. They are now used in the solution of the axial heat transfer problem.

Using Equation 3.71 to define the heat transfer into the wellbore makes it possible to reduce the single one-dimensional problem into two one-dimensional problems. The next step is to determine $\hat{T}_2(r, s)$ and $\frac{2\alpha\lambda_s}{\rho C_f r_i} \frac{1}{\partial r} \frac{\partial T_2(r, t)}{\partial r} \Big|_{r=r_i}$.

3.4.2 Determination of $\hat{T}_2(r, s)$ and derivative

The unknown coefficients, $C(s)$, $D(s)$, $E(s)$ and $F(s)$ in Equations 3.15 and 3.49 are determined from the boundary conditions applied at $r = r_i$, $r = r_w$, and $r = r_e$. At $r = r_i$ and $r = r_w$ the temperatures must be continuous as stated by the following boundary conditions,

$$\begin{aligned} \hat{T}_2(r_i, s) &= \hat{T}_1(z, s) \\ \hat{T}_2(r_w, s) &= \hat{T}_3(r_w, s) \end{aligned} \quad (3.74)$$

It is emphasized that the temperature distribution in the *wellbore* is assumed not to change in the radial direction. This, as previously mentioned, leads to a simplification of the radial semi-analytic model, which, in turn, makes possible the derivation of the axial temperature distribution.

At $r = r_w$, the heat flux across the boundary must be continuous,

$$\lambda_s \frac{d\hat{T}_2}{dr} \Big|_{r=r_w} = \lambda_r \frac{d\hat{T}_3}{dr} \Big|_{r=r_w} \quad (3.75)$$

At the boundary, $r = r_e$, the temperature is equal to the initial reservoir temperature. Applying these boundary conditions to the Equations 3.8, 3.15, and 3.49 results in the following system of linear equations in matrix form:

$$\begin{vmatrix}
I_0(r_i \sqrt{s\beta_s}) & K_0(r_i \sqrt{s\beta_s}) & 0 & 0 \\
I_0(r_w \sqrt{s\beta_s}) & K_0(r_w \sqrt{s\beta_s}) & -\frac{I_p(r_w \sqrt{s\beta_r})}{r_w^p} & -\frac{K_p(r_w \sqrt{s\beta_r})}{r_w^p} \\
I_1(r_w \sqrt{s\beta_s}) & -K_1(r_w \sqrt{s\beta_s}) & -\frac{\lambda_r}{\lambda_s} \sqrt{\frac{\beta_r}{\beta_s}} \frac{I_{p+1}(r_w \sqrt{s\beta_r})}{r_w^p} & \frac{\lambda_r}{\lambda_s} \sqrt{\frac{\beta_r}{\beta_s}} \frac{K_{p+1}(r_w \sqrt{s\beta_r})}{r_w^p} \\
0 & 0 & \frac{I_p(r_e \sqrt{s\beta_r})}{r_e^p} & \frac{K_p(r_e \sqrt{s\beta_r})}{r_e^p}
\end{vmatrix}
\begin{pmatrix}
C(s) \\
D(s) \\
E(s) \\
F(s)
\end{pmatrix}
=
\begin{pmatrix}
\hat{T}_1(z, s) - \frac{q_2(z)}{s^2 \beta_s \lambda_s} - \frac{T_0}{s} \\
-\frac{q_2(z)}{s^2 \beta_s \lambda_s} - \frac{T_0}{s} \\
\frac{1}{\sqrt{s\beta_s}} \frac{\lambda_r}{\lambda_s} \frac{dT_p(r_w, s)}{dr} \\
-\hat{T}_p(r_e, s)
\end{pmatrix} \quad (3.76)$$

This system of equations is simpler than Equation 3.54 by virtue of the fact that the temperature in the wellbore is no longer a function of the radial coordinate.

Since an expression for the heat flow into the wellbore is necessary to solve Equation 3.73, the coefficients for $\hat{T}_2(r, s)$ must be stated explicitly. It is unnecessary to obtain explicit expressions for $E(s)$ or $F(s)$. The coefficients are obtained from the solution of Equation 3.76 and are,

$$C(s) = g_1(s) \hat{T}_1(z, s) + [g_2(s) - g_1(s)] \left(\sum_{i=0}^k \eta_i(s) z^{i+2} + \frac{T_0}{s} \right) + g_3(s) T_p(r, s) \Big|_{r=r_e} \quad (3.77)$$

$$D(s) = g_4(s) \hat{T}_1(z, s) + [g_5(s) - g_4(s)] \left(\sum_{i=0}^k \eta_i(s) z^{i+2} + \frac{T_0}{s} \right) + g_6(s) T_p(r, s) \Big|_{r=r_e} \quad (3.78)$$

where,

$$\begin{aligned}
g_1(s) = \frac{1}{d(s)} \frac{\mathbf{K}_0(r_w \sqrt{s\beta_s})}{(r_w r_e)^p} \frac{\lambda_r}{\lambda_s} \sqrt{\frac{\beta_r}{\beta_s}} & \left[-\mathbf{I}_{p+1}(r_w \sqrt{s\beta_r}) \mathbf{K}_p(r_e \sqrt{s\beta_r}) - \right. \\
& \left. \mathbf{K}_{p+1}(r_w \sqrt{s\beta_r}) \mathbf{I}_p(r_e \sqrt{s\beta_r}) \right] + \\
\frac{1}{d(s)} \frac{\mathbf{K}_1(r_w \sqrt{s\beta_s})}{(r_w r_e)^p} & \left[-\mathbf{I}_p(r_w \sqrt{s\beta_r}) \mathbf{K}_p(r_e \sqrt{s\beta_r}) + \right. \\
& \left. \mathbf{K}_p(r_w \sqrt{s\beta_r}) \mathbf{I}_p(r_e \sqrt{s\beta_r}) \right] \quad (3.79)
\end{aligned}$$

$$\begin{aligned}
g_2(s) = \frac{1}{d(s)} \frac{\mathbf{K}_0(r_i \sqrt{s\beta_s})}{(r_w r_e)^p} \frac{\lambda_r}{\lambda_s} \sqrt{\frac{\beta_r}{\beta_s}} & \left[-\mathbf{I}_{p+1}(r_w \sqrt{s\beta_r}) \mathbf{K}_p(r_e \sqrt{s\beta_r}) - \right. \\
& \left. \mathbf{K}_{p+1}(r_w \sqrt{s\beta_r}) \mathbf{I}_p(r_e \sqrt{s\beta_r}) \right] \quad (3.80)
\end{aligned}$$

$$\begin{aligned}
g_3(s) = \frac{1}{d(s)} \frac{\mathbf{K}_0(r_i \sqrt{s\beta_s})}{(r_w r_e)^p} \frac{\lambda_r}{\lambda_s} \sqrt{\frac{\beta_r}{\beta_s}} & \left[-\mathbf{I}_p(r_w \sqrt{s\beta_r}) \mathbf{K}_{p+1}(r_w \sqrt{s\beta_r}) - \right. \\
& \left. \mathbf{K}_p(r_w \sqrt{s\beta_r}) \mathbf{I}_{p+1}(r_w \sqrt{s\beta_r}) \right] \quad (3.81)
\end{aligned}$$

$$\begin{aligned}
g_4(s) = \frac{-1}{d(s)} \frac{\mathbf{I}_0(r_w \sqrt{s\beta_s})}{(r_w r_e)^p} \frac{\lambda_r}{\lambda_s} \sqrt{\frac{\beta_r}{\beta_s}} & \left[-\mathbf{I}_{p+1}(r_w \sqrt{s\beta_r}) \mathbf{K}_p(r_e \sqrt{s\beta_r}) - \right. \\
& \left. \mathbf{K}_{p+1}(r_w \sqrt{s\beta_r}) \mathbf{I}_p(r_e \sqrt{s\beta_r}) \right] + \\
\frac{1}{d(s)} \frac{\mathbf{I}_1(r_w \sqrt{s\beta_s})}{(r_w r_e)^p} & \left[-\mathbf{I}_p(r_w \sqrt{s\beta_r}) \mathbf{K}_p(r_e \sqrt{s\beta_r}) + \right. \\
& \left. \mathbf{K}_p(r_w \sqrt{s\beta_r}) \mathbf{I}_p(r_e \sqrt{s\beta_r}) \right] \quad (3.82)
\end{aligned}$$

$$\begin{aligned}
g_5(s) = \frac{-1}{d(s)} \frac{\mathbf{I}_0(r_i \sqrt{s\beta_s})}{(r_w r_e)^p} \frac{\lambda_r}{\lambda_s} \sqrt{\frac{\beta_r}{\beta_s}} & \left[-\mathbf{I}_{p+1}(r_w \sqrt{s\beta_r}) \mathbf{K}_p(r_e \sqrt{s\beta_r}) - \right. \\
& \left. \mathbf{K}_{p+1}(r_w \sqrt{s\beta_r}) \mathbf{I}_p(r_e \sqrt{s\beta_r}) \right] \quad (3.83)
\end{aligned}$$

and finally,

$$g_6(s) = \frac{1}{d(s)} \frac{I_0(r_i \sqrt{s\beta_s}) \lambda_r}{(r_w r_e)^p \lambda_s} \sqrt{\frac{\beta_r}{\beta_s}} \frac{1}{r_w \sqrt{s\beta_r}} \quad (3.84)$$

The denominator, $d(s)$ is given explicitly by the following expression:

$$d(s) = \frac{1}{(r_w r_e)^p \lambda_f} \sqrt{\frac{\beta_s}{\beta_f}} \left\{ \left[I_0(r_i \sqrt{s\beta_s}) K_0(r_w \sqrt{s\beta_s}) - K_0(r_i \sqrt{s\beta_s}) I_0(r_w \sqrt{s\beta_s}) \right] \cdot \left[-I_{p+1}(r_w \sqrt{s\beta_r}) K_p(r_e \sqrt{s\beta_r}) - K_{p+1}(r_w \sqrt{s\beta_r}) I_p(r_e \sqrt{s\beta_r}) \right] \cdot \left[-I_0(r_i \sqrt{s\beta_s}) - K_1(r_w \sqrt{s\beta_s}) + K_0(r_i \sqrt{s\beta_s}) I_1(r_w \sqrt{s\beta_s}) \right] \cdot \left[I_p(r_w \sqrt{s\beta_r}) K_p(r_e \sqrt{s\beta_r}) + K_p(r_w \sqrt{s\beta_r}) I_p(r_e \sqrt{s\beta_r}) \right] \right\} \quad (3.85)$$

Up to this point, an explicit expression for the heat flow into the wellbore has been developed. This was accomplished by solving for the temperature distribution in the casing and determining its derivative with respect to r at r_i . With $C(s)$ and $D(s)$ evaluated from the boundary conditions (Equations 3.76 to 3.85) the heat flow into the wellbore can be stated as follows,

$$\frac{2\alpha\lambda_s}{r_i \rho C_f} \frac{d\hat{T}_2(r, s)}{dr} \Big|_{r=r_i} + \hat{T}_2(r, s) \Big|_{r=r_i} = \varpi(s) \hat{T}_1(z, s) + \gamma(s) \sum_{i=0}^k \eta_i(s) z^{i+2} + \nu(s) T_p(r_e, s) + \gamma(s) \frac{T_0}{s} \quad (3.86)$$

where,

$$\varpi(s) = g_1(s) \left(I_0(r_i \sqrt{s\beta_s}) + \frac{2\alpha\lambda_s}{r_i \rho C_f} \sqrt{s\beta_s} I_1(r_i \sqrt{s\beta_s}) \right) + g_4(s) \left(K_0(r_i \sqrt{s\beta_s}) - \frac{2\alpha\lambda_s}{r_i \rho C_f} \sqrt{s\beta_s} K_1(r_i \sqrt{s\beta_s}) \right) \quad (3.87)$$

$$\begin{aligned} \gamma(s) = [g_2(s) - g_1(s)] & \left(I_0 \left(r_i \sqrt{s\beta_s} \right) + \frac{2\alpha\lambda_s}{r_i} \rho C_f \sqrt{s\beta_s} I_1 \left(r_i \sqrt{s\beta_s} \right) \right) + \\ & [g_5(s) - g_4(s)] \left(K_0 \left(r_i \sqrt{s\beta_s} \right) - \frac{2\alpha\lambda_s}{r_i} \rho C_f \sqrt{s\beta_s} K_1 \left(r_i \sqrt{s\beta_s} \right) \right) + 1 \end{aligned} \quad (3.88)$$

$$\begin{aligned} \nu(s) = g_3(s) & \left(I_0 \left(r_i \sqrt{s\beta_s} \right) + \frac{2\alpha\lambda_s}{r_i \rho C_f} \sqrt{s\beta_s} I_1 \left(r_i \sqrt{s\beta_s} \right) \right) + \\ & g_6(s) \left(K_0 \left(r_i \sqrt{s\beta_s} \right) - \frac{2\alpha\lambda_s}{r_i \rho C_f} \sqrt{s\beta_s} K_1 \left(r_i \sqrt{s\beta_s} \right) \right) \end{aligned} \quad (3.89)$$

Equation 3.73 is the axial heat transfer model developed for the wellbore and is repeated here for convenience.

$$z \frac{\partial T_1(z, t)}{\partial z} + T_1(z, t) = -\alpha \frac{\partial T_1}{\partial t} + \frac{2\alpha\lambda_s}{\rho C_f} \frac{1}{r_i} \frac{\partial T_2(r, t)}{\partial r} \Bigg|_{r=r_i} + T_2(r, t) \Bigg|_{r=r_i} \quad (3.90)$$

Substitution of the explicit expression for the heat flow into the wellbore into the above equation, (Equation 3.86 into Equation 3.90) and taking the Laplace transform results in the following

$$z \frac{d\hat{T}_1}{dz} + b(s)\hat{T}_1 = (-s\alpha + \gamma(s)) \frac{T_0}{s} + \gamma(s) \sum_{i=0}^k \eta_i(s) z^{i+2} + \nu(s) \hat{T}_p(r_e, s) \quad (3.91)$$

where, $b(s) = (1 + s\alpha - \varpi(s))$

Equation 3.91 is a simple first order non-homogeneous differential equation that can be solved using elementary calculus methods [115]. It is noted that the generation of a polynomial expression for $\hat{q}_2(z)$ has made it possible to solve this equation analytically.

The particular solution is obtained by assuming a solution of the form

$$\hat{T}_{1,p}(z, s) = \sum_{i=0}^{k+2} a_i z^i,$$

and substituting this solution into Equation 3.91 and solving for the unknown

coefficients, a_i , in the series. This results in the following particular solution,

$$\hat{T}_{1,p}(z, s) = \frac{(s\alpha + \gamma(s))T_0}{b(s)} \frac{1}{s} + \frac{\nu(s)}{b(s)} \hat{T}_p(r_e, s) + \gamma(s) \sum_{i=0}^k \frac{\eta_i(s) z^{i+2}}{i + b(s) + 2} \quad (3.92)$$

The complementary solution, which is the solution to the homogeneous form of Equation 3.91, is obtained directly and is,

$$\hat{T}_{1,c}(z, s) = G(s) z^{-(1+s\alpha-\varpi(s))} \quad (3.93)$$

The constant of integration $G(s)$ must now be determined and requires the assumption that the temperature is known at some location near the toe of the horizontal well, Z_0 . This will set a boundary condition for the determination of $G(s)$. For a very long horizontal well, it may be sufficient to state that $\hat{T}_1(Z_0, s) = T_0/s$, the initial temperature in the wellbore. In circumstances when the reservoir electrical heating may be sufficient to cause a rise in temperature along the entire length of the horizontal well, a method to estimate the temperature at z_0 must be devised.

In this thesis, the approach involves the solution of the radial semi-analytic model to estimate the temperature at z_0 , where the axial flow velocities are negligible, and using this temperature as the boundary condition, determine $G(s)$, (refer to Figure 3.2). Thus, from Equations 3.92 and 3.93, and using that the complete solution of $\hat{T}_1(z, s)$ is the sum of the particular solution and the complementary solution, $G(s)$ can be stated as follows,

$$G(s) = \left(\hat{T}_1(r_i, s) - \frac{T_0 (s\alpha + \gamma(s))}{s b(s)} \right) \left(\frac{1}{z_0} \right)^{-b(s)} - \frac{\nu(s)}{b(s)} \left(\frac{1}{z_0} \right)^{-b(s)} \hat{T}_p(r_e, s) - \gamma(s) \left(\frac{1}{z_0} \right)^{-b(s)} \sum_{i=0}^k \frac{\eta_i(s) z_0^{i+2}}{i + b(s) + 2} \quad (3.94)$$

Finally, the expression for $\hat{T}_1(z, s)$ is:

$$\begin{aligned} \hat{T}_1(z, s) = & \hat{T}_1(r_i, s) \left(\frac{z}{z_0}\right)^{-b(s)} + \gamma(s) \sum_{i=0}^k \frac{\eta_i(s) z^{i+2}}{i + b(s) + 2} + \\ & \left(\frac{(s\alpha + \gamma(s)) T_0}{b(s)} \frac{1}{s} + \frac{\nu(s)}{b(s)} \hat{T}_p(r_e, s)\right) \left[1 - \left(\frac{z}{z_0}\right)^{-b(s)}\right] - \\ & \gamma(s) \left(\frac{z}{z_0}\right)^{-b(s)} \sum_{i=0}^k \frac{\eta_i(s) z_0^{i+2}}{i + b(s) + 2} \quad (3.95) \end{aligned}$$

where z_0 is the location of the boundary.

To obtain the temperature distribution in the time domain requires inversion of Equation 3.95. An analytic inversion of Equation 3.95 is not feasible. Thus, Equation 3.95 is inverted numerically using the *Stehfest Inversion Algorithm* to obtain a solution of the problem in the time domain.

3.4.3 Validation of the axial semi-analytic model using *TETRAD*

In this section *TETRAD* is used to validate the axial semi-analytic model. Specific considerations for *TETRAD* to model this problem are listed here. A full description of *TETRAD* and the features referred to here are documented in References [82], [110], and [111].

1. Set the values of the gravity term, g , in *TETRAD* in all the grid blocks to zero to eliminate the pressure gradient. The $+z$ direction in *TETRAD* defaults to increasing depth below the surface of the earth, whereas the z direction in the semi-analytic model is horizontal.
2. Set the transmissibility in the wellbore in *TETRAD* to a sufficiently large value so that there is minimal pressure drop in the axial direction in the wellbore. This will ensure that the fluid will flow radially into the wellbore and the flow velocity at $r = r_w$ will have minimum variation along the length of the horizontal well. Large wellbore transmissibility is also required so that a well can be located in a single grid block at the heel of the well and axial accumulation of flow $Q(z) = Q_t \cdot \frac{z}{l}$ in the wellbore can be properly modeled.

The longer the wellbore, the greater the axial pressures drop between the heel and toe of the well and the larger the variation of the radial flow along the length of the well. This is the single most important issue that must be properly considered to ensure comparability between the axial semi-analytic model and *TETRAD*. Otherwise, the radial fluid flow into the wellbore along its length is not uniform and the temperature profiles obtained with *TETRAD* can not be compared with those obtained from the axial semi-analytic model.

3. Set the z direction permeability in the reservoir to a small value to further restrict the fluids to flow radially into the wellbore and minimize axial flow in the reservoir.
4. Set the electrical conductivity for the casing grid block and ground grid block, which is located at near r_e at the outer boundary of the problem domain, to a very large value to ensure that the current density, J , along the length of the well at $r = r_w$ is uniform.
5. Model the hysteresis and eddy current losses in the casing using the input data set, *ENFLUX*. This data set allows the input of energy in $kJ/(m^3 day)$ into a grid block. Based on the current, the hysteresis and eddy current power losses are determined in these units and input into the grid block using this data set.
6. A limitation of *TETRAD* is that only one value for the reservoir heat capacity can be input into the program. Since the wellbore consists entirely of fluid, the heat capacity for the fluid was used for all the regions. This value was input into the numerical model and the axial semi-analytic model so that a valid comparison could be made between the results obtained with the two models.
7. Attach a grid block at the heel of the well as the production grid block. This step tends to improve the axial flow of fluids into the wellbore.

It is necessary to input a very large transmissibility for the grid blocks used to model the wellbore so that the resistance to flow in the axial direction is negligible. This approach will result in the calculation of the temperature distribution to become sensitive to small changes in the input data. For example, a change in the overall pressure drop along the length of the horizontal well of only $3 kPa$ results in

a 6 °C difference in the calculation of the peak temperature. Attempts were made to minimize the impact of these sensitivities by designing a stable grid and input data set.

Ideally, an infinitely large wellbore transmissibility is chosen so that the pressure drop in the wellbore is zero. Under these conditions, the flow into the wellbore from the reservoir is evenly distributed along the length of the horizontal well. As the axial pressure drop in the wellbore increases due to a finite resistance to flow in the wellbore, a variation of the radial fluid velocity distribution along the length of the wellbore will result. The greater the axial pressure drop in the wellbore, the more distorted the radial fluid velocity distribution. This distorted velocity distribution contradicts the assumption of uniform radial flow into the horizontal well made in the development of the axial semi-analytic model. This may introduce differences in the temperature profiles calculated with *TETRAD* and the semi-analytic model.

Several sensitivity simulation runs were performed to determine a wellbore permeability that minimized the pressure drop in the wellbore and at the same time resulted in a stable solution to the problem. Figure 3.11 shows the radial pressure drop between the reservoir and the wellbore along the axial length of a 1,000-meter long horizontal well. For these calculations, the wellbore was modeled using grid blocks with a permeability of 100,000 Darcies. The total fluid production rate from the well was chosen to be 50 m^3/day , which is a typical production rate for a very good horizontal well in heavy oil. For larger production rates, the pressure drops will be greater. The grid designed for the wellbore at 50 m^3/day represents a practical upper limit of the flow rate from a horizontal well producing from a heavy oil reservoir and the grid should be adequate for modeling lower total fluid production rates.

Figure 3.11 shows the variation of the pressure drop between the reservoir and the wellbore along the length of the horizontal well. The variation of the radial flow velocity along the wellbore is proportional to the pressure drop. Using a very large permeability in the wellbore, it was possible to achieve a fairly uniform flow distribution along the length of the well. The pressure drops vary from 38.5 kPa at the heel of the well, to 33.3 kPa at the toe, resulting in a total pressure drop of only

5 kPa along the length of the well. Larger wellbore transmissibility values were tested, yielding smaller axial pressure drops. However, the calculations were unstable when small changes to the input data were made. A permeability of 100,000 Darcies in the wellbore grid blocks was used to model the uniform flow of fluids into the wellbore for all of the *TETRAD* runs.

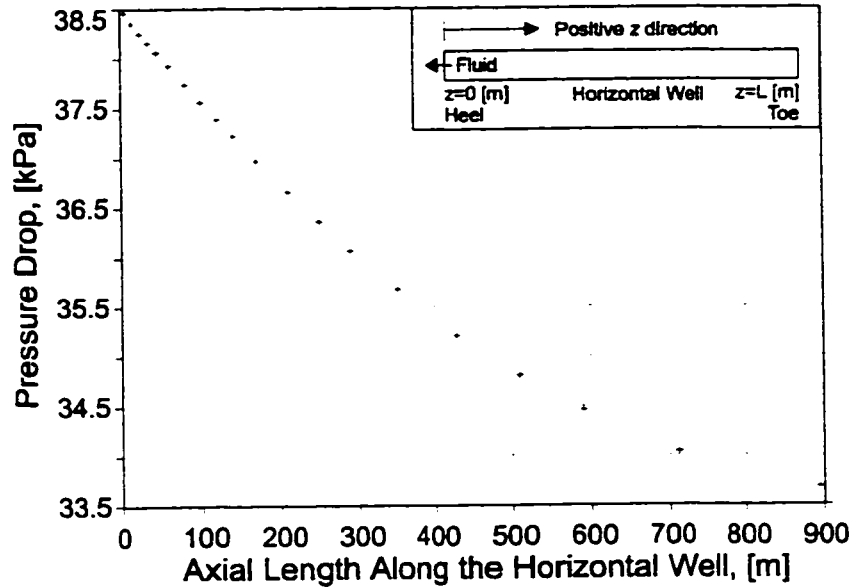


Figure 3.11: Numerical calculation of the pressure drop between the reservoir and the wellbore along the length of a 1,000-meter long horizontal well. The wellbore is modeled using grid blocks that have a permeability of 100,000 Darcies.

Coarse and fine grids are used in the validation. The coarse grid is designed to model the problem with no radial temperature gradient in the wellbore by using a single radial grid block to model the wellbore. This satisfies the assumption of constant radial temperature distribution in the wellbore, which was required to obtain the axial semi-analytic model.

The fine grid is designed to take into account the radial temperature variation in the wellbore so that the assumption of constant radial temperature distribution in the wellbore can be tested. The steel casing was modeled in the radial direction with one radial grid block. A finer grid to model the casing was tested and compared with the single grid block model with no significant difference in the results.

Figures 3.12 and 3.13 show the grids used in the numerical simulation for validation of the axial semi-analytic model. Only the first several grids, extending to about three wellbore radii ($r = 3r_w$), are shown. For the fine grid, 23 radial blocks

and 21 axial blocks were found to be necessary to model the problem. For the coarse grid, a single grid block replaces all of the radial grid blocks in the wellbore and thus 20 radial blocks and 21 axial blocks are required to model the complete problem.

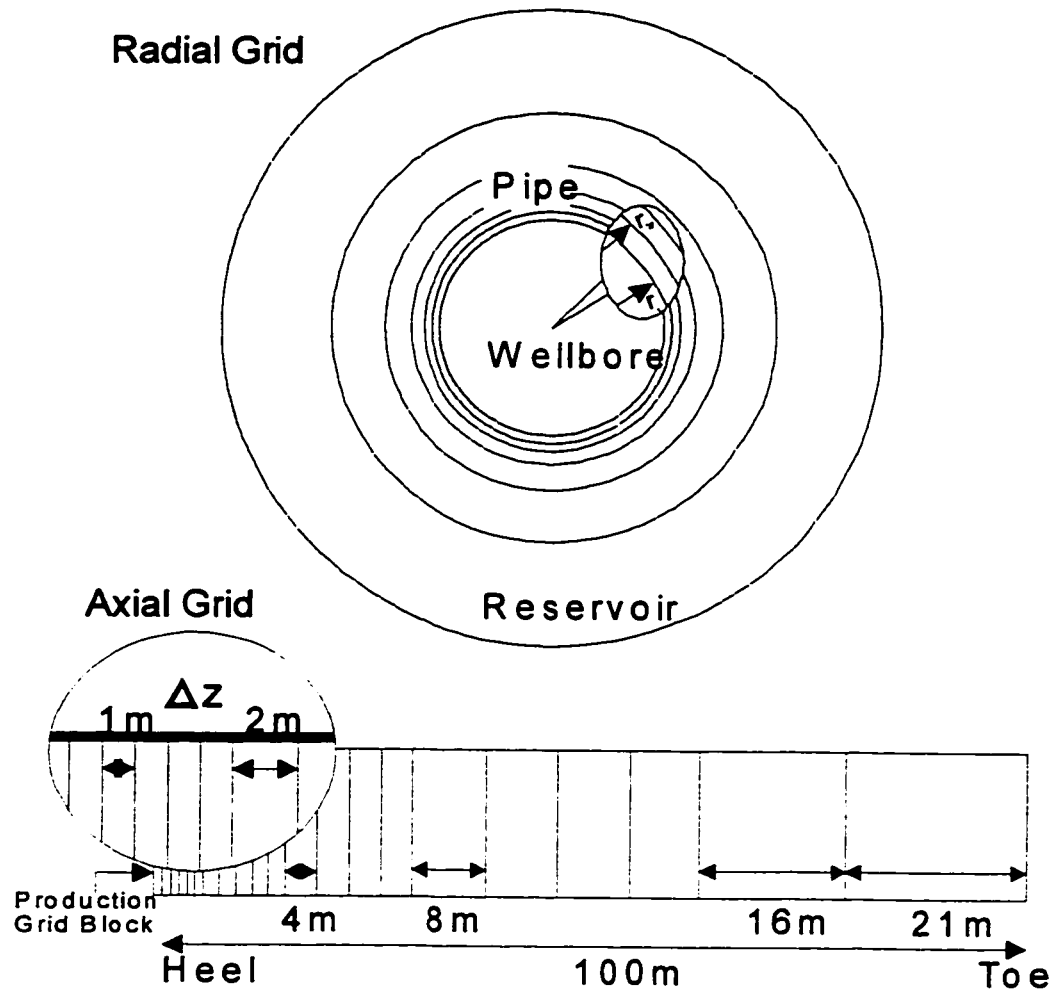


Figure 3.12: Coarse grid used in *TETRAD* for validating the axial semi-analytic model.

Two horizontal well lengths are modeled, 100 meters and 1,000 meters. The 100-meter well is sufficiently short so that there is no single heat transfer mechanism dominating the thermal response of the well. The 1,000-meter length well is typical of the length of horizontal wells drilled in heavy oil. For the longer well, the important heating mechanism is thermal conduction from the casing into the wellbore and reservoir as the casing increases in temperature as a result of hysteresis and eddy current losses. The grid used to simulate the longer well is similar to the grid used for the shorter well with the axial grid block sizes multiplied by a factor of

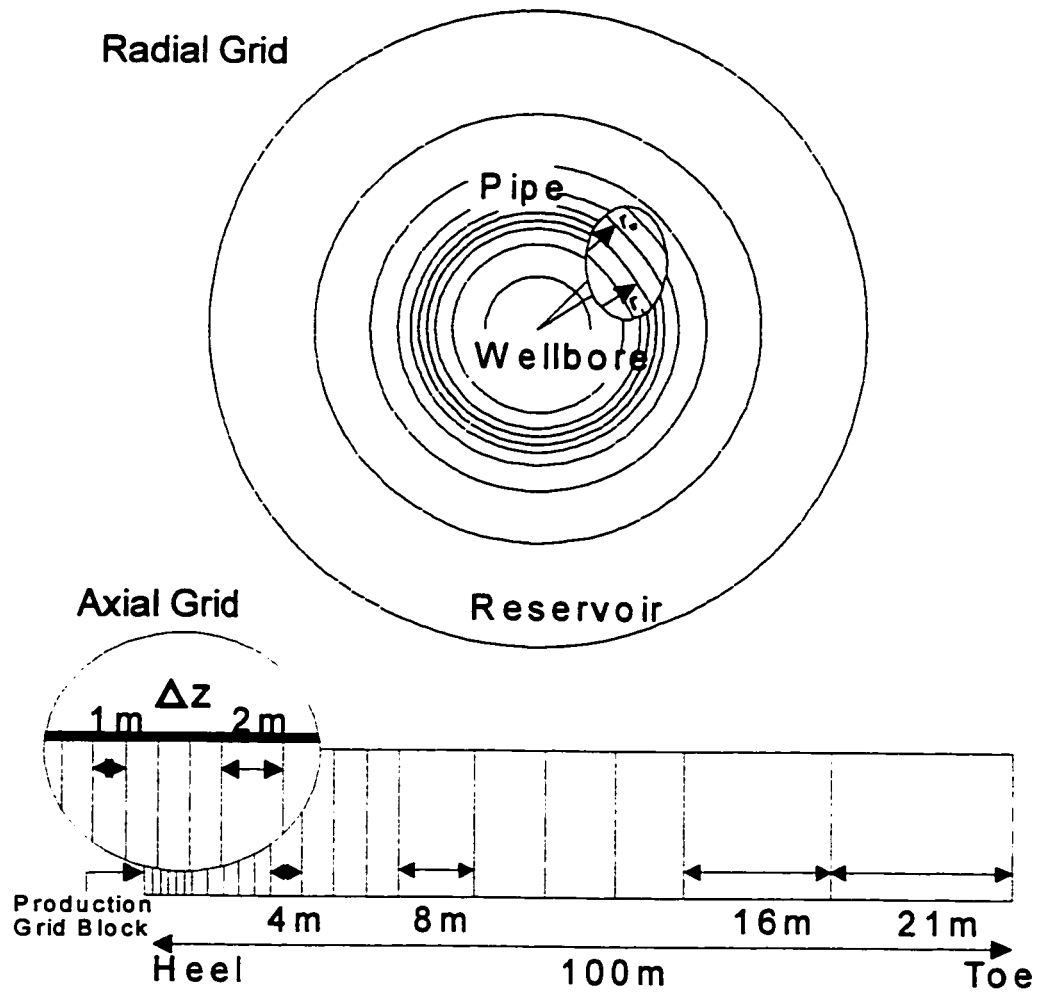


Figure 3.13: Fine grid used in *TETRAD* for validating the axial semi-analytic model.

10.

The temperature dependence of the electrical conductivity of the reservoir, (neglected in the semi-analytic models), is investigated using *TETRAD*. This investigation is done for both the long and short horizontal wells. The impact of assuming constant electrical conductivity in the development of the axial semi-analytic model can therefore be tested.

The simulation runs conducted for the validation are summarized in Table 3.7. Unless otherwise stated, the input current is adjusted so that the peak temperature does not exceed 100 °C. Also, all the calculations for all the runs are for a heating duration of 30 days and the initial reservoir temperature is 20 °C.

Runs with the *same regional properties* means that the thermal conductivity of all the regions is set to the thermal conductivity of the reservoir. The same

thermal conductivity was used in all of the regions so that the effect of total fluid production rate on the results could be isolated from other effects and more readily analysed. The impact of using the thermal conductivity particular to a region is analysed in *Run 4* and *Run 9*. For these runs the *different* thermal conductivity of each region is used, i.e., λ_f , λ_s , or λ_r . Table 3.8 summarizes the operating input

Run	Regional Properties	Grid Type	Temperature Dependent Conductivity, $\sigma_r(T)$ <i>S/m</i>	Flow Rate <i>m³/day</i>
100 meter runs				
1	Same	Coarse and Fine	No	0.5
2	Same	Coarse and Fine	No	5.0
3	Same	Coarse and Fine	No	10.0
4	Different	Coarse and Fine	No	5.0
5	Same	Fine Only	Yes	5.0
1,000 meter runs				
6	Same	Coarse and Fine	No	10.0
7	Same	Coarse and Fine	No	25.0
8	Same	Coarse and Fine	No	50.0
9	Different	Coarse and Fine	No	25.0
10	Same	Fine Only	Yes	25.0

Table 3.7: Summary of the simulation runs used to validate the axial semi-analytic model.

data for the different runs.

100-meter long horizontal well validation runs

The first five runs in Table 3.7 are for a shorter, 100-meter long horizontal well. In the first three runs, the only parameters that are varied are the flow rate and the electrical current. The electrical current is adjusted so that a peak temperature of 100 °C is achieved after 30 days of heating. The purpose of these runs is to investigate the effect of flow rate and compare the results obtained to results from the axial semi-analytic model for the situation in which none of the

Run	Flow Rate m^3/day	Current A RMS	$T_1(z)_{max}$ $^{\circ}C$	$1 + \frac{Q_i \rho C_f}{2\pi \lambda_r l}$
100 meter runs				
1	0.5	480	99.56	1.02
2	5.0	530	99.07	1.13
3	10.0	580	99.36	1.25
4	5.0	530	100.27	2.00
5	5.0	732	101.67	2.00
1,000 meter runs				
6	10.0	880	99.94	1.02
7	25.0	1000	101.59	1.06
8	50.0	1000	82.88	1.13
9	25.0	1000	105.28	1.06
10	25.0	1000	100.93	1.06

Table 3.8: *TETRAD* validation runs operating data. In all of the runs the initial reservoir temperature is 20 $^{\circ}C$.

heat transfer mechanisms can be ignored.

Run 4 compares the effect of different thermal properties in all the regions on the results obtained by *TETRAD* and the axial semi-analytic model. The final run tests the effect of assuming constant electrical conductivity with temperature in the reservoir in the axial semi-analytic model.

For the coarse grid the axial temperature profiles along $r = r_i$ are compared for each of the validation runs. Since *TETRAD* calculates the temperature at the grid block centers, the temperature at r_i is obtained by harmonically averaging the temperatures at the grid block centers [82]:

$$T_1(r_i) = \frac{\ln(r_{i+1/2}/r_i)\lambda_f T_{i-1/2} + \ln(r_i/r_{i-1/2})\lambda_s T_{i+1/2}}{\ln(r_{i+1/2}/r_i)\lambda_f + \ln(r_i/r_{i-1/2})\lambda_s} \quad (3.96)$$

where, $T_{i+1/2}$ and $T_{i-1/2}$ are the temperatures calculated by *TETRAD* at the grid block centers adjacent to r_i .

For the fine grid, the temperatures of the grid blocks used to model the

wellbore are averaged and the result is compared to the temperatures obtained with the axial semi-analytic model. The temperature that is calculated in the wellbore using the semi-analytic model assumes that temperature in the wellbore does not vary radially. Thus the semi-analytic solution can be viewed as calculating an average temperature in the wellbore.

Figure 3.14 shows a comparison of the temperature distribution calculated along the length of a 100-meter horizontal well with a total fluid production rate of $0.5 \text{ m}^3/\text{day}$ using the axial semi-analytic model and *TETRAD*. Calculations for both the coarse and fine grids are shown. At such a low production rate, the flow velocities along the length of the casing are so small that thermal conduction and electrical heating are the dominant heat transfer mechanisms.

Also shown on Figure 3.14 are the percent differences between the temperatures calculated using the axial semi-analytic model and the numerical calculations using the fine grid. The semi-analytic model and *TETRAD* calculations compare very well with a maximum difference of less than 1.75% between the calculated temperatures. The calculations using the coarse and fine grid are almost identical.

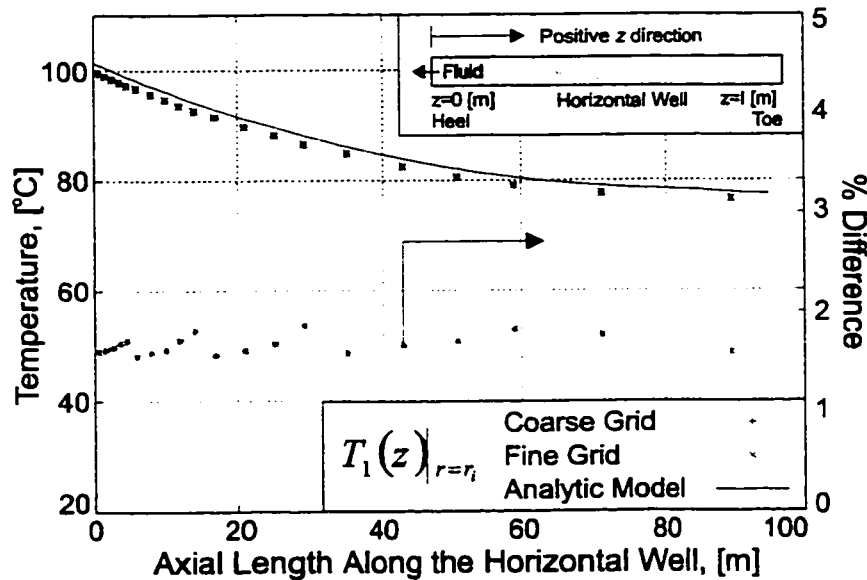


Figure 3.14: *Run 1*. Comparison of the axial temperature distribution obtained from the axial semi-analytic model to results obtained from numerical simulation for a 100-meter long well, same regional thermal properties, constant $\sigma_r(T)$, low fluid production rate of $Q_t = 0.5 \text{ m}^3/\text{day}$, and after 30 days of heating.

Fairly uniform heating along the length of the well is achieved during the heating process as a consequence of electrical heating in the reservoir. The temperature variation from the toe to the heel of the well is mainly due to the variation of hysteresis and eddy current losses along the length of the casing.

The total fluid production rate is now increased to $5.0 \text{ m}^3/\text{day}$. Figure 3.15 shows the comparison of the temperature distribution along the length of the 100-meter long horizontal well using the axial semi-analytic model and numerical calculations. This flow rate per unit length of horizontal well is typical of an excellent horizontal well in a heavy oil reservoir. The input current is adjusted so that the maximum operating temperature is maintained at $100 \text{ }^\circ\text{C}$, as indicated in Table 3.8.

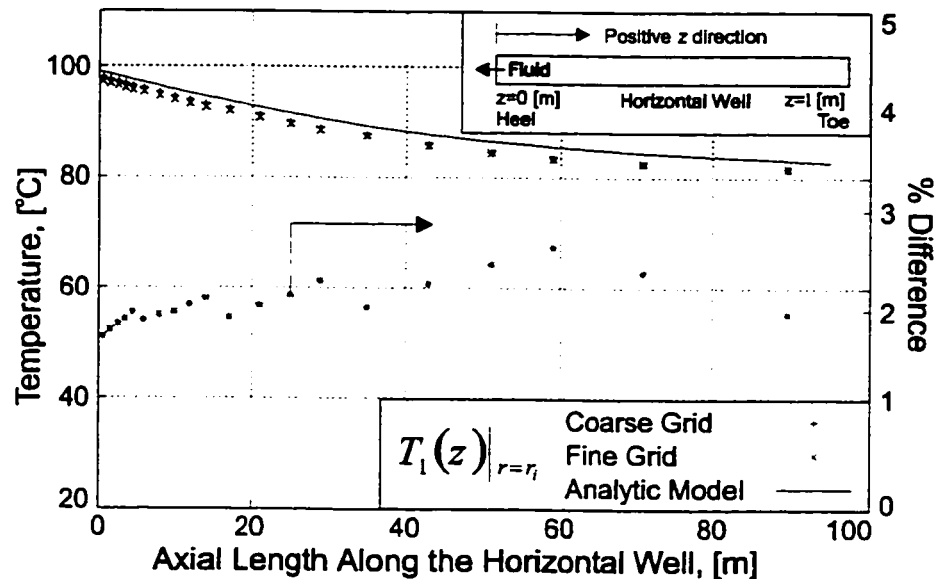


Figure 3.15: *Run 2*. Comparison of the axial temperature distribution obtained from the axial semi-analytic model to results obtained from numerical simulation for a 100-meter long well, same regional thermal properties, constant $\sigma_r(T)$, moderate fluid production rate of $Q_t = 5.0 \text{ m}^3/\text{day}$, and after 30 days of heating.

Uniform heating along the length of the well is achieved with electrical heating. The axial semi-analytic model calculates a slightly higher average temperature than the values calculated using *TETRAD*. The maximum percent difference between the results obtained with the axial semi-analytic model and the numerical calculations is about 2.5%. For the case with increased fluid production rate, small differences between the semi-analytic and numerical model, and between

the coarse and fine grid become apparent. For greater production rates, these differences become even more significant as illustrated in the next example.

The total fluid production rate is now increased to $10.0 \text{ m}^3/\text{day}$. Figure 3.16 shows the comparison of the temperature distribution along the length of the 100-meter long horizontal well calculated using the axial semi-analytic model and *TETRAD*. Under these conditions, radial flow into the wellbore from the reservoir and axial flow in the wellbore are substantial. The equivalent flow rate for a horizontal well 1,000 meters long is $100 \text{ m}^3/\text{day}$, which is considered a very prolific rate for a horizontal well producing from a heavy oil reservoir. It is noted that the axial semi-analytic model begins to show signs of instability during the numerical inversion of the Laplace transform towards the toe of the horizontal well. Calculations beyond 90 meters were not possible.

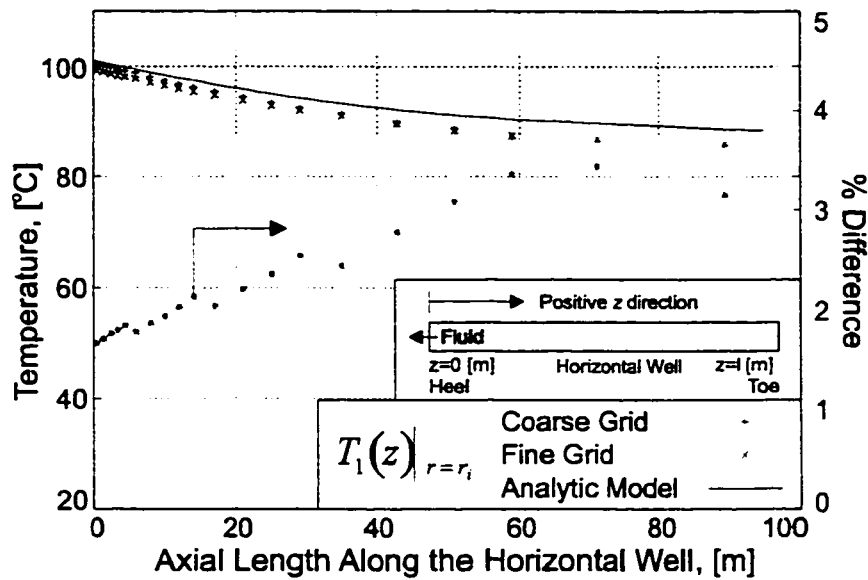


Figure 3.16: *Run 3*. Comparison of the axial temperature distribution obtained from the axial semi-analytic model to results obtained from numerical simulation for a 100-meter long well, same regional thermal properties, constant $\sigma_r(T)$, high fluid production rate of $Q_t = 10.0 \text{ m}^3/\text{day}$, and after 30 days of heating.

Comparing Figure 3.16 with the previous calculations shows that the maximum error has increased as the production rate has increased. The maximum percent error rose from 2.5 to 3.5%. Also, larger differences between the coarse and fine grid numerical calculations are evident. The differences between the fine and coarse grid calculations may suggest that at higher flow rates the radial temperature gradient in the wellbore is significant. Also, the axial pressure drop along the length of wellbore increases with increasing flow rate, which begins to invalidate the comparison between the results of the calculations. The results at the higher flow rates however still compare favourably to each other. These higher flow rates represent the upper limit for most horizontal wells.

Figure 3.17 shows a comparison of the temperature distribution calculated along the length of a 100-meter horizontal for a *typical* production rate of $5.0 \text{ m}^3/\text{day}$ and with the correct thermal conductivity properties in each of the regions. The results compare favourably. The maximum percent difference in the temperature calculations is less than 2.5%. For the shorter well, where electrical heating in the reservoir is the dominant heat transfer mechanism, the impact of the thermal properties in the wellbore on the results is marginal.

The plots shown on Figure 3.17 reveal no obvious impact of neglecting axial heat transfer in the casing by thermal conduction in the axial semi-analytic model. Assuming that the heat flow in the casing is primarily by thermal conduction in the radial direction seems to be a valid assumption for the type of problems solved here.

Figure 3.18 shows the radial temperature distribution near the toe of the horizontal well for the previous case. Near the toe of the well, there is effectively no current flow in the casing to cause heating and the total fluid production rate in the wellbore is minimum. Therefore, the radial semi-analytic model can be used to calculate the radial temperature distribution since the temperature is essentially determined by the electrical heating in the reservoir and radial heat transfer by conduction and convection between the three regions. There is excellent agreement between the semi-analytic and numerical calculations. This example calculation confirms that the radial semi-analytic model can be used to determine the temperature boundary condition for the axial semi-analytic model near the toe of the well, as done in Section 3.4.3.

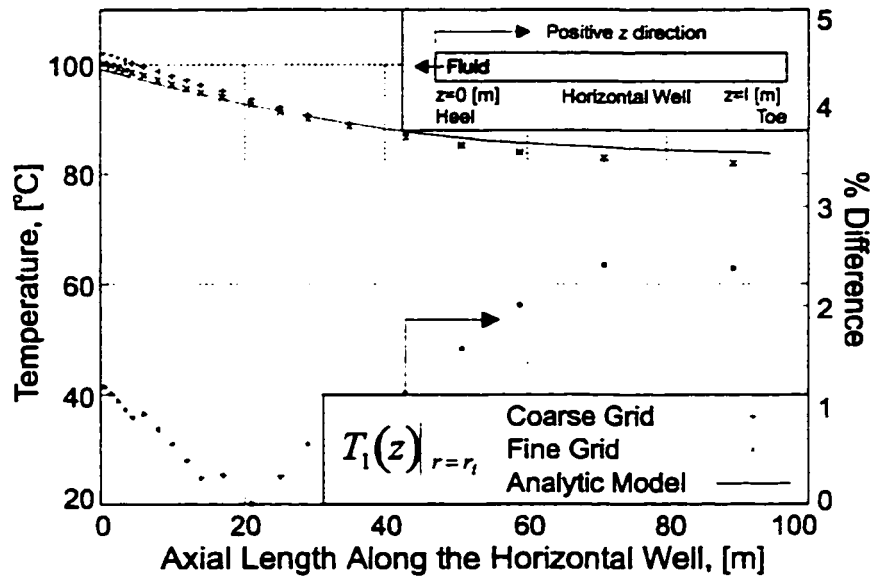


Figure 3.17: *Run 4*. Comparison of the axial temperature distribution obtained from the axial semi-analytic model to results obtained from numerical simulation for a 100-meter long well, correct regional thermal properties, constant $\sigma_r(T)$, moderate fluid production rate of $Q_t = 5.0 \text{ m}^3/\text{day}$, and after 30 days of heating.

1,000-meter long horizontal well validation runs

The heat transfer mechanisms that control the thermal response of a long horizontal well are substantially different than those for a short well. The heating process consists almost entirely of hysteresis and eddy current losses in the casing and heat transfer by conduction to the wellbore and the reservoir. For a typical 1,000 m horizontal well, producing $25 \text{ m}^3/\text{day}$, α_r , which is a measure of the relative importance of the conductive and convective heat transfer mechanism, is 1.06. This near unity value of α means that heat transfer is almost entirely by conduction.

The peak temperature in the reservoir, initially at $20 \text{ }^\circ\text{C}$, was calculated for the case of no electrical losses in the casing, no fluid flow, and only electrical heating in the reservoir. The calculated peak temperature was $22.46 \text{ }^\circ\text{C}$ after 30 days of heating with 1,000 A of current. Even after one year of heating the temperature only increased to $24.12 \text{ }^\circ\text{C}$. If the electrical heating system can be operated so that an unrealistically large current of 2,000 A *RMS* flows through the reservoir, the peak temperature in the reservoir reached after 30 days of heating is only $30.55 \text{ }^\circ\text{C}$. These simple example calculations demonstrate how insignificant electrical heating in the reservoir for a long horizontal well is. The magnitude of the total current will

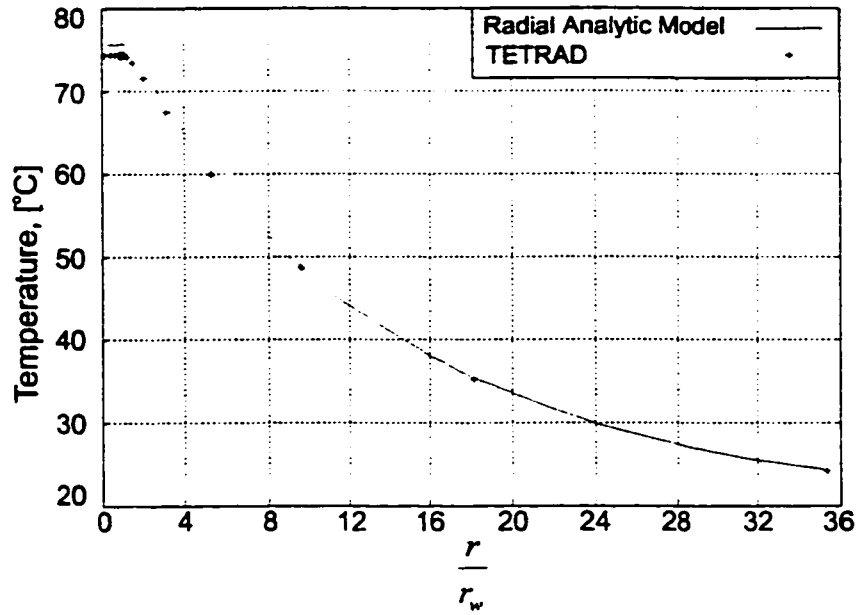


Figure 3.18: *Run 4*. Comparison of the radial temperature distribution at the toe of the horizontal well obtained from the radial semi-analytic model to results obtained from numerical simulation for a 100-meter long well, correct regional thermal properties, constant $\sigma_r(T)$, moderate fluid production rate of $Q_t = 5.0 \text{ m}^3/\text{day}$, and after 30 days of heating.

have to be unrealistically large to bring about any heating in the reservoir of any significance.

Figure 3.19 shows the temperature distribution along the length of the 1,000-meter long horizontal well after 30 days of heating for *Run 6*, (see Tables 3.7 and 3.8). The total fluid production rate is $10.0 \text{ m}^3/\text{day}$. The thermal conductivity and heat capacity in all the regions are set to the reservoir values. The axial semi-analytic model and numerical calculations produce almost identical results with a maximum percent difference less than 2.0%.

The total current to bring about the temperature response shown in Figure 3.19 is less than 1,000 A. Since only a minor increase in temperature is expected as a result of electrical heating in the reservoir, *the thermal response of the horizontal well is almost entirely a result of hysteresis and eddy current losses in the casing.*

Figure 3.20 shows the temperature distribution along the length of the 1,000-meter long horizontal well after 30 days of heating for *Run 7*, (see Tables 3.7 and 3.8). The total fluid production rate is increased from $10.0 \text{ m}^3/\text{day}$ to $25.0 \text{ m}^3/\text{day}$. The axial semi-analytic model and numerical calculations produce almost

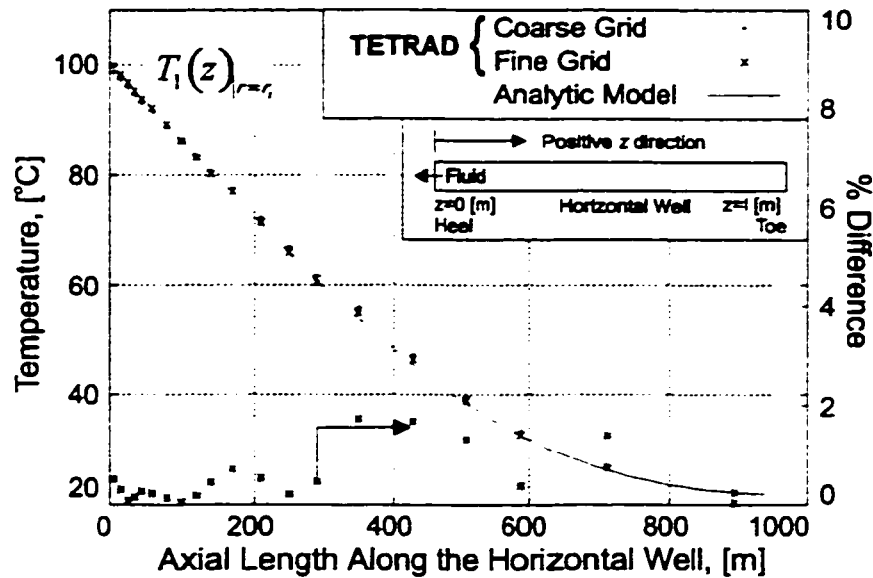


Figure 3.19: *Run 6*. Comparison of the axial temperature distribution obtained from the axial semi-analytic model to results obtained from numerical simulation for a 1,000-meter long well, same regional thermal properties, constant $\sigma_r(T)$, low fluid production rate of $Q_t = 10.0 \text{ m}^3/\text{day}$, and after 30 days of heating.

identical results with a maximum difference of less than 3.0%. The increase in production rate resulted in a small increase in the difference between the semi-analytic and numerical calculations. The same trend was observed for the 100-meter long horizontal well.

Figure 3.21 shows the temperature distribution along the length of the 1,000-meter long horizontal well after 30 days of heating corresponding to *Run 8* in Tables 3.7 and 3.8. The thermal properties are the same for all of the regions. The total fluid production rate is increased from $25.0 \text{ m}^3/\text{day}$ to $50.0 \text{ m}^3/\text{day}$. The results calculated with the axial semi-analytic model and the numerical models still compare well with a maximum percent difference of less than 6.0%.

As with the 100-meter long horizontal well comparisons, the increase in flow rate increases the difference between the calculations. Due to the large number of details that are present in the calculation of the temperature distribution using the numerical model, it is difficult to quantify the increasing difference between the two models as the total fluid production rate increases. It is noted that as the total fluid production rate increases, the total pressure drop along the length of the horizontal well calculated in *TETRAD* also increases. Since the axial semi-analytic model

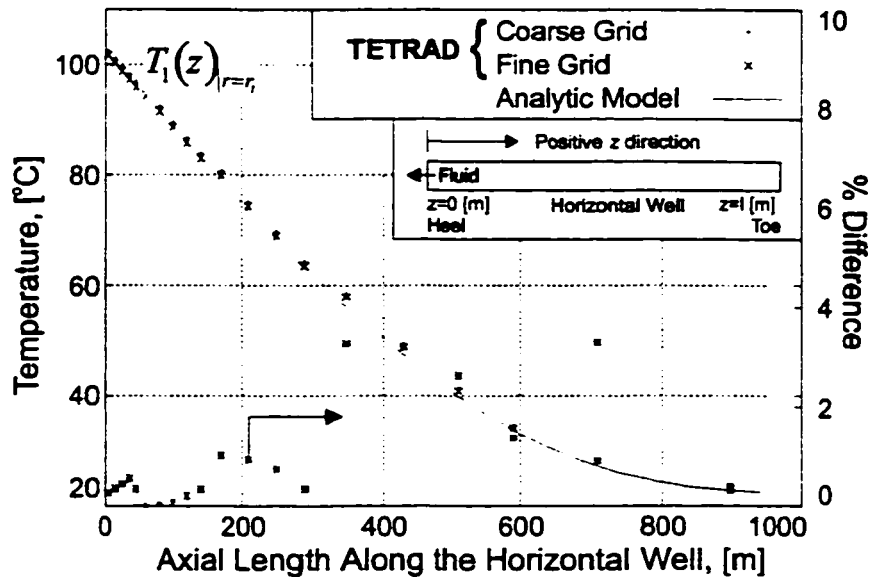


Figure 3.20: *Run 7*. Comparison of the axial temperature distribution obtained from the axial semi-analytic model to results obtained from numerical simulation for a 1,000-meter long well, same regional thermal properties, constant $\sigma_r(T)$, moderate fluid production rate of $Q_t = 25.0 \text{ m}^3/\text{day}$, and after 30 days of heating.

assumes a *zero* pressure drop along the length of the well, this may be an explanation why there is an increasing difference between the calculations as the total fluid production rate increases. However, for the practical production rates used when comparing the two models, the results compare favourably.

Figure 3.22 shows the temperature distribution along the length of the 1,000-meter long horizontal well after 30 days of heating, corresponding to *Run 9* in Tables 3.7 and 3.8. For this case, the total fluid production rate is $25.0 \text{ m}^3/\text{day}$ and the correct thermal properties in the regions are used in the numerical calculation. Thus the thermal conductivity of the casing is set to $50.00 \text{ W}/(\text{m}^\circ\text{C})$, $0.27 \text{ W}/(\text{m}^\circ\text{C})$ for the fluids in the wellbore and $2.04 \text{ W}/(\text{m}^\circ\text{C})$ for the reservoir. The purpose of this run is to determine the impact of assuming that the heat flow into the wellbore from the casing can be modeled using thermal conduction from the casing. The results of calculations using the axial semi-analytic model and numerical models still compare very well, with a maximum percent difference between the fine grid model and axial model of less than 6.0%. The maximum percent difference between the coarse grid model and axial model is greater, however it is still less than 8.0%.

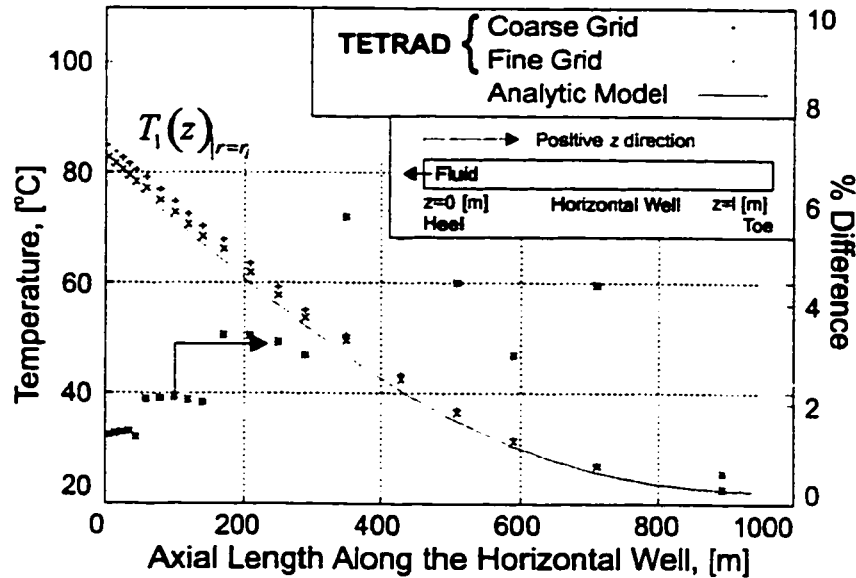


Figure 3.21: Run 8. Comparison of the axial temperature distribution obtained from the axial semi-analytic model to results obtained from numerical simulation for a 1,000-meter long well, same regional thermal properties, constant $\sigma_r(T)$, high fluid production rate of $Q_t = 50.0 \text{ m}^3/\text{day}$, and after 30 days of heating.

For the fine grid model, the temperature that is used in all of the comparisons and plots is the volumetrically weighted average temperature of the grid blocks used to model the wellbore. If the thermal conductivity of the wellbore grid blocks is set to a large value, for example the thermal conductivity of steel, then the radial heat transfer in the wellbore is very efficient and the temperatures of the wellbore grid blocks at various radial distances, at any given axial location are all approximately the same. Thus the assumption of constant radial temperature distribution in the wellbore that was used to derive the axial semi-analytic model is, in this case, very reasonable. When the thermal conductivity of the wellbore is set to the thermal conductivity of the fluids in the wellbore, the volumetrically weighted average temperatures of the wellbore grid blocks still compare favourably with the calculations obtained using the axial semi-analytic model (and the coarse grid numerical model). However, the temperature of the center grid block in the wellbore is $12.5 \text{ }^\circ\text{C}$ cooler than the temperature at $r = r_i$. Thus the *peak temperature* calculated using the fine grid numerical model is approximately $9.5 \text{ }^\circ\text{C}$ greater than the peak temperature calculated using the axial semi-analytic model. This is likely due to a significant radial temperature gradient in the wellbore resulting from the

low thermal conductivity of the fluids in the wellbore. Thus the axial analytic model will have a tendency to calculate a *peak temperature* that is conservative.

The volumetrically weighted average temperature of the fluids in the wellbore calculated using the fine grid model and the axial semi-analytic model are comparable. This suggests that the net heat flow into the wellbore calculated using the axial semi-analytic model is approximately the same as the heat flow into the wellbore calculated using the fine grid numerical model. For the axial semi-analytic model it was assumed that the heat flow into the wellbore from the casing is determined from the temperature gradient in the casing

$$\left. \frac{\partial T_2(r, t)}{\partial r} \right|_{r=r_i}$$

which is a direct result of using the Neumann boundary condition at the boundary between the two regions,

$$\lambda_s \left. \frac{\partial T_2(r, t)}{\partial r} \right|_{r=r_i} = \lambda_f \left. \frac{\partial T_1(r, t)}{\partial r} \right|_{r=r_i}$$

and assuming heat transfer in the radial direction in the wellbore is by thermal conduction. Based on the calculations from the fine grid numerical model, the heat flow into the wellbore from the casing can be approximated using this approach with the caveat that the actual temperatures in the radial direction in the wellbore may vary.

The impact of using the thermal conductivity of the fluids in the wellbore for the 100-meter long horizontal well on the numerical calculation of the peak temperature was not as significant as for the longer well. The difference in peak temperatures calculated using the axial model and the fine grid numerical model was less than 5.3 °C. This may be a result of the influence of the multiple heat transfer mechanisms that happen for the shorter well, whereas for the long horizontal well, nearly all of the heat is transferred through the regions by thermal conduction.

The above example runs demonstrate that when the thermal conductivities of the wellbore and the casing are the same and equal to the thermal conductivity of the reservoir, the calculated axial temperature distribution along the length of the

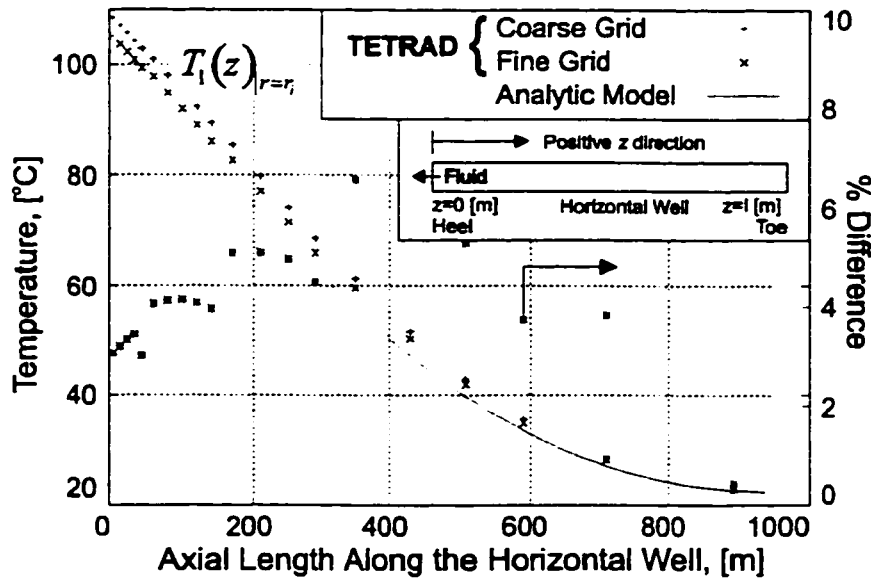


Figure 3.22: *Run 9*. Comparison of the axial temperature distribution obtained from the axial semi-analytic model to results obtained from numerical simulation for a 1,000-meter long well, correct regional thermal properties, constant $\sigma_r(T)$, moderate fluid production rate of $Q_t = 25.0 \text{ m}^3/\text{day}$, and after 30 days of heating.

horizontal well obtained with the axial semi-analytic model and numerical models compare favourably for both the long and short horizontal wells. When the thermal conductivity of the fluids is used to model the wellbore and the thermal conductivity of steel is used to model the casing, the average temperature in the wellbore calculated using the fine grid numerical model compares favourably with the temperatures obtained using the axial model. The significant difference between the numerical and the axial semi-analytic model is in the calculation of the *peak temperature* in the wellbore when the thermal conductivity of the fluids is used in the wellbore. These results were observed for both the long and short horizontal wells over a nominal range of total fluid production rates.

For increasing fluid production rates the percent difference between the numerical and semi-analytic calculations tended to increase. This increase is likely due to the increase in pressure drop along the length of the horizontal well associated with the increase in flow rate. This effect is accounted for in the numerical but not the semi-analytic model. An increase in the pressure drop along the length of the horizontal well creates an increase in the variation of the radial flow distribution along the wellbore which will create a difference between the

results of the numerical and semi-analytic calculations.

The numerical and axial semi-analytic models calculate axial temperature distributions for the horizontal wells that compare favourably for the examples summarized in Tables 3.7 and 3.8. For the 1,000-meter long horizontal well, the axial semi-analytic model calculates a comparable average temperature for the fluids in the wellbore. However, the peak temperature calculated with the axial semi-analytic model is conservative by about 10% as a result of ignoring the radial temperature gradient in the wellbore. In the next section, the impact of ignoring the temperature dependence of the reservoir electrical conductivity on the results obtained with the semi-analytic model is investigated. The axial semi-analytic model was developed with the assumption that the electrical conductivity is independent of temperature.

3.4.4 The impact of temperature dependent electrical conductivity

One of the assumptions made in the derivation of the axial semi-analytic model is that the reservoir electrical conductivity is independent of temperature. In actuality the electrical conductivity of the reservoir is a function of temperature and increases with temperature, $\sigma_r(T)$. Using *TETRAD* it is possible to test the effect of the assumption of temperature independent electrical conductivity. In the first case examined, the effect of $\sigma_r(T)$ on the temperature response of the 100-meter long horizontal well is calculated (*Run 5* of Tables 3.7 and 3.8). For the second case the 1,000-meter long well is modeled, (*Run 10* of Tables 3.7 and 3.8).

Temperature dependent electrical conductivity affects the distribution of heating along the length of the horizontal well primarily for two reasons:

1. The total resistance of the formation will likely decrease with increasing temperature and therefore more current may be required to reach the 100 °C operating temperature limit. With increased levels of current, the losses in the casing increase and thus the casing heating becomes more substantial. Since the heating in the casing is non-uniform with axial location, the temperature distribution along the length of the wellbore will be more non-uniform

2. As the temperature distribution along the length of the wellbore becomes more non-uniform, the reservoir electrical conductivity adjacent to the wellbore will also become more non-uniform. The electrical conductivity will be greater in regions with higher temperatures. The current will seek the path of least resistance and thus more of the current will enter the casing towards the heel of the well where the temperature is greatest. This non-uniform distribution of current creates additional heating in the casing towards the heel of the well. As a consequence the non-uniformity of the temperature increases even further.

The correlation of electrical conductivity with temperature was obtained from *Sumbar, et. al.*, [80]. Using data from *Chute, et. al.* [108], and fitting the correlation so that the ambient electrical conductivity is 0.025 S/m at the initial reservoir temperature of 20.0 °C, results in the following:

$$\begin{aligned}\sigma(T) &= \sigma_0 (1 + a_1(T - T_0) + \\ &\quad a_2(T - T_0)^2 + a_3(T - T_0)^3) \\ a_1 &= 2.630 \cdot 10^{-2} \\ a_2 &= 1.706 \cdot 10^{-4} \\ a_3 &= 9.774 \cdot 10^{-7}\end{aligned}\tag{3.97}$$

Using Equation 3.97 the electrical conductivity of the reservoir at 100 °C is calculated and is 4.7 times greater than the electrical conductivity at initial reservoir temperature.

The electrical conductivity is calculated in *TETRAD* using the following equation,

$$\sigma(S_w, T) = f(T) \left(\sigma_w \frac{\phi^n}{P_\phi} S_w^2 + (1 - \phi) \sigma_r \right)\tag{3.98}$$

where σ_w and σ_r are the electrical conductivity of the connate water and rock, ϕ^n and P_ϕ are determined empirically from data, and S_w is the saturation of water in the void space of the reservoir defined by the porosity, ϕ . Using equations 3.97 and 3.98, Table 3.9 is produced and these data are input into the *TETRAD* numerical model.

Temperature °C	Electrical Conductivity	$f(T)$
20.0	0.025	1.00
30.0	0.032	1.28
40.0	0.040	1.60
50.0	0.049	1.97
60.0	0.060	2.39
70.0	0.072	2.86
80.0	0.085	3.40
90.0	0.100	4.01
100.0	0.117	4.70

Table 3.9: Electrical conductivity data for the reservoir as a function of temperature calculated using Equation 3.98 and the correlation shown in Equation 3.97.

To determine the effect that the temperature dependent electrical conductivity has on the axial temperature distribution, the input data for *TETRAD* invokes Table 3.9. The total current and production rate are fixed at 500 A RMS and 5.0 m³/day.

Since the temperature distribution in the reservoir is not uniform, the temperature dependent electrical conductivity will vary as the reservoir temperature changes. Thus the distribution of current in the reservoir along the length of the horizontal well is no longer constant, as shown on Figure 3.23, and the current in the well casing no longer increases linearly with distance towards the heel of the well. Consequently the power losses along the length of the casing, $\dot{q}_2(z)$, must be re-calculated by using the most recent current distribution along the length of the well. This is an iterative process that continues until there is no change in the current distribution along the length of the horizontal well for the updated calculation of the temperature distribution. Convergence of the current distribution is normally achieved in two to four iterations.

The variation of the current distribution along the length of the well becomes more pronounced when the axial temperature distribution is more variable, as is usually the case for the 1,000-meter long horizontal well. Four iterations are

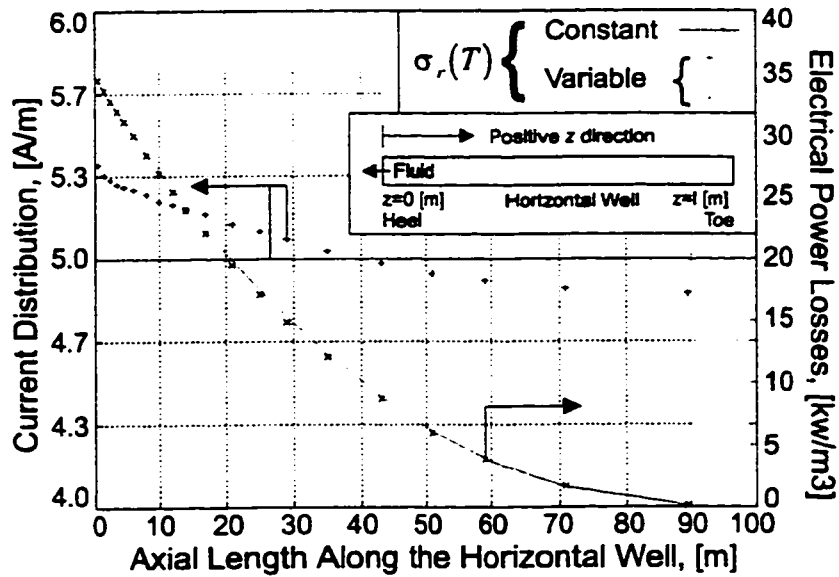


Figure 3.23: Run 5. Numerically calculated current distribution, $I(z)$, and electrical power losses, $q_2(z)$, along the length of the 100-meter long horizontal well, for constant and temperature dependent $\sigma_r(T)$, same regional thermal properties, moderate fluid production rate of $Q_t = 5.0 \text{ m}^3/\text{day}$, and after 30 days of heating. The current is adjusted to maintain a maximum operating temperature of $100 \text{ }^\circ\text{C}$.

necessary to achieve convergence for the horizontal well calculations. For the case of the 100-meter long well the axial temperature distribution is more uniform and satisfactory convergence is achieved in two iterations.

Figure 3.24 shows a comparison of the normalized temperature distribution calculated along the length of the 100-meter long horizontal well for temperature dependent and constant reservoir electrical conductivity. For these runs the current is adjusted to maintain a maximum temperature of $100 \text{ }^\circ\text{C}$. Also shown are the hysteresis and eddy current losses, $q_2(z)$, in the casing for the two cases. The total fluid production rate is $5.0 \text{ m}^3/\text{day}$ for both cases. The following inferences, which are valid only for the 100-meter long well, can be made from the calculation results shown in Figure 3.24. When the electrical conductivity of the formation is temperature dependent rather than constant, then:

1. The axial temperature distribution along the length of the well is less uniform as a result of redistribution of the current in the reservoir.
2. The hysteresis and eddy current losses in the casing increase dramatically as a result of the greater current needed to achieve a peak temperature of $100 \text{ }^\circ\text{C}$.

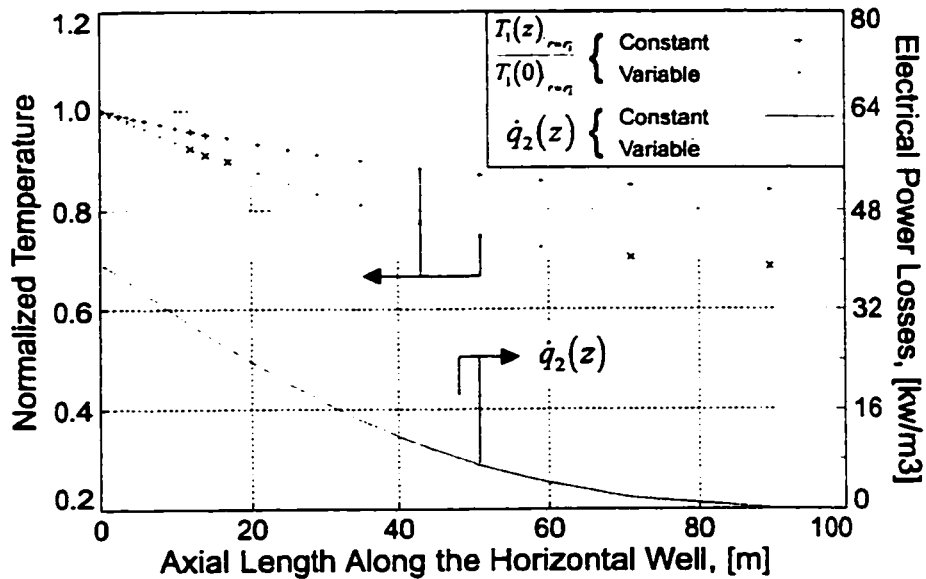


Figure 3.24: *Run 5*. The effect of the temperature dependent $\sigma_r(T)$ on the numerical calculation of the axial temperature distribution and the electrical power losses in the casing, $\dot{q}_2(z)$, along the length of the 100-meter long horizontal well, for same regional thermal properties, moderate fluid production rate of $Q_t = 5.0 \text{ m}^3/\text{day}$, and after 30 days of heating. The current is adjusted to maintain a maximum operating temperature of $100 \text{ }^\circ\text{C}$.

3. Hysteresis and eddy current losses are re-distributed and are greatly increased towards the heel of the well since the electrical conductivity of the reservoir is greater there, and thus more current enters the casing near the heel of the well.

Figure 3.25 shows the axial temperature distribution for the constant and temperature dependent electrical conductivity along the length of the 100-meter long horizontal well. For this example the input current is fixed at 500 A RMS for both cases. This figure shows that for the temperature dependent electrical conductivity, the maximum attainable temperature for a given electrical current is smaller than if the electrical conductivity is constant. This is consistent with expectations, since the increase in temperature increases the electrical conductivity (decreases the resistance) of the formation, thus enabling the current to flow through the formation with fewer losses and therefore less heating.

An important conclusion can be drawn from the analysis of temperature dependent electrical conductivity for the short, i.e., 100-meter long horizontal well. The axial analytic model will not accurately calculate the peak temperature or

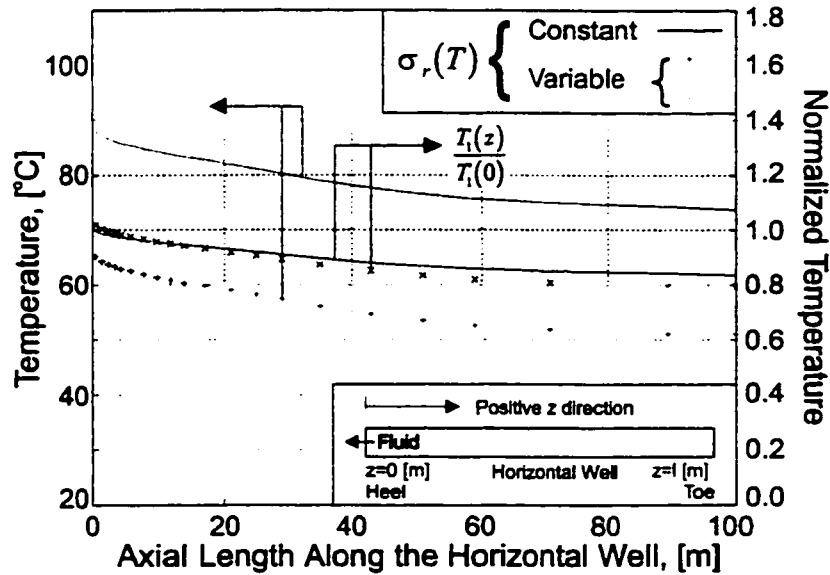


Figure 3.25: *Run 5*. Comparison of the numerically calculated temperature distribution along the length of a 100-meter long horizontal well for constant and temperature dependent $\sigma_r(T)$ with a constant total current of 500 A *RMS*, for same regional thermal properties, moderate fluid production rate of $Q_t = 5.0 \text{ m}^3/\text{day}$, and after 30 days of heating.

associated current requirements for a short electrically heated horizontal well in an oil reservoir. The calculated peak temperature will be overestimated and the current will be underestimated. This is a direct consequence of significant electrical heating occurring in the reservoir for the shorter well. However, the axial semi-analytic model can be used to obtain a qualitative appraisal of the uniformity of the axial temperature distribution along the horizontal well.

The second test of temperature dependent electrical conductivity is done for the 1,000-meter long horizontal well. The procedure for the defining input data set is as follows,

1. Set the operating current for the temperature dependent electrical conductivity case to a maximum value 1,000 A *RMS* and adjust the flow rate until the maximum peak temperature in the casing is 100 °C. This step is required since the interpolation function for $\dot{q}_2(z)$ is only valid for currents less than 1,000 A *RMS*.
2. For the constant electrical conductivity case set the flow rate to the value determined in the previous step and adjust the electrical current until a

maximum peak temperature in the casing of $100\text{ }^{\circ}\text{C}$ is obtained. This step is performed since a smaller current will be required to achieve the desired peak temperature if the electrical conductivity is constant.

3. Normalize the temperature profiles for the two cases and compare the results.
4. Now calculate the constant electrical conductivity case using the axial semi-analytic model.

Figure 3.26 compares the normalized temperature profiles for the two different cases. The required flow rate to give a peak temperature of $100\text{ }^{\circ}\text{C}$ for the temperature dependent electrical conductivity case is $13.0\text{ m}^3/\text{day}$.

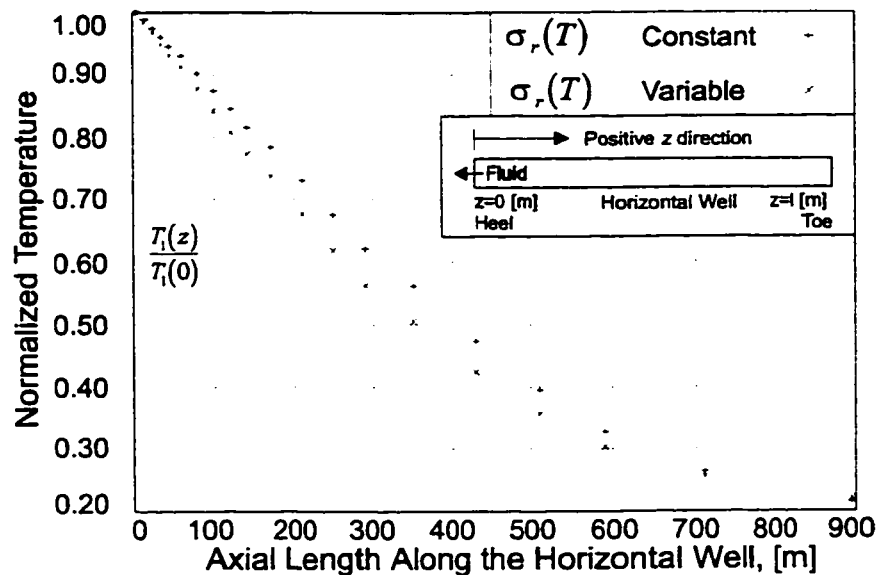


Figure 3.26: *Run 10*. Comparison of the normalized temperature distribution for variable and constant $\sigma_r(T)$, along the length of a 1,000-meter long horizontal well, calculated using numerical simulation, with the same regional thermal properties, moderate fluid production rate of $Q_t = 25.0\text{ m}^3/\text{day}$, and after 30 days of heating.

The effect of variable electrical conductivity is minimal for the 1,000-meter long horizontal well as shown in Figures 3.26 and 3.27. The current for the constant electrical conductivity case had to be decreased by only 98.3 A (about 10%) to achieve the desired peak temperature of $100\text{ }^{\circ}\text{C}$. Even though there is a minor redistribution of the current along the length of the horizontal well as a result of the temperature dependent electrical conductivity, as suggested in Figure 3.26, the hysteresis and eddy current losses in the casing control the thermal response of the

horizontal well for both cases and the temperature distribution remains virtually unchanged. Redistribution of current in the formation is relatively minor. This calculation demonstrates that for a long horizontal well the assumption of constant electrical conductivity that was necessary to derive the axial semi-analytic model is valid. For shorter wells this may not be the case.

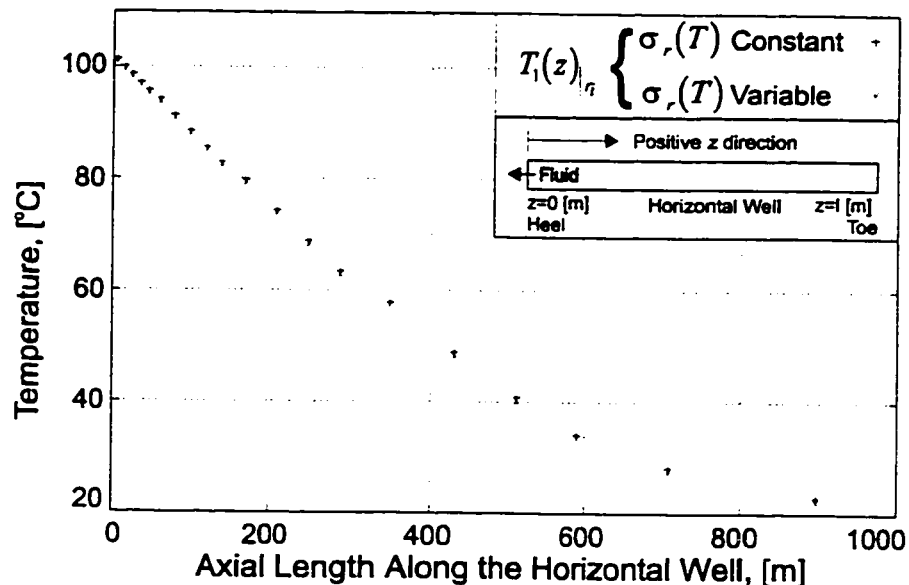


Figure 3.27: *Run 10*. Comparison of the temperature distribution for variable and constant $\sigma_r(T)$, along the length of a 1,000-meter long horizontal well, calculated using numerical simulation and the axial semi-analytic model (constant $\sigma_r(T)$ only), with the same regional thermal properties, moderate fluid production rate of $Q_t = 25.0 \text{ m}^3/\text{day}$, and after 30 days of heating.

Table 3.10 summarizes the power losses in the casing and reservoir, the effective resistance of the casing and reservoir, and the electrical-oil ratio for each of the runs summarized in Tables 3.7 and 3.8. For consistency, only the data calculated using *TETRAD* is presented in Table 3.10. For all the data summarized in Table 3.10, the input current is adjusted so that a maximum operating temperature after 30 days of heating of $100 \text{ }^\circ\text{C}$ is obtained. The magnitudes of the resulting currents are summarized in Table 3.8. The electrical-oil ratio is the ratio of total input power divided by the total *oil* flow rate and is presented in common oil field units: $\text{kW} \cdot \text{hr}/\text{barrel}$.

The following inferences are made from these summary data,

1. The electrical-oil ratio is the ratio of electrical energy consumed to volume of

Run	Losses		Resistance		Electrical- Oil Ratio <i>kW · hr/barrel</i>
	Casing <i>kW</i>	Reservoir <i>kW</i>	Casing <i>mΩ</i>	Reservoir <i>mΩ</i>	
100 meter runs					
1	3.07	58.45	13.32	253.68	469.47
2	3.90	71.26	13.94	253.68	57.36
3	4.85	85.34	14.42	253.68	34.41
4	3.90	71.26	13.94	253.68	57.36
5	8.28	89.42	15.45	166.90	74.56
1,000 meter runs					
6	122.95	19.65	158.77	25.37	54.41
7	159.01	25.37	159.01	25.37	28.14
8	159.01	25.37	159.01	25.37	14.07
9	159.01	25.37	159.01	25.37	28.14
10	159.01	19.83	159.01	19.83	27.30

Table 3.10: Summary of the validation runs.

produced oil. For small production rates, this ratio is large. It becomes smaller as the production rate increases. Of interest is how low the electrical energy costs are. If the cost for electrical power is $\$0.05/(kW \cdot hr)$, then the energy costs range from $\$0.70/\text{barrel}$ to $\$3.73/\text{barrel}$ (Run 1 is not included in the calculation since the low rate makes the well uneconomic).

2. For the shorter well, at least 90% of the electrical power is dissipated in the reservoir. For the longer well, most of the power is dissipated in the casing with only 13.76% of the power used to electrically heat the reservoir. It is worth restating at this point that previous authors ignored the hysteresis *and* eddy current losses in the casing, thus assuming that enormous currents can be used to heat the reservoir, [3], [27], [2], and [28], made a critical error in their analysis.
3. The overall resistance of the casing for the shorter well is much smaller than the resistance of the reservoir. For the longer well, the opposite is true. In a

field application of electrical heating using a long horizontal well the actual resistance of the casing will affect the uniformity with which the current collects along the length of the well. In this thesis, except for *Run 5* and *10*, it was assumed that the system is engineered so that the current distribution is uniform along the length of the horizontal well. The semi-analytic treatment of non-uniform current distribution along the length of the horizontal well is an issue for further research.

In conclusion, the solution for the heat transfer problem for electrical heating of an oil reservoir from a horizontal well has been presented. The semi-analytic models have been validated using simplified analytic models and numerical simulation.

The models can be used for many different types of calculations. They can for instance, be used to calculate power requirements and power supply specifications, cable sizing and cooling system requirements. The mathematical techniques and approach used to solve the multi-region problem can, with little modification, be used to solve many different types of physical problems.

Chapter 4

Conclusions and Recommendations for Further Study

4.1 Conclusions

It has been shown through semi-analytic models developed in this thesis and by adaptation of a commercial numerical simulator, that electrical heating can be an effective method to heat a long horizontal well.

A finite-difference time-domain solution of Maxwell's equations was developed to determine the hysteresis and eddy current losses in the casing. The hysteresis and eddy current losses were expressed as a polynomial function of total current in the casing. This function was then incorporated into the heat transfer problem for a long horizontal well so that radial and axial semi-analytic solutions could be derived.

The magnitude of the hysteresis and eddy current losses calculated for the casing in a long horizontal well cannot be ignored. The increase in temperature resulting from these losses limits the magnitude of the current that can be used in the electrical heating process using long horizontal wells. Typical operating currents are limited to less than 1,000 to 1,500 A *RMS*. To design a system to handle larger currents, special non-magnetic material, like aluminium, may be required in the construction of the tubing and casing to eliminate the effect of hysteresis losses.

The analysis of the hysteresis and eddy current losses in a typical casing indicates that *hysteresis losses can account for up to 30 % of the total losses at relatively small current levels of 250 A RMS*. At current levels between 250 and 400

A *RMS* hysteresis losses can account for as much as 40 % of the total losses. Also, the hysteresis effect will cause a re-distribution of the current in the casing which can result in total power losses that are *three* times greater than if there was no hysteresis.

Subject to the assumptions made in this thesis, the following conclusions arise from the radial and axial semi-analytic solutions of the heat transfer problem:

1. The temperature distribution along the length of a long horizontal wellbore is not uniform and depends almost entirely on the hysteresis and eddy current losses in the casing and heat transfer from the casing into the wellbore and adjacent reservoir, rather than the direct resistive heating of the reservoir.
2. The hysteresis and eddy current losses in the casing of a long horizontal well will limit the total current to values that are relatively small over much of the length of the well. For the properties of steel casing considered in this thesis, 1,000 *A RMS* poses an upper limit to the total current that can be used.
3. For a long horizontal well, electrical heating by current flow in the reservoir adjacent to the casing is insignificant, contributing to a temperature rise of less than 5.0 °C over a heating period of one year.
4. Electrically heated long horizontal wells may not heat the reservoir as efficiently as electrically heated short wells. Short wells, between 100 and 200 meters long, promote direct heating of the reservoir by current flow in the reservoir for total currents less than 1,000 *A RMS*. This results in a temperature distribution that is relatively uniform along the length of the wellbore when compared to the temperature distribution for a long horizontal well.
5. The impact of temperature dependent electrical conductivity on the temperature distribution and total current in a long horizontal well is minor. On the other hand, the impact of temperature dependent electrical conductivity on the temperature distribution and the total current for a short horizontal well is significant.

6. The validity of the axial semi-analytic model is restricted to problems in which the effects of temperature dependent electrical conductivity are minimal, i.e., long horizontal wells.

4.2 Recommendations for Further Study

There are many opportunities for additional research. The following are recommendations that will immediately advance the work that has been presented in this thesis.

1. Develop the boundary condition for heat flow into the wellbore from the steel pipe so that an overall heat transfer coefficient can be used to determine the heat flow as a function of z . Overall heat transfer coefficients for oilfield tubulars, particularly for steam and hot water injection, have been presented in the literature. However, they do not account for variable flow velocity in the pipe, [113], [116], and [114], and [25]. This may require that a numerical solution to the heat transfer models in the three regions be derived. The model can then be made sufficiently general to be used for thermal processes such as steam assisted gravity drainage (SAGD) by incorporating the conservation equations of mass, momentum, and energy and various correlations for the variation of physical properties, such as fluid viscosity, as a function of temperature.
2. The analytic or numerical treatment of a non-uniform current distribution along the length of the horizontal is an issue for additional research. In this thesis, the current is assumed to collect uniformly along the length of the horizontal well. However, wavelength effects and the inherent resistance of the pipe will influence the uniformity of the current distribution.
3. A fully integrated numerical model is the next step for the advancement of the solution of the heat transfer problem. The approach might be to incorporate the hysteresis and eddy current losses in the casing into an existing commercial reservoir model, like *TETRAD*. The numerical model can then be developed to account for the variation of the electrical conductivity of the

steel as a function of temperature, the non-uniform current and fluid distribution in the reservoir, the change in total production rate due to the change in oil viscosity, and so on. The analytic tools developed in this thesis provide a check for additional numerical work.

4. The numerical representation of the hysteresis loops in the finite difference time domain model should be further investigated. The *EM Pipe Loss* model uses a novel technique that worked well. However the technique depends on obtaining actual data, which can be expensive. Other numerical methods, primarily the finite element approach, have successfully used Preisach's Theory to model hysteresis loops, however, for different types of problems than presented in this thesis, [117], [93], [90], [92], and [91]. The claim of *Preisach's Theory* is that the technique actually models the physical process of hysteresis. It may be possible to extract the essential properties of the oil field tubulars so that *Preisach's Theory* can be used to generate the family of hysteresis loops and be used in the finite difference time domain solution.

Bibliography

- [1] T. Loga, "Finite Element Method Solutions For Eddy Current Losses In Steel Wellbore Casings," Master's thesis, University of Alberta, Edmonton, Alberta, Canada, 1994.
- [2] M. R. Islam, S. S. Wadadar, and A. Bansal, "Enhanced Oil Recovery of Ugnu Tar Sands of Alaska Using Electromagnetic Heating With Horizontal Wells," in *The International Arctic Technology Conference*, no. SPE 22177, (Anchorage, Alaska), SPE, May 29-31, 1991.
- [3] J. E. Killough and J. A. Gonzalez, "A Fully Implicit Model for Electrically Enhanced Oil Recovery," in *The 61st Annual Technical Conference and Exhibition*, no. SPE 15605, (New Orleans, USA), Society of Petroleum Engineering, October 5-8, 1986.
- [4] T. N. T. F. on Oil Sands Strategies of the Alberta Chamber of Resources, "The Oil Sands: A New Energy Vision for Canada," April, 1995. Erdal Yildirim, D. Eng. Sc., Chairman, National Task Force on Oil Sands Strategies.
- [5] S. J. Springer, P. D. Flach, D. S. Christie, K. Porter, and G. C. Scott, "A Review of the First Five Hundred Horizontal Wells in Western Canada," in *The CIM 1993 Annual Technical Conference in Calgary*, no. CIM 93-19, pp. 102-118, Canadian Institute of Mining Petroleum Division, May 9-12, 1993.
- [6] S. J. Springer, P. D. Flach, D. S. Christie, K. Porter, and G. C. Scott, "A Review of the First 1,500 Hundred Horizontal Wells in Western Canada," in *The Fourth SPE/CIM Annual One Day Conference on Horizontal Well*

Technology and Economics, no. CIM 94-11-22, pp. 1-18, Canadian Institute of Mining Petroleum Division, November 22, 1994.

- [7] J. P. Fossey, R. J. Morgan, and L. A. Hayes, "Development of the Pelican Lake Area: Reservoir Considerations and Horizontal Technologies.," *Journal of Canadian Petroleum Technology*, pp. 53-56, June, 1997.
- [8] T. Fontaine, L. Hayes, and G. Reese, "Development of Pelican Lake Area Using Horizontal Well Technologies," *Journal of Canadian Petroleum Technology*, vol. 32, pp. 32-45, March-April, 1993.
- [9] R. M. Butler, G. S. McNab, and H. Y. Lo, "Theoretical Studies on the Gravity Drainage of Heavy Oil During In-Situ Steam Heating," *Journal of Canadian Petroleum Technology*, vol. 59, pp. 455-460, August, 1979.
- [10] R. M. Butler and D. J. Stephens, "The Gravity Drainage of Steam-Heated Oil to Parallel Horizontal Wells," *Journal of Canadian Petroleum Technology*, vol. 20, pp. 90-96, April-May, 1979.
- [11] R. M. Butler, "A New Approach to the Modeling of Steam-Assisted Gravity Drainage," *Journal of Canadian Petroleum Technology*, vol. 24, pp. 42-52, May-June, 1985.
- [12] N. R. Edmunds, J. A. Haston, and D. A. Best, "Analysis and Implementation of Steam Assisted Gravity Drainage at the AOSTRA UTF," in *The 4th International Conference of Heavy Crude and Tar Sands*, UNITAR/UNDP, no. 125, (Edmonton, Alberta, Canada), pp. 95-103, AOSTRA/UNDP, August, 1988.
- [13] N. R. Edmunds, J. A. Kovalsky, and S. D. Gittins, "Review of the Phase A Steam Assisted Gravity Drainage Test at the AOSTRA UTF," in *The First International Thermal Operations Symposium*, no. SPE 21529, (Bakersfield, USE), pp. 182-189, Society of Petroleum Engineers, February 7-8, 1991.
- [14] N. R. Edmunds and S. D. Gittins, "Effective Steam Assisted Gravity Drainage to Long Horizontal Well Pairs," in *The CIM/AOSTRA Technical Conference of the Petroleum Society of CIM*, no. CIM/AOSTRA 91-65, (Banff, Alberta, Canada), April 21-24, 1991.

- [15] R. M. Butler, "Gravity Drainage to Horizontal Wells," *Journal of Canadian Petroleum Technology*, vol. 31, pp. 31–37, April, 1992.
- [16] S. Sugianto and R. M. Butler, "The Production of Conventional Heavy Reservoirs with Bottom Water Using Steam-Assisted Gravity Drainage," *Journal of Canadian Petroleum Technology*, vol. 29, pp. 78–86, March-April, 1990.
- [17] K. E. Kisman and K. C. Yeung, "Numerical Study of the SAGD Process in the Burnt Lake Oil Sands Lease," in *The International Heavy Oil Symposium*, no. SPE 30276, (Calgary, Alberta, Canada), pp. 275–286, Society of Petroleum Engineers, June 19-21, 1995.
- [18] N. R. Edmunds and J. C. Suggett, "Design of a Commercial SAGD Heavy Oil Project," in *The International Heavy Oil Symposium*, no. SPE 30277, (Calgary, Alberta, Canada), pp. 286–294, Society of Petroleum Engineers, June 19-21, 1995.
- [19] N. R. Edmunds, R. Penny, and P. J. Jespersen, "Sceptre Tangleflags: Successful Conversion of a Horizontal Thermal Producer to a Flowing Well," in *The Third SPE/CIM Annual One Day Conference on Horizontal Well Technology and Economics*, (Calgary, Alberta, Canada), pp. 188–202, Society of Petroleum Engineers, November 15, 1993.
- [20] P. J. Jespersen and T. J. C. Fontaine, "The Tangleflags North Pilot: A Horizontal Well Steamflood," *Journal of Canadian Petroleum Technology*, vol. 32, pp. 52–57, May, 1993.
- [21] J. K. Donnelly and M. J. Chmilar, "The Commercial Potential of Steam Assisted Gravity Drainage," in *The International Heavy Oil Symposium*, no. SPE 30278, (Calgary, Alberta, Canada), pp. 295–308, Society of Petroleum Engineers, June 19-21, 1995.
- [22] V. Oballa and W. L. Buchanan, "Single Horizontal Well in Thermal Recovery Processes," in *The Society of Petroleum Engineering, Canadian Section, 2nd International Conference and Trade Show on Horizontal Well Technology*, no. SPE 37115, (Calgary, Alberta, Canada), pp. 659–670, November 18-20, 1996.

- [23] E. B. M., "Conceptual Steamflood Designs Using Horizontal Wells to Maximize Project Profitability," in *The International Heavy Oil Symposium*, no. SPE 30279, (Calgary, Alberta, Canada), pp. 309–318, Society of Petroleum Engineers, June 19-21, 1995.
- [24] B. D. Huff, "Horizontal Well Applications: Present and Future," in *The International Heavy Oil Symposium*, no. SPE 30283, (Calgary, Alberta, Canada), pp. 359–368, Society of Petroleum Engineers, June 19-21, 1995.
- [25] D. A. Best, R. P. Lesage, and J. E. Arthur, "Steam Circulation in Horizontal Wellbores," in *The Seventh Symposium on Enhanced Oil Recovery in Tulsa, Oklahoma*, no. SPE paper 20203, pp. 299–312, April 22-25, 1990.
- [26] N. Edmunds, "Private Communication," April, 1997.
- [27] S. Wadadar and M. Islam, "Numerical Simulation of Electromagnetic Heating of Alaskan Tar Sands Using Horizontal Wells," in *The CIM/AOSTRA Technical conference of the Petroleum Society of CIM*, no. CIM/AOSTRA 91-35, (Banff, Alberta, Canada), Canadian Institute of Mining Petroleum Division, 1991.
- [28] M. McBride, R. D. Ostermann, A. Chakma, and M. Islam, "Numerical Simulation of a Novel Recovery Technique for Heavy Oil Reservoirs with Bottom Water," in *The Fifth UNITAR/UNDP Conference on Heavy Crude and Tar Sands, postponed until 1992*, no. 84, (Caracas, Venezuela), 1991.
- [29] C. P. Stroemich, F. E. Vermeulen, F. S. Chute, and E. Sumbar, "Wellbore Power Transmission For In-Situ Electrical Heating," *Alberta Oil Sands Technology and Research Journal of Research*, vol. 6, pp. 273–294, 1990.
- [30] T. K. Perkins, "Viscous Oil Production Using Electrical Current Heating and Lateral Drain Holes," *U.S. Patent No. 4,489,782*, 1984.
- [31] E. R. Abernathy, "Production Increase of Heavy Oils by Electromagnetic Heating," *Journal of Canadian Petroleum Technology*, pp. 44–49, July-September, 1976.
- [32] R. G. Bosisio, J. L. Cambon, C. Chavarie, and D. Klavana, "Experimental Results on the Heating of Athabasca Tar Sand Samples with Microwave Power," *Journal of Microwave Power*, vol. 12, pp. 301–307, 1977.

- [33] J. E. Bridges, A. Taflove, and R. H. Snow, "Net Energy Recoveries for the In-Situ Dielectric Heating of Oil Shales," in *The Proceedings of the 1978 Oil Shale Symposium*, (Colorado School of Mines, Golden Colorado, USA), April 22-24, 1978.
- [34] F. E. Vermeulen, F. S. Chute, and M. R. Cervenak, "Physical Modeling of the Electromagnetic Heating of Oil Sand and Other Earth-Type and Biological Materials," *Canadian Electrical Engineering Journal*, vol. 4, pp. 19-28, 1979.
- [35] J. E. Bridges, G. C. Sresty, A. Taflove, and R. H. Snow, *The Future of Heavy Crudes and Tar Sands*, ch. RF Heating To Recover Oil From Utah Tar Sands, pp. 396-409. New York: McGraw-Hill Inc., 1981.
- [36] F. S. Chute, F. E. Vermeulen, and M. R. Cervenak, "On the Electromagnetic Heating of Low Loss Materials Using Induction Coils," *Canadian Electrical Engineering Journal*, vol. 6, pp. pages 20-28, May, 1981.
- [37] F. E. Vermeulen and F. S. Chute, "Electromagnetic Techniques in the In-Situ Recovery of Heavy Oils," *Journal of Microwave Power*, vol. 18, no. 1, pp. 15-29, 1983.
- [38] W. B. Bleakley, "Unique Electrothermic Recovery Method Gets Rocky Mountain Test," *Oil and Gas J*, pp. 162-163, December 29, 1969.
- [39] R. G. McPherson, F. S. Chute, and F. E. Vermeulen, "Recovery of Athabasca Bitumen with the Electromagnetic Flood (EMF) Process," *Journal of Canadian Petroleum Technology*, vol. 24, no. 1, pp. 45-51, 1985.
- [40] J. E. Bridges, G. C. Sresty, H. L. Spencer, and R. A. Wattenbarger, "Electromagnetic Stimulation of Heavy-Oil Wells," in *The 3rd International Conference of Heavy Crude and Tar Sands*, UNITAR/UNDP, UNITAR/UNDP paper 1221, (Long Beach, California, USA), pp. 615-622, July 22-31, 1985.
- [41] J. E. Bridges, G. C. Sresty, and H. Dev, "In-Situ RF Heating For Oil Sand and Heavy Oil Deposits," in *The 3rd International Conference of Heavy Crude and Tar Sands*, UNITAR/UNDP paper 1236, (Long Beach, California, USA), pp. 797-803, July 22-31, 1985.

- [42] G. C. Sresty, H. Dev, R. H. Snow, and J. E. Bridges, "Recovery of Bitumen from Tar Sand Deposits with Radio Frequency Process," *Society of Petroleum Engineering*, pp. 85–94, January, 1986.
- [43] E. S. Kim, *Reservoir Simulation of In-Situ Electromagnetic Heating of Heavy Oils*. PhD thesis, Texas A and M University, College Station, Texas, 1988.
- [44] G. T. Perry and W. S. Warner, "Heating Oil Wells by Electricity," *U.S. Patent No. 45,584*, July 4, 1865.
- [45] A. A. Popov, "Experimental Introduction of Electric Heating of Wellbore Area in Wells of Volvoxhskil Npu Fields," *Nauch. - Tekh. Sb. Ser. Neftepromyslovoe Delo*, vol. 3, pp. 23–25, 1969.
- [46] W. Gill, "Method and Apparatus for Secondary Recovery of Oil," *U.S. Patent No. 3,507,330*, 1970.
- [47] Editorial, "Alternating Current Heats Heavy Oil for Extra Recovery," *World Oil*, May, 1970.
- [48] J. C. Todd and E. P. Howell, *The Oil Sands of Canada-Venezuela*, vol. 17, ch. Numerical Simulation of In-Situ Electrical Heating to Increase Oil Mobility, pp. 631–647. Canadian Institute of Mining Petroleum Division, 1977.
- [49] S. A. El-Feky, *Theoretical and Experiment Investigation of Oil Recovery by the Electrothermic Technique*. PhD thesis, University of Missouri-Rolla, 1977.
- [50] A. H. Harvey and S. A. El-Fekey, "Selective Heating Could Boost Oil Recovery," *Journal of Petroleum Technology*, vol. 76, no. 46, pp. 185–190, 1978.
- [51] F. S. Chute, F. E. Vermeulen, and M. R. Cervenak, "Physical Modeling of the Electrical Heating of the Oil Sand Deposits," Tech. Rep. AOSTRA Agreement No. 31, Applied Electromagnetics Group at the University of Alberta, 1978.
- [52] A. H. Harvey, M. D. Arnold, and S. A. El-Fekey, "Selective Electric Reservoir Heating," *Journal of Canadian Petroleum Technology*, pp. 47–57, July-September, 1979.

- [53] D. E. Towson, *The Future of Heavy Crudes and Tar Sands*, ch. The Electric Pre-heat Recovery Process, pp. 410–412. New York, NY, USA: McGraw-Hill Inc., 1980.
- [54] A. H. Harvey and M. D. Arnold, “A Radial Model For Estimating Heat Distribution in Selective Electric Reservoir Heating,” *Journal of Canadian Petroleum Technology*, pp. 37–41, October-December, 1980.
- [55] W. Gill, *The Future of Heavy Crudes and Tar Sands*, ch. The Electrothermic System for Enhanced Oil Recovery, pp. 469–473. New York: McGraw-Hill Inc., 1981.
- [56] A. H. Harvey, “Influence of Adjacent Conductive Formations on the Selective Electric Reservoir Heating Process,” *Society of Petroleum Engineering Journal*, vol. 22, no. 5, pp. 750–754, 1982.
- [57] A. D. Hiebert, F. E. Vermeulen, F. S. Chute, and C. E. Capjack, “A Simulation Code for Investigating the 2-D Heating of Material Bodies by the Action of Low Frequency Electric Fields,” *Appl. Math. Modeling*, vol. 7, pp. 366–371, 1983.
- [58] A. Khosla and D. E. Towson, “Application of Computer Modeling to the PCEJ Electric Pre-heat/Steam-Drive Athabasca,” in *The 36th annual meeting of the Petroleum Society of CIM*, no. 85-36-51, p. 15, Soc. of CIM, Edmonton, June 2-5, 1985.
- [59] B. Rintoul, “Electromagnetic Well Stimulation at White Wolf,” *Pacific Oil World*, pp. 10–11, October, 1986.
- [60] D. A. Hiebert, *Numerical Simulation of the Electric-Preheat and Steam-Drive Bitumen Recovery Process for the Athabasca Oil Sands*. PhD thesis, University of Alberta, Edmonton, Alberta, Canada, 1986.
- [61] A. D. Hiebert, F. E. Vermeulen, F. S. Chute, and C. Capjack, “Numerical Simulation Results for the Electrical Heating of Athabasca Oil-Sand Formations,” *Society of Petroleum Engineering Journal*, pp. 76–84, 1986.
- [62] F. S. Chute and F. E. Vermeulen, “Present and Potential Applications of Electromagnetic Heating in the In-situ Recovery of Oil,” *Alberta Oil Sands Technology and Research Journal of Research*, vol. 4, pp. 19–33, 1987.

- [63] F. S. Chute, F. E. Vermeulen, and L. G. Stevens, "A Numerical Simulation of an Electric Pre-heat Pilot for In-Situ Recovery of Oil from the Athabasca Oil Sands," *Alberta Oil Sands Technology and Research Journal of Research*, vol. 3, no. 3, pp. 139–154, 1987.
- [64] H. L. Spencer, K. A. Bennett, and J. E. Bridges, "Application of the IITRI/Uentech Electromagnetic Stimulation Process to Canadian Heavy Oil Reservoirs," in *The 4th International Conference of Heavy Crude and Tar Sands, UNITAR/UNDP*, no. 42, (Edmonton, Alberta, Canada), pp. 7–12, AOSTRA/UNDP, August, 1988.
- [65] L. E. Doublet, "Evaluation of Electromagnetic Stimulation of Texas Heavy Oil Reservoirs," Master's thesis, Texas A and M University, College Station, 1988.
- [66] F. E. Vermeulen, F. S. Chute, and R. G. McPherson, "Physical Modeling of Electrothermal Processes in Oil Sand," *Alberta Oil Sands Technology and Research Journal of Research*, vol. 4, pp. 299–305, 1988.
- [67] R. A. Wattenbarger and F. W. McDougal, "Oil Production Response to In-Situ Electrical Resistance Heating (ERH)," *Journal of Canadian Petroleum Technology*, pp. 45–50, November-December, 1988.
- [68] F. S. Chute and F. E. Vermeulen, *AOSTRA Technical Handbook on Oils Sands*, ch. Bitumens and Heavy Oils Chapter 13, pp. 339–376. Edmonton, Alberta: AOSTRA, 1989.
- [69] E. Sumbar, F. E. Vermeulen, and F. S. Chute, "MEGAERA 4.0 A Code for Modeling Transient Heat Flow Induced by Quasi-static Electric Fields in Lossy Media," tech. rep., University of Alberta, Applied Electromagnetics Group, 1989. Applied Electromagnetics Group Internal Report.
- [70] A. D. Hiebert, F. E. Vermeulen, F. S. Chute, and C. Capjack, "Application of Numerical Modeling the Simulation of the Electric-Preheat Steam-Drive (EPSD) process in Athabasca Oil Sands," *Journal of Canadian Petroleum Technology*, vol. 28, pp. 74–86, September-October, 1989.
- [71] B. C. W. McGee, "The 'Visco-Skin' Effect in Heavy Oil Reservoirs," Master's thesis, University of Calgary, Calgary, Alberta, Canada, 1989.

- [72] F. S. Chute and F. E. Vermeulen, "Physical Modeling of Systems Involving Electromagnetic Heating of Materials," *IEEE Transactions on Education*, vol. 33, May, 1990.
- [73] B. C. W. McGee, "EORSIM An Electromagnetic Stimulation Productivity Calculation Program," *SPE Computer Applications*, pp. 12-18, September-October, 1990.
- [74] B. A. Baylor, J. B. Maggard, and R. A. Wattenbarger, "Improved Calculation of Oil Production Response to Electrical Resistance Heating," in *The 65th SPE Annual Technical Conference and Exhibition, New Orleans*, no. SPE paper 20482, pp. 23-26, September, 1990.
- [75] J. O. S. Pizarro and O. V. Trevisan, "Electrical Heating of Oil Reservoir Numerical Simulation and Field Test Results," *Journal of Petroleum Technology*, pp. 1320-1326, October, 1990.
- [76] R. J. Davison, "Electromagnetic Stimulation of Lloydminster Heavy Oil Reservoirs: Field Test Results," in *The CIM/AOSTRA Technical conference of the Petroleum Society of CIM*, no. CIM/AOSTRA 91-49 in CIM/AOSTRA 91-31, pp. 31-1 to 31-17, April 21-24, 1991.
- [77] G. A. Romney, A. Wong, and J. H. McKibbin, "A Preview of an Electromagnetic Heating Project," in *The CIM/AOSTRA Technical conference of the Petroleum Society of CIM*, no. CIM/AOSTRA 91-109, (Banff, Alberta, Canada), April 21-24, 1991.
- [78] B. C. W. McGee, P. Sigmund, and H. L. Spencer, "Visco-Skin Effect in Heavy Oil Reservoirs," in *The Fifth UNITAR/UNDP Conference on Heavy Crude and Tar Sands*, no. 1, (Caracas, Venezuela), pp. 157-165, 1991.
- [79] S. A. Rice, A. L. Kok, and C. J. Neate, "A Test of the Electric Heating Process as a Means of Stimulating the Productivity of an Oil Well in the Schoonebeek Field," in *The CIM 1992 Annual Technical Conference in Calgary*, (Calgary, Alberta, Canada), Canadian Institute of Mining Petroleum Division, August, 1992.
- [80] E. Sumbar, F. S. Chute, and F. E. Vermeulen, "Electromagnetic In-Situ

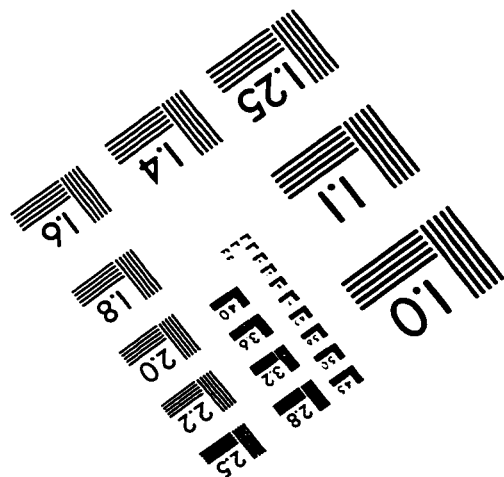
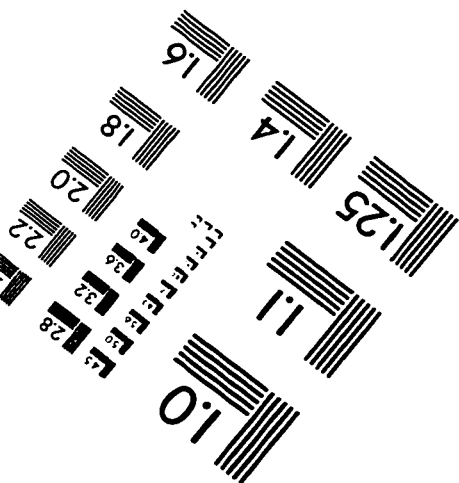
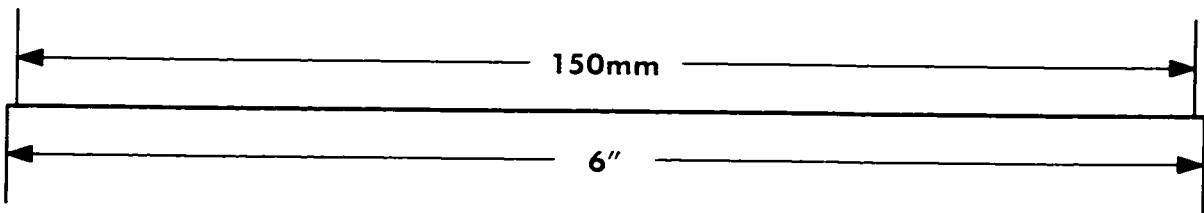
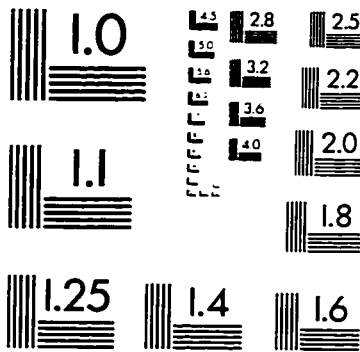
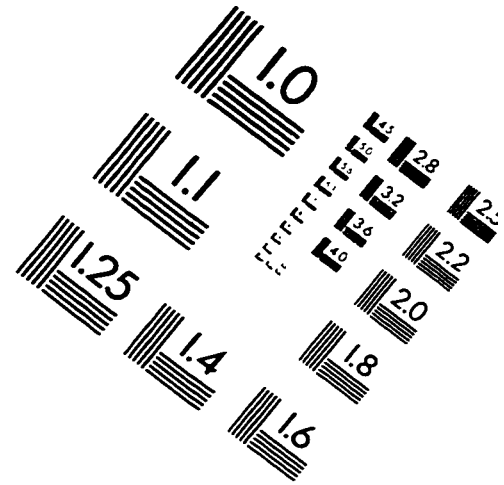
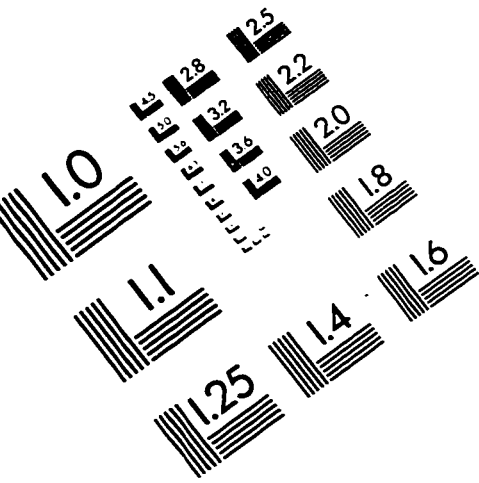
- Heating of Heavy Oil Reservoirs to Increase Production Rates,”
International Microwave Power Institute, vol. 27, no. 2, pp. 67–74, 1992.
- [81] L. Yu, B. C. W. McGee, F. Chute, and F. E. Vermeulen, “Electromagnetic Reservoir Heating With Vertical Well Supply and Horizontal Well Return Electrodes,” *U.S. Patent Number: 5,339,898*, 1994.
- [82] P. K. W. Vinsome, B. C. W. McGee, F. E. Vermeulen, and S. F. Chute, “Electrical Heating,” *Journal of Canadian Petroleum Technology*, vol. 33, pp. 29–35, April, 1994.
- [83] B. C. W. McGee, F. E. Vermeulen, and C. L. Yu, “Electrical Heating with Horizontal and Vertical Wells,” in *The Petroleum Society 47th Annual Technical Meeting on Advances in Resource Development*, 1995-12-30, (Calgary, Alberta), June 10-12, 1996.
- [84] B. C. W. McGee and F. E. Vermeulen, “Electrical Heating with Horizontal Wells, the Heat Transfer Problem,” in *The Society of Petroleum Engineering, Canadian Section, 2nd International Conference and Trade Show on Horizontal Well Technology*, no. SPE 37117, (Calgary, Alberta, Canada), pp. 685–698, November 18-20, 1996.
- [85] R. M. Bozorth, *Ferromagnetism*. Piscataway, New Jersey: IEEE Press, 1993. An IEEE Press Classic Reissue.
- [86] K. Zakrzewski and F. Pietras, “Method of Calculating the Electromagnetic Field and Power Losses in Ferromagnetic Materials, Taking into Account Magnetic Hysteresis,” *Proc. IEE*, vol. 118, November, 1971.
- [87] F. S. Chute, “FDTD Course Notes.” University of Alberta, 1994.
- [88] C. C. Mattax and L. Dalton, Robert, *Reservoir Simulation*. Richardson, Texas: Society of Petroleum Engineers Inc., First Edition ed., 1990.
- [89] R. L. Stoll, *The Analysis of Eddy Currents*. Clarendon Press - Oxford, 1974.
- [90] S. N. Talukdar and J. R. Bailey, “Hysteresis Models for System Studies,” *IEEE Transactions on Power Apparatus and Systems*, vol. PAS-95, pp. 1429–1434, July-August, 1976.

- [91] J. W. Macki, P. Nistri, and P. Zecca, "Mathematical Models for Hysteresis," *Society for Industrial and Applied Mathematics*, vol. 35, pp. 94–123, March, 1993. SIAM Review.
- [92] M. A. Coulson, R. D. Slater, and R. R. S. Simpson, "Representation of Magnetic Characteristic, Including Hysteresis, using Preisach's Theory," *IEE Proceedings*, vol. 124, pp. 895–898, October, 1977.
- [93] S. R. Naidu, "Simulation of the Hysteresis Phenomenon using Preisach's Theory," *IEE Proceedings*, vol. 137, pp. 73–79, March, 1990.
- [94] E. C. Jordan and K. G. Balmain, *Electromagnetic Waves and Radiating Systems*. Englewood Cliffs, New Jersey: Prentice-Hall Electrical Engineering Series, Second Edition ed., 1968.
- [95] D. G. Fink, ed., *Electronics Engineers Handbook*. New York, New York, USA: McGraw-Hill Book Company, 1975. First Edition.
- [96] F. S. Chute and F. E. Vermeulen, "A Simple Method for Determining Electrical Resistivity and Relative Magnetic Permeability of Steel Tubulars," *Canadian Journal of Electrical and Computer Engineering*, vol. 16, pp. 154–156, April, 1991.
- [97] J. R. Welty, C. E. Wicks, and R. E. Wilson, *Fundamentals of Momentum, Heat, and Mass Transfer*. New York, New York: John Wiley and Sons, third edition ed., 1984.
- [98] D. Perterman, "Private Communication," May, 1997.
- [99] F. R. Newbold and T. K. Perkins, *The Oil Sands of Canada-Venezuela*, vol. 17, ch. Wellbore Transmission of Electrical Power, pp. 631–647. Canadian Institute of Mining Petroleum Division, 1977.
- [100] S. M. Farouq Ali, "Numerical Simulation of Thermal Recovery Methods." The Petroleum Society of CIM, Calgary Alberta Canada., October 10-12, 1989.
- [101] H. Stehfest, "Algorithm 368, Numerical Inversion of Laplace Transforms," *Communications of ACM*, vol. 13, p. 49, January, 1970.
- [102] C. Chakrabarty, S. M. Farouq Ali, and W. S. Tortike. "Effects of the Non-linear Gradient Term on the Transient Pressure Solution for a Radial

- Flow System,” *Journal of Petroleum Science and Engineering*, vol. 8, pp. 241–256, 1993.
- [103] H. J. Ramey, “Approximate Solutions for Unsteady Liquid Flow in Composite Reservoirs,” *Journal of Canadian Petroleum Technology*, pp. 32–37, January-March, 1970.
- [104] D. Bourdet, J. A. Ayoub, and Y. M. Pirard, “Use of Pressure Derivative in well Test Interpretation,” in *The 1984 California Regional Meeting*, no. SPE 12777, pp. 431–447, April 11-13, 1984.
- [105] F. J. Kuchuk, P. A. Goode, D. J. Wilkinson, and R. K. M. Thambynayagam, “Pressure Transient Behavior of Horizontal Wells With and Without Gas Cap or Aquifer,” in *The 1988 Annual SPE California Regional Meeting on Technology*, (Long Beach, California, USA), pp. 141–153, March 23-25, 1988.
- [106] F. B. Hilderbrand, *Advanced Calculus for Engineers*. Englewood Cliffs, N.J.: Prentice-Hall Inc., Ninth Edition ed., 1960.
- [107] J. Jakob, *Heat Transfer*. New York, New York: Wiley, 1949.
- [108] F. S. Chute, F. E. Vermeulen, M. R. Cervenak, and F. McVea, “Electrical Properties of Athabasca Oil Sands,” *Canadian Journal of Earth Sciences*, vol. 16, no. 10, pp. 2009–2021, 1979.
- [109] J. Lee, *Well Testing*. New York, New York, USA: Society of Petroleum Engineers of AIME, 1982.
- [110] P. W. K. Vinsome, “ORTHOMIN, An Iterative Method for Solving Sparse Sets of Simultaneous Linear Equations,” in *The Fourth Symposium of Reservoir Simulation*, no. SPE 5729, (Los Angeles, California, U.S.A), Society of Petroleum Engineering, 1976.
- [111] J. W. Grabowski, P. W. K. Vinsome, R. C. Lin, A. Behie, and B. Rubin, “A Fully Implicit General Purpose Finite-Difference Thermal Model for In Situ Combustion and Steam,” in *The 54th Annual Fall Technical Conference and Exhibition*, no. SPE 8396, (Los Vegas, California, U.S.A), Society of Petroleum Engineering, 1979.

- [112] L. G. Hepler and C. Hsi, eds., *AOSTRA Technical Handbook on Oil Sands, Bitumens and Heavy Oils*. Edmonton, Alberta, Canada: Alberta Oil Sands Technology and Research Journal of Research, 1989. AOSTRA Technical Publication Series Number 6.
- [113] G. P. Willhite, "Overall Heat Transfer Coefficients in Steam and Hot Water Injection Wells," *Journal of Petroleum Technology*, pp. 607–615, May, 1967.
- [114] H. J. Ramey, "Wellbore Heat Transmission," *Journal of Petroleum Technology*, pp. 427–435, April, 1962.
- [115] E. D. Rainville and E. P. Bedient, *Elementary Differential Equations*. New York: Macmillan Publishing Co., Inc., fifth edition ed., 1974.
- [116] H. D. Beggs and J. P. Brill, "A Study of Two-Phase Flow in Inclined Pipes," *Journal of Petroleum Technology*, pp. 607–617, May, 1973.
- [117] I. D. Mayergoyz, *The Preisach Model for Hysteresis*. Berlin, New York: Springer-Verlag, First Edition ed., 1991.

IMAGE EVALUATION TEST TARGET (QA-3)



APPLIED IMAGE, Inc
 1653 East Main Street
 Rochester, NY 14609 USA
 Phone: 716/482-0300
 Fax: 716/288-5989

© 1993, Applied Image, Inc., All Rights Reserved